PROCEEDINGS OF THE 3RD WORKSHOP
ON WENDELSTEIN VII-X

Schloß Ringberg near Lake Tegernsee

26 - 30 June 1989

Fritz Rau, editor

IPP 2/302 November 1989

MAX-PLANCK-INSTITUT FÜR PLASMAPHYSIK

8046 GARCHING BEI MÜNCHEN

MAX-PLANCK-INSTITUT FÜR PLASMAPHYSIK
Garching bei München

PROCEEDINGS OF THE 3RD WORKSHOP
ON WENDELSTEIN VII-X
Schloß Ringberg near Lake Tegernsee

26 - 30 June 1989

Fritz Rau, editor

Table of contents

ABSTRACT

This report presents the major part of the information given at the 3rd Workshop on Wendelstein VII-X, held at Schloß Ringberg near Lake Tegernsee, 26 - 30 June 1989. A number of 9 papers by members of the INTERATOM study group has been summarized. The ongoing work of the development of W VII-X is concentrated on a small number of Helias configurations with five field periods, in order to define their coil systems and the attainable parameter range. This effort aims at a simultaneous realization of the desired numbers of plasma aspect ratio, stability-β, transport, improvement in bootstrap current, etc., in order to arrive at a 'reference configuration' for this experiment.

INTRODUCTION

The third workshop on Wendelstein VII-X was held at Schloss Ringberg near Lake Tegernsee, Bavaria (FRG) from 26 to 29 June 1989.

It started with an overview on the Wendelstein VII-X project by H. Wobig, describing various critical issues of 5-period Helias configurations. Presently, the main dimensions of the Wendelstein VII-X device are : major radius 6.5 m, averaged plasma radius 0.6 m, and magnetic field 3 T.

Optimization of Helias configurations was discussed by J. Nührenberg, who found a plasma equilibrium with average beta approximately 5 % stable against ideal ballooning modes. Stability of non-local MHD-modes was analyzed numerically by C. Schwab, showing roughly the same beta-limits as the ballooning modes. Resistivity, however, leads to slowly growing modes below the threshold of ideal MHD-theory as pointed out by H. Wobig, J. Geiger and H. P. Zehrfeld.

Four papers by W. Lotz, C. Beidler, H. Maassberg and U. Gasparino, and by H. J. Gardner and A. H. Boozer were concerned with neoclassical transport and bootstrap current, utilizing Monte-Carlo computations and solutions of the drift-kinetic equation. Localized particles trapped in the modular ripples cause additional neoclassical losses. C. Beidler showed that with 12 modular coils per field period these losses are below the neoclassical ones for the whole configuration, and with 10 coils per field period within 50 % of the minor radius.

A large part of the workshop was technology-oriented. In contrast to the two preceding workshops on Wendelstein VII-X also a number of representatives of INTERATOM participated during one day. They presented the results of a feasibility study for W VII-X , dealing with the superconductor, the winding technique, cooling system, support system, time schedule of construction, and rough cost estimates. The result of the study is positive, solutions of the main problems could be found, and it was concluded that superconducting coils envisaged for Wendelstein VII-X are feasible.

The methods to derive modular coils from the finite-beta fields were discussed by P. Merkel; the contribution by J. Kißlinger was concerned with two topics: further smoothing of the coil shapes according to criteria not yet incorporated into the numerical procedures, and means to ensure a certain parameter range in the vacuum fields by use of additional external coil sets or by utilizing non-planar 'double-layer' coils.

In papers by E. Harmeyer, J. Sapper, and J. Simon-Weidner results of the electro-mechanical behaviour of non-planar modular coil systems and the resulting forces and stresses were presented, both for superconducting and water-cooled coil systems. They also commented the status of the W VII-AS coil system, where certain unexpected coil motions had been observed at fields of 2.5 T . Means to counteract these motions were discussed.

For Wendelstein VII-X , superconducting coils are preferred to water-cooled copper coils. Tests of short conductor samples in large background fields and considerations of the investigation of a small superconducting test coil and a full-size prototype coil were discussed in a contribution by W. Maurer from the Karlsruhe Institute.

Edge fields and limiter-wall loads were discussed for vacuum fields for a particular coil system, at three values of the rotational transform by F. Rau. These studies were complemented by the investigation of the neutral gas behaviour at the edge, contributed by R. Scardovelli and F. Sardei.

A different topic were studies of magnetic islands, presented by H. Wobig, F. Herrnegger, and F. Rau. The 'natural' islands and their residues were investigated for one of the various coil topologies, another contribution compared different modular Helias systems and showed the effect of external perturbations.

The last day of the workshop concentrated on experiments in Wendelstein VII-AS and projections to Wendelstein VII-X given by H. Renner, estimates of plasma parameters for this experiment by H. Wobig, and papers by V. Erckmann, F. Wesner, F. P. Penningsfeld and E. Speth on the three main heating schemes, ECRH, ICRH and NBI. Anomalous transport in Tokamaks and Stellarators was discussed in a contribution by A. Boozer.

G. Grieger summarized the highlights of the workshop.

Thus, the workshop was a critical survey of the present state of the work performed so far on Wendelstein VII-X , in order to arrive at a 'reference configuration' for this experiment. Regarding the estimated time schedule and cost estimates a reduction of the main geometrical parameters of Wendelstein VII-X has been discussed. The implications of such a reduction will be investigated in the future.

OVERVIEW ON WENDELSTEIN VII-X

H. Wobig

- Main Results of Preceding Workshops

- Physics and Engineering Design
  for Wendelstein VII-X

  - Basic Data of Wendelstein VII–X
    ⇒ Example : HS 5-8
  - Plasma Equilibrium
  - Coils and Vacuum Field
  - Particle Orbits
  - Neoclassical Transport
  - Bootstrap Current
  - Boundary Region
  - Variation of Magnetic Field
  - Forces and Stresses
  - Time Scales for Experiments in W VII-X
  - Pulse Length in W VII-X

- Summary and Conclusions

At IPP Garching, the experiment Wendelstein VII-X is being developed. The goals of this experiment are to continue the development of the modular advanced stellarator line, and to achieve quasi-steady-state operation in a temperature regime above 5 keV. This temperature regime can be reached in Wendelstein VII-X if neoclassical transport plus the anomalous transport found in Wendelstein VII-A prevails. A heating power of 20 MW will be applied to reach the reactor-relevant parameter regime.

A Helias configuration (Helical Advanced Stellarator) has been chosen because of its confinement and stability properties. This was the result of the first Workshop on Wendelstein VII-X , held at Schloß Ringberg from 18 - 20 March 1987, and published in [1] . In the 2nd Workshop on Wendelstein VII-X more detailed differences in Helias systems with four and five field periods were presented [2]. The main result was that with four field periods the β-limits of stability against ideal ballooning modes are lower than those at five field periods. Although engineering aspects of the modular coils favour solutions with four field periods because of their smaller coil aspect ratio, it was concluded to concentrate on systems with five field periods.

Other basic data of Wendelstein VII-X are [3] : major radius $R_0 = 6.5$ m, magnetic induction $B_0 = 3$ T and stored magnetic energy $W \approx 0.88$ GJ. The average plasma radius is 0.65 m. Superconducting coils are favoured because of their steady-state field, but pulsed water-cooled copper coils are also being investigated. Unlike planar circular magnetic field coils which experience only a radially directed force, twisted coils are subject to a lateral force component as well. Studies of various superconducting coil systems for Helias configurations have shown that the magnitudes of these radial and lateral force components are comparable. Based on a support model the mechanical stresses are calculated; all components of the stress tensor are of equal importance. Other studies are concerned with the many complex engineering aspects presented by the construction of non-planar superconducting coils.

- Plasma Equilibrium

  Helias equilibria are characterized by

  - a large reduction of Pfirsch-Schlüter currents
    $(j_\parallel < j_\perp)$
  - a very small Shafranov-shift
  - a small variation of ι with finite β
  - a small variation of the plasma boundary

  The ideal equilibrium is sufficiently optimized. Further study is needed with respect of non-ideal effects and island formation.

- Coils and Vacuum Field

  The NESCOIL-Code provides a method to find modular coils starting from a last magnetic surface.

  Some additional corrections of the coils are made.

- Particle Orbits

  Circulating particles are optimized ⇒
  drift orbits are close to magnetic surfaces :
  $(\Delta << \rho/\iota$, $\rho =$ Larmor-radius)

  Fraction of trapped particles is kept
  relatively small $(f_t \approx 30 - 60\%)$

  Quasi-helically invariant equilibria provide complete confinement of trapped particles.

  Problem : α-particles in reactor ⇒
  Finite-β effects reduce α-particle losses.

[1] Proceedings of the Workshop on Wendelstein VII-X , EUR 11058 EN, ISBN 92-825-7480-6, Brussels and Luxembourg 1987, F. Rau and G.G. Leotta, editors.

[2] Proceedings of the 2nd Workshop on Wendelstein VII-X , EUR 11705 EN, ISBN 92-825-9010-0, Brussels and Luxembourg 1988, F. Rau and G.G. Leotta, editors.

[3] Physics and Engineering Design for Wendelstein VII-X , C. Beidler et al., IPP Garching Report IPP 2/300, 1989.

- Neoclassical Transport

  Methods :

  Monte-Carlo technique

  Solution of bounce-averaged drift kinetic equation

  DKES-Code

  Results :

  In the $1/\nu$-regime neoclassical transport is characterized by an effective ripple $\epsilon_{eff} \leq 1\%$.

  The effect of modular ripple can be kept small.

  Neoclassical transport in Helias - configurations is sufficiently optimized.

- Bootstrap Current

  Methods of calculation :

  Analytic methods
  Monte-Carlo technique
  DKES-Code

  Maximum current in the $lmfp$-regime
  Evaluation of geometrical factor G_b
  In quasihelical equilibria a finite bootstrap current exists.

  Zero bootstrap current is possible by proper balance of toroidal and helical effects

  $$B = B_o \left(1 + \epsilon_t cos\theta + \epsilon_h cos(\theta - 5\varphi) + \ldots\right)$$

  If $\epsilon_t \approx 1/3\epsilon_h \rightarrow G_b \approx 0$

  Example : HS 5-7 and HS 5-8

  Maximum bootstrap current in W VII-X : ≤ 50 kA .

- Boundary Region   *Scardovelli, Sardei, Rau*

  Problems :

  Particle orbits, wall loading, plasma model, divertor geometry.

  Methods :

  Field line tracing, particle orbit calculations, Monte-Carlo technique, neutral gas code (DEGAS).

  The aim is to achieve a high recycling regime and to minimize wall loading by high-energy particles.

  A certain control of neutral particles is possible by appropriate sreening plates.

- Variation of Magnetic Field   *Kißlinger*

  Experimental flexibility requires the possibility to vary the rotational transform.

  Two concepts have been developed :

  - Double-layer concept
  - Additional TF-coils

  A small vertical field is possible with the TF-coils.

  ι-variation in HS 5-8 :

  - $\iota(0) = 0.9 \rightarrow 1.2$
  - $\iota(a) = 1.0 \rightarrow 1.4$

- Forces and Stresses   *Harmeyer, Jaksic*

  Methods :

  EFFI, SAP and ADINA

  Problems :

  Boundary conditions, geometry of support system.

  Maximum von Mises stress in HS 5-8 :

  $\sigma_{vM} \approx 150$ MPa

  Maximum shear stress in HS 5-8 :

  $\sigma_{ST} \approx 38$ MPa

- Time Scales in Wendelstein VII-X

  Estimated energy confinement times, $T \approx 2 - 5$ keV

  a) Neoclassical confinement and extrapolation from W VII-A and W VII-AS
  $\Rightarrow \tau_E = 0.5 - 1.0$ s

  b) LHS-scaling, K.G.-Scaling
  $\Rightarrow \tau_E = 0.2 - 0.5$ s

  Particle confinement time $\tau_p \approx 5\tau_E$
  $\Rightarrow \tau_p = 2.2 - 5$ s

  Resistive time $\tau_R = L/R \approx 2.4 \cdot 10^{-4}\bar{T}_e^{3/2}$ s
  $\bar{T}_e \approx 1$ keV $\Rightarrow \tau_R = 7.6$ s

  Equilibrium time for limiters, temperature $= const.$
  $\tau_{Lim} \geq 5$ s .

- Pulse Length in Wendelstein VII-X

  For steady state operation of W VII-X a pulse length of several confinement times is necessary.

  The pulse length is determined by :

  - the maximum confinement times,
  - the need to combine various heating methods and a time dependent heating programme during one pulse,
  - the need to reach equilibrium of net toroidal currents, either bootstrap currents or currents driven by the heating systems, $\rightarrow$ the characteristic time scale being the resistive time,
  - the need to reach equilibrium of plasma-wall interaction.

  $\Rightarrow$ For these reasons the pulse length for steady state operation in Wendelstein VII-X should be

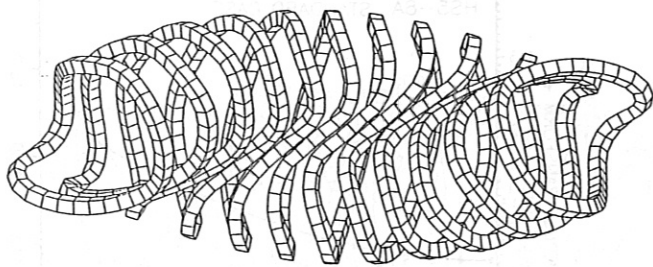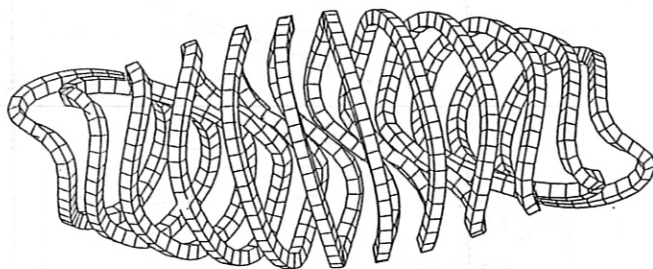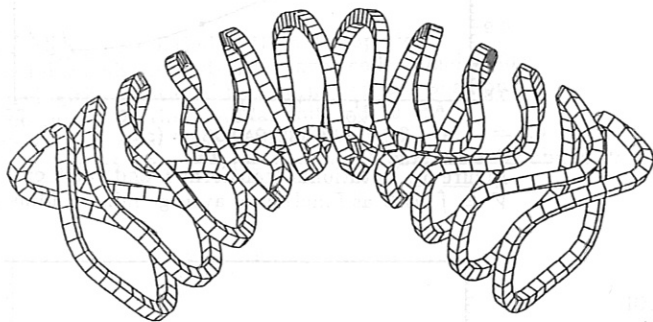 $$\tau_{pulse} \approx 10 - 30 \text{ s} .$$

4

Figure 1 : Coil system HS 5-8 .
From top to bottom: radial inside, top and radial outside.
The minimum distance between two centers is 22 cm
(coil 1 and coil 2) .

HS 5-8
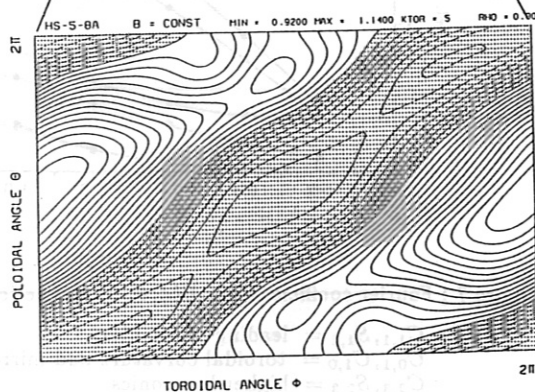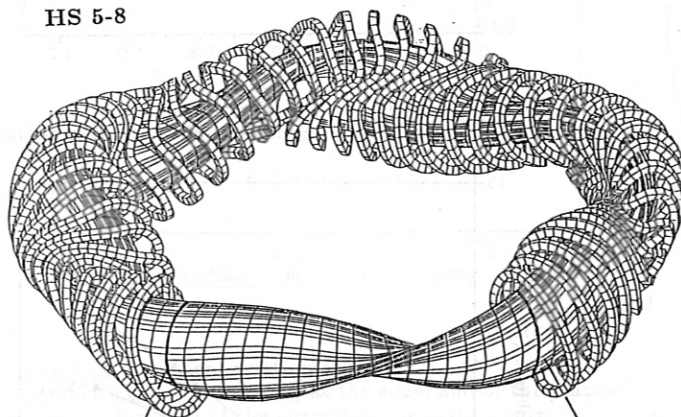
Figure 2 : Magnetic surface and $|B|$ = const on a field period.
$r = 0.8$ a, $B_{min} = 0.92$, $B_{max} = 1.14$.

Figure 3 :

Perspective view of a flux surface (top).

Lines of $|B|$ = const. and the shape of the Pfirsch - Schlüter currents in the $\varphi - \theta$ plane (bottom).

From the low value of $\langle |j_{\parallel}/j_{\perp}| \rangle = 0.63$, a small Shafranov-shift and small changes of ι and shear with β are expected.

5

STANDARD CASE

$\iota_0 = 1.02, \iota_a = 1.18$

3.0 T

2.0 T

100.7

0.0
625.0

825.0

-100.

INNER
OUTER
BOUNDARY OF THE COIL

2.0 T

LINER

100.0

3.0 T

0.0
525.0   625.0   125.0

-100.0

100.0

3.0 T

2.5 T

0.0
5.5.0   625.0   725.0
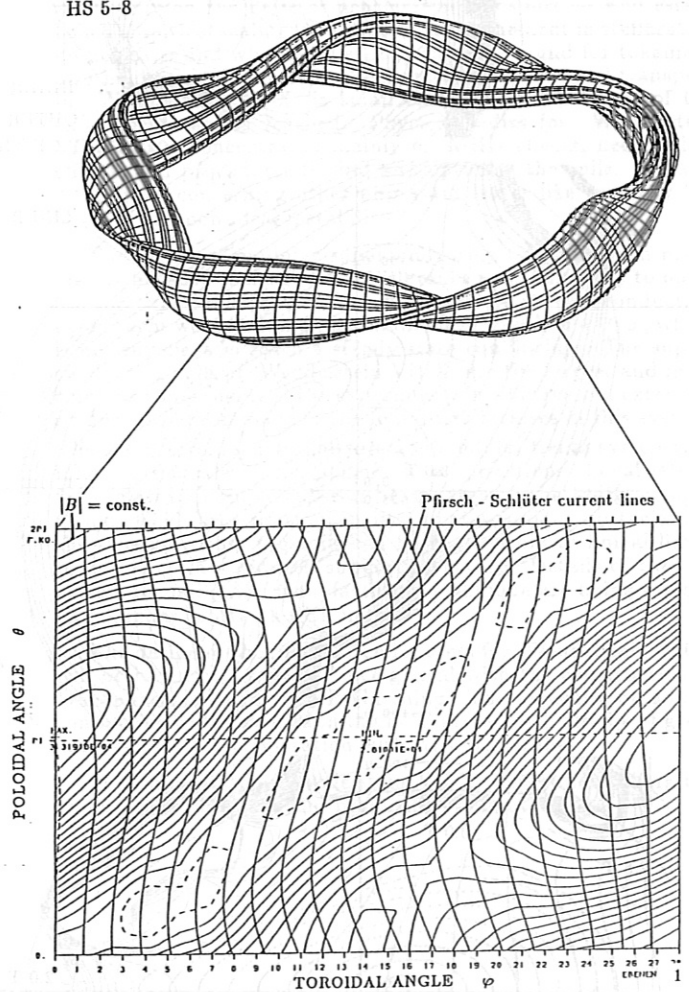
2.0 T

-100.0

0

1/4

1/2
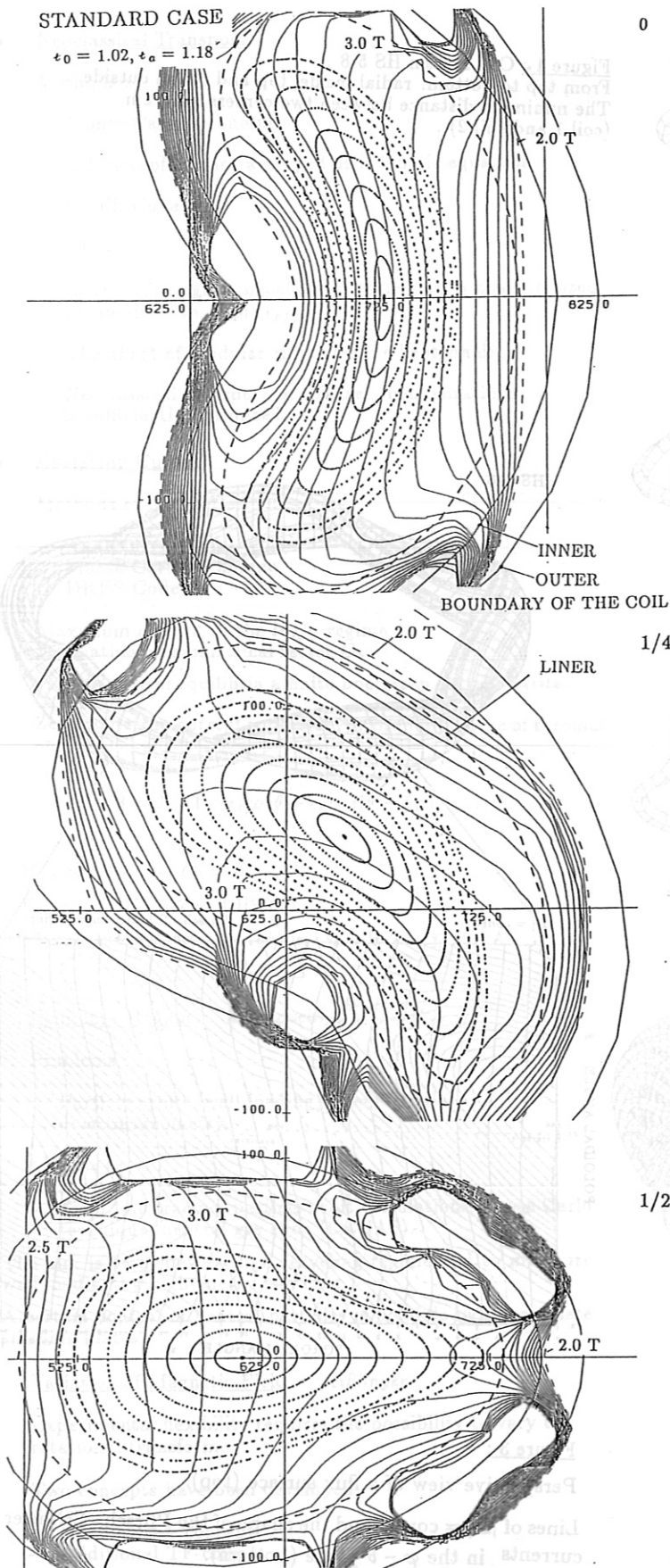
Figure 4 : Poincaré plots of the vacuum magnetic fields and lines of $|B| = const.$ The dashed line indicates the position of a tentative first wall.

HS-5-8A   (R = 6.5 m   A = 0.62 m)

Figure 5 : Rotational transform ι and value of $V' = \int dl/B$ as function of average minor radius.

Figure 6 : HS 5-8 Standard Case : B_{min} and B_{max} versus normalized plasma radius.

Figure 7 : Fourier coefficients on $B(\phi, \theta)$ in magnetic coordinates.

$C_{1,1}, S_{1,1} =$ leading harmonics,
$C_{0,1}, C_{1,0} =$ toroidal curvature and mirror terms,
$C_{2,3}, S_{2,3} =$ higher harmonics.

6

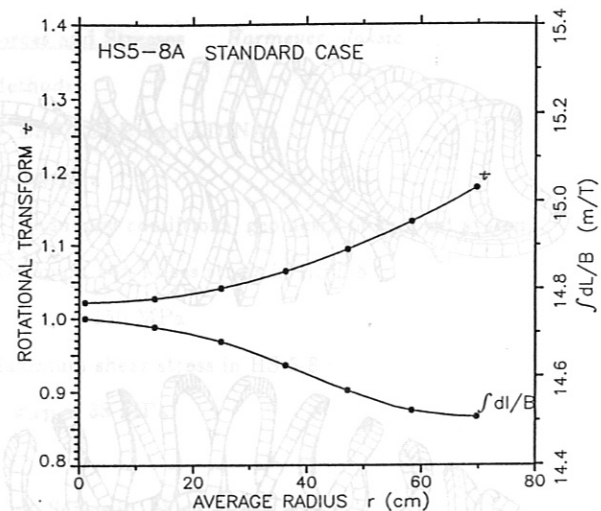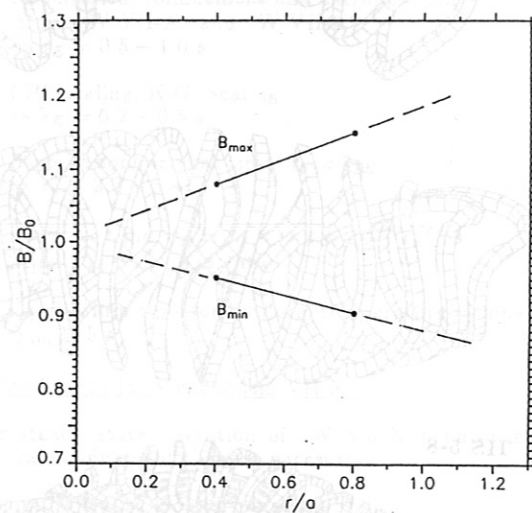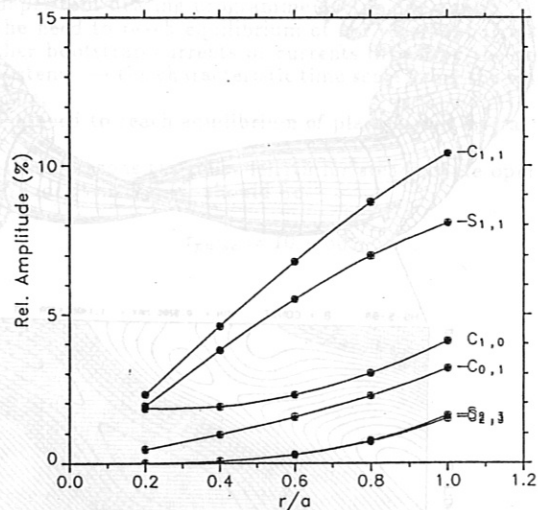Figure 8 : One period of HS 5-8 , top view .
modular coils and external planar coils A and B for
varying the rotational transform and axis position.
The current in the modular coils is 1.75 MA .
HS 5-8 Standard Case: $t(0) = 0.9 \rightarrow 1.2$, $t(a) = 1.0 \rightarrow 1.4$
A current of ± 0.5 MA per planar coil changes t by about 20 % .

Figure 9 : Parameter variation of HS 5-8 .
Dependence of t_o on axis, t_a at the edge, and of the magnetic well
$\Delta V'/V'$ as function of the current in the planar coils.
The current in the modular coils is 1.75 MA .

SUMMARY AND CONCLUSIONS

Optimization of stellarator equilibria has led to the Helias concept, which is characterized by a low Shafranov shift and MHD stability limits up to $\langle \beta \rangle \approx 5\%$. The present Helias configurations HS 5-7 and HS 5-8 have stability limits of $\bar{\beta} \leq 4\%$, further modification is needed to improve this value. Neoclassical transport and the bootstrap current have been reduced to a tolerable level by optimization of the structure of B on magnetic surfaces. Based on these theoretical results, the Wendelstein VII-X experiment is being planned with the goals of achieving reactor-relevant parameters and demonstrating the reactor capability of this stellarator line.

In order to reach these goals requires a heating power of 20 MW; several heating scenarios with ECRH, NBI and ICRH are envisaged. Presently a prediction of plasma parameters can be made only on the basis of neoclassical transport — well established empirical scaling laws of plasma confinement in stellarators do not exist and whether the empirical laws found for tokamaks also hold for stellarators is questionable. Neoclassical transport in Wendelstein VII-X is small enough that the goals of the experiment can be reached. Physics studies for Wendelstein VII-X have concentrated mainly on MHD effects, neoclassical effects, and procedures to find and optimize the coils. Work is in progress concerning other important issues like impurity behaviour and non-ideal instabilities.

The choice of modular superconducting coils has been made mainly because of their reactor relevance and the ability to operate the experiment in quasi-steady state. A normal conducting experiment would allow a maximum pulse length of 4 - 5 s , which is not sufficient to reach a steady state equilibrium. The superconducting coils of Wendelstein VII-X are the largest and most complex components of the experiment; for this reason, extensive studies have been made of the forces and stresses in this system.

The net electromagnetic coil forces in modular Helias systems are inhomogeneous with components in all directions. Local lateral forces within a single coil can be as large as the radial components. This force inhomogeneity is not a serious obstacle and the stresses within the coils can be kept within technical limits by utilizing an optimized support structure. Details of the coil system including the manufacturing technique are being investigated under contracts with industry.

The design of the modular coil system for Wendelstein VII-X will be based on the experience gained with the construction of Wendelstein VII-AS at IPP Garching. The expertise on superconducting coils obtained in the LCT-project will also be of great influence via the cooperation with KfK Karlsruhe.

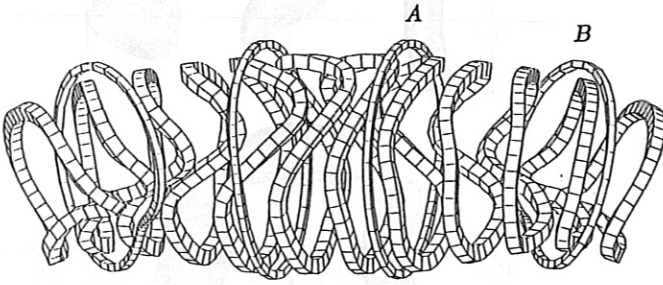In summary, the Wendelstein VII-X experiment offers the opportunity for a new and promising stellarator line .
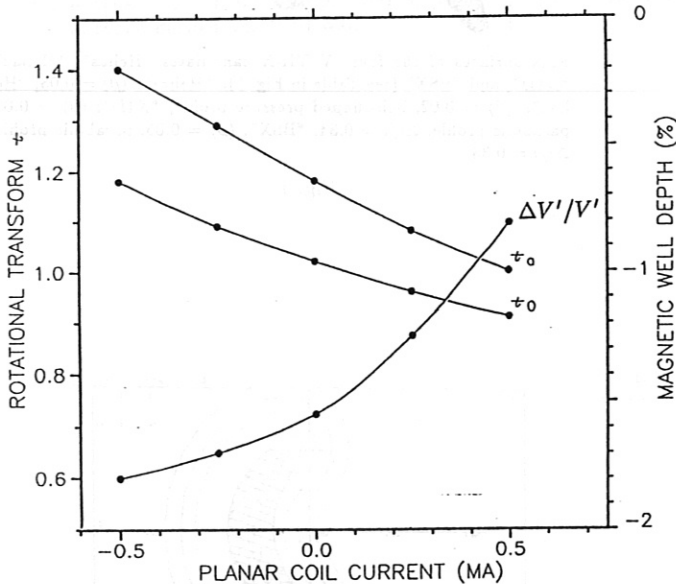
Optimization of Helias for W VII-X

W. Lotz, P. Merkel, J. Nührenberg,
A. Schlüter, R. Zille

Max-Planck-Institut für Plasmaphysik
IPP-EURATOM Association
D-8046 Garching bei München
Federal Republic of Germany

Optimization of Helias[1] equilibria at finite-β was attempted with respect to the following set of criteria: 1. high quality of vacuum field magnetic surfaces, 2. good finite-β equilibrium properties, 3. good MHD stability properties, 4. small neoclassical transport in the $\frac{1}{\nu}$-regime, 5. small bootstrap current in the lmfp-regime, 6. good collisionless α-particle containment, 7. good modular coil feasibility. Criteria 1 and 7 are taken into account by solving Helias boundary value problems with side conditions on the shaping parameters. Criteria 2 and 3 are satisfied by maintaining resistive-interchange and ballooning stability at $\langle \beta \rangle \approx 0.05$ for configurations with 5 periods and aspect ratio of approximately 10. While maintaining resistive-interchange stability is directly incorporated into the optimization, ballooning

---

[1] Nührenberg, J., R. Zille, Phys. Letters A **114A** (1986) 129; **129** (1988) 113

stability is taken into account through its driving terms.[2] Criteria 4, 5, and 6 are taken into account by optimizing the structure of $B(\theta, \phi)$ in magnetic coordinates. The figure shows flux surface cross-sections at $\langle \beta \rangle = 0.05$ of a particular example (Helias50B) obtained in this way.
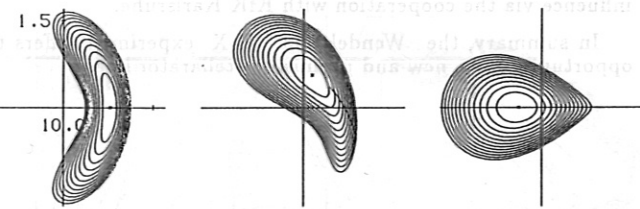

Further parameters of this example are: magnetic well of 0.015, $\iota(0) \approx 5/6$, $\iota(1) = 0.96$ in the vacuum field; δ_e (equivalent ripple characterizing the $\frac{1}{\nu}$ transport and obtained by Monte Carlo simulations)[3] approximately 0.01 at half the plasma radius; reduction of the bootstrap current (obtained by Monte Carlo simulation of a stationary distribution function)[4] as compared to its value in the equivalent tokamak by a factor of approximately 10; collisionless α-particle loss (obtained by following guiding centre orbits of a representative set of α-particles) of approximately 10%.

---

[2] Nührenberg, J., R. Zille, Sherwood Theory Conf. 1989, San Antonio

[3] Lotz, W., J. Nührenberg, Phys. Fluids **31** (1988) 2984

[4] Lotz, W., J. Nührenberg, A. Schlüter, JCP **73** (1987) 73
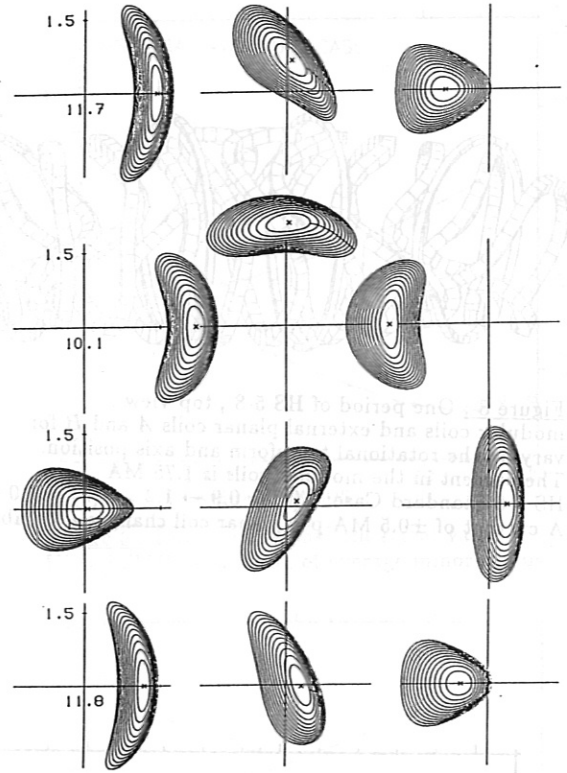
Flux surfaces of the four W VII-X candidates "Helias", "Heliac", "X1D", and "BSX" (see Table in Fig. 5). "Helias": $\langle \beta \rangle = 0.05$; "Heliac": $\langle \beta \rangle = 0.02$, bell-shaped pressure profile; "X1D": $\langle \beta \rangle = 0.02$, parabolic profile, $\Delta \iota / \iota = 0.34$; "BSX": $\langle \beta \rangle = 0.05$, parabolic profile, $\Delta \iota / \iota = 0.33$.

Fig. 1
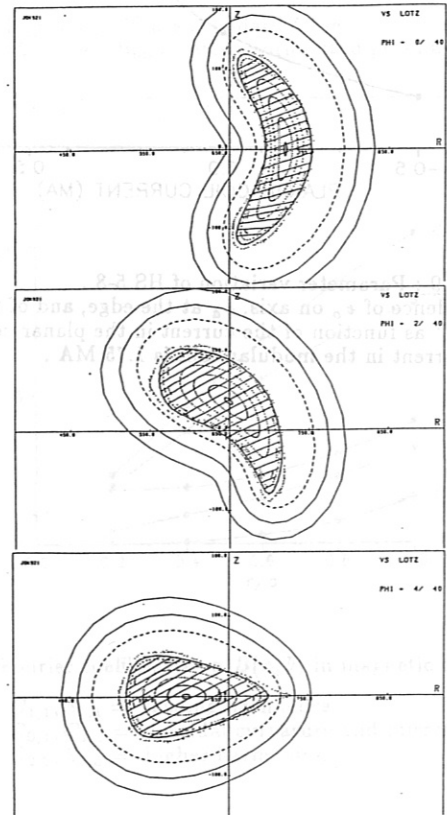
Cross section of magnetic surfaces in HS5-8 with enlarged dimensions. The dashed line indicates the first wall.

Fig. 2

Cross section of the vacuum magnetic surfaces of HS-5-8 at: (left) the beginning of a field period, (center) 1/4 field period, (right) 1/2 field period. Solid lines: coil contours, dashed line: first wall.
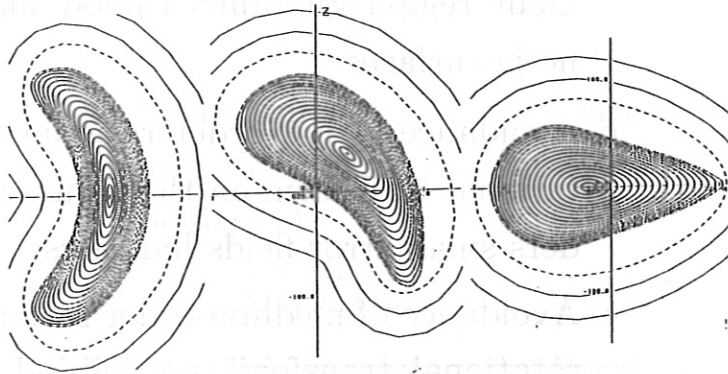
Fig. 3

IPP-CRAY JUN909

13.07.89
02.03.89

Fig. 4

OPTIMIZATION PROCEDURE

- Optimization of plasma behaviour in the confinement region

- The geometry of the confinement boundary region (last closed flux surface) completely determines the properties of the confinement region

- Optimization by solving boundary value problems, the geometry parameters of the boundary being the optimization variables
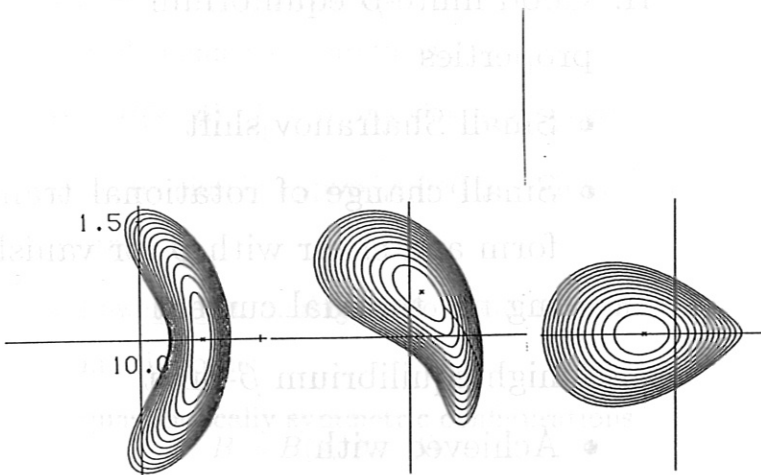
Fig. 5

OPTIMIZATION PROCEDURE
continued

- In a second step: optimization of coils, again by solving boundary value problems at the boundary of the confinement region

- Boundary value problems as basic steps in the optimization procedure allow large steps in the stellarator configurational space

Fig. 6

BOUNDARY REPRESENTATION

$$R = R_0 + R_{0,1}\cos V + R_{0,2}\cos 2V$$
$$+ (1 - \Delta_{1,0})\cos U$$
$$- \Delta_{1,-1}\cos(U - V)$$
$$- \Delta_{1,-2}\cos(U - 2V)$$
$$+ \Delta_{1,1}\cos(U + V)$$
$$+ \Delta_{1,2}\cos(U + 2V)$$
$$+ \Delta_{2,0}\cos 2U$$
$$+ \Delta_{2,-1}\cos(2U - V)$$
$$+ \Delta_{2,-2}\cos(2U - 2V)$$

Fig. 7

$$Z = \quad Z_{0,1}\sin V + R_{0,2}\sin 2V$$
$$+ (1 + \Delta_{1,0})\sin U$$
$$+ \Delta_{1,-1}\sin(U - V)$$
$$+ \Delta_{1,-2}\sin(U - 2V)$$
$$+ \Delta_{1,1}\sin(U + V)$$
$$+ \Delta_{1,2}\sin(U + 2V)$$
$$+ \Delta_{2,0}\sin 2U$$
$$+ \Delta_{2,-1}\sin(2U - V)$$
$$- \Delta_{2,-2}\sin(2U - 2V)$$

Fig. 8

PRINCIPLES OF OPTIMIZATION

I. High quality of vacuum field magnetic surfaces

- A regular boundary of the confinement region guarantees good magnetic surfaces.
- Avoidance of low-order rational rotational transform on the torus renders small error fields harmless.
- Avoidance of medium-order rational rotational transform per period or use of significant shear ($\Delta\iota/\iota \sim 0.2$)
- Controlled positioning of island chain at the boundary as the basis of a divertor concept

Fig. 9

II. Good finite-β equilibrium properties

- Small Shafranov shift
- Small change of rotational transform and shear with β for vanishing net toroidal current
- $\rightarrow$ high equilibrium β-limit
- Achieved with

$$\langle j_{\parallel}^2 / j_{\perp}^2 \rangle \lesssim 1$$

Fig.10

III. Good MHD stability properties

Stability of small-shear equilibria governed by:

o Magnetic well stabilization: creation of vacuum field magnetic well of $\approx 2\%$ by exploiting the helical curvature and flux surface shaping (ellipticity, indentation, triangularity)

o
$$\langle j_\parallel^2 / j_\perp^2 \rangle \lesssim 1$$

o Side conditions on geometry (local curvature, flux surface spacing) to avoid ballooning instabilities

Fig.11

IV. Good neoclassical transport properties in the $\frac{1}{\nu}$-regime

o Lower theoretical limit:

isodynamic configurations

$B = B(s, \phi)$, $j_\parallel \equiv 0$, classical transport;

cannot be closely approximated at finite aspect ratio

o Lower limit analogous to ideal axisymmetric torus:

quasi-helically symmetric configurations,
$B = B(s, \theta - \phi)$,

neoclassical banana transport without $\frac{1}{\nu}$-regime

o General case:
$$D_R^* \propto \delta_e^{3/2} L^*$$

configurations with $\delta_e \approx 0.02$

Fig.12

V. Small bootstrap current in the long mean free path regime

o Configurations dominated by toroidal curvature show bootstrap current

o Quasi-helically symmetric configurations show reverse bootstrap current

o Configurations with vanishing bootstrap current exist

Fig.13

VI. Good α-particle confinement

o Stellarator with $B_{m,n}$ spectrum as complicated as in W VII-AS does not confine reflected α-particles

o Quasi-helically symmetric configurations completely confine collisionless α-particles

o Configurations with 3D-structure of $B(s, \theta, \phi)$ exist for which fraction of prompt losses $\lesssim .1$ at $\langle \beta \rangle \approx 0.05$

Fig.14

VII. Good modular coil feasibility

- Strong shaping of the plasma boundary yields better results

- Side conditions on shaping parameters qualitatively ensure modular coil feasibility

Can configurations satisfying
I – VII be found?

Fig.15

1. Vacuum field surfaces
   (regular boundary, resonances, shear)
   $$\delta_{\frac{1}{6}} \lesssim .1 \qquad .2$$

2. Equilibrium
   (Shafranov-shift, $\iota(\beta)$) $\langle j_\parallel^2/j_\perp^2 \rangle \lesssim 1$

3. Stability
   (resistive interchanges, ballooning)
   $\langle \beta \rangle \gtrsim .05$

4. Neoclassical transport
   $(\delta_e \leftarrow B_{mn}s)$ $\delta_e \lesssim .02$

5. Bootstrap current
   $(B_{1,0} \leftrightarrow B_{1,-1})$ $J_{BS} \lesssim 0.1 J_{BS,tok}$

6. α-particle confinement
   $(B_{mn}s)$ $f_\alpha \lesssim .1$

7. Modular coils
   (distances,   curvatures)
   $D_{wall} \gtrsim .1$ m $R_{curv} \gtrsim .2$ m

Fig.16

BALLOONING OPTIMIZATION OF HELIAS EQUILIBRIA

Most unfavorable curvature at

$$s, \; \theta = 0, \; \phi = 0$$

Minimization of

$$a\tilde{D} \approx \sqrt{g}|\nabla s|^2 (\sqrt{g}p'^2/B^2 - p'\sqrt{g}_{,s})$$

at finite β and keeping the resistive interchange criterion satisfied.

Fig.17

IPP–CRAY JUN89Ø

24.07.89   17.47:11
01.03.89   11:57:12

1.5
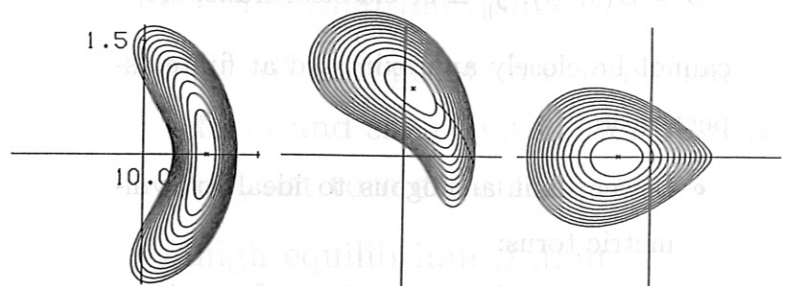
10.0

Fig.18

12

HELIASNURBINB2 BETA=5.0

Fig.19

EXISTENCE OF 'PERFECT' (I-VII)-STELLARATORS

- Strictly
  according to present knowledge:
  no
  probably: no

- But, according to present knowledge:
  yes, if finite-β improvement of α-particle confinement is sufficient for viability
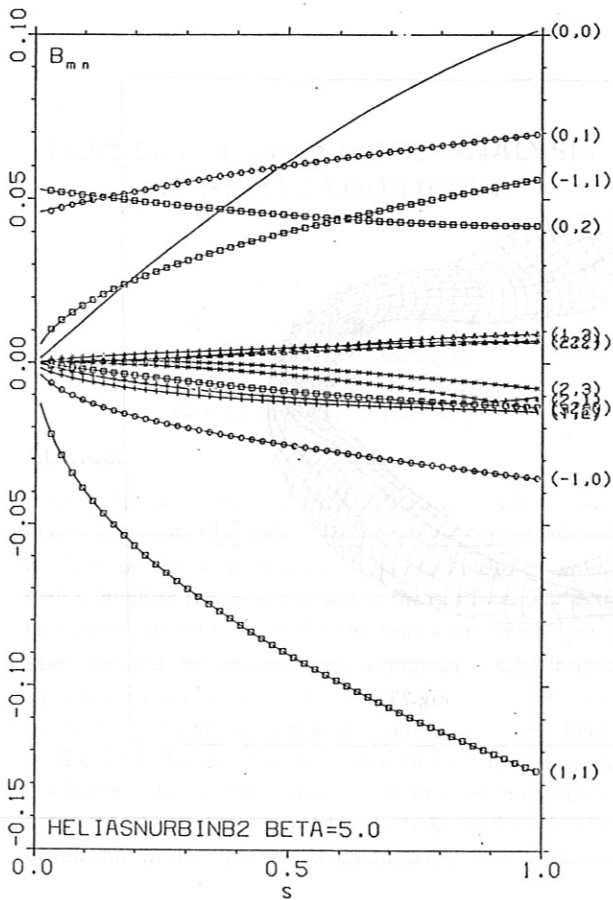
Fig.21

OVERALL OPTIMIZATION OF HELIAS CONFIGURATIONS

At finite β

- Side conditions on shaping parameters

- Resistive interchange criterion satisfied

- Ballooning optimization

- $B_{m,n}$ optimization

Evaluation of $\langle\beta\rangle, \delta_e, BS, \alpha$'s
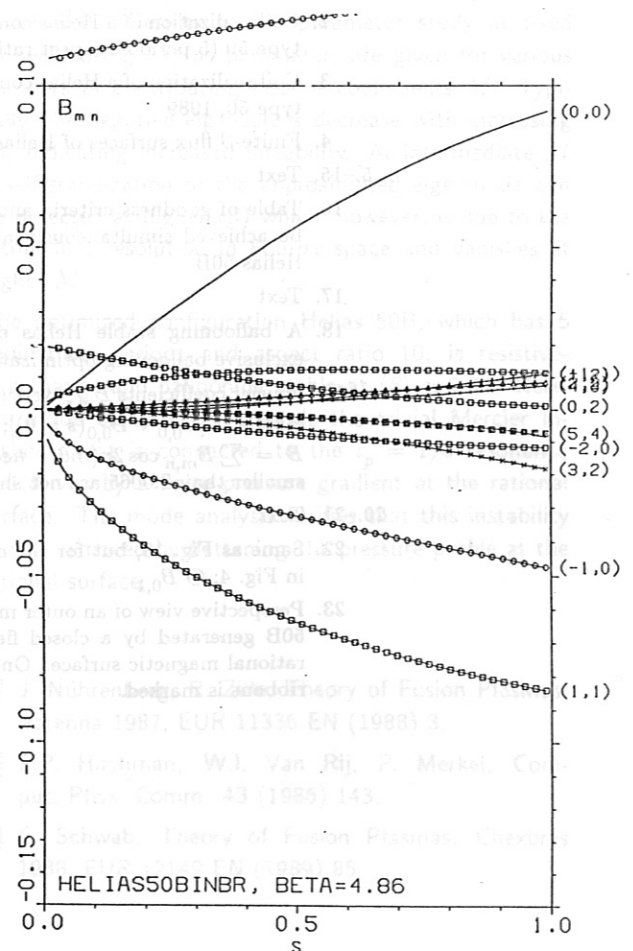
- Coil optimization

Fig.20

HELIAS50BINBR, BETA=4.86
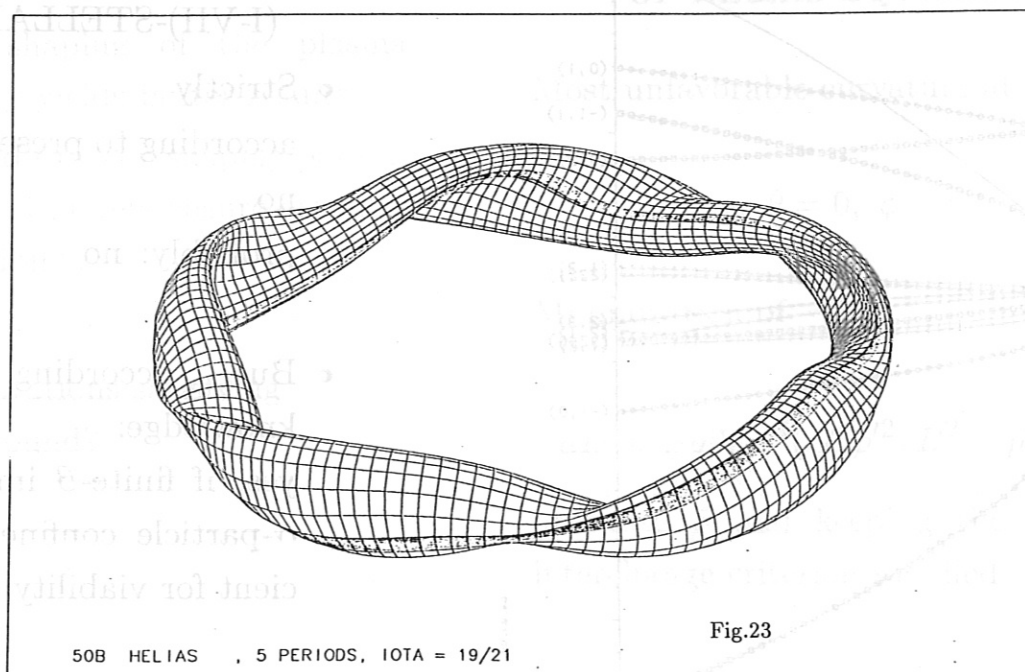
Fig.22

50B HELIAS , 5 PERIODS, IOTA = 19/21

Fig.23

FIGURE CAPTIONS

1. W VII-X candidates 1987
2. Coil realization of a Helias configuration (HS5-8) of the type 50 (5 periods, aspect ratio 10) 1988
3. Coil realization of a Helias configuration (HS5-8) of the type 50, 1989
4. Finite-β flux surfaces of Helias 50B

5.–15. Text

16. Table of goodness criteria and characteristic values to be achieved simultaneously and actually achieved by Helias 50B

17. Text

18. A ballooning stable Helias equilibrium obtained by exclusive ballooning optimization

19. Fourier coefficients $B_{m,n}$ versus normalized flux surface label s; $-[B_{0,0} - B_{0,0}(s = 0)]$;
    $B = \sum B_{m,n} \cos 2\pi(m\theta - n\phi)$. Fourier coefficients smaller than 0.0065 are not shown.

20.–21. Text

22. Same as Fig. 19, but for the configuration 50B shown in Fig. 4; $\bigcirc B_{0,1}$

23. Perspective view of an outer magnetic surface of Helias 50B generated by a closed field line on a high-order rational magnetic surface. One of the 19 poloidal flux ribbons is marked.

NON-LOCAL MHD-MODE ANALYSIS
OF HELIAS EQUILIBRIA

C. Schwab

Max-Planck-Institut für Plasmaphysik
IPP-EURATOM Association
D-8046 Garching bei München
Federal Republic of Germany

Abstract

A formulation of the ideal MHD energy principle in magnetic coordinates [1] yields the basis for a computational analysis of non-local modes in 3D-stellarator equilibria which involves two components of the displacement vector (code version CAS3D2*), the third component being used for the incompressibility condition. Equilibrium calculations are performed with a 3D-code which exploits the assumption of nested magnetic surfaces (here, VMEC [2]); the results can readily be used to construct the input data for the stability code in magnetic coordinates [1]. A combination of two techniques, i.e. Fourier expansion in the angle-like coordinates and a simple finite element method in the radial direction, is used to set up the matrix which corresponds to the energy functional [3]. A negative lowest eigenvalue, computed from a suitable matrix eigenvalue problem, indicates an unstable equilibrium.

Unstable toroidal $\ell = 1, 2$ equilibria require only one Fourier component in the perturbation functions for a demonstration of instability. This shows that the equilibrium geometry and the structure of the energy minimization decouple to a large extent. The mode analysis of less unstable configurations has of course to be based on a large number of Fourier components. So, as the size of the matrices increases quadratically with the number of Fourier components, it is crucial to determine the dominant components. An approximation to the eigenvector corresponding to the lowest eigenvalue is used to recalculate the various contributions to the energy functional and thus information on an improved approximation to the eigenvector can be obtained. These energy contributions clearly separate into stabilizing and destabilizing parts, an effect that is due to the formulation of the energy principle [3]. This gives rise to an algorithm which iteratively selects the Fourier components that dominate the minimization problem. In Helias equilibria the dominant coupling process is

---

*Code for the Analysis of the MHD Stability of 3D equilibria using 2 perturbation functions

the interaction of the eigenvector approximation with the fundamental helical and toroidal components of the parallel current density. The mode structure found in this way is then used to investigate related, less unstable configurations.

It is computationally demonstrated that energy minimization occurs simultaneously with annihilation of the field compression term of the energy functional, which leads to a linear relation between the two components of the perturbation vector. An improved code version (CAS3D1) takes this relation into account, so that the discrete problem is reduced to the determination of one component of the displacement vector. This causes the matrices to be a quarter of their original size, so that Helias equilibria can easily be investigated where the mode analysis needs at least 20 Fourier components in order to show instability.

Applications include studies on Helias configurations with 4 equilibrium periods, aspect ratio 8, $\langle j_\parallel^2 / j_\perp^2 \rangle \approx 1$ and iota profiles with small shear, where the rational $\iota = 3/4$ surface occurs at approximately $s = 0.5$. Vacuum field magnetic well and the value of $\langle \beta \rangle$ serve as stability parameters and cover regions that are relevant to experimental work. One-dimensional parameter studies, either at fixed $\langle \beta \rangle$ or at fixed vacuum field (VF) magnetic well, are used to derive stability limits which can be compared to those given by local criteria. So far, the Mercier criterion and the mode analysis yield consistent stability limits, the results differ only in 10^{-3} in VF-well. Results of the parameter study at fixed VF-well, using $\langle \beta \rangle$ as parameter, are given for various numbers of contributing Fourier coefficients M. Typically, the negative eigenvalues decrease with increasing $\langle \beta \rangle$ indicating increased instability. At intermediate M a self-stabilization of the approximated eigenmode can be detected at higher $\langle \beta \rangle$ which, however, is due to the insufficient resolution in Fourier space and vanishes at higher M.

The optimized configuration Helias 50B, which has 5 equilibrium periods and aspect ratio 10, is resistive-interchange and ballooning stable at $\langle \beta \rangle \approx 0.05$. Here, the mode analysis only reveals the trivial Mercier instability that is connected to the $\iota_p = 1/6$ resonance and driven by a finite pressure gradient at the rational surface. The mode analysis verifies that this instability can be removed by flattening the pressure profile at the rational surface.

[1] J. Nührenberg, R. Zille, Theory of Fusion Plasmas, Varenna 1987, EUR 11336 EN (1988) 3.

[2] S.P. Hirshman, W.I. Van Rij, P. Merkel, Comput. Phys. Comm. **43** (1986) 143.

[3] C. Schwab, Theory of Fusion Plasmas, Chexbres 1988, EUR 12149 EN (1989) 85.

MAGNETIC COORDINATES

- equilibrium calculations by 3D codes exploiting the assumption of nested surfaces (here: VMEC)

  → results handy for the construction of magnetic coordinates

- description of coordinates

  s radial, labelling the flux surfaces

  θ poloidal

  ϕ toroidal

- toroidal domain consists of N field periods, one given by

  $\vec{r} = \vec{r}(s, \theta, \phi)$ for all

  $(s, \theta, \phi) \in \Omega = [0, 1] \times [0, 1] \times [0, 1]$

Fig. 1

- Jacobian

$$\sqrt{g} = \vec{r}_{,s} \cdot \vec{r}_{,\theta} \times \vec{r}_{,\phi}$$

- representation of the magnetic field

$$\vec{B} = -\frac{F_T'}{\sqrt{g}}\vec{r}_{,\phi} - \frac{F_P'}{\sqrt{g}}\vec{r}_{,\theta}$$

$$= I\nabla\phi + J\nabla\theta + \tilde{\beta}\nabla s$$

- magnetic DE for $\tilde{\beta}$

$$\sqrt{g}\vec{B} \cdot \nabla\tilde{\beta} = p'(\sqrt{g} - V')$$

- equation for the current density

$$\sqrt{g}\vec{j} = (\tilde{\beta}_{,\phi} - I')\vec{r}_{,\theta} + (J' - \tilde{\beta}_{,\theta})\vec{r}_{,\phi}$$

Fig. 2

STELLARATOR SYMMETRY

$$R(s, \theta, \phi) = R(s, -\theta, -\phi)$$

$$Z(s, \theta, \phi) = -Z(s, -\theta, -\phi)$$

(cylindrical coordinates)

→ purely even or odd Fourier decompositions for the equilibrium quantities

Fig. 3

MHD ENERGY PRINCIPLE

$$\delta^2 W = \frac{1}{2} \iiint d^3r [\vec{C}^2 - A(\vec{\xi} \cdot \nabla s)^2]$$

where

$$\vec{C} = \nabla \times (\vec{\xi} \times \vec{B}) + \frac{\vec{j} \times \nabla s}{|\nabla s|^2}\vec{\xi} \cdot \nabla s$$

and

$$A = 2|\nabla s|^{-4}(\vec{j} \times \nabla s) \cdot (\vec{B} \cdot \nabla)\nabla s$$

- $\delta^2 W$ is a quadratic form

Fig. 4

• evaluation of A

$$\sqrt{g}\,A = \frac{\vec{\jmath}^{\,2}\sqrt{g}}{|\nabla s|^2} + F_T''I' + F_P''J' - F_T''\tilde{\beta}_{,\phi} - F_P''\tilde{\beta}_{,\theta}$$

$$+ \sqrt{g}\,\vec{B}\cdot\nabla\frac{\sqrt{g}j^\phi g^{\theta s} - \sqrt{g}j^\theta g^{\phi s}}{|\nabla s|^2} - p'\sqrt{g}_{,s}\;,$$

where

$$|\vec{\jmath}|^2 = \frac{1}{B^2}\left[(\vec{\jmath}\cdot\vec{B})^2 + p'^2|\nabla s|^2\right]$$

• decomposition of $\vec{C}$

$$\vec{C} = C^1\vec{e}_1 + C^2\vec{e}_2 + C^3\vec{e}_3$$

basis vectors (orthonormal system)

$$\vec{e}_1 = \frac{\nabla s}{|\nabla s|}, \qquad \vec{e}_2 = \frac{\nabla s \times \vec{B}}{|\nabla s|B}, \qquad \vec{e}_3 = \frac{\vec{B}}{B}$$

Fig. 5

contravariant components of $\vec{C}$

$$C^1 = \frac{1}{|\nabla s|}\vec{B}\cdot\nabla\xi^s$$

$$C^2 = -\frac{|\nabla s|}{B\sqrt{g}}\left[\sqrt{g}\vec{B}\cdot\nabla\eta - (F_T'F_P'' - F_T''F_P')\xi^s\right.$$

$$\left. + \frac{\vec{\jmath}\cdot\vec{B}}{|\nabla s|^2}\sqrt{g}\xi^s - \frac{1}{F_T'|\nabla s|^2}(B^2 g_{s\theta} - J\tilde{\beta})\sqrt{g}\vec{B}\cdot\nabla\xi^s\right]$$

$$C^3 = \frac{1}{B\sqrt{g}}\left[J\eta_{,\phi} - I\eta_{,\theta} + (F_T'I + F_P'J)\xi^s{}_{,s}\right.$$

$$\left. + (JF_P'' + IF_T'')\xi^s - p'\sqrt{g}\xi^s + \tilde{\beta}\sqrt{g}\vec{B}\cdot\nabla\xi^s\right]$$

Fig. 6

• displacement vector $\vec{\xi}$:
decomposed into three scalar components $\xi^s = \vec{\xi}\cdot\nabla s$, η, μ

divergence-free, if $\vec{\xi}$ satisfies the integrability condition

$$\iint \sqrt{g}\,\vec{\xi}\cdot\nabla s\,\mathrm{d}\theta\,\mathrm{d}\phi = 0$$

$\rightarrow$ magnetic DE for μ, which decouples from the problem

$\rightarrow$ two unknowns ξ^s and η

boundary condition

$$\xi^s(1,\theta,\phi) \equiv 0$$

$\leftrightarrow$ fixed-boundary modes

Fig. 7

NUMERICAL APPROACH

• periodicity of the perturbation functions ξ^s and η

periodicity interval in ϕ: $[0, N_p]$

N_p and N/N_p integers

$\rightarrow$ suggests transformation of coordinates to s, θ and $\bar{\phi}$

$$\bar{\phi} = \phi/N_p$$

$$\bar{\phi} \in [0,1]$$

Fig. 8

17

- Fourier decompositions in θ and $\bar{\phi}$

$$\xi^s(s,\theta,\bar{\phi}) = \sum_{l=1}^{M} \hat{\xi}^s{}_l(s) \cos 2\pi(m_l\theta + n_l\bar{\phi})$$

$$\eta(s,\theta,\bar{\phi}) = \sum_{l=1}^{M} \hat{\eta}_l(s) \sin 2\pi(m_l\theta + n_l\bar{\phi}) .$$

M: finite number of Fourier components

The index pairs (m_l, n_l) are chosen such that the integrability condition holds for ξ^s.

Due to the stellarator symmetry the energy functional splits into two problems for the "even" (s.a) and "odd" perturbations. Both types of perturbations have been used.

Fig. 9

- radial discretization (s)

o simple FEM for both unknowns

$$\hat{\xi}^s{}_l(s) = f_l(s) \sum_{i=0}^{N_s} x_{li}\, e_i(s)$$

e_i: hat functions, f_l: shape function

$$\hat{\eta}_l(s) = \sum_{i=1}^{N_s} r_{li-\frac{1}{2}}\, c_{i-\frac{1}{2}}(s)$$

$c_{i-\frac{1}{2}}$: piecewise constant functions

mesh points $s_i = i\Delta s$, $i = 0,\ldots,N_s$, with $N_s \Delta s = 1$

Fig.10

- derivation of the energy matrix

$$w_\Delta : \quad \Omega \longrightarrow \mathbb{R}^2$$

$$(s,\theta,\bar{\phi})\longmapsto w_\Delta(s,\theta,\bar{\phi}) = \left(\xi_\Delta^s, \eta_\Delta\right)^T$$

$$= \sum_{i=0}^{L-1} v_i\, t_i(s,\theta,\bar{\phi})$$

matrix

$$\delta^2 W(w_\Delta, w_\Delta) = \delta^2 W\left(\sum_{i=0}^{L-1} v_i t_i, \sum_{j=0}^{L-1} v_j t_j\right)$$

$$= \sum_{i=0}^{L-1}\sum_{j=0}^{L-1} v_i v_j\, \delta^2 W(t_i, t_j) .$$

matrix element

$$a_{ij} = \delta^2 W\left(t_i, t_j\right)$$

Fig.11

- definition of the basis functions t_i

$$t_i : \quad \Omega \longrightarrow \mathbb{R}^2$$

$$(s,\theta,\bar{\phi})\longmapsto t_i(s,\theta,\bar{\phi})$$

with

$$t_i(s,\theta,\bar{\phi}) = \begin{cases} \left(f_m(s)e_{i-i_L}(s)\cos 2\pi(m_m\theta + n_m\bar{\phi}), 0\right)^T, \\ \qquad \text{if } 0 \le i - i_L \le N_s \\ \left(0, c_{i-i_L-\frac{1}{2}}(s)\sin 2\pi(m_m\theta + n_m\bar{\phi})\right)^T, \\ \qquad \text{if } N_s + 1 \le i - i_L \le 2N_s \end{cases}$$

where $f_m : I \to I; s \mapsto f_m(s) = s^{m_m/2}(1-s)$
and $i_L = (m-1)(2N_s + 1)$ for $m = 1,\ldots,M$.

- vector $v \in \mathbf{R}^L$, with $L = M(2N_s + 1)$

$$(v_0, \ldots, v_{L-1}) =$$

$$(\ldots, x_{m0}, \ldots, x_{mN_s}, r_{m\frac{1}{2}}, \ldots, r_{mN_s-\frac{1}{2}}, \ldots) ,$$

$$\qquad\quad \uparrow \qquad\quad \uparrow \qquad\qquad \uparrow$$

$$\qquad\quad v_{i_L} \qquad v_{i_L+N_s} \qquad\quad v_{i_L+2N_s}$$
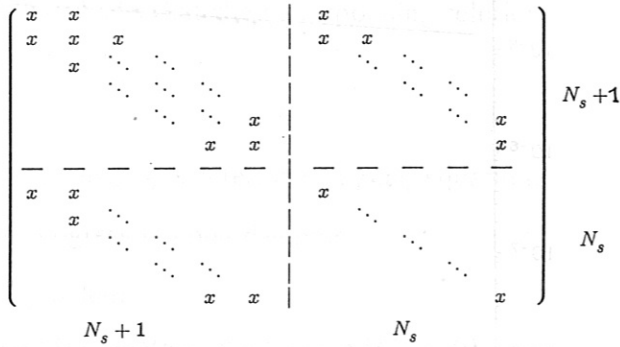
where

$$x_{mi} f_m(s_i) = \hat{\xi}^s{}_{m_m n_m}(s_i) \quad \text{and} \quad r_{mi-\frac{1}{2}} = \hat{\eta}_{m_m n_m}(s_{i-\frac{1}{2}})$$

Fig.12

- matrix corresponding to the symmetric bilinear form $\delta^2 W$

M-by-M-block matrix A

structure of one block A_{ij}

$$\left(\begin{array}{ccccccc|ccccc}
x & x & & & & & & x & & & & \\
x & x & x & & & & & x & x & & & \\
& x & & \ddots & & & & & & \ddots & & \\
& & & \ddots & \ddots & \ddots & & & & & \ddots & \\
& & & & \ddots & \ddots & x & & & & & x \\
& & & & x & x & & & & & & x \\
\hline
x & x & & & & & & x & & & & \\
& x & & \ddots & & & & & & \ddots & & \\
& & \ddots & \ddots & \ddots & & & & \ddots & & & \\
& & & \ddots & \ddots & & & & & \ddots & & \\
& & & & x & x & & & & & & x
\end{array} \right)
\begin{array}{l}
\\[4ex] N_s + 1 \\[6ex] \\[2ex] N_s \\[2ex]
\end{array}$$

$$\begin{array}{cc}
N_s + 1 & N_s
\end{array}$$

different matrix structures possible (e.g. blockbanded matrices)

Fig.13

- eigenvalue problem for matrix A

$$Av = \lambda \Delta s v$$

o instability, if $\widetilde\lambda < 0$, where $\widetilde\lambda$ is the lowest eigenvalue

o corresponding eigenvector $\widetilde v$

- Fourier components of ξ^s and η

- calculation of energy contributions

Fig.14

FOURIER COEFFICIENTS

HELIAS4, B1P
NS = 24
(4, -3)
FACTOR = 5.0

Fig.17

CONTRIBUTIONS TO ENERGY INTEGRAL

HELIAS4, B1P
NS = 24
(4, -3)

Fig.18

L =1.2 STELLARATOR, 4 PERIODS, IOTA= 16/21
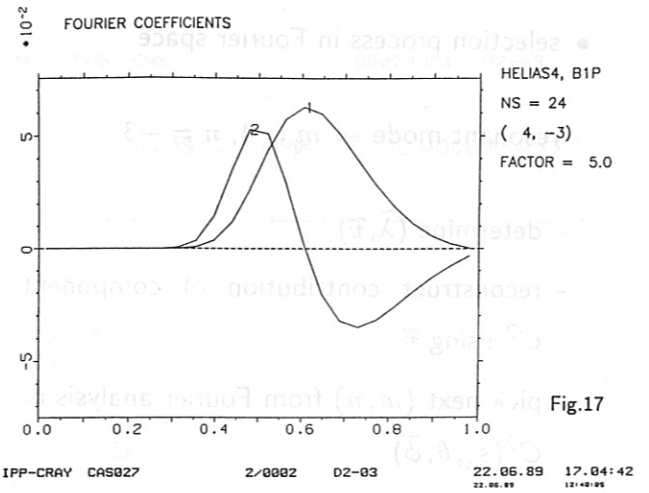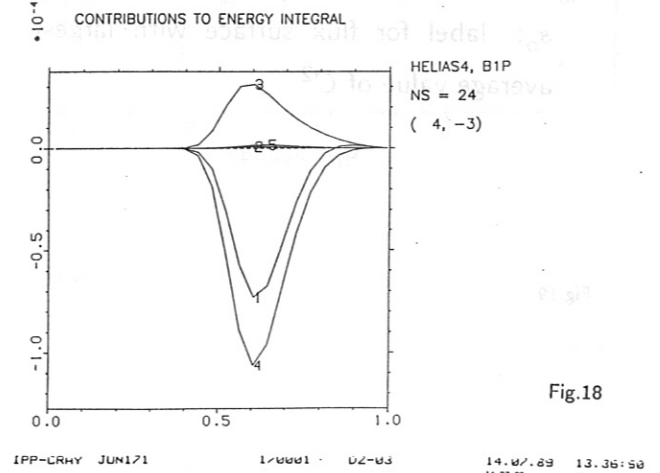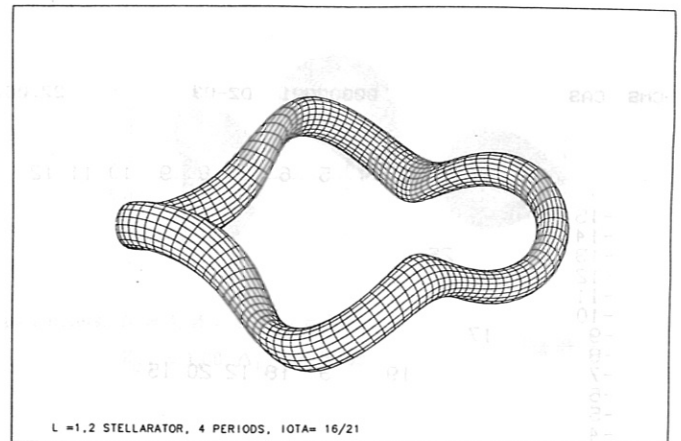
Fig.15

Flux surface cross-sections
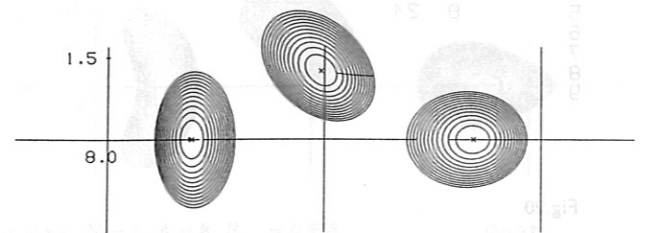
parameters: $N = 4$, $A = 8$, $R_{0,1} = 1.49$,
$Z_{0,1} = 1.34$, $\Delta_{1,-1} = 0.185$

Fig.16

- selection process in Fourier space

resonant mode $\rightarrow m = 4,\ n = -3$

- determine $(\widetilde{\lambda}, \widetilde{v})$

- reconstruct contribution of component C^2 using $\widetilde{v}$

- pick next (m, n) from Fourier analysis of $C^2(s_o, \theta, \bar{\phi})$

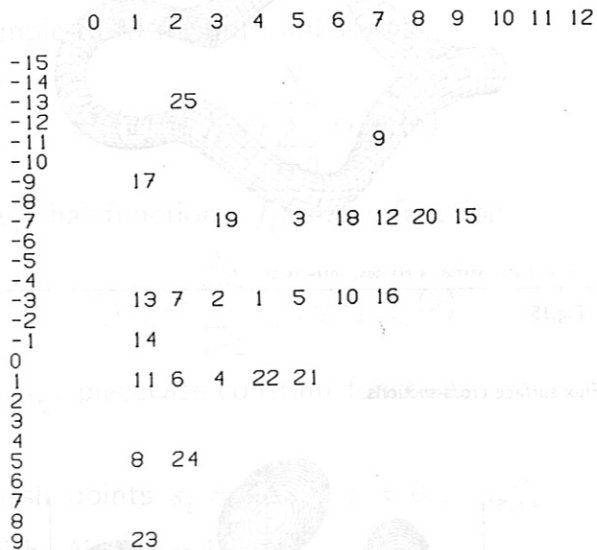s_o: label for flux surface with largest average value of C^2

Fig.19

DEPENDENCE ON NUMBER OF FOURIER COMPONENTS
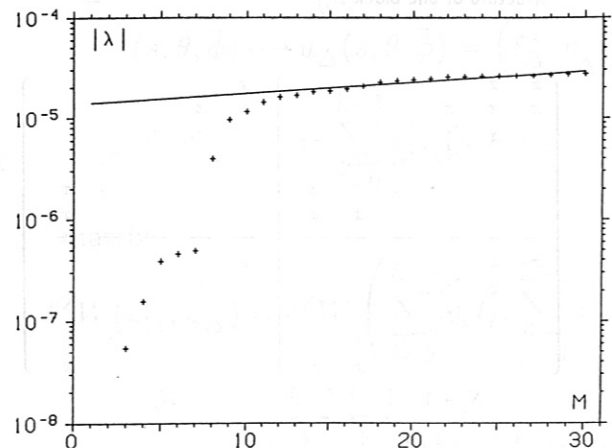
Fig.21

```
        0  1  2  3  4  5  6  7  8  9  10 11 12
-15
-14
-13         25
-12
-11                              9
-10
 -9      17
 -8
 -7         19     3  18 12 20 15
 -6
 -5
 -4
 -3      13 7  2  1  5  10 16
 -2
 -1      14
  0
  1      11 6  4  22 21
  2
  3
  4
  5       8 24
  6
  7
  8
  9      23
```

Fig.20

$* 10^{-5}$

CONTRIBUTIONS TO ENERGY INTEGRAL

CASE 5,

NS = 48

(4, -3)
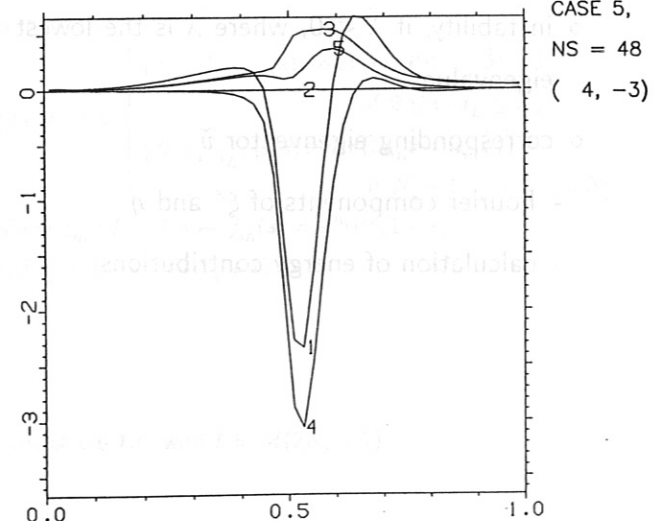
Fig.22

o structure of minimizing modes

$\xi^s \eta$-problem:

discrete problem determines: ξ^s and η

Minimization of the discrete energy functional shows that the corresponding solution satisfies

$$C^3 \equiv 0 \quad .$$

For given ξ^s η is determined by this equation.

$\rightarrow$ progress in code delopment

ξ^s-problem:

Uses the relation of ξ^s and η $(C^3 \equiv 0)$;

$\rightarrow$ discrete problem determines: ξ^s

Fig.23

HELIAS EQUILIBRIA FOR THE MODE ANALYSIS

Fig.25

APPLICATIONS

- Helias equilibria HS48

  o 4 equilibrium periods

  o aspect ratio approximately 8

  o small shear

  o location of $\iota = \frac{3}{4}$ surface

    between $s = 0.4$ and $s = 0.6$

  o range of vacuum field magnetic well:

    -0.008 to +0.03

  o $\langle j_{\parallel}^2 / j_{\perp}^2 \rangle \approx 1$

  o range of $\langle \beta \rangle$:

    0.01 to 0.06

Fig.24
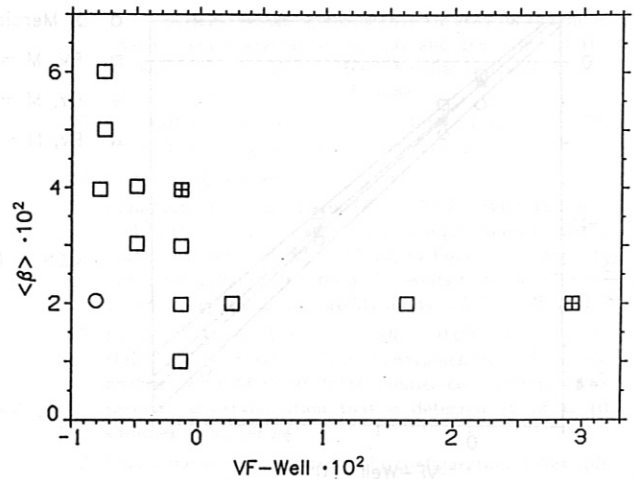
Flux surface cross-sections: VF-well = + 0.03, $\langle \beta \rangle = 0.02$
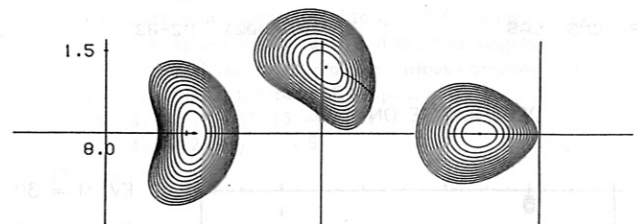
parameters: $N = 4$, $A = 8$, $R_{0,1} = 1.23$,
$Z_{0,1} = 1.08$, $\Delta_{1,-1} = 0.185$

Fig.26

Flux surface cross-sections: VF-well = - 0.001, $\langle \beta \rangle = 0.02$
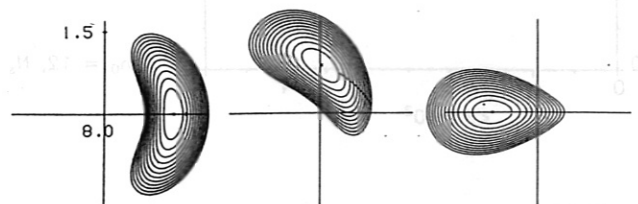
parameters: $N = 4$, $A = 8$, $R_{0,1} = 0.856$,
$Z_{0,1} = 0.69$, $\Delta_{1,-1} = 0.336$

Fig.27

21

IPP--CMS CAS   00000001   D2-03

DEPENDENCE ON VF—MAGNETIC WELL DEPTH

o Σ Mercier

□   EV, M = 10

+   EV, M = 20

△   EV, M = 30

$\langle \beta \rangle = 0.02$

$m_0 = 12$, N

$\lambda \cdot 10^4$
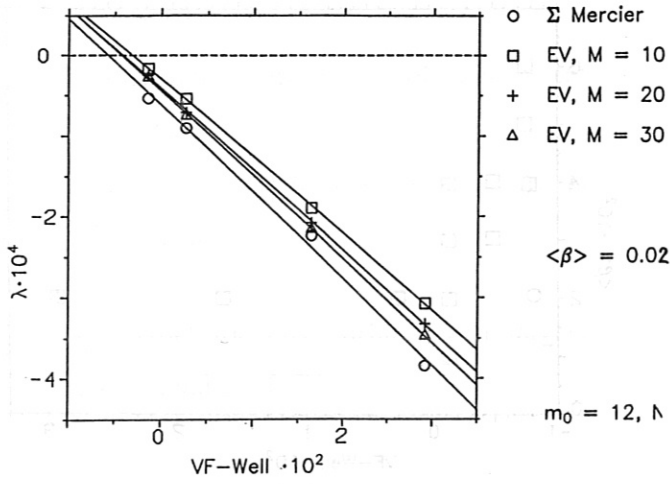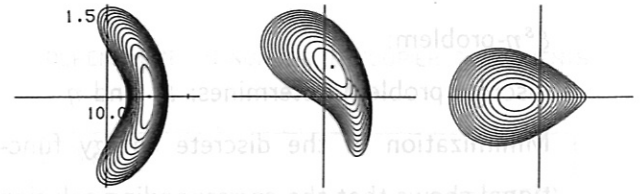
VF—Well $\cdot 10^2$

Fig.28

Fig.30

IPP--CMS CAS   1/0001   D2-03   27.07.89   11.02:38
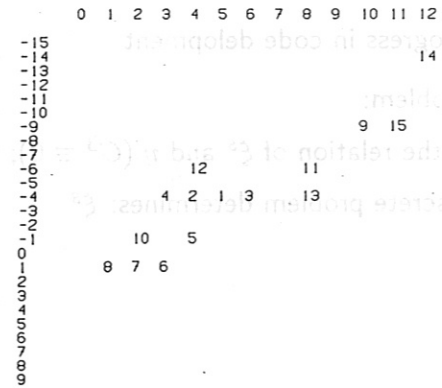
Fig.31

IPP--CMS CAS   00000001   D2-03   22.0
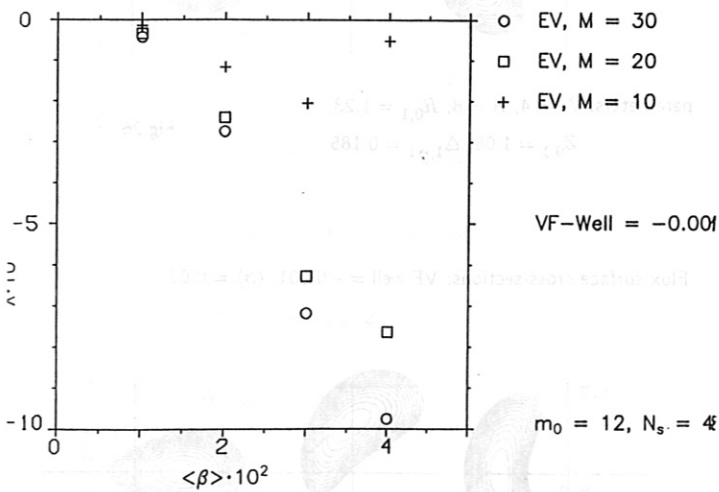
DEPENDENCE ON $\langle \beta \rangle$

o   EV, M = 30

□   EV, M = 20

+   EV, M = 10

VF—Well $= -0.00$

$m_0 = 12$, $N_s = 4$

$\langle \beta \rangle \cdot 10^2$

Fig.29

IPP-CRAY CAS243   2/0002   D2-03   27

$*10^{-3}$

CONTRIBUTIONS TO ENERGY INTEGRAL

50B, B486P

NS = 48

(5, −4)

1 : C^1
2 : C^2
3 : C^3
4 : sqrtg A
5 : $\delta^2 W$
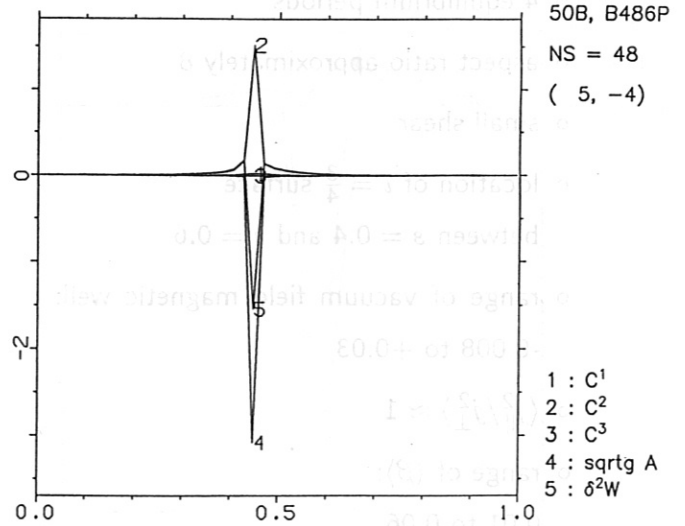
Fig.32

	Vac. Well	$\langle j_\parallel^2/j_\perp^2\rangle$	$\langle\beta\rangle$	STABILITY
HS48	0.1 %	≈ 1	0.02	$m = 4, n = -3$ mode $\delta_{well} \approx 0.1$ %
HS48	0.7 %	≈ 1	0.06	$m = 4, n = -3$ mode $\langle\beta\rangle \approx 0.04$ marginal
50B	1.8 %	≈ 0.5	0.05	$m = 5, n = -4$ mode trivial Mercier instability $(\iota_p = 1/6)$ via mode coupling

Fig.33

FIGURE CAPTIONS

1.–14. Text

15. This outer magnetic surface of an $\ell = 1, 2$ toroidal equilibrium is generated by the $\iota = 16/21$ rational magnetic field line. Note the strong 3D nature of the equilibrium. The configuration has 4 field periods and aspect ratio 8.

16. Flux surface cross-sections at the beginning of, at quarter of and at half a period of the equilibrium of Fig.15. The ι-profile of this configuration has small shear and contains the rational $\iota = 3/4$, $\langle\beta\rangle = 0.01$.

17. Result of the mode analysis for the equilibrium of Fig.15 and 16; Fourier coefficients for the resonant component ($m = 4, n = -3$) versus normalized flux surface label s: label 1 for $\hat{\xi}^s_{4,-3}$, label 2 for $\hat{\eta}_{4,-3}$.

18. For the configuration of Fig 15. and 16 instability can be demonstrated with one Fourier component contributing to the discrete problem. Here, the values of $\delta^2 W$ (label 1) and the different contributions to the energy functional are given versus the normalized flux surface label s: C^1 (label 5), C^2 (3), C^3 (2) and $\sqrt{g}A\xi^s$ (4).

19. Text

20. Fourier index pairs (m, n): $0 \leq m \leq 12$, $-15 \leq n \leq 9$ Iterative application of the selection process described in Fig.19 yields the Fourier spectrum that dominates the minimization problem (numbers 1 to 25). Examples for the coupling process: $1 \to 2$ and $4 \to 6$ via toroidal component of $j_\parallel$ ($m = 1, n = 0$), $1 \to 3$ and $6 \to 8$ via helical component ($m = 1, n = -4$).

21. Dependence of the eigenvalue on the number of contributing Fourier components M. Exponential convergence can be observed.

22. Energy contributions for a case with VF-well = -0.001 and $\langle\beta\rangle = 0.02$ (for the labels: see Fig 18.) The contribution of the component C^2 ($\to$ field compression term) vanishes.

23.–24. Text

25. The 4-periodic Helias equilibria that are used for the mode analyses are characterized by $\langle\beta\rangle$ and the value of the VF-well. □: unstable, +: test of radial convergence, ○: stable to the $m = 4, n = -3$ mode

26. Flux surface cross-sections; parameters: VF-well = +0.03, $\langle\beta\rangle = 0.02$, 4 field periods, aspect ratio 8.

27. same as Fig. 26, VF-well = -0.001

28. Parameter study at fixed $\langle\beta\rangle = 0.02$, using the VF-well as stability parameter: □, +, △ eigenvalues from the mode analyses with $M = 10, 20, 30$ Fourier components in the perturbation functions; ○ results from the Mercier criterion. Difference in stability limits: 10^{-3} in VF-well.

29. Parameter study at fixed VF-well = -0.001, using $\langle\beta\rangle$ as stability parameter: +, □, △ eigenvalues from the mode analyses with $M = 10, 20, 30$ Fourier components. The seeming self-stabilization that is detected at $M = 10$ vanishes at higher M.

30. Flux surface cross-sections of the configuration Helias 50B at $\langle\beta\rangle = 0.0486$.

31. Application of the selection process described in Fig.20 yields the Fourier spectrum for a case with 5 field periods (rational $\iota = 4/5$).

32. For Helias 50B the mode analysis, which uses the Fourier spectrum given in Fig.31, reveals the trivial Mercier instability, which is connected to $\iota_p = 1/6$ (corresponding to $\iota = 5/6$) and located at $s = 0.45$. The singularity in $j_\parallel$ is detected via coupling of the various components in the perturbation functions. Examples: $(4, -4) \leftrightarrow (10, -9) : (6, -5)$ and $(4, -4) \leftrightarrow (2, -1) : (6, -5)$

33. Table

RESISTIVE BALLOONING MODES IN STELLARATORS

H. Wobig

Abstract

The resistive ballooning mode in general stellarator geometry is analyzed following the theory of D. Correa-Restrepo published in Z. f. Naturforsch. 37a, 848 (1982). The two coupled differential equations with s along the field line as independent variable can be simplified by taking the limit $\gamma_H = c_p/c_v \to 0$. (Neglect of sound waves). The remaining equation (1) yields the equation of ideal ballooning modes if $S_M \to \infty$, where S_M is the magnetic Reynolds number.

It can be shown that an unstable solution exists at any β if S_M is finite and if a finite region of unfavourable curvature exists.

For Helias configurations (low shear, low geodesic curvature) a model equation of the Mathieu type can be derived, which leads to a cubic dispersion relation for the growth rate, equ. (6) .

In the limit $S_M \to \infty$ the critical beta of ideal ballooning modes can be recovered :

$$\beta_{crit} \sim \frac{aR}{L^2}\frac{\kappa_0}{\kappa_1^2},$$

where a = minor radius, R = major radius, L = connection length, κ_0 = averaged curvature, and κ_1 = maximum unfavourable curvature.

It can be shown that sound waves $(\gamma_H \beta \neq 0)$ tend to stabilize resistive ballooning modes.

Limit $\quad \gamma_H = \dfrac{c_p}{c_v} \longrightarrow 0 \quad$ (Neglect of sound waves)

$$\boxed{\begin{aligned}&\Big\{-\frac{d}{ds}\frac{B}{D|\nabla V|^2}(1+S^2)\frac{d}{ds} +(\gamma\tau_A)^2\frac{B}{|\nabla V|^2}(1+S^2)\\ &-\beta'(r)\frac{L^2}{Ra}\frac{B}{|\nabla V|^2}(\varkappa_n -\varkappa_g S)\Big\}f = 0\end{aligned}}$$

⓵

with $\quad \varkappa_n, \varkappa_g$ = normal, geodesic curvature

R, a = major, minor radius, L = length of period
$\beta = \dfrac{2\mu_0 P}{B^2}$, τ_A = Alfvén time

V = Volume of magnetic surface
r = average minor radius
γ = growth rate

$$\vec{B} = \nabla V \times \nabla \tau$$

$$\nabla \tau = \Lambda \nabla V + \frac{\vec{B} \times \nabla V}{|\nabla V|^2}$$

and $\quad \tau = \Theta - t(V)\varphi$

(magnetic coordinates)

⇓

$$\Lambda = -t'(V)\varphi + \frac{1}{|\nabla V|^2}(\nabla\Theta - t\nabla\varphi)\cdot\nabla V$$

↑ secular   ↑ periodic

$$S = \Lambda \frac{|\nabla V|^2}{B} = S_0(s) + S_1(s)$$

$$D = 1 + \frac{\eta}{\mu_0 \gamma}[\frac{2\pi n}{t}V']^2|\nabla\tau|^2$$

η = resistivity , n = poloidal mode number

D. Correa - Restrepo , Z. f. Naturforsch. 37a 848 , (1982)

H.P. Zehrfeld , K. Grassie
JPP-Report JPP 5/16 (1987)

Definitions:

$$\tau_R = \frac{\mu_0 L^2}{\eta} \qquad \text{resistive time}$$

$$S_M = \frac{\tau_R}{\tau_A} \qquad \text{magnet. Reynolds number}$$

$$N^2 = \frac{L^2 B^2}{|\nabla V|^2}\left(\frac{2\pi}{t}\right)^2 [V']^2\, n^2$$

↑ Mode number   ⇓

$$A =: \frac{1+S^2}{D} = \frac{\gamma\tau_A(1+S^2)}{\gamma\tau_A + \frac{N^2}{S_M}(1+S^2)}$$

$\boxed{\eta \to 0}$ } $\tau_R \to \infty$ } $S_M \to \infty$

(ideal ballooning)

⇓

$$A = 1+S^2 \quad \text{(unbounded)}$$

$\boxed{\eta \neq 0}$ } $0 < A \leq \gamma\tau_A S_M/N^2$

(bounded)

$$A \to 0 \quad \text{for} \quad \gamma\tau_A \to 0 \quad !$$

Definitions

$$V(s) = -\beta'(r)\frac{L^2 B}{Ra|\nabla V|^2}(x_n - x_g\, s)$$

$$V_1(s) = (\gamma\tau_A)^2 \frac{B}{|\nabla V|^2}(1+S^2)$$

$$\left[\mathcal{L}(\gamma\tau_A) := -\frac{d}{ds}A\frac{B}{|\nabla V|^2}\frac{d}{ds} + V_1(s) + V(s)\right]$$

It can be shown that for

$$\gamma > 0 \quad \text{and} \quad t'(V) \neq 0$$

a) $\mathcal{L}$ is selfadjoint and has a discrete spectrum of eigenvalues $\{\lambda_k\}$ $\mathcal{L}^{-1}$ is compact!

b) The spectrum is bounded from below

c) $\lambda_0(\gamma\tau_A) = \text{Min} \int_{-\infty}^{+\infty} f\cdot\mathcal{L}f\, ds$

with $\|f\| = 1$

d) $\lambda_0(\gamma\tau_A)$ is monotonic

e) $\exists\, \gamma\tau_A > 0 : \lambda_0(\gamma\tau_A) = 0$

‖ There exists an unstable solution for any $\beta'(r) \neq 0$ ‖

Model for Helias

$$t'(V) \to 0 ; \quad x_g \to 0$$

$$\frac{B}{|\nabla V|^2} \approx const , \quad S \ll 1$$

⇓

$$\mathcal{L}f = 0$$

⇓   (2)

$$\left\{-\frac{d}{ds}A\frac{d}{ds} + (\gamma\tau_A)^2 - \beta'(r)\frac{L^2}{Ra}x_n\right\}f = 0$$

$$A = \frac{\gamma\tau_A}{\gamma\tau_A + \frac{N^2}{S_M}}^2$$

Fourier exp. of x_n:

$$x_n = x_0 + x_1\cos\frac{2\pi}{L}s + x_2\cos\frac{4\pi}{L}s + \ldots$$

↑ av. curvature   ↖ ~ max. local curvature

~ $\frac{\delta V'}{V'}$

Definition

$$a = -\frac{(\gamma\tau_A)^2}{A} + \frac{L^2}{\pi^2 aR}\frac{\beta' x_0}{A}$$

$$16q = \frac{L^2}{\pi^2 aR}\frac{\beta'}{A}x_1 \qquad ; \quad x = \frac{\pi}{L}s$$

⇓   (3)

$$\frac{d^2 f}{dx^2} + (a + 16q\cos 2x)f = 0$$

(Mathieu equation)

⇓   (4)

Dispersion relation

$$\left[(\gamma\tau_A)^2 + \frac{L^2}{\pi^2 aR}\beta' x_0 = \frac{1}{8}\left(\frac{L^2}{\pi^2 aR}\beta' x_1\right)^2\frac{1}{A(\gamma\tau_A)}\right]$$

$S_M \to \infty$ } $A = 1$ (5)

⇓

$$\boxed{\gamma\tau_A = \frac{1}{\sqrt{8}}\frac{L^2}{\pi^2 aR}x_1\sqrt{\beta'(\beta'-\beta'_{crit})}}$$

with $\beta'_{crit} = \frac{8\pi^2 aR}{L^2 x_1^2}x_0$

$x_o \approx$ average curvature $\sim$ magnet. well
$x_1 \approx$ maximum curvature
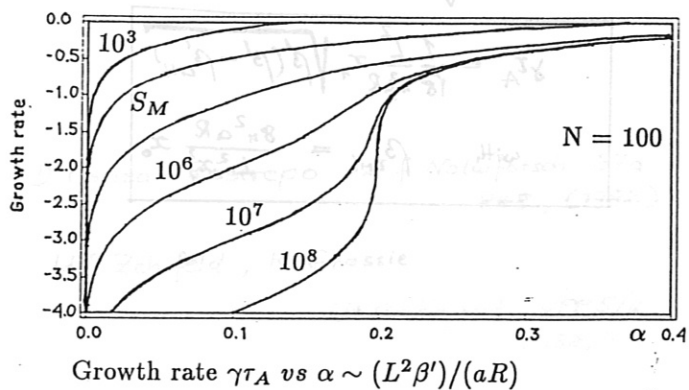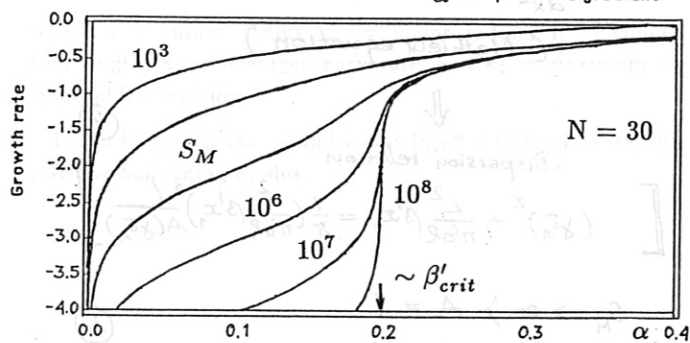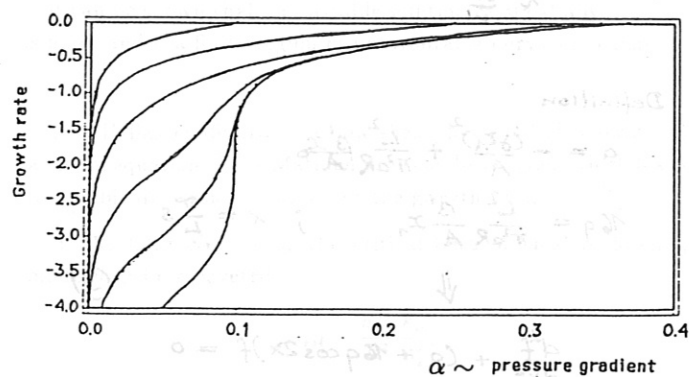
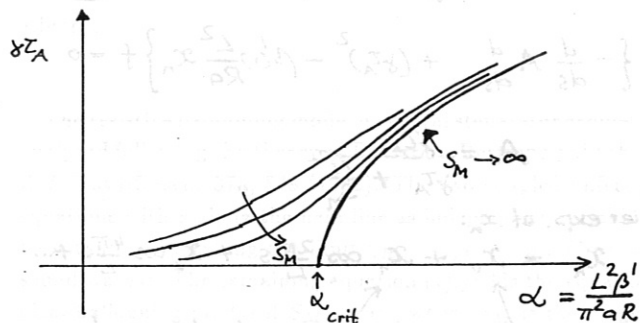Def. $\qquad \alpha = \dfrac{L^2 \beta'}{\pi^2 q R}$

⑥

$$\left(\delta \tau_A\right)^2 + \alpha x_o = \frac{1}{8}\left(\alpha x_1\right)^2 \frac{\delta \tau_A + \frac{N^2}{S_M}}{\delta \tau_A}$$

cubic equation

Solution:
$$\delta \tau_A = g\left(\alpha, x_o, x_1, N^2, S_M\right)$$

Growth rate $\gamma \tau_A$ vs $\alpha \sim (L^2 \beta')/(a R)$

Approximate dispersion relation

General case : $t' \neq 0$

Let be $\quad f_T(s) \in L_2 \left[-\infty, +\infty\right]$
a trial function with

a.) $\left| f_T'(s) \right| \leq M < \infty$
(bounded derivative)

b.) $\displaystyle\int_{-\infty}^{+\infty} V(s) f_T^2 \, ds < 0$

(Localisation to regions of unfavourable curvature)

⇓

$$g(\delta \tau_A) = \int_{-\infty}^{+\infty} A(\delta \tau_A)\left(\frac{df_T}{ds}\right)^2 + (\delta \tau_A)^2 \int_{-\infty}^{+\infty} \frac{B}{|\nabla r|^2}(1+s^2) f_T^2 \, ds$$

$$+ \int_{-\infty}^{+\infty} V(s) f_T^2 \, ds = 0$$

is the dispersion relation.
There exists always a solution !

$$\left(\delta \tau_A\right)_{f_T} \leq \text{exact value} !$$

First equation:

$$\mathcal{L}_1(\gamma) F + \nabla g \, \mathcal{L}_2^{-1} \nabla F = 0$$

The operator $\left(\mathcal{L}_1 + g \nabla \mathcal{L}_2^{-1} \nabla\right)F =: HF$
is selfadjoint and bounded from below.

$$\left(F, \mathcal{L}_1 F\right) + g\left(\nabla F, \mathcal{L}_2^{-1} \nabla F\right)$$
$$\geq \left(F, \mathcal{L}_1 F\right) \geq \text{Min}\left(V_1 - V\right) \|F\|^2$$

The eigenvalue equation

$$H(\gamma) F = E F$$

yields a spectrum $E_k(\gamma)$

with
$$E_o(\gamma) = \text{Min}\left(F, HF\right)$$

$E_o(\gamma)$ not monotonous

26
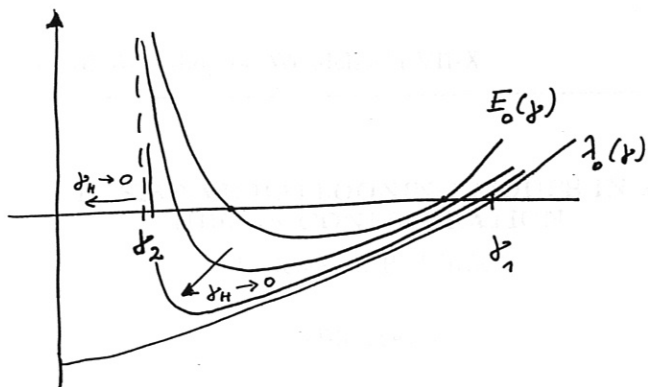
With $\delta_H \to 0$ $(\delta_H \beta \ll \delta^\tau_R)$

we find $V_2 \to \infty$ $\rangle$ $\mathcal{L}_2^{-1} \to 0$

In this case $\delta_2 \to 0$ and $\boxed{\delta \to \delta_1}$

Statement:

   If $\delta_H \beta$ small enough, a solution
with $\delta \approx \delta_1$ exists.

Helias 5-7
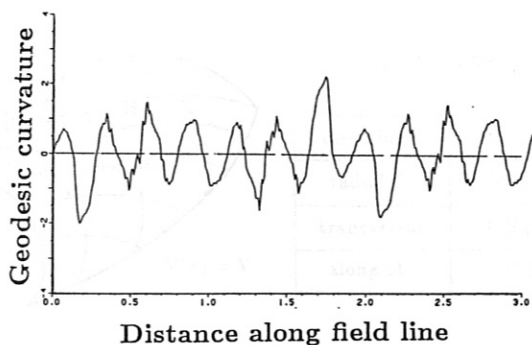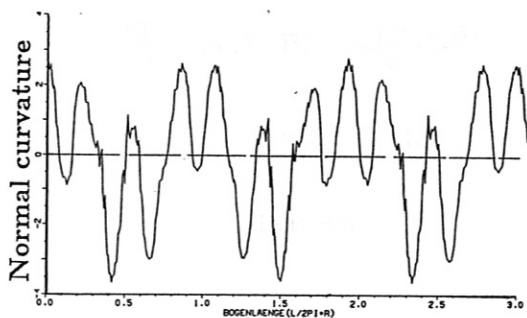
Distance along field line
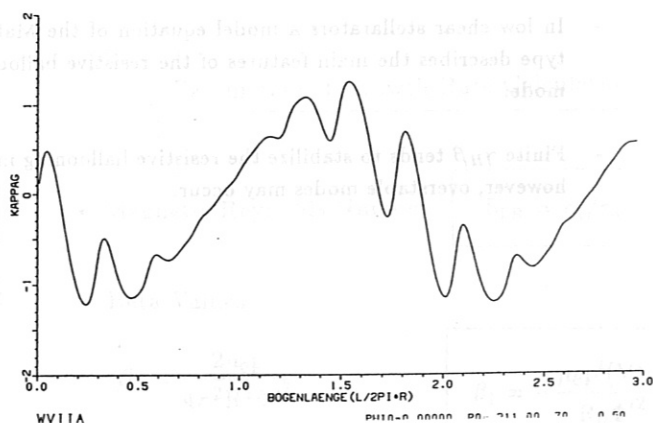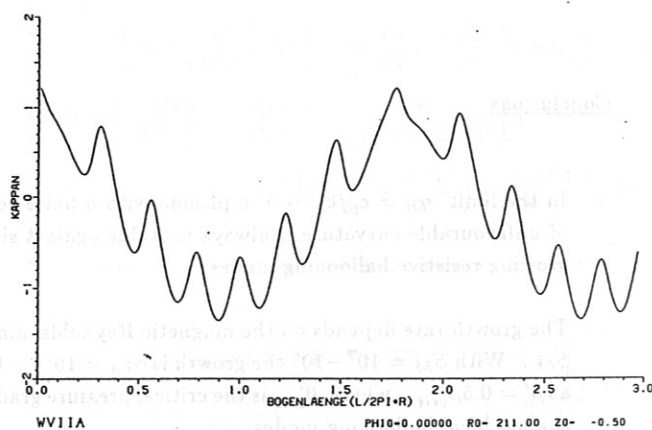
Geodesic and normal curvature *versus* distance along field line for HS 5-7 and W VII-A.

W VII-AS

$R = 2$ m, $a = 0.18$ m, $B = 1.25$ T.

$$\tau_R = \mu_o a^2/\eta\,, \quad \tau_A = a/v_A$$

T_e (keV)	T_i (keV)	n (10^{13}cm^{-3})	τ_R (s)	τ_R (s)	S_M
0.02	0.02	0.5	$5.5\ 10^{-3}$	$1.5\ 10^{-8}$	$3.5\ 10^5$
0.05	0.05	0.5	$2.0\ 10^{-2}$	$1.5\ 10^{-8}$	$1.4\ 10^6$
0.1	0.1	0.5	$4.5\ 10^{-2}$	$1.5\ 10^{-8}$	$3.7\ 10^6$
1.0	0.2	1.2	1.5	$2.3\ 10^{-8}$	$6.6\ 10^7$

W VII-X

$R = 6.5$ m, $a = 0.5$ m, $B = 2.5$ T.

T_e (keV)	T_i (keV)	n (10^{14}cm^{-3})	τ_R (s)	τ_R (s)	S_M
0.03	0.03	0.1	$7.7\ 10^{-2}$	$2.9\ 10^{-8}$	$2.7\ 10^6$
0.1	0.1	0.1	$4.3\ 10^{-1}$	$2.9\ 10^{-8}$	$1.5\ 10^7$
0.1	0.1	0.5	$4.5\ 10^{-1}$	$6.5\ 10^{-8}$	$7.0\ 10^6$
1.0	1.0	0.5	12.0	$6.5\ 10^{-8}$	$1.9\ 10^8$
4.0	4.0	1.0	92.0	$9.6\ 10^{-8}$	$9.6\ 10^8$

Conclusions

- In the limit $\gamma_H = c_p/c_v \to 0$ a plasma with a finite region of unfavourable curvature is always unstable against slowly growing resistive ballooning modes.

- The growth rate depends on the magnetic Reynolds number S_M. With $S_M = 10^7 - 10^8$ the growth is $\gamma\tau_A = 10^{-4} - 10^{-3}$ at $\beta' = 0.5\beta'_{crit}$, where β'_{crit} is the critical pressure gradient against ideal ballooning modes.

- In low shear stellarators a model equation of the Mathieu type describes the main features of the resistive ballooning mode.

- Finite $\gamma_H\beta$ tends to stabilize the resistive ballooning mode, however, overstable modes may occur.

28

RESISTIVE BALLOONING MODES IN A HELIAS CONFIGURATION

J. Geiger, H.P. Zehrfeld

ABSTRACT

The Garching resistive ballooning code GARBO which was developed for stability analyzes of axisymmetric plasmas is about to include the treatment of three-dimensional equilibria as well.

Preliminary results are presented for a sample configuration of HELIAS. Although this model does not represent a consistent finite-pressure stellarator equilibrium configuration, its general features as magnetic surface geometry and field line curvature properties are expected to reflect the reality of HELIAS.

Real growth rates are calculated in a beta range from one to five percent with the magnetic Reynolds number as parameter. The stabilizing effect of shear is demonstrated.

Linearized Resistive MHD Equations

$$\rho\frac{\partial \tilde{v}}{\partial t} = \frac{1}{\mu_0}\left(\text{rot}\tilde{B}\times B + \text{rot}B\times\tilde{B}\right) - \nabla\tilde{p}$$

$$\frac{\partial\tilde{B}}{\partial t} = \text{rot}(\tilde{v}\times B) - \text{rot}(\frac{\eta}{\mu_0}\text{rot}\tilde{B})$$

$$\frac{\partial\tilde{p}}{\partial t} = -\tilde{v}\cdot\nabla p - \gamma_T p\,\text{div}\tilde{v}$$

$$\text{div}\tilde{B} = 0$$

Field Line Coordinates and Ballooning Ordering
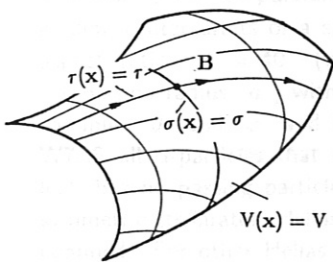
$$B = \nabla V\times\nabla\tau$$

direction	coordinate
radial	$V \in (0, V_B)$
transversal	$\tau \in (0, V'(\Phi))$
along B	$\sigma \in (0, \Phi'(V))$

$$V\frac{\partial}{\partial V} \sim \Psi'(V)\frac{\partial}{\partial\tau} \sim \frac{1}{\epsilon} \sim n$$

$$\Phi'(V)\frac{\partial}{\partial\sigma} \sim 1$$

In the limit $n\to\infty$ the ballooning equations reduce for given values of V and τ to a system of ordinary differential equations for the envelope $\tilde{U}$ on the interval $\sigma\in(-\infty,+\infty)$. Formally the equations look like

$$\frac{d}{d\sigma}\left(A\cdot\frac{d\tilde{U}}{d\sigma}\right) + C\cdot\tilde{U} = 0$$

In the case of axisymmetry the equations depend on the toroidal mode number n and a free parameter $\sigma_0\in(-\infty,\infty)$.
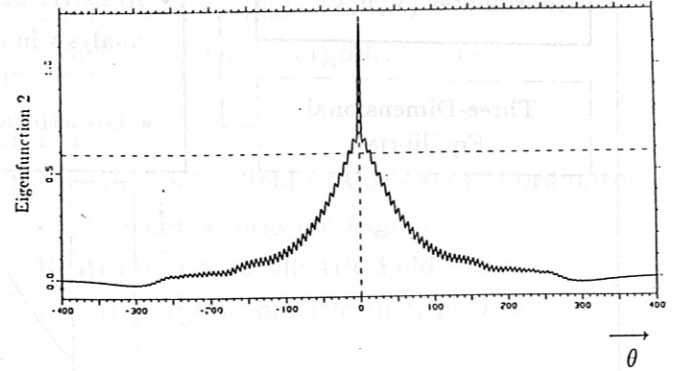
θ - poloidal angle along localization field line abszissa in arbitrary units

$$\frac{1}{\mu_0}B\cdot\nabla\left(\frac{k^2}{DB^2}B\cdot\nabla u\right) + \left(K\frac{dp}{dV} - \frac{\rho\gamma^2 k^2}{B^2}\right)u + K\frac{dp}{dV}v = 0$$

$$B\cdot\nabla\left(\frac{B\cdot\nabla v}{B^2}\right) - K\frac{dp}{dV}\left\{\frac{\eta}{\gamma} + \frac{\rho\gamma^2}{((\nabla p\cdot(k\times\nabla\sigma))^2}\right\}u$$

$$-\left\{\frac{\eta}{\gamma}\left(K\frac{dp}{dV} + \frac{\rho\gamma^2 k^2}{B^2}\right) + \frac{\mu_0\rho\gamma^2}{B^2}\frac{1+\beta}{\beta}\right\}v = 0$$

$$K \equiv 2\kappa\cdot(k\times\nabla\sigma)(k\times\nabla\sigma)\cdot\nabla V \qquad D \equiv 1 + \frac{\eta k^2}{\mu_0\gamma}$$

$$k \equiv -\frac{2\pi n}{\Psi'(V)}\nabla\tau \qquad \beta \equiv \frac{\mu_0\gamma_T p}{B^2}$$

Parameters of Growth Rate Calculation

- **Magnetic Reynolds Number** $\boxed{S_{LR} = \tau_R/\tau_A}$
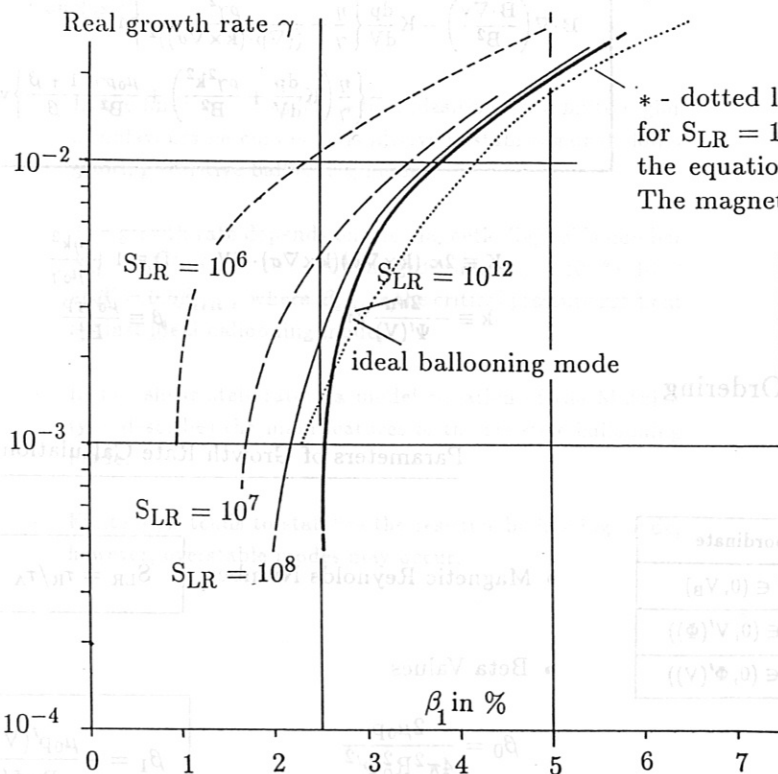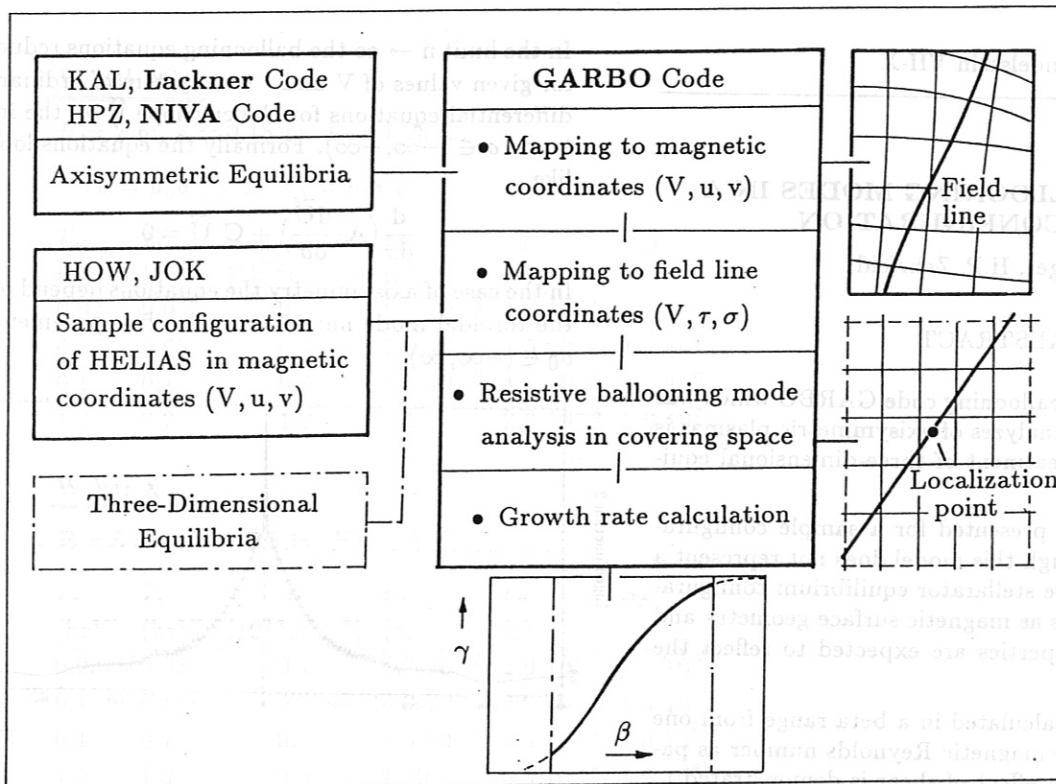
- **Beta Values**

$$\beta_0 = \frac{2\mu_0 P}{4\pi^2 R_0^2\Phi'^2} \qquad \boxed{\beta_1 = -\frac{\mu_0 P'(V)r^2}{R_0\Phi'^2}}$$

$$\beta = \frac{2\pi^2 R_0^2\Phi'^2}{B^2}\gamma_T\beta_0$$

KAL, **Lackner** Code
HPZ, **NIVA** Code

Axisymmetric Equilibria

HOW, JOK

Sample configuration
of HELIAS in magnetic
coordinates (V, u, v)

Three-Dimensional
Equilibria

GARBO Code

- Mapping to magnetic
  coordinates (V, u, v)
- Mapping to field line
  coordinates (V, τ, σ)
- Resistive ballooning mode
  analysis in covering space
- Growth rate calculation

Field line

Localization point

γ

β

Real growth rate γ

10^{-2}

$S_{LR} = 10^6$

$S_{LR} = 10^{12}$

$S_{LR} = 10^7$

ideal ballooning mode

10^{-3}

$S_{LR} = 10^8$

10^{-4}

β_1 in %

0   1   2   3   4   5   6   7

∗ - dotted line shows the stabilizing effect of shear
for $S_{LR} = 10^8$. The shear explicitly showing up in
the equations has been scaled with a factor 1.5 .
The magnetic configuration remained unchanged.

Monte Carlo Calculations
for Helias Configurations

W. LOTZ

Max-Planck-Institut für Plasmaphysik
IPP-EURATOM Association
D-8046 Garching bei München
Federal Republic of Germany

Transport coefficients obtained with monoenergetic particles (using pitch angle scattering and energy relaxation) have been convoluted with a Maxwellian particle distribution [W. Lotz, Ringberg 1988]. Transport coefficients with Maxwellian particle distributions are shown for the configuration **Helias 50 B 5** ($\beta = 4.9\%$). Particle transport coefficients as well as energy transport coefficients for this configuration have been computed for ions (deuterons) as well as for electrons. From these, estimates of **confinement times** have been derived [W. Lotz, J. Nührenberg, Phys. Fluids **31** (1988) 2984].

The Monte Carlo computation of a **"stationary"** monoenergetic distribution not only yields estimates of loss rates [W. Lotz, J. Nührenberg, A. Schlüter, J. Comp. Phys. **73** (1987) 73] but also the toroidal current carried by this distribution. In an axisymmetric field (tokamak) this current increases the rotational transform. The scaling of the asymmetry of the parallel velocity ($\langle \eta \rangle = \langle v_\| \rangle / v = 1.4\sqrt{A_a/ t Q_\rho}$) has been verified so that $\langle \eta \rangle$ may be interpreted as a measure of the **bootstrap current.** In quasi-helically symmetric configurations it reverses its sign and is smaller in size. Adjustment of Fourier components of B leads to configurations (e.g. Helias50B) in which the bootstrap current is expected to be an order of magnitude smaller than in the equivalent tokamak case.

The collisionless **α-particle confinement** is assessed by guiding center orbits of a sample of α-particles started at aspect ratio $A = 40$ (which corresponds to $\frac{1}{4}$ of the plasma radius a) with random values in the angular variables ϑ and φ and the pitch angle $\eta = v_\|/v$. In W7AS all α-particles that undergo reflections are quickly lost, but no passing particle is lost. In the quasi-helically symmetric stellarator Helias61 all particles are completely confined. For other Helias configurations the dependence on the β-value is shown. In the configuration Helias 50 B the β-effect at $\langle \beta \rangle \approx 5\%$ is sufficient to improve the α-particle confinement in such a way that the fraction of prompt losses is reduced to approximately 0.1.   Ring89AB

Monte Carlo Simulation
of Neoclassical Transport

Two Code Realizations

a) **Boozer, Fowler, Rome, Lyon**
   $B(\psi, \Theta, \varphi)$ **Magnetic coordinates**
   Needs additional code for B
   Easy: electric field
   Not easy: islands, ergodic regions

b) **Lotz**
   Any magnetic field in Cartesian coordinates
   Easy: islands, ergodic region
   Restrictions: no electric field
   Monoenergetic particle distribution

Ring8901

Convenient Approximations

Pitch angle scattering

Monoenergetic particle distribution

Initial energy of test particles equal to temperature of background plasma

Mean free path constant over plasma cross section

Temperature and density of background plasma constant over cross section

Ring8902

Normalizations

Monoenergetic particle distribution

Normalized mean free path:

$$L^* = \frac{\Lambda}{L_c}, \qquad L_c = \frac{\pi R_0}{t},$$

L_c = half the connection length.

Normalized collision frequency:

$$\nu^* = \frac{1}{L^*} = \frac{L_c}{\Lambda}.$$

Plateau regime starts at $L^* = 1$.

Loss Rates
without Electric Field

Plateau value of loss rate: $S_P = \dfrac{3.6\, v}{Q_\varrho^2\, t\, \pi R_0}$

Ratio of plateau values: $\dfrac{D_P}{S_P} = \left(\dfrac{a}{2.4}\right)^2$

Normalized loss rates: $S^* = \dfrac{S}{S_P}$; $\qquad S_P^* = 1$

Pfirsch - Schlüter regime: $S_{PS}^* = \dfrac{1}{L^*} = \nu^*$

Banana regime: $S_B^* \approx \dfrac{A^{3/2}}{L^*} = A^{3/2}\nu^*$

Ripple regime: $S_R^* = 1.65\, \delta_e^{3/2}\, L^*$

ν-regime: $S_\nu = \nu = \dfrac{v}{\Lambda}$

Transport Coefficients
without Electric Field

Plateau value of transport coefficient:

$$D_P = 0.64\, \frac{\varrho^2\, v}{t\, \pi R_0}, \qquad \varrho = \frac{m v}{e B_0}.$$

Normalized transport coefficient:

$$D^* = \frac{D}{D_P}, \qquad D_P^* = 1.$$

Pfirsch - Schlüter regime:

$$D_{PS}^* = \frac{1}{L^*} = \nu^*.$$

Banana regime: $D_B^* \approx \dfrac{A^{3/2}}{L^*} = A^{3/2}\nu^*.$

Plateau regime: $1 \le L^* \le A^{3/2}.$

Ripple regime: $D_R^* = 1.65\, \delta_e^{3/2}\, L^*.$

Simulations
with Electric Field

Electric Potential:

$$\phi = \phi_0 (1 - \psi).$$

Electric Field:

$$F = \phi_0 \frac{2\, r}{a^2}.$$

Energy relaxation of test particles
is used with same time constant
as pitch angle scattering.

Formulas

Numerical results suggest the following formulas:

$$\sqrt{\nu}-\text{regime}: \quad D^*_{\sqrt{\nu}} = C_{\sqrt{\nu}} \, H^{1.5} \, \sqrt{\nu^*}$$

$$\text{with} \quad C_{\sqrt{\nu}} = C_{11} \frac{1 + C_{12} \frac{A}{H^{1.5}}}{1 + C_{11}\left(\frac{H}{H_c}\right)^{1.5}},$$

$$\nu-\text{regime}: \quad D^*_{\nu} = C_{\nu} \, H^2 \, \nu^*$$

$$\text{with} \quad C_{\nu} = C_{21} \frac{1 + C_{22} \frac{A^{1.5}}{H^2}}{1 + C_{21}\left(\frac{H}{H_c}\right)^2},$$

at aspect ratio $A = R_0/r_0$

with $H_c = 0.53 \, \ell \, Q_\varrho$ and $H > 1$,

$$H = \frac{2 \, \ell \, E}{A \, \varrho \, eF} = \frac{\ell \, Q_\varrho \, a \, E}{R_0 \, e\phi_0} = \frac{\Omega_{\text{pass}}}{\Omega_F}.$$

Ring8907

The constants C_{ik} are given in the following table:

	C_{11}	C_{12}	C_{21}	C_{22}	$C_{11} \cdot C_{12}$	$C_{21} \cdot C_{22}$
$\ell = 2$ Stellarator	0.11	1.9	1.1	0.7	0.21	0.8
W VII-AS	0.09	1.0	1.0	0.7	0.09	0.7
Helias49	0.03	2.7	0.4	1.7	0.08	0.7
Helias5081	0.011	3.5	0.15	1.0	0.04	0.15
Helias50 B 5	0.0042	4.0	0.09	4.0	0.02	0.36
Helias61	0.00065	37.	0.012	13.	0.02	0.16
ATF	0.18	0.8	1.9	0.3	0.14	0.6
Heliotron-E	0.19	0.5	1.2	0.6	0.10	0.7
TJ-II	0.50	0.7	3.5	0.55	0.35	1.9

29.6.1989   Ring8908

33

Maxwellian Distribution

Maxwellian distribution:

$$f(E) \, dE = \frac{2}{\sqrt{\pi}} \left(\frac{E}{kT}\right)^{1/2} \exp\left(-\frac{E}{kT}\right) \frac{dE}{kT},$$

or

$$f(v) \, dv = \frac{4}{\sqrt{\pi}} \left(\frac{v}{v_T}\right)^2 \exp\left[-\left(\frac{v}{v_T}\right)^2\right] \frac{dv}{v_T},$$

with

$$E = \frac{m}{2} v^2 \quad \text{and} \quad kT = \frac{m}{2} v_T^2.$$

With the mean energy

$$E_0 = \langle E \rangle = \frac{m}{2} v_0^2 = \frac{3}{2} kT, \quad v_0^2 = \frac{3}{2} v_T^2,$$

we can rewrite the Maxwellian distribution:

$$f(v) \, dv = \sqrt{\frac{24}{\pi}} \frac{3}{2} \left(\frac{v}{v_0}\right)^2 \exp\left[-\frac{3}{2}\left(\frac{v}{v_0}\right)^2\right] \frac{dv}{v_0}.$$

Ring8909

Convolution of Monoenergetic Results with Maxwellian Distribution

Three transport coefficients:

$$D_k^* = \sqrt{\frac{24}{\pi}} \int \frac{D(v)}{D_0} \left(\frac{3}{2}\right)^k \left(\frac{v}{v_0}\right)^{2k} \exp\left[-\frac{3}{2}\left(\frac{v}{v_0}\right)^2\right] \frac{dv}{v_0}$$

with $\quad k = 1, 2, 3, \quad$ and

$$\frac{D(v)}{D_0} = \frac{D^*(v) \, D_P(v)}{D_0} = D^*(v) \left(\frac{v}{v_0}\right)^3.$$

Calculation of transport coefficients for a Maxwellian distribution with the formulas for monoenergetic particles:

$$D^*_{\sqrt{\nu}} = C_{\sqrt{\nu}} \, H^{1.5} \, \sqrt{\nu^*},$$

$$D^*_{\nu} = C_{\nu} \, H^2 \, \nu^*,$$

and $D_X^*(L^*)$ as upper Limit $(X = \text{PS, B, R})$.

For convolution the formula

$$D^*(\nu^*) = \left(\frac{1}{D_X^*} + \frac{1}{\min(D^*_{\sqrt{\nu}}, D^*_{\nu})}\right)^{-1}$$

was used in the ripple regime, and

$$D^*(\nu^*) = \min(D_X^*, D^*_{\sqrt{\nu}}, D^*_{\nu})$$

otherwise (for smaller L^*).

Ring8910

Additional Confinement Times

Plateau value of the transport coefficient

$$D_0 = 0.64\, \varrho_0^2\, v_0 / t\pi R_0 ,$$

Plateau value of the loss rate

$$S_0 = 5.7\, D_0 / a^2 ,$$

Plateau value of the confinement time

$$\tau_0 = 1/S_0 .$$

Three additional confinement times :

$$\tau_1 = \frac{a^2}{5.7\, D_1}, \quad \tau_2 = \frac{a^2}{4.6\, D_2}, \quad \tau_3 = \frac{a^2}{2.6\, D_3} .$$

Particle confinement time $\quad \tau_N \approx \tau_2$,

Energy confinement time $\quad \tau_W \approx \tau_3$,

as long as the quantity $\quad -\dfrac{1}{2} + \dfrac{q\phi_0}{kT_0}$

can be neglected.

Various Parameters for Configuration Helias50B

		Helias50B	Helias50B	Helias50B	Helias50B
R_o	[m]	5.0	6.5	13.0	26.0
a	[m]	0.50	0.65	1.30	2.60
A		20	20	20	20
r_o	[m]	0.25	0.325	0.65	1.30
$t(r_o)$		0.816	0.816	0.816	0.816
L_c	[m]	19.3	25	50	100
B_o	[T]	4.0	3.0	4.0	5.0
$kT(r_o)$	[keV]	6.4	6.1	10	10
E_o	[keV]	9.6	9.1	15	15
v_o	[10^5 m/s]	9.59	9.34	12.0	12.0
ϱ_o	[10^{-3} m]	5.00	6.50	6.26	5.01
$Q_{o\varrho}$		100	100	210	520
$\beta(r_o)$	[%]	5.0	5.0	5.0	5.0
$n_e(r_o)$	[10^{19} m^{-3}]	15.5	9.2	9.9	15.5
Λ_o	[10^3 m]	3.6	5.4	13.6	8.7
L_o^*		18_5	21_5	27_0	8_7
D_o	[m^2/s]	1.20	1.52	0.90	0.29
S_o	[s^{-1}]	27	20	3.0	0.24
C_ϕ		±1	±1	±1	±1
τ_o	[ms]	37	49	33_0	41_{00}
τ_1	[ms]	2400	3200	13300	84000
τ_2	[ms]	900	1200	5200	32000
τ_3	[ms]	360	480	2100	12800
τ_c	[ms]	3.7	5.8	11.3	7.3
W	[MJ]	3.5	4.3	61	770
P	[MW]	9.7	9.0	29	60

Parameters for various Configurations

		W VII-AS	Helias5081	Helias50B5	Helias61
R_o	[m]	5.0	5.0	5.0	5.0
a	[m]	0.50	0.50	0.50	0.50
A		20	20	20	20
r_o	[m]	0.25	0.25	0.25	0.25
$t(r_o)$		0.389	0.882	0.816	1.531
L_c	[m]	40.4	17.8	19.3	10.3
B_o	[T]	4.0	4.0	4.0	4.0
$kT(r_o)$	[keV]	6.4	6.4	6.4	6.4
E_o	[keV]	9.6	9.6	9.6	9.6
v_o	[10^5 m/s]	9.59	9.59	9.59	9.59
ϱ_o	[10^{-3} m]	5.00	5.00	5.00	5.00
$Q_{o\varrho}$		100	100	100	100
$\beta(r_o)$	[%]	2.0	4.0	5.0	5.0
$n_e(r_o)$	[10^{19} m^{-3}]	6.2	12.4	15.5	15.5
Λ_o	[10^3 m]	8.9	4.4	3.6	3.6
L_o^*		22_0	25_0	18_5	35_0
D_o	[m^2/s]	2.52	1.11	1.20	0.64
S_o	[s^{-1}]	57	25	27	15
C_ϕ		±1	±1	±1	±1
τ_o	[ms]	17	40	37	69
τ_1	[ms]	160	640	2400	12000
τ_2	[ms]	60	240	900	3800
τ_3	[ms]	27	100	360	1500
τ_c	[ms]	9.3	4.6	3.7	3.7

"Stationary" Monoenergetic Distribution Function

A constant value of mean free path is assumed throughout the plasma volume.

A particle lost out of this volume is replaced by another particle with the same initial energy by doubling a particle of the remaining test distribution.

The particle to be doubled is selected according to a cyclic procedure which leads to the eventual doubling of every particle.

This process leads to an asymptotic distribution (in time).

The loss rate associated with this distribution corresponds to the asymptotic rate of decay.

"Bootstrap Current"

The "stationary" monoenergetic distribution function also yields the toroidal current carried by this distribution.

In an axisymmetric field the scaling

$$\langle \eta \rangle = \frac{\langle v_{\parallel} \rangle}{v} = \frac{1.4\sqrt{A_a}}{\epsilon\, Q_\varrho} = \langle \eta \rangle_{\text{Tok}}$$

was verified so that $\langle \eta \rangle$ may be used as a measure for the bootstrap current.

In quasi-hellically symmetric configurations it reverses its sign and is smaller in size.

α-Particle Confinement

The collisionless α-particle confinement $(Q_\varrho = 30)$ is assessed by following guiding centre orbits of a sample of 64 (or more) α-particles at aspect ratio $A = 40$ (which is approximately equivalent to $1/4$ of the plasma radius a) with random values in the angular variables ϑ and φ, and the pitch angle $\eta = v_{\parallel}/v$.

Calculations have been done up to $N_{\text{hcl}} = 5 \cdot 10^5$ half connection lengths.

"Bootstrap" Current (Asymmetry in $v_{\parallel}$)

at $Q_\varrho = 100$ and $L^* = 1000$

$$\left(\langle \eta \rangle_{\text{Tok}} = \frac{1.4\sqrt{A_a}}{\epsilon\, Q_\varrho} \right)$$

Configuration	$\langle \beta \rangle$ [%]	$\epsilon(20)$	A_a	E_p	N_{col}	lost	$\langle \eta \rangle$ [%]	$\langle \eta \rangle_{\text{Tok}}$ [%]	$\frac{\langle \eta \rangle}{\langle \eta \rangle_{\text{Tok}}}$	$\delta_e(20)$ [%]
Tokamak				+1	1024	5904	+10.3		+1.10	
Tokamak	0	0.47	10.0	0	1024	4478	+9.5	9.4	+1.01	0.0
Tokamak				−1	1024	3131	+7.9		+0.84	
Helias61				+1	1024	168	−1.9		−0.6	
Helias61	0	1.53	13.8	0	1024	602	−2.6	3.4	−0.8	0.3
Helias61				−1	1024	99	−0.8		−0.2	
Helias5081				+1	1024	887	−0.8		−0.15	
Helias5081	0	0.88	12.0	0	1024	17082	−1.5	5.5	−0.27	2.5
Helias5081				−1	1024	387	−0.5		−0.09	
Helias50 B 0				+1	512	484	+1.2		+0.22	
Helias50 B 0	0	0.85	11.0	0	512	10672	+1.2	5.5	+0.22	1.4
Helias50 B 0				−1	512	266	+0.7		+0.13	
Helias50 B 5				+1	1024	684	+0.3		+0.05	
Helias50 B 5	5	0.82	11.3	0	1024	6386	+0.6	5.7	+0.11	0.7
Helias50 B 5				−1	1024	330	+0.2		+0.04	

29.6.1989

α-Particle Losses, starting with 64 Particles

$A = 40 \qquad Q_\varrho = 30 \qquad E_{pot} = 0$

Configuration	$\langle \beta \rangle$ [%]	$\epsilon(40)$	A_a	N_{hcl} [1000]	lost	refl	$\delta_e(20)$ [%]	$\delta_e(40)$ [%]
DOM25	0	0.43	8.65	1	12	12	1.1	0.3
W7AS	0	0.39	11.2	1	13	13	3.6	2.4
W7ASG	0	0.38	10.6	32	20	21	4.2	
Helias0	0	0.79	13.4	32	24	26	1.4	
Helias5	5	0.79	13.6	128	20	21	1.4	
Helias9	9	0.77	13.8	256	20	21	1.3	
Helias15	15	0.76	14.0	512	3	26	1.3	
Helias61	0	1.48	13.8	512	0	18	0.3	
Helias5081	0	0.83	12.0	512	3	8	2.5	
Helias50 B 0	0	0.82	11.0	256	15	21	1.4	
Helias50 B 2	2.4	0.80	11.2	256	12	21	0.8	
Helias50 B 5	5	0.77	11.3	256	7	21	0.7	0.6

29.6.1989
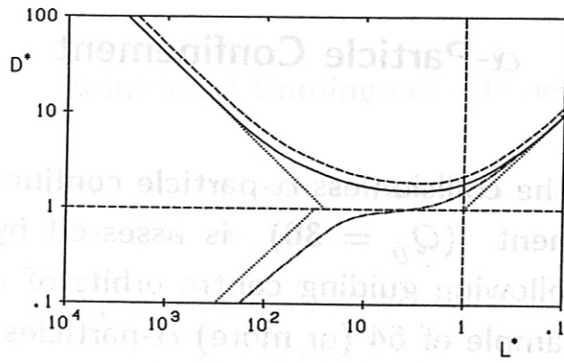
FIG. 1: Normalized transport coefficients D^* for three configurations at $A = 10$, $\iota = 0.5$:
upper curve: - - - $\ell = 2$ stellarator (DOM2A), $\delta_e = 8.4\%$, $N = 10$,
middle curve: — rippled tokamak with $\delta_e = 8.4\%$,
lower curve: - - - tokamak without ripple.
The dotted lines represent D_R^*, D_B^*, and D_{PS}^*.
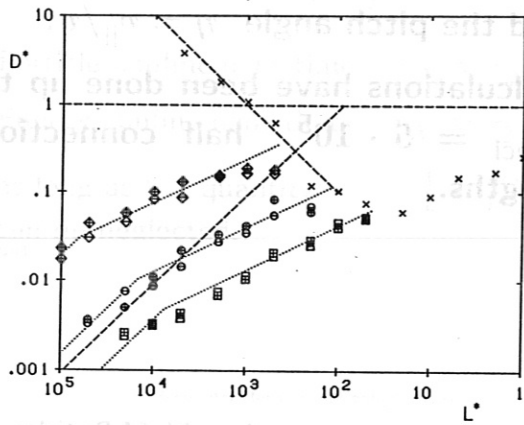
FIG. 2: Normalized transport coefficients D^* for the stellarator Helias50 B 5 for various values of Q_ϱ and electric fields.
$A = 11.3$, $N = 5$, $\iota = 0.82$, $\delta_e \approx 0.7\%$.
($\times$): $Q_\varrho = 2 \cdot 10^4$, $e\phi_o/E = 0$.
($\diamond$): $Q_\varrho = 4 \cdot 10^3$, $e\phi_o/E = \pm 2$, $H = 147$, $H_c = 176_0$.
($\bigcirc$): $Q_\varrho = 2 \cdot 10^3$, $e\phi_o/E = \pm 4$, $H = 36.7$, $H_c = 88_0$.
($\square$): $Q_\varrho = 1 \cdot 10^3$, $e\phi_o/E = \pm 10$, $H = 7.34$, $H_c = 44_0$.
The dotted lines represent $D_{\nu, \frac{1}{2}}^*$ and D_ν^* given by the respective formulas using the calculated C_{ik}.
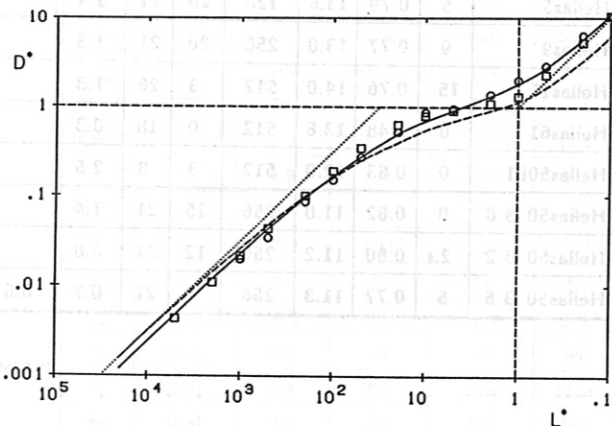
FIG. 3: Normalized transport coefficients D^* for a tokamak with aspect ratio $A = 10$. Monoenergetic results ($\square$) and results using a Maxwellian energy distribution with full energy scattering ($\bigcirc$) are shown. The continuous curve was computed by convoluting the monoenergetic results with a Maxwellian energy distribution. The dashed curve was computed by using the theoretical values of Hazeltine et al. The dotted line on the left-hand side represents $D_B^* = A^{3/2}/L^*$.
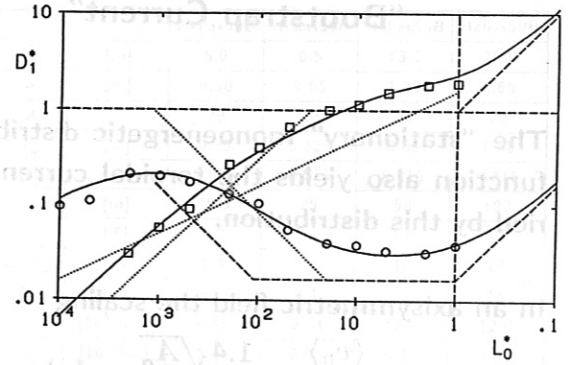
FIG. 4: Normalized transport coefficients D_1^* for ion and electron particle transport (—) calculated by convoluting the monoenergetic results with a Maxwellian energy distribution. Shown are results obtained for an $\ell = 2$ stellarator (DOM25) at $A = 12.5$ with $e\phi_o/E_o = \pm 10$ and $Q_{o\varrho} = a/\varrho_o = 10^3$ for deuterons and $Q_{o\varrho} = 6 \cdot 10^4$ for electrons, $\varrho_o = mv_o/eB_o$.
Further results were obtained by using a Maxwellian energy distribution with full energy scattering for ions ($\square$) and for electrons ($\bigcirc$).
The dotted lines represent D_{1R}^*, $D_{1\nu, \frac{1}{2}}^*$, and $D_{1\nu}^*$, it being assumed that $C_{12} = 0$ and $C_{22} = 0$. The dotted lines are equivalent to the results of Ho and Kulsrud [Phys. Fluids 30, 442 (1987)].
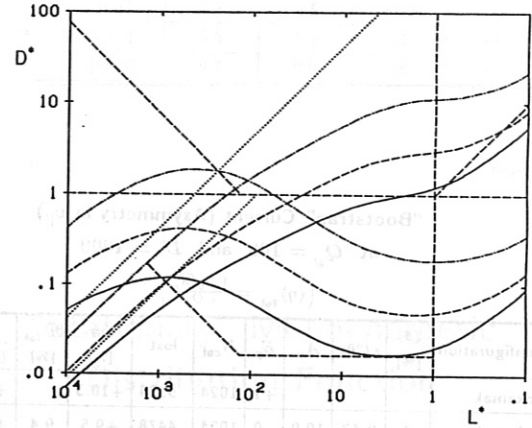
FIG. 5: Transport coefficients D_1^* (—), D_2^* (- - -), and D_3^* (- · ·) obtained for the stellarator W7AS at $A = 20$ with $Q_{o\varrho} = 100$ (deuterons), $Q_{o\varrho} = 6 \cdot 10^3$ (electrons), and $e\phi_o/E_o = \pm 1$. Dotted lines represent $D_B^* = A^{3/2}/L^*$ and $D_{\nu c}^* = H_c^2 \nu^*$, which, in turn, corresponds to $S_\nu = \nu$.
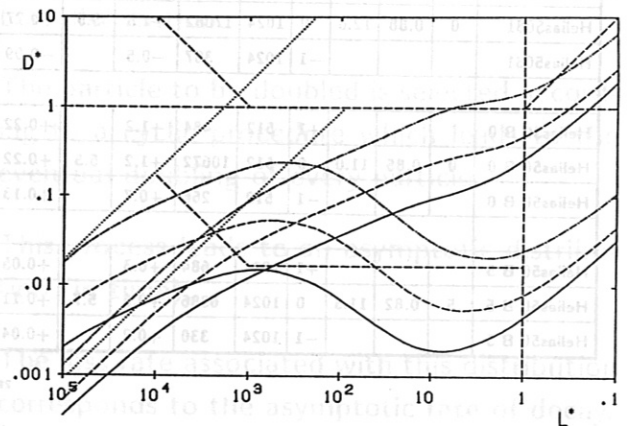
FIG. 6: Transport coefficients D_1^* (—), D_2^* (- - -), and D_3^* (- · ·) obtained for the stellarator Helias50 B 5 at $A = 20$ with $Q_{o\varrho} = 100$ (deuterons), $Q_{o\varrho} = 6 \cdot 10^3$ (electrons), and $e\phi_o/E_o = \pm 1$. Dotted lines represent $D_B^* = A^{3/2}/L^*$ and $D_{\nu c}^* = H_c^2 \nu^*$, which, in turn, corresponds to $S_\nu = \nu$.
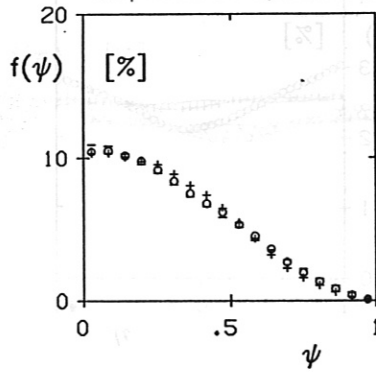
FIG. 7: "Stationary" distribution function $f(\psi)$ for a tokamak with $A_a = 10$, $\iota = 0.94$, $Q_\varrho = 50$ (deuterons), $L^* = 1000$, $e\phi_o/E_o = +1$, 0, -1.
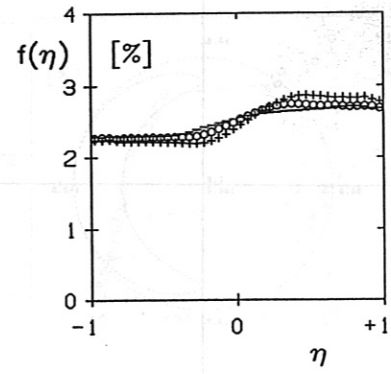
FIG. 10: "Stationary" distribution function $f(\eta)$ for a tokamak with $A_a = 10$, $\iota = 0.94$, $Q_\varrho = 100$ (deuterons), $L^* = 10^3$, $e\phi_o/E_o = +1$, 0, -1.
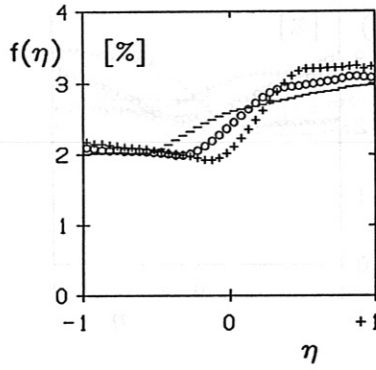
FIG. 8: "Stationary" distribution function $f(\eta)$ for a tokamak with $A_a = 10$, $\iota = 0.94$, $Q_\varrho = 50$ (deuterons), $L^* = 1000$, $e\phi_o/E_o = +1$, 0, -1.
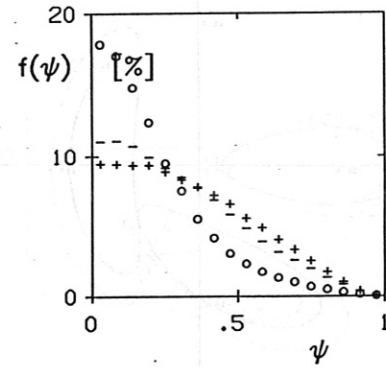
FIG. 11: "Stationary" distribution function $f(\psi)$ for the stellarator Helias61 with $\beta = 0$, $A_a = 13.8$, $\iota(20) = 1.53$, $Q_\varrho = 50$ (deuterons), $L^* = 1000$, $e\phi_o/E_o = +1$, 0, -1.
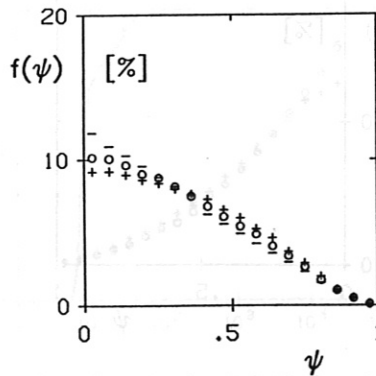
FIG. 9: "Stationary" distribution function $f(\psi)$ for a tokamak with $A_a = 10$, $\iota = 0.94$, $Q_\varrho = 100$ (deuterons), $L^* = 10^3$, $e\phi_o/E_o = +1$, 0, -1.
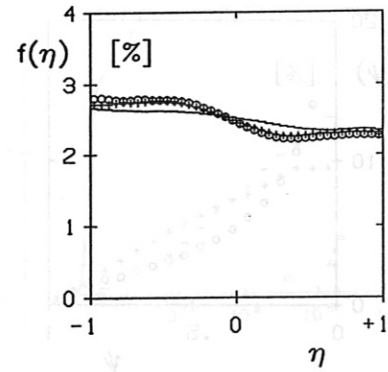
FIG. 12: "Stationary" distribution function $f(\eta)$ for the stellarator Helias61 with $\beta = 0$, $A_a = 13.8$, $\iota(20) = 1.53$, $Q_\varrho = 50$ (deuterons), $L^* = 1000$, $e\phi_o/E_o = +1$, 0, -1.
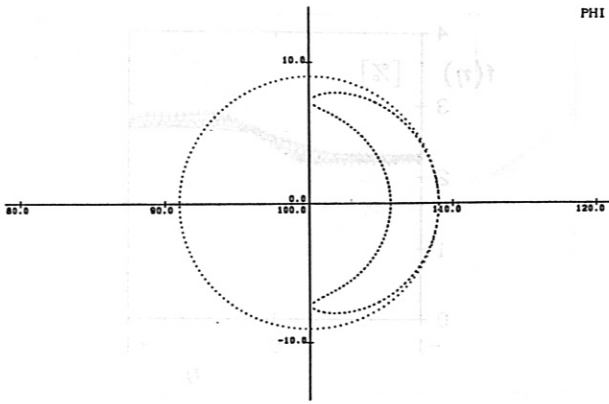
FIG. 13: Cross section through a magnetic surface and a drift surface in a tokamak with $A = 11$ and $\iota = 0.47$.

FIG. 16: "Stationary" distribution function $f(\eta)$ for the stellarator Helias5081 with $\beta = 0$, $A_a = 12.0$, $\iota(20) = 0.88$, $Q_\varrho = 100$ (deuterons), $L^* = 1000$, $e\phi_o/E_o = +1,\ 0,\ -1$.
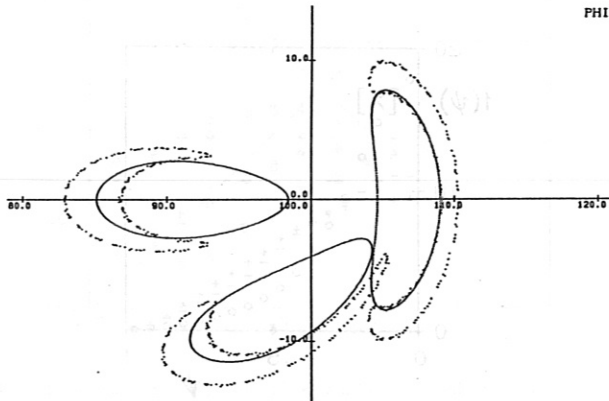
FIG. 14: Cross section through a magnetic surface and a drift surface in the stellarator Helias61 at three different toroidal angles with $A = 24$ and $\iota = 1.52$.
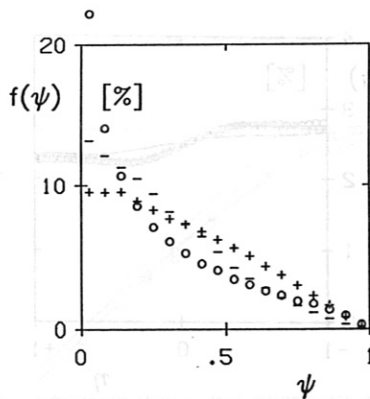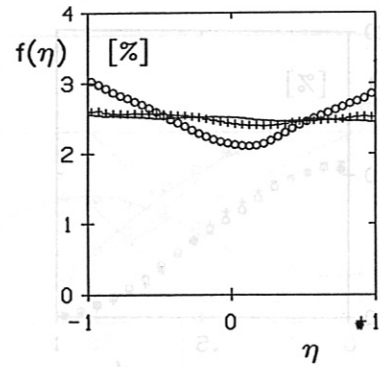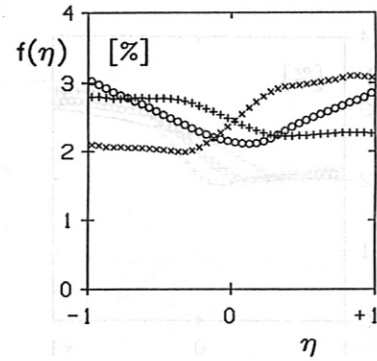
FIG. 17: "Stationary" distribution function $f(\eta)$ for a tokamak ($\times$), and stellarators Helias61 (+) and Helias5081 (O). For particulars see Figs. 8, 12, and 16.

FIG. 15: "Stationary" distribution function $f(\psi)$ for the stellarator Helias5081 with $\beta = 0$, $A_a = 12.0$, $\iota(20) = 0.88$, $Q_\varrho = 100$ (deuterons), $L^* = 1000$, $e\phi_o/E_o = +1,\ 0,\ -1$.
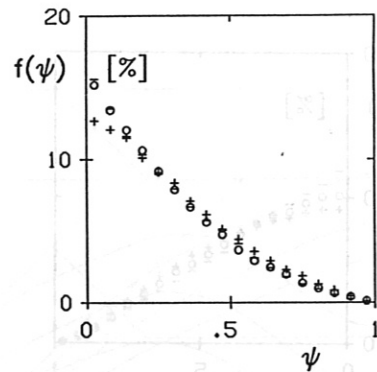
FIG. 18: "Stationary" distribution function $f(\psi)$ for the stellarator Helias50 B 5 with $\beta = 4.9\%$, $A_a = 11.3$, $\iota(20) = 0.82$, $Q_\varrho = 100$ (deuterons), $L^* = 1000$, $e\phi_o/E_o = +1,\ 0,\ -1$.

FIG. 19: "Stationary" distribution function $f(\eta)$ for the stellarator Helias50 B 5 with $\beta = 4.9\%$, $A_a = 11.3$, $\iota(20) = 0.82$, $Q_\varrho = 100$ (deuterons), $L^* = 1000$, $e\phi_o/E_o = +1$, 0, -1.

FIG. 22: α-particle losses in "Kyoto-Helias" with $\beta = 0(\bigcirc)$, $5(\times)$, $9(\triangle)$, and $15(+)$ [%]; $Q_\varrho = 30$, $A = 40$. Number of reflected particles ($= 100\%$) is 26, 21, 21, 26, respectively. Alltogether there are 64 particles, i.e. ca. 40 passing particles.
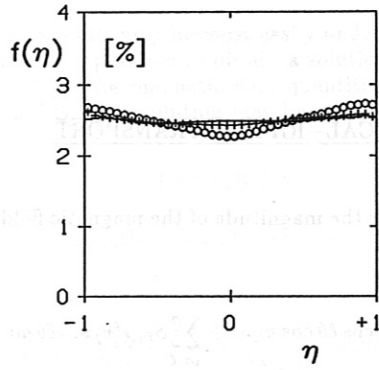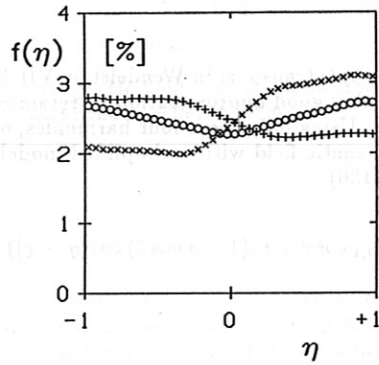
FIG. 20: "Stationary" distribution function $f(\eta)$ for a tokamak ($\times$), and stellarators Helias61 ($+$) and Helias50 B 5 ($\bigcirc$). For particulars see Figs. 8, 12, and 19.
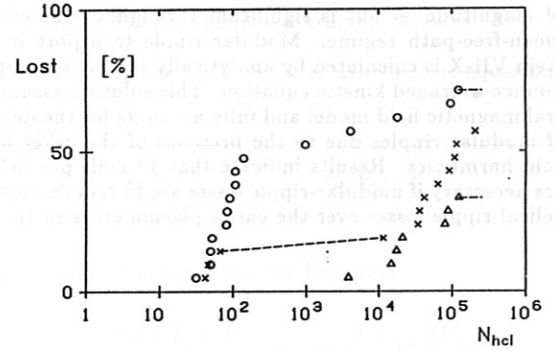
FIG. 23: α-particle losses in Helias50B with $\beta = 0(\bigcirc)$, $2.4(\times)$, and $4.9(\triangle)$ [%]; $Q_\varrho = 30$, $A = 40$. Number of reflected particles ($= 100\%$) is 21 in all cases. Alltogether there are 64 particles, i.e. 43 passing particles.

FIG. 21: α-particle losses in stellarator W7AS, $Q_\varrho = 30$, $A \approx 40$. All 100 reflected particles ($= 100\%$) are lost within $N_{hcl} \approx 100$ half connection lengths. No particle of 400 passing particles is lost.
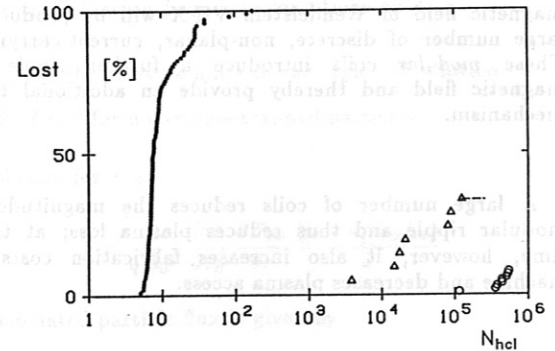
FIG. 24: α-particle losses in stellarators W7AS ($\bullet$), Helias50 B 5 ($\triangle$), and Helias61 ($\bigcirc$). W7AS and Helias61 have been calculated in Cartesian coordinates with 100 reflected particles. Helias50 B 5 has been calculated in magnetic coordinates. See Figs. 21 and 23 for particulars.

RIPPLE TRANSPORT IN A MODULAR HELIAS

C.D. Beidler
Max-Planck-Institut für Plasmaphysik
EURATOM-IPP Association
D-8046 Garching, FRG

Neoclassical transport rates are determined for Helical-Axis Advanced Stellarators (Helias). Special emphasis is given to Wendelstein VII-X candidates, for which the magnetic field is produced by a large number of discrete non-planar coils. The investigation is concentrated on the long-mean-free-path regime where particles trapped in local *ripple* wells of the magnetic field make the dominant contribution to transport. For Wendelstein VII-X, such particles fall into two classes; those localized in the *helical* ripple common to all stellarator-type devices and those very-localized particles which are trapped in the *modular* ripples existing between the individual coils. Using analytical techniques it is shown that helical-ripple transport rates are substantially reduced for all Wendelstein VII-X candidates relative to classical stellarator/torsatron configurations. This reduction is most pronounced in the $1/\nu$ regime — equivalent helical ripples of less than 1% lead to reduction factors of more than an order of magnitude — but is significant throughout the entire long-mean-free-path regime. Modular ripple transport in Wendelstein VII-X is calculated by analytically solving the appropriate bounce-averaged kinetic equation. This solution assumes a general magnetic field model and fully accounts for the deformation of modular ripples due to the presence of the other magnetic-field harmonics. Results indicate that 12 coils per field period are necessary if modular-ripple losses are to remain smaller than helical-ripple losses over the entire plasma cross section.

INTRODUCTION

- One of the advantages of Helias relative to conventional stellarator/torsatron devices is a much smaller rate of neoclassical transport in the long-mean-free-path (*lmfp*) regime where particles trapped in the *helical* ripple of the stellarator's magnetic field provide the dominant transport mechanism.

- Unlike the conventional stellarator/torsatron, however, the magnetic field of Wendelstein VII-X will be produced by a large number of discrete, non-planar, current-carrying coils. These *modular* coils introduce a further ripple in the magnetic field and thereby provide an additional transport mechanism.

- A large number of coils reduces the magnitude of the modular ripple and thus reduces plasma loss; at the same time, however, it also increases fabrication costs of the machine and decreases plasma access.

- In the current work, the neoclassical transport levels resulting from both the helical and modular ripples will be estimated for Wendelstein VII-X candidates using analytic theories. Results will be used to find the optimum number of coils per field period insuring that modular-ripple losses are tolerable over the entire plasma cross section.

HELICAL–RIPPLE TRANSPORT

A general model for the magnitude of the magnetic field is given by

$$\frac{B}{B_0} = \sum_{m,\ell} C_{m,\ell}(r) \cos \ell\theta \cos mp\phi + \sum_{m,\ell} S_{m,\ell}(r) \sin \ell\theta \sin mp\phi.$$

For convenience, the magnetic field harmonics of Helias configurations may be classified as follows:

1) The Principal Harmonics $C_{0,1}, C_{1,0}, C_{1,1}, S_{1,1}$

2) The Remaining   **HS4-8** $S_{2,1}$
   Low-Order   **HS5-6** $C_{0,2}, C_{2,2}, S_{2,2}, C_{2,3}, S_{2,3}$
   Harmonics   **HS5-7** $C_{2,1}, C_{2,3}, S_{2,3}$

3) The Modular-Ripple Harmonics

To estimate *helical-ripple* transport in Wendelstein VII-X candidates, it is a reasonably good approximation to retain only the principal harmonics. Using only these four harmonics, one may approximate the magnetic field with a simplified model (Phys. Fluids, **26**, (1983) 2136)

$$B = B_0 \big(1 - C_{0,1} \cos \theta + \epsilon_h (1 - \sigma \cos \theta) \cos(\eta - \chi)\big) .$$

In this equation

$$\epsilon_h = \left(C_{1,0}^2 + \frac{C_{1,1}^2 + S_{1,1}^2}{2}\right)^{1/2} , \qquad \sigma = -\frac{C_{1,0} C_{1,1}}{\epsilon_h{}^2} ,$$

$$\eta = p\phi ,$$

$$\sin \chi = \frac{S_{1,1} \sin \theta}{\epsilon_h (1 - \sigma \cos \theta)} , \qquad \cos \chi = \frac{C_{1,0} + C_{1,1} \cos \theta}{\epsilon_h (1 - \sigma \cos \theta)} .$$

This is an example of a so-called *transport-optimized* stellarator field (Phys. Rev. Lett., **48**, (1982) 322). The model field of a *classical* stellarator is recovered by setting $C_{0,1} = \epsilon_t = r/R_0$ and $\sigma = 0$. Comparisons of the model field with the general field for Wendelstein VII-X candidates are given in the figures.

A general theory of *lmfp* transport in this model field has been developed (Phys. Rev. Lett., **58**, (1987) 1745), and has been used to predict neoclassical transport coefficients in Wendelstein VII-X candidates; results obtained are in good agreement with those of numerical Monte Carlo simulations (see figures).

- Results confirm the very significant reduction of transport rates relative to the equivalent classical stellarator (*ecs*). This is a general property of Wendelstein VII-X candidates.

- The numerical results increase by a factor of 2-3 when the Remaining Low-Order Harmonics are accounted for. The scaling of the results with collision frequency, ν, remains unchanged.

This favorable result may be most easily understood in the ν^{-1} regime where it is possible to obtain a solution for the particle flux, Γ, in which the magnetic field quantities $C_{0,1}$, ϵ_h and σ appear explicitly. This solution may be written in the form

$$\Gamma = A_h W(\kappa),$$

where $W(\kappa)$ is a function only of energy and

$$A_h \approx \frac{64}{9}\epsilon_h^{3/2}\left(\frac{C_{0,1}}{\epsilon_t}\right)^2\left\{1 - \frac{6}{5}\frac{\sigma\epsilon_h}{C_{0,1}} + 0.385\left(\frac{\sigma\epsilon_h}{C_{0,1}}\right)^2\right\}$$

contains all information relating to the structure of the magnetic field. Note that for the equivalent classical stellarator,

$$A_h = A_h^{(ecs)} = \frac{64}{9}\epsilon_h^{3/2}.$$

The above expression for A_h offers Helias configurations two routes for significant reduction of neoclassical transport.

• Reduce the ratio $C_{0,1}/\epsilon_t$.

• Adjust the magnetic field harmonics so that $\sigma\epsilon_h/C_{0,1} \approx 1.56$ as this minimizes the bracketed term.

Various Wendelstein VII-X candidates utilize both of these routes to different degrees as illustrated in the table below. The results obtained for HS4-8 and HS5-6 confirm those obtained previously by analytical and numerical calculations. Note that HS5-7 is particularly well optimized; a decrease of neoclassical transport rates in the ν^{-1} regime of almost two orders of magnitude is predicted.

	ϵ_h	σ	$C_{0,1}/\epsilon_t$	$\sigma\epsilon_h/C_{0,1}$	$A_h/A_h^{(ecs)}$	$\bar{\epsilon}_h$
HS4-8	0.0502	0.4775	0.5178	1.0284	0.0464	0.0065
HS5-6	0.0666	0.0525	0.1848	0.4112	0.0195	0.0048
HS5-7	0.0626	0.4852	0.4004	1.6429	0.0109	0.0031

Values given above are taken at half plasma radius ($r/a = 1/2$). The "equivalent helical ripple", $\bar{\epsilon}_h$, is defined by the equation

$$A_h = \frac{64}{9}\bar{\epsilon}_h^{3/2}.$$

IMPORTANT POINTS

• Helical-ripple transport in Helias is greatly reduced compared with that of conventional stellarators. In the ν^{-1} regime, the equivalent helical ripple at half radius satisfies $\bar{\epsilon}_h \leq 0.01$ in all cases.

• Analytic theory underestimates helical-ripple transport by a factor of 2-3 since it is unable to account for the Remaining Low-Order Harmonics.

MODULAR–RIPPLE TRANSPORT

Guiding-Center Drift-Kinetic Equation

$$\frac{v_\|}{R}\frac{\partial F}{\partial \phi} + \dot{\theta}_0\frac{\partial F}{\partial \theta_0} + \dot{r}\frac{\partial F}{\partial r} = \nu B^{-1}v_\|\frac{\partial}{\partial\mu}\left(m v_\|\mu\frac{\partial F}{\partial\mu}\right)$$

expressed in magnetic coordinates, (r, θ_0, ϕ). The magnitude of the magnetic field is assumed to be of the form

$$\frac{B}{B_0} = -\delta(r)\cos Np\phi + \sum_{m,\ell}C_{m,\ell}(r)\cos\ell\theta\cos mp\phi$$
$$+\sum_{m,\ell}S_{m,\ell}(r)\sin\ell\theta\sin mp\phi$$

The first term represents the modular ripple with magnitude δ — the Fourier harmonic expansions encompass both the Principal Harmonics and the Remaining Low-Order Harmonics.

In the long-mean-free-path regime

$$J = \oint mv_\| \, dl \qquad \text{constant of the motion}$$
$$\oint dl/v_\| \qquad \text{bounce-averaging operator}$$

are used to simplify the guiding-center drift-kinetic equation.

Assumptions:

$$F = F_M + f$$
$$\dot{\theta}_0/\nu_{eff} < 1$$

Yield the Bounce-Averaged Kinetic Equation

$$\frac{1}{qB_0 r}\frac{\partial B}{\partial\theta_0}\frac{\partial F_M}{\partial r}\frac{\partial}{\partial\mu}(\mu J) = \nu\frac{\partial}{\partial\mu}\left(\mu J\frac{\partial f}{\partial\mu}\right)$$

The form of this equation is possible since particles trapped in modular ripple wells have very low $v_\|$, and hence

$$\dot{r} \approx -(\mu/qB_0 r)(\partial B/\partial\theta_0)$$
$$(\partial/\partial\mu)(\mu J) \approx -\oint(\mu B/v_\|)\,dl$$

Modular ripple wells exist for $\kappa/B_{max} < \mu < \kappa/B_{min}$, where $\kappa = mv^2/2$ and B_{max}, B_{min} are the local maximum and minimum value of B which define the ripple well.

Require the following boundary conditions on f

1) $\partial f/\partial\mu$ must be finite in the region of solution

2) $f = 0$ for non-ripple-trapped particles

The solution for f is

$$f = \frac{1}{qB_0 r}\frac{\partial B}{\partial\theta_0}\frac{\partial F_M}{\partial r}\frac{(\mu - \kappa/B_{max})}{\nu}$$

The associated particle flux is given by

$$\Gamma_\delta = \frac{1}{\pi(2m^3)^{1/2}}\int d\theta_0 \int d\phi \int d\kappa \int d\mu \frac{B}{\sqrt{\kappa - \mu B}}\dot{r}f$$

Carrying out the μ integration, one may once again write

$$\Gamma_\delta = A_\delta(\theta_0, \phi) W(\kappa)$$

where

$$A_\delta = \frac{2\sqrt{2}}{15\pi} \int\limits_0^{2\pi} d\theta_0 \int\limits_0^{2\pi} d\phi \left(\frac{1}{B\epsilon_t}\frac{\partial B}{\partial \theta_0}\right)^2 \left(1 - \frac{B}{B_{max}}\right)^{3/2}\left(4 + \frac{B}{B_{max}}\right)$$

A general analytic solution for $A_\delta(\theta_0, \phi)$ is not possible given the complicated magnetic field profile which has been assumed. Instead, numerical integration is used with the condition

$$\partial B / \partial \phi = 0 \quad \text{along a field line}$$

being *numerically* solved to determine whether a local modular ripple well exists at a given point in (θ_0, ϕ), and if so, what the local value of B_{max} is.

IMPORTANT POINTS

• The idealized model used for the modular ripple may overestimate the transport rate for HS5-7. The analytic theory is currently being modified to handle any modular ripple profile (i.e. to handle the full Fourier spectrum of B).

• The presence of the modular ripple alters the bounce points of particles trapped in the helical ripple — this leads to the stellarator counterpart of 'ripple plateau' diffusion in tokamaks. This is not accounted for in the present theory.

CALCULATING A_δ / A_h FOR WENDELSTEIN VII–X

For illustration purposes, the Wendelstein VII-X candidate HS5-7 will be used. HS5-7 is a five field period Helias with major radius of 6.5 meters, plasma radius of ≈ 0.65 meters and a rotational transform profile which varies from $\iota = 0.75$ on axis to $\iota = 0.95$ at the plasma edge.

HS5-7 has been considered in both $N = 10$ and $N = 12$ versions. The Principal and Remaining Low-Order Fourier Harmonics of the HS5-7 magnetic field are shown in Figure 7 (these harmonics are essentially identical in the two cases) along with the relative magnitude of the modular ripple for both versions (dashed line).

The location and depth of modular ripples are shown for each of the two HS5-7 versions in Figures 8 and 9. The plots are shown over one field period for the flux surface $r/a = 0.8$.

The ratio of A_δ/A_h is calculated for several flux surfaces according to the results given here and is plotted in Figure 10 for the $N = 10$ and $N = 12$ versions of HS5-7. The $N = 10$ case shows values of this ratio considerably in excess of one near the plasma edge. On the other hand, $A_\delta/A_h < 1$ at all radii for the $N = 12$ version. As this latter version also allows sufficient plasma access, 12 coils per field period is deemed to be optimum for HS5-7.

SUMMARY

• Wendelstein VII-X candidates show greatly reduced levels of helical-ripple-induced neoclassical transport relative to classical stellarator configurations; for HS5-7 a reduction of two orders of magnitude is achieved in the $1/\nu$ regime. These results have been confirmed numerically with Monte Carlo simulations.

• The neoclassical transport level due to particles trapped in the local ripples of a modular stellarator's magnetic field has been calculated by solving the bounce-averaged kinetic equation.

• The solution assumes a general magnetic field model so that arbitrarily complex stellarator configurations may be handled.

• As a specific example, modular-ripple transport in the Wendelstein VII-X candidate HS5-7 has been calculated. Results indicate that 12 modular coils per field period are necessary if modular-ripple losses are to remain smaller than helical-ripple losses across the entire plasma cross section.
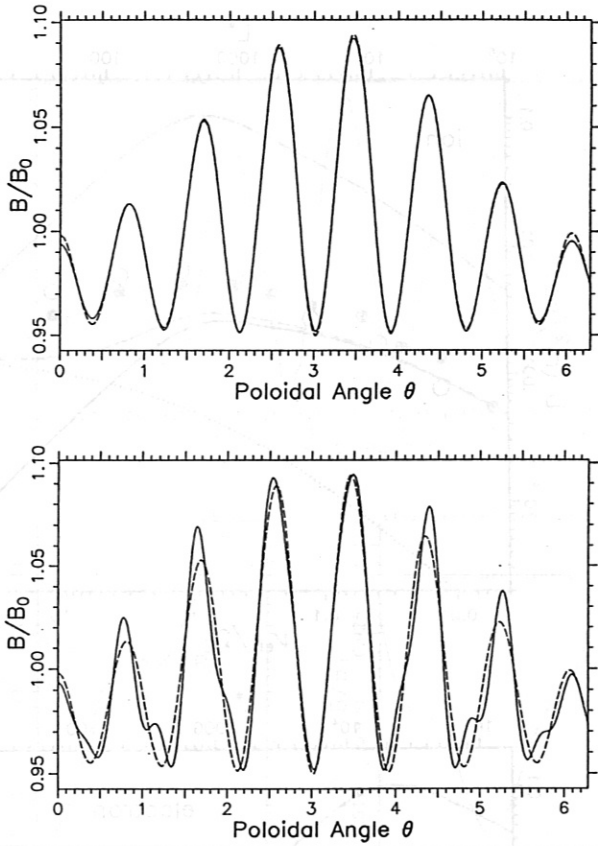
FIGURE 1. The magnitude of B/B_0 along a field line for HS4-8 at half plasma radius. ABOVE: solid line — Fourier decomposition with $C_{0,1} = -.02325$, $C_{1,0} = .0442$, $C_{1,1} = -.0272$, $S_{1,1} = -.0197$; dashed line — model field given in the text with $\epsilon_h = 0.0502$ and $\sigma = 0.4775$. BELOW: solid line — Fourier decomposition with the four Principal Harmonics, as given above, and the Remaining Low-Order Harmonic $S_{2,1} = -.019$; dashed line — the model field is shown again for comparison. The rotational transform is $\iota = 0.55$.

FIGURE 3. The magnitude of B/B_0 along a field line for HS5-7 at half plasma radius. ABOVE: solid line — Fourier decomposition with $C_{0,1} = -.0185$, $C_{1,0} = .034$, $C_{1,1} = -.056$, $S_{1,1} = -.049$; dashed line — model field given in the text with $\epsilon_h = 0.0626$ and $\sigma = 0.4852$. BELOW: solid line — Fourier decomposition with the four Principal Harmonics, as given above, and the Remaining Low-Order Harmonics $C_{2,1} = .0025$, $C_{2,3} = -.0025$, $S_{2,3} = -.0025$; dashed line — the model field is shown again for comparison. The rotational transform is $\iota = 0.809$.

FIGURE 2. The magnitude of B/B_0 along a field line for HS5-6 at half plasma radius. ABOVE: solid line — Fourier decomposition with $C_{0,1} = -.0105$, $C_{1,0} = .00525$, $C_{1,1} = -.0685$, $S_{1,1} = -.0685$; dashed line — model field given in the text with $\epsilon_h = 0.0666$ and $\sigma = 0.0525$. BELOW: solid line — Fourier decomposition with the four Principal Harmonics, as given above, and the Remaining Low-Order Harmonics $C_{0,2} = -.0055$, $C_{2,2} = -.00175$, $C_{2,3} = -.00119$, $S_{2,2} = -.00175$, $S_{2,3} = -.00119$; dashed line — the model field is shown again for comparison. The rotational transform is $\iota = 0.90$.

FIGURE 4. The diffusion coefficient, D, vs. normalized collision frequency, ν_{eff}/Ω_E, for ions (protons) and electrons in the Wendelstein VII-X candidate HS4-8 at half plasma radius, $\rho = 0.5$. The solid line is the analytic estimate of the diffusion coefficient due to ripple transport in the model magnetic field given in the text (assuming only the Principal Harmonics $C_{0,1}$, $C_{1,0}$, $C_{1,1}$, and $S_{1,1}$). The dotted line is an analytic estimate of the expected axisymmetric transport while the dashed line is the sum of the solid and dotted lines. The dot-dash line is the expected ripple transport rate in the equivalent classical stellarator ($\epsilon_h = 0.0502$, $\sigma = 0$, $\epsilon_t = C_{0,1} = 0.05$). Monte Carlo numerical results are shown for: (•) the four Principal Harmonics; (o) these four harmonics plus the Remaining Low-Order Harmonic $S_{2,1}$ (the magnitudes of all harmonics may be found in Figure Caption 1).
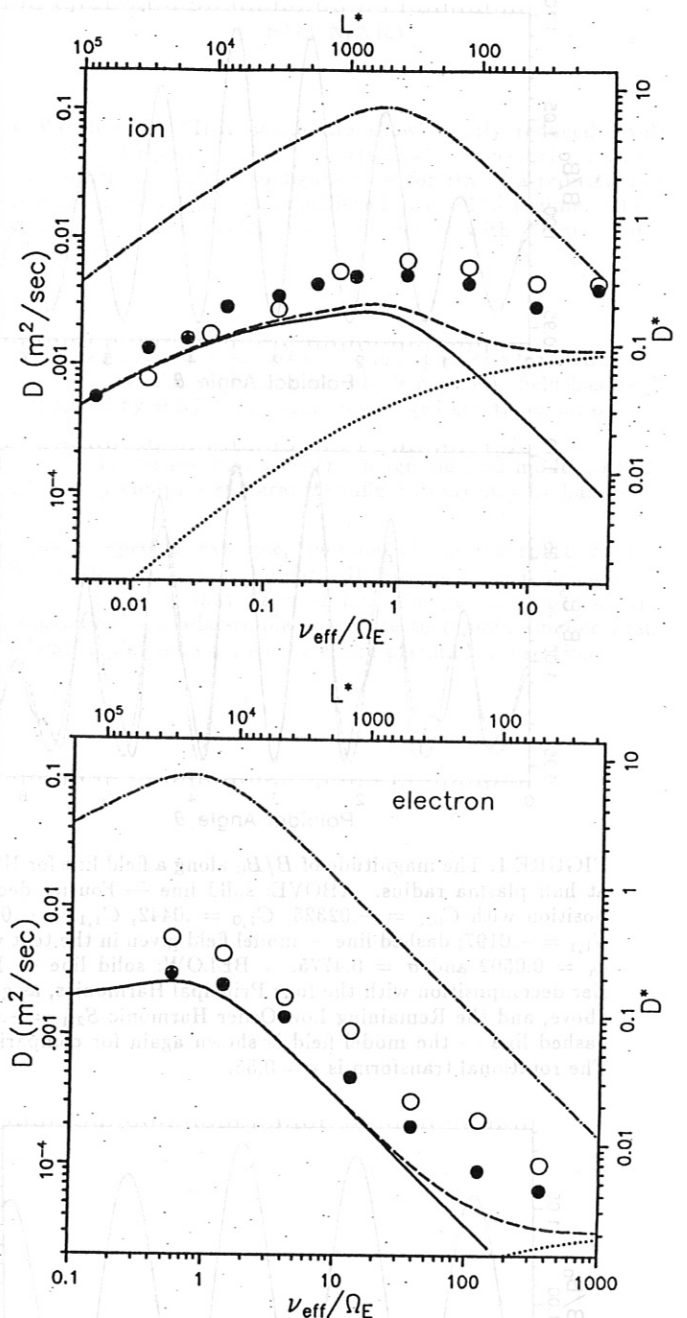
FIGURE 5. As in Figure 4 for the configuration HS5-6 (equivalent classical stellarator: $\epsilon_h = 0.0666$, $\sigma = 0$, $\epsilon_t = C_{0,1} = 0.05$). Monte Carlo numerical results are shown for: (•) the four Principal Harmonics; (o) these four harmonics plus the Remaining Low-Order Harmonics $C_{0,2}$, $C_{2,2}$, $C_{2,3}$, $S_{2,2}$ and $S_{2,3}$ (the magnitudes of all harmonics may be found in Figure Caption 2).
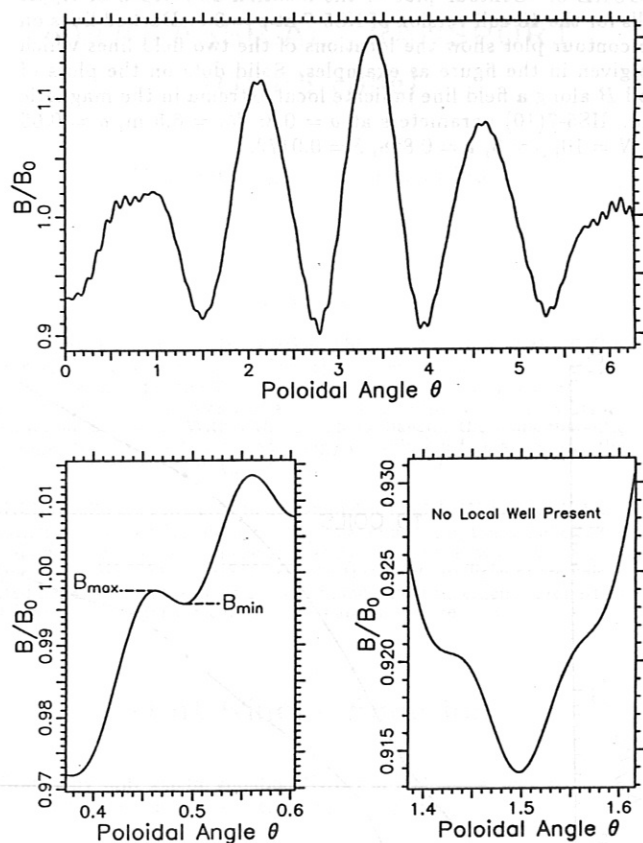
FIGURE 6. ABOVE – The magnitude of B along a field line is shown for a modular Helias (the 12-coil version of HS5-7 at $\rho = 0.8$). The *modular-ripple* wells are most clearly visible at the left- and righthand sides of the plot. BELOW LEFT – A greatly enlarged detail from the above, illustrating the definitions of B_{max} and B_{min} for a single modular-ripple well. BELOW RIGHT – Another detail, illustrating a case in which the presence of other harmonics of the magnetic field does not allow the formation of the local ripple.
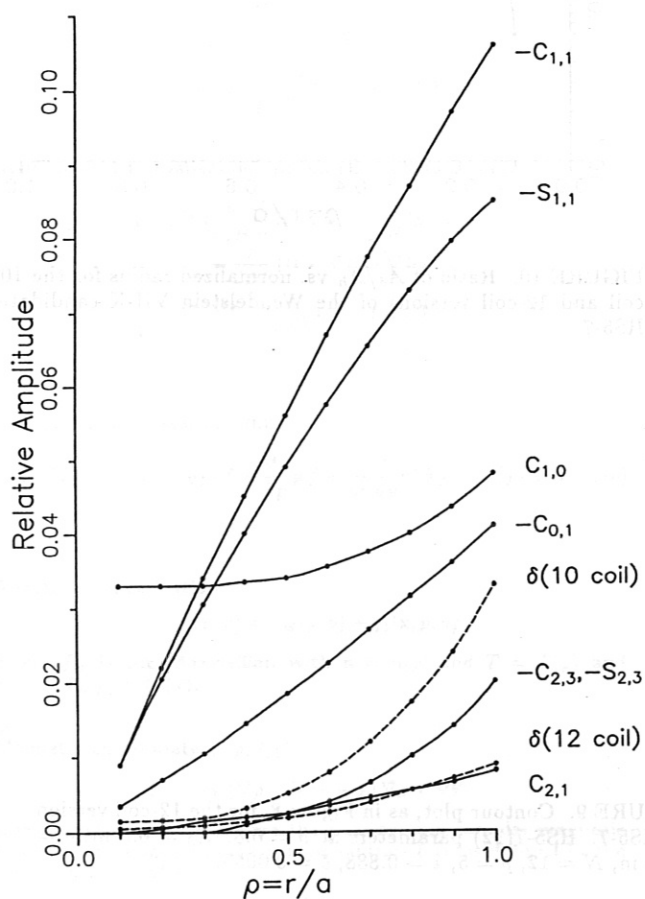
FIGURE 7. The relative magnitudes of the Fourier components of the HS5-7 magnetic field are plotted vs. normalized radius. The magnitudes of the *modular* ripple appear as the dashed lines for versions of HS5-7 with 10 and 12 coils per field period.

45
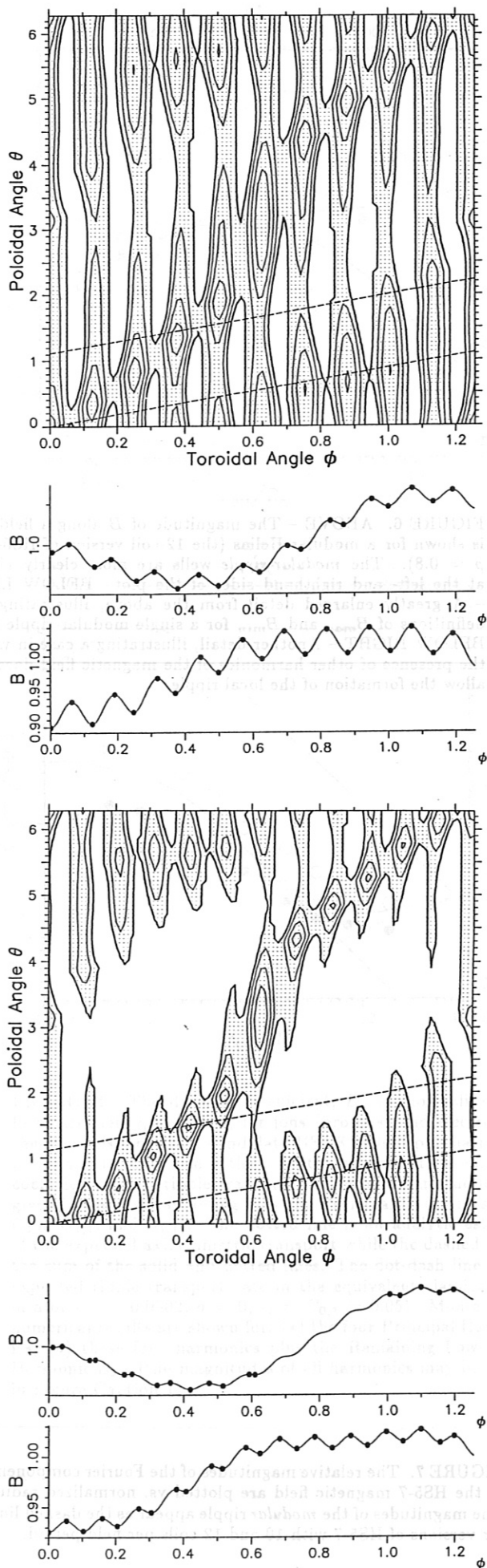
FIGURE 8. Contour plot of the location and depth of ripple wells for the 10 coil version of HS5-7 at $\rho = 0.8$. Dashed lines on the contour plot show the locations of the two field lines which are given in the figure as examples. Solid dots on the plots of Mod B along a field line indicate local extrema in the magnetic field. HS5-7(10) parameters at $\rho = 0.8$: $R_0 = 6.5$ m, $a = 0.65$ m, $N = 10$, $p = 5$, $\ell = 0.888$, $\delta = 0.0172$.
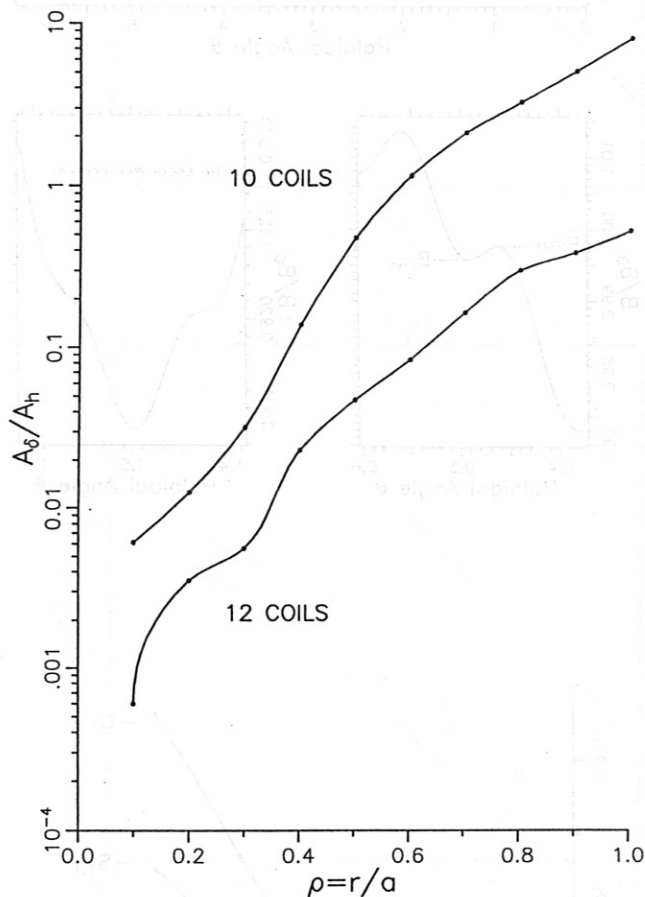
FIGURE 10. Ratio of A_δ/A_h vs. normalized radius for the 10-coil and 12-coil versions of the Wendelstein VII-X candidate, HS5-7.

FIGURE 9. Contour plot, as in Figure 8, for the 12-coil version of HS5-7. HS5-7(12) parameters at $\rho = 0.8$: $R_0 = 6.5$ m, $a = 0.65$ m, $N = 12$, $p = 5$, $\ell = 0.888$, $\delta = 0.0055$.

NEOCLASSICAL TRANSPORT
(DKES code)

H. Maaßberg and U. Gasparino

Abstract:

The linearized drift kinetic equation which is the basis of the DKES code (Drift Kinetic Equation Solver) is given, approximations in the collision term and in the Vlasov operator are discussed. The relation to Monte Carlo simulation as well as to the formalism based on invariants of motion is shown. Within the DKES formalism, the monoenergetic Onsager transport relation, the energy convolution formalism and the relation to the current drive problem are described.

DKES results are compared to axisymmetric models (Monte Carlo Simulation and Hinton-Hazeltine model), the influence of the radial electric field on the transport coefficients is analyzed. For the two W VII-X configurations, HS5081 and HS50B49, the transport coefficients are calculated depending on the collisionality. Finally, the convergence properties of DKES-2 code for typical W VII-X parameters are shown.

Drift Kinetic Equation

Stationary drift kinetic equation (DKE) in real space, and with polar co-ordinates in velocity space, $(p; v)$, with $p = v_\parallel/v$:

$$(v_\parallel + v_{E\times B} + v_{\nabla B}) \cdot \nabla f + \dot{p}\, \frac{\partial f}{\partial p} + \dot{v}\, \frac{\partial f}{\partial v} = C(f) + S \qquad (1a)$$

where $C(f)$ is the Fokker-Planck collision term, S is the particle and energy source function and

$$v_\parallel = \frac{p\,v}{B}\, \mathbf{B}$$
$$v_{E\times B} = \frac{1}{B^2}\, \mathbf{B} \times \nabla\Phi$$
$$v_{\nabla B} = \frac{m}{q}\, \frac{1+p^2}{2B^3}\, v^2\, \mathbf{B} \times \nabla B.$$

From (adiabatic) invariants of motion ($\dot{E} = 0$ and $\dot{\mu} = 0$):

$$\dot{p} = -(1-p^2)\,\{\frac{q}{mB}\,\frac{1}{v}\,\mathbf{B}\cdot\nabla\Phi + \frac{v}{2B^2}\,\mathbf{B}\cdot\nabla B$$
$$+ \frac{p}{2B^3}\,(\mathbf{B}\times\nabla B)\cdot\nabla\Phi\}$$
$$\dot{v} = -\frac{q}{mB}\,p\,\mathbf{B}\cdot\nabla\Phi - \frac{1}{2B^3}\,v(1+p^2)\,(\mathbf{B}\times\nabla B)\cdot\nabla\Phi.$$

DKE (1a) in conservative form:

$$\nabla \cdot (v_\parallel + v_{E\times B} + v_{\nabla B})\,f + \frac{\partial}{\partial p}\,\dot{p}\,f + \frac{1}{v^2}\,\frac{\partial}{\partial v}\,v^2\,\dot{v}\,f = C(f) + S \qquad (1b)$$

Ansatz for linearization:

$$f(x, p, v) = f_M(\rho, v) + f_1(x, p, v)$$

where f_M is the Maxwellian with $n = n(\rho)$ and $T = T(\rho)$ and $\Phi(x) = \Phi_0(\rho) + \Phi_1(x)$.

Magnetic co-ordinates, $(\rho, \theta, \varsigma)$:

$$\mathbf{B} = -\chi'(\nabla\rho \times \nabla\varsigma) + \psi'(\nabla\rho \times \nabla\theta)$$

where $2\pi\chi(\rho)$ and $2\pi\psi(\rho)$ are the poloidal and toroidal magnetic fluxes, respectively, and the rotational transform is defined by the derivatives: $\iota = \chi'/\psi'$.

DKE in magnetic flux coordinates (neglecting poloidal component of $v_{\nabla B}$ and corresponding acceleration):

$$\frac{\partial}{\partial\rho}\,\frac{m}{q}\,\frac{1+p^2}{2B}\,v^2\,d_\perp B \overset{*}{f_1} + \frac{\partial}{\partial\theta}\{\frac{pv}{B}\chi' + \frac{\Phi_0'}{B^2}B_\varsigma\}\,f_1 + \frac{\partial}{\partial\varsigma}\,\frac{pv}{B}\,\psi'\,f_1$$
$$- \frac{\partial}{\partial p}(1-p^2)\frac{v}{2B}\,d_\parallel B \cdot f_1 \qquad (2)$$
$$= -\frac{m}{q}\,\frac{1+p^2}{2B}\,v^2\,(\frac{n'}{n} + \frac{q}{T}\Phi_0' + (\frac{v^2}{v_{th}^2} - \frac{3}{2})\frac{T'}{T})\,f_M\,d_\perp B$$
$$- \frac{q}{T}\,p\,v\,d_\parallel\Phi_1 \cdot f_M + \sqrt{g}\,(C(f) + \overset{*}{S})$$

with the abbreviations for the differential operations

$$d_\parallel = \frac{1}{B}\{\psi'\frac{\partial}{\partial\varsigma} + \chi'\frac{\partial}{\partial\theta}\}$$

$$d_\perp = \frac{1}{B^2}\{B_\theta\frac{\partial}{\partial\varsigma} - B_\varsigma\frac{\partial}{\partial\theta}\}$$

$*$ *not included in DKES code*

Fokker-Planck collision operator

$$C(f_\alpha) \equiv \left(\frac{\partial f_\alpha}{\partial t}\right)_c = \Gamma_\alpha \cdot \frac{1}{v^2} \cdot \Big[\frac{\partial}{\partial v}(A_1 f_\alpha) + \frac{1}{2}\frac{\partial^2}{\partial v^2}(A_2 f_\alpha) + \frac{\partial^2}{\partial v\partial p}(C f_\alpha)$$
$$+ \frac{\partial}{\partial p}(B_1 f_\alpha) + \frac{1}{2}\frac{\partial^2}{\partial p^2}(B_2 f_\alpha)\Big] \qquad (1)$$

f_α is the distribution function of species α, v the absolute value of the velocity, p the pitch ($v_\parallel/v$), and

$$\Gamma_\alpha = \frac{\ln\Lambda}{4\pi} \cdot \left(\frac{Z_\alpha e^2}{\epsilon_0 m_\alpha}\right)^2.$$

The coefficient functions A_1, A_2, B_1, B_2 and C in eq. (1) are defined by derivatives of the Rosenbluth potentials h_α and g:

$$A_1 = -v^2\frac{\partial h_\alpha}{\partial v} - \frac{\partial g}{\partial v} - \frac{1}{2v}\frac{\partial}{\partial p}(1-p^2)\frac{\partial g}{\partial p}$$

$$A_2 = v^2\frac{\partial^2 g}{\partial v^2}$$

$$B_1 = -(1-p^2)\frac{\partial h_\alpha}{\partial p} + \frac{1}{2v}\Big\{(1-p^2)(\frac{p}{v}\frac{\partial^2 g}{\partial p^2} + 2\frac{\partial^2 g}{\partial v\partial p}) + 2p\frac{\partial g}{\partial v} - \frac{2}{v}\frac{\partial g}{\partial p}\Big\}$$

$$B_2 = \frac{1-p^2}{v}\Big\{\frac{1-p^2}{v}\frac{\partial^2 g}{\partial p^2} + \frac{\partial g}{\partial v} - \frac{p}{v}\frac{\partial g}{\partial p}\Big\}$$

$$C = (1-p^2)\Big\{\frac{\partial^2 g}{\partial v\partial p} - \frac{1}{v}\frac{\partial g}{\partial p}\Big\}. \qquad (2)$$

The Rosenbluth potentials h_α and g are defined by the differential equations:

$$\Delta h_\alpha = -4\pi\sum_\beta Z_\beta^2 (1 + \frac{m_\alpha}{m_\beta})\,f_\beta$$

$$\Delta\Delta g = -8\pi\sum_\beta Z_\beta^2\,f_\beta, \qquad (3)$$

where Δ is the Laplace operator and the summation is carried out with respect to all plasma species β. h_α and g are given by the explicit formulas:

$$h_\alpha = \sum_\beta Z_\beta^2 (1 + \frac{m_\alpha}{m_\beta}) \int\int\int_{-\infty}^{+\infty} \frac{1}{|\underline{v} - \underline{v}'|}\,f_\beta(\underline{v}')\,d^3v'$$

$$g = \sum_\beta Z_\beta^2 \int\int\int_{-\infty}^{+\infty} |\underline{v} - \underline{v}'|\,f_\beta(\underline{v}')\,d^3v'. \qquad (4)$$

DKES code:

$$C(f_\kappa) \approx \frac{T_\kappa}{2v^3} \frac{\partial g}{\partial v} \frac{\partial}{\partial \rho} (1-\rho^2) \frac{\partial}{\partial \rho} f_\kappa$$

$$h_\kappa = h_\kappa(v); \quad g = g(v) \qquad \text{mono-energetic}$$

↝ parallel momentum not conserved ?
(problem for estimating $\sigma_\parallel$)

Monte Carlo Simulation (MCS)

- distribution function f is represented by the phase space density of the simulation particles.

 ↝ simulation of global distribution with Maxwellian included → statistical accuracy for deviations

- simulation particle trajectories ≙ characteristics of Vlasov operator ↝ particle tracing

- diffusion in velocity space (collision term $C(f)$)
 ↝ particle scattering (random process corresponding to $C(f)$)

- Source and loss terms:
 simple: collisional energy transfer } (e.g. NBI)
 particle sources
 complicate: energy and/or momentum sources
 (e.g. ECH and current drive)
 → statistical accuracy

- problem is less complex for estimation of transport coefficients (diffusion in configuration space only)

Velocity space: invariants of motion

Using the (adiabatic) invariants of motion, E and μ, for velocity variables; transform collision term on E and μ:

$$\leadsto \quad (\underline{v}_v + \underline{v}_{E\times B} + \underline{v}_{\nabla B}) \cdot \nabla_\perp f \Big|_{\substack{E=const \\ \mu}} = \hat{C}(f) + \hat{S}(f)$$

advantage: no mirror term
      simple classification of particle type
      (e.g. trapped particles, ...)

↝ bounce average of drift kinetic equation

problem: collision term in E, μ ($C(f)$ is local term)
    momentum conservation?

    theory and codes available for simple geometry (e.g. Tokamak, mirror),
    not for general Stellarator geometry

At present time, a solution of the full Fokker-Planck equation is not available for general Stellarator geometry.

 → separated models must be used

"neoclassical" model (DKES code):
- equilibrium distribution ≡ Maxwellian (no energy and particles sources)

- simplified Fokker-Planck collision term (only pitch-angle scattering with Maxwellian, mono-energetic)

- deviations from the Maxwellian driven by source or loss terms cannot be included

"Fokker-Planck" model:
- transport effects in DKE disregarded

- effect of loss terms in velocity space (transport)?

- parallel momentum damping (trapped particles)?
 (↝ reduced current drive efficiency)

e.g.:
bootstrap current from "neoclassical" model
ECF current drive from "Fokker-Planck" model

HNM

Neoclassical Transport Coefficients: D_{ij} (DKES, H–H, Kov. and S–H)

configuration: TOKA5

electrons $Z_{eff} = 1.0$

minor radius: 10.00 cm
major radius: 200.0 cm
$B_0 = 2.50$ T ⊹ = 0.510
$T_e = 1000$ eV (const.)
H–H: $\epsilon_t = 0.0500$

—— DKES code
– – – Hinton–Hazelline
········· Spitzer–Haerm
electric fields:
● $E_r = 0$ V/cm

HNM

Neoclassical Transport Coefficients: D_{ij} (DKES, H–H, Kov. and S–H)

configuration: TOKA5

electrons $Z_{eff} = 5.0$

minor radius: 10.00 cm
major radius: 200.0 cm
$B_0 = 2.50$ T ⊹ = 0.510
$T_e = 1000$ eV (const.)
H–H: $\epsilon_t = 0.0500$

—— DKES code
– – – Hinton–Hazelline
········· Spitzer–Haerm
electric fields:
● $E_r = 0$ V/cm

49
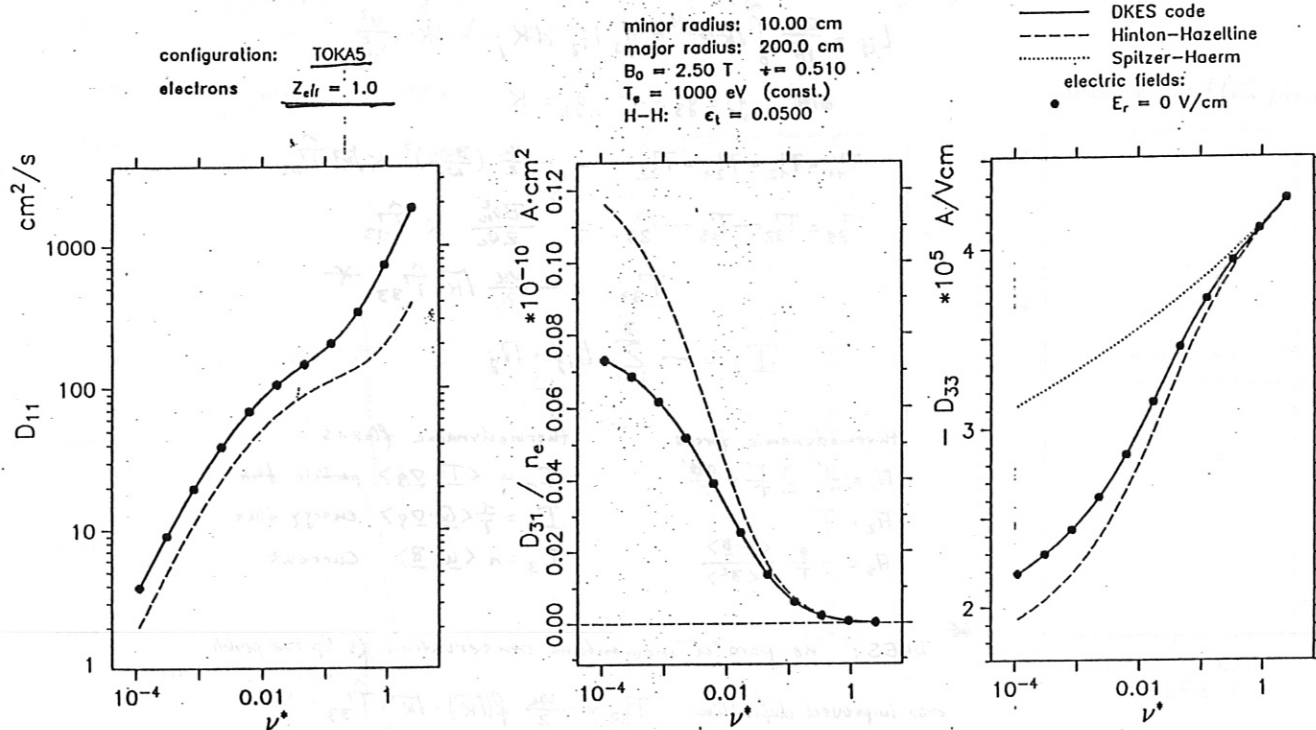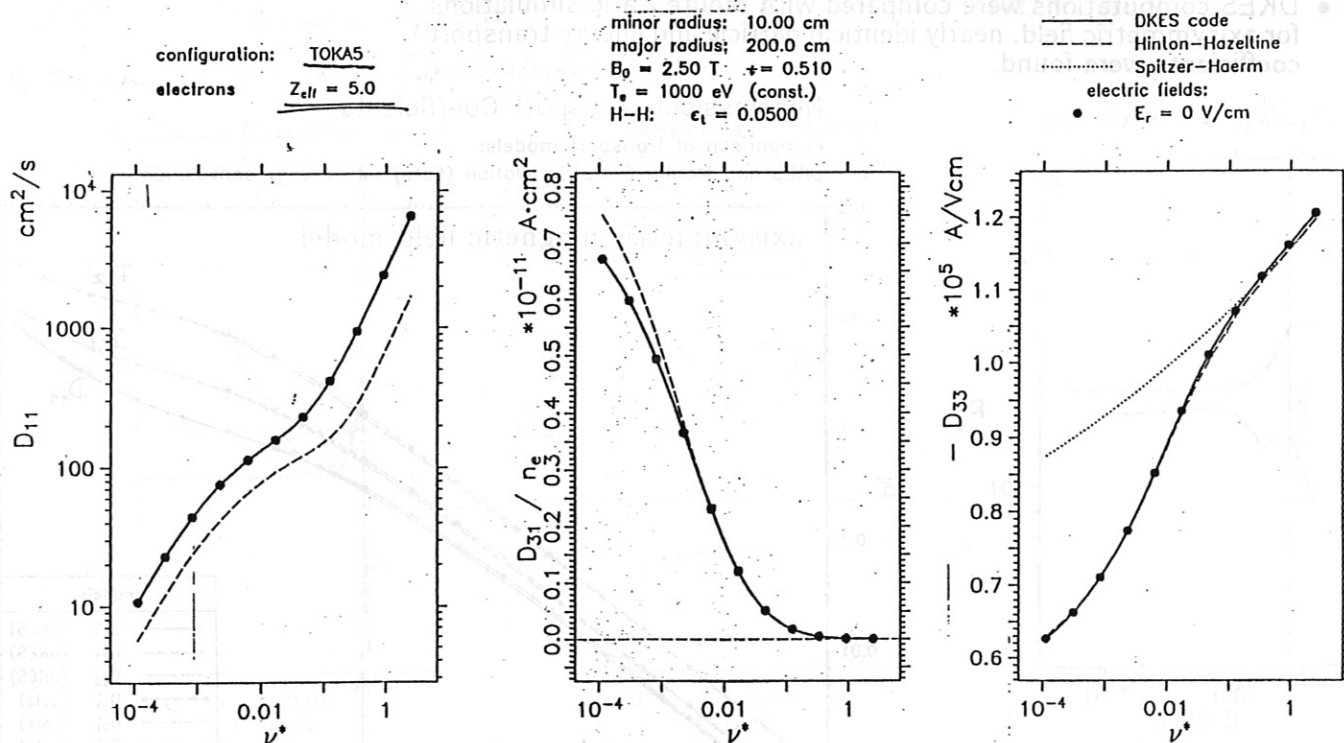
DKES code

DKES solves the mono-energetic DKE (v is parameter)

$\rightarrow$ transport coefficients $\hat{T}_{11}, \hat{T}_{13}$ and $\hat{T}_{33}$

energy convolution $\rightarrow$ Onsager transport matrix L_{ij}

$$L_{ij} = \frac{2n}{\sqrt{\pi}} \int_0^\infty \sqrt{K}\, e^{-K} g_i\, g_j\, T_{ij}\, dK; \qquad K = \frac{v^2}{v_{th}^2}$$

with $g_1 = g_3 = 1; \quad g_2 = K$

$$T_{11} = T_{12} = T_{21} = T_{22} = -\frac{v_{th}}{2} \left(\frac{B v_{th}}{\omega_c}\right)^2 K \sqrt{K}\, \hat{T}_{11}$$

$$T_{31} = T_{32} = -T_{13} = -T_{23} = \frac{B v_{th}^2}{2\omega_c} K\, \hat{T}_{13}$$

$$T_{33} = -\frac{v_{th}}{2} \sqrt{K}\, \hat{T}_{33} \quad *$$

$$I_i = -\sum_{j=1}^{3} L_{ij} \cdot A_j$$

thermodynamic forces

$A_1 = \frac{n'}{n} - \frac{3}{2}\frac{T'}{T} + \frac{q\phi'}{T}$

$A_2 = \frac{T'}{T}$

$A_3 = -\frac{q}{T} \frac{\langle E \cdot B \rangle}{\langle B^2 \rangle}$

thermodynamic fluxes

$I_1 = \langle \Gamma \cdot \nabla g \rangle$ particle flux

$I_2 = \frac{1}{T}\langle Q \cdot \nabla g \rangle$ energy flux

$I_3 = n \langle u \cdot B \rangle$ current

$*$ DKES: no parallel momentum conservation (s. Spitzer probl.)

$\rightsquigarrow$ improved definition: $T_{33} = -\frac{v_{th}}{2} f(\sqrt{K}) \cdot \sqrt{K} \cdot \hat{T}_{33}$

$$f(\sqrt{K}) = \frac{\bar{\eta}(\sqrt{K}) + z_{eff}}{K^2} \cdot D^{SP}(\sqrt{K}, z_{eff})$$

$$D^{SP} \hat{=} \text{ Spitzer function}$$

- DKES computations were compared with Monte Carlo simulations for axisymmetric field, nearly identical particle and energy transport coefficients were found.

Neoclassical Transport Coefficients

comparison of transport models:
DKES and Monte–Carlo Simulation (Lotz) with energy convolution

axisymmetric magnetic field model

models:

D_{11}	(DKES)	
D_{21}	(DKES)	
D_{22}	(DKES)	
D_{11}	(Lotz)	
D_{21}	(Lotz)	
D_{22}	(Lotz)	

$W \overline{VII} - AS5$

$t \approx 0.5$
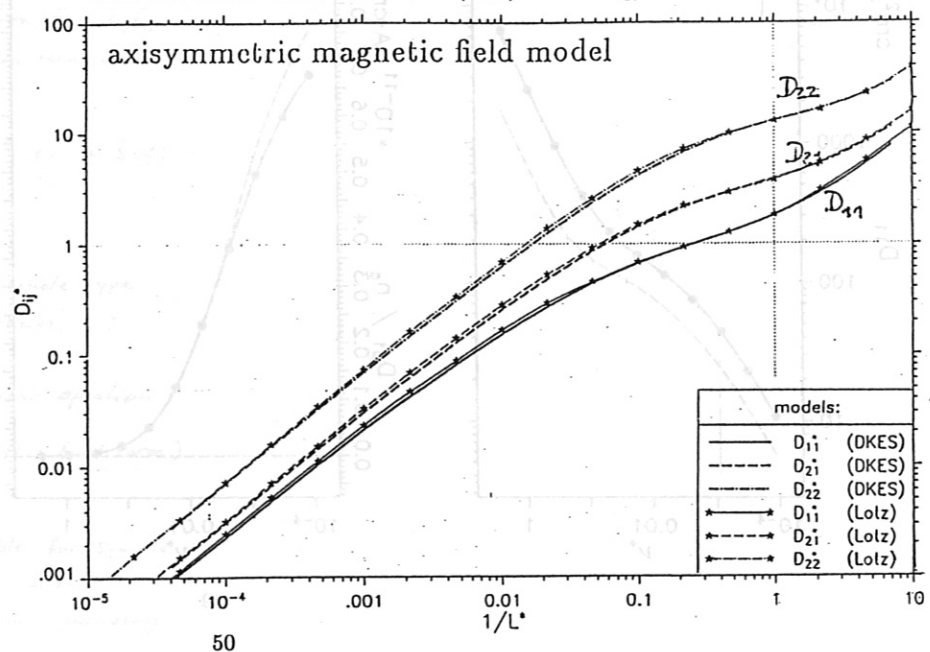
$r = 9.97\,cm$

Test of DKES Transport Coefficients: CMUL $= 1.0 \cdot 10^{-2}$

(monoenergetisch) $EFIELD = \dfrac{Er}{V}$; $CMUL = \dfrac{t}{R} v^+_{mono}$

———— äquivalenter Tokamak

Teilchen- + Energietransport   Bootstrap - Strom   parallele Leitfähigkeit
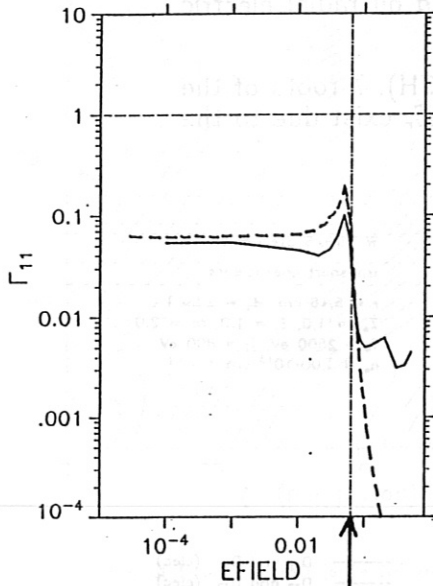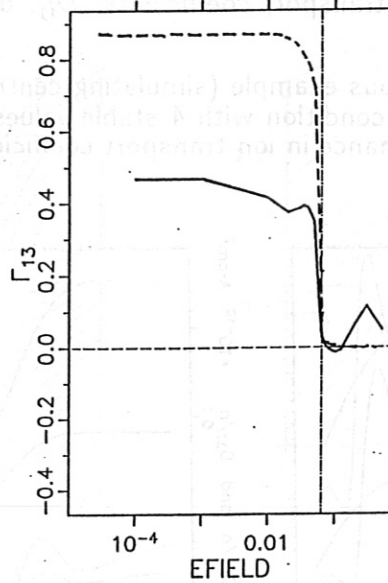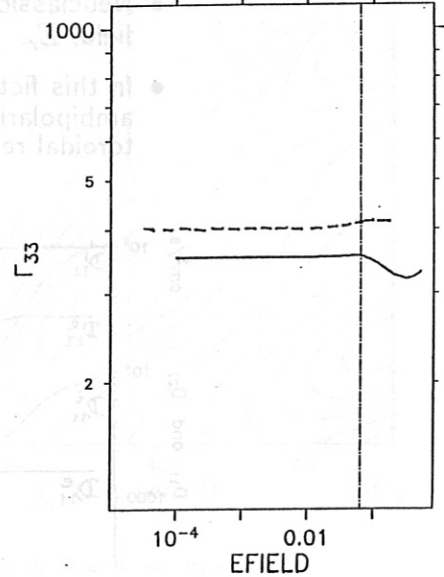
toroidale Resonanz:

$\dfrac{Er}{V} \approx t \dfrac{r}{R} B_0$

Plateau - Regime

$W \overline{VII} - AS5$

$t \approx 0.5$

$r = 9.97\,cm$

Test of DKES Transport Coefficients: CMUL $= 2.0 \cdot 10^{-4}$

(monoenergetisch) $EFIELD = \dfrac{Er}{V}$; $CMUL = \dfrac{t}{R} v^*_{mono}$

———— äquivalenter Tokamak

Teilchen- + Energietransport   Bootstrap - Strom   parallele Leitfähigkeit
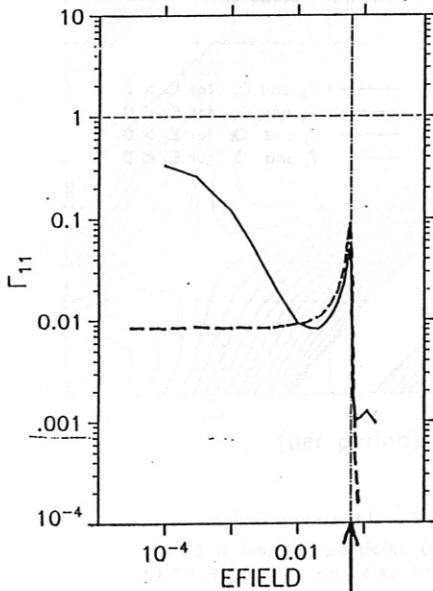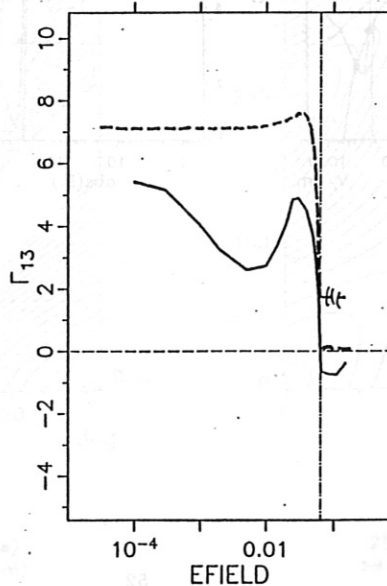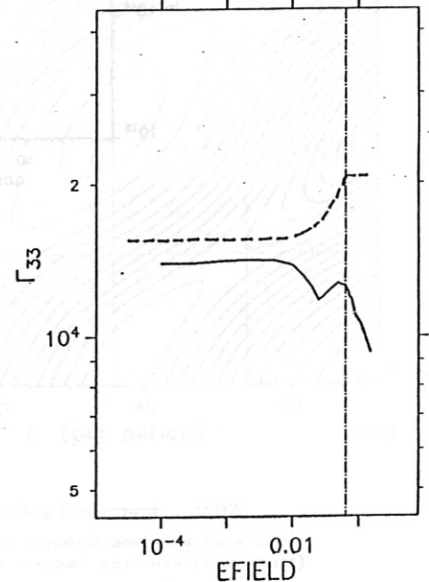
toroidale Resonanz:

$\dfrac{Er}{V} \approx t \dfrac{r}{R} B_0$

$\dfrac{1}{v}$ — Regime

51

DKES: Transport Coefficients

- Neoclassical transport coefficients, D_{ij}, depend on radial electric field, E_r.

- In this fictitious example (simulating central ECH), 7 roots of the ambipolarity condition with 4 stable values of E_r exist due to the toroidal resonance in ion transport coefficients.
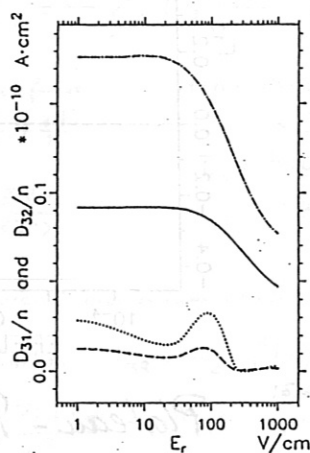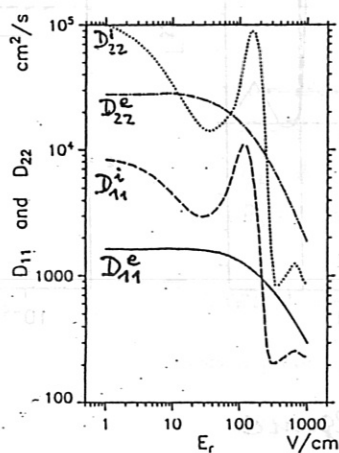
W WII–AS Stellarator

transport coefficients

$r = 5.16$ cm, $B_0 = 2.50$ T
$Z_{eff} = 1.0$, $Z_i = 1.0$, $m_i = 2.0$
$T_e = 2500$ eV, $T_i = 800$ eV
$n_e = 3.00 \cdot 10^{13}$ cm^{-3}

- - - D_{11} and D_{31} (elec)
——— D_{22} and D_{32} (elec)
— — — D_{11} and D_{31} (ions)
········· D_{22} and D_{32} (ions)
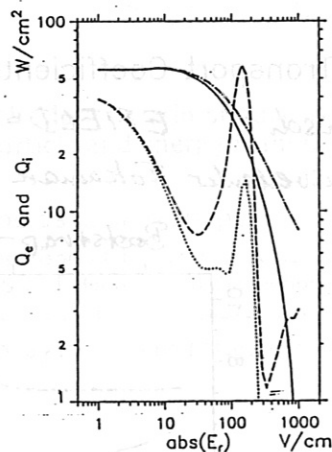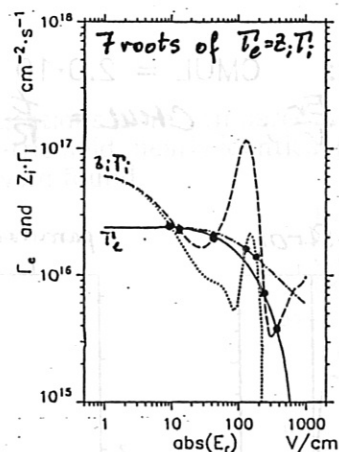
W WII–AS Stellarator

neoclassical fluxes

$r = 5.16$ cm, $B_0 = 2.50$ T
$Z_{eff} = 1.0$, $Z_i = 1.0$, $m_i = 2.0$
$T_e = 2500$ eV, $T_i = 800$ eV
$n_e = 3.00 \cdot 10^{13}$ cm^{-3}

$n'/n = -0.070$ cm^{-1}
$T_e'/T_e = -0.150$ cm^{-1}
$T_i'/T_i = -0.080$ cm^{-1}

——— Γ_e and Q_e for $E_r > 0$
——— Γ_e and Q_e for $E_r < 0$
— — — Γ_i and Q_i for $E_r > 0$
········· Γ_i and Q_i for $E_r < 0$

file with Fourier coefficients: <u>HS5081</u> $\rho = 38.55$ cm; $t = 0.9014$

mod B on flux surface
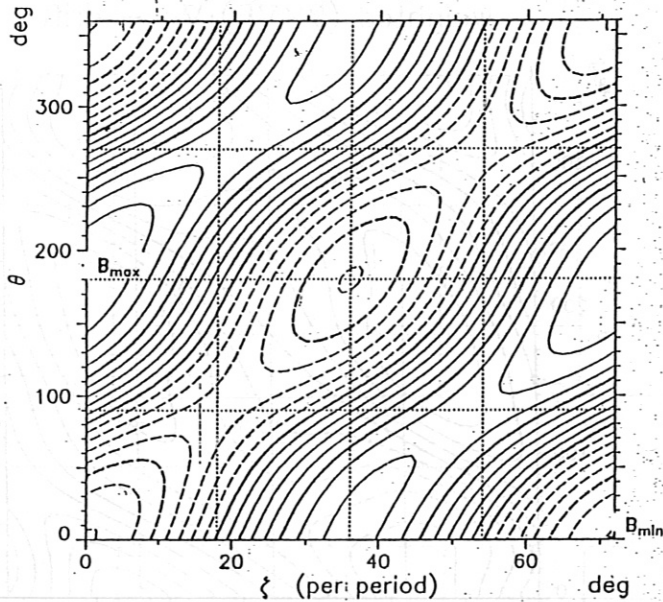
no. of Fourier coefficients for mod B: 8
Increment of mod B values: 0.01
$B_{max} / B_0 = 1.089$ $B_{min} / B_0 = 0.929$

weighted $(B \times \nabla B) \cdot \nabla \rho$ — drift
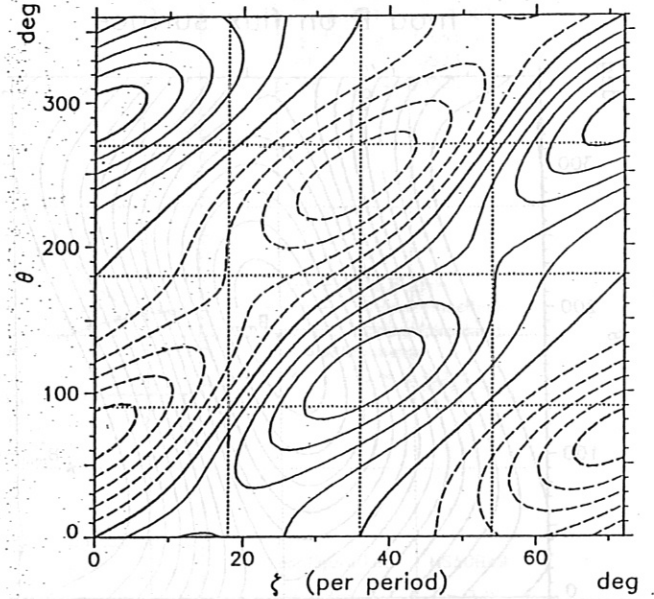
$(B \times \nabla B) \cdot \nabla \rho$ — drift $\propto$ $\partial(\ln B) / \partial\theta$
Increment of v^B values: 0.01
$v^D_{max} = 0.056$ $v^D_{min} = -0.056$

deeply trapped particle fraction
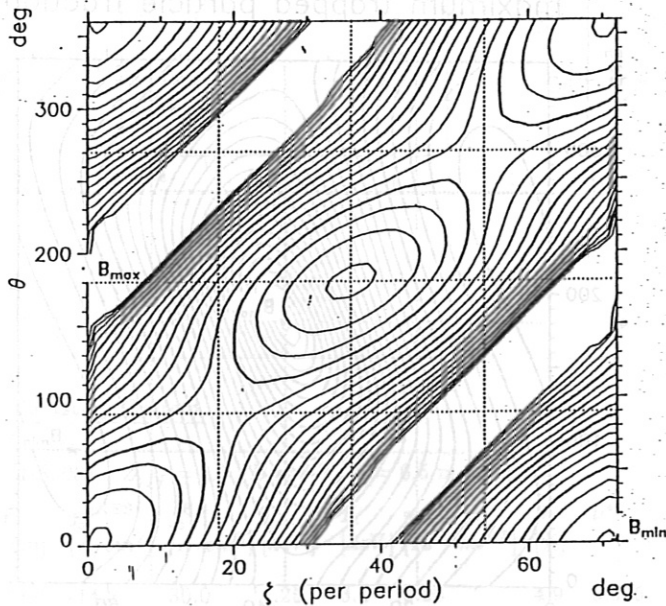
isoline increment: 0.02
19.03 % trapped particles (average)
36.36 % trapped particles (maximum)

maximum trapped particle fraction
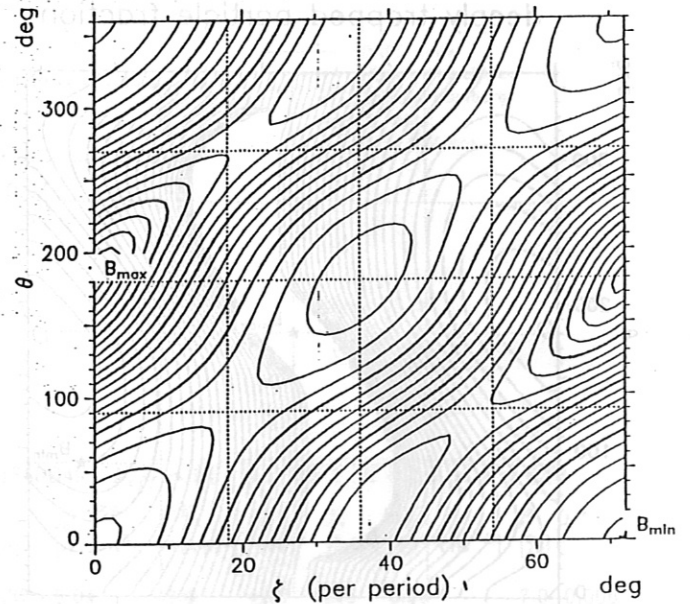
isoline increment: 0.02
25.06 % trapped particles (average)
38.38 % trapped particles (maximum)

file with Fourier coefficients: __HS50B49__

$\rho = 28.75$ cm; $t = 0.8044$

mod B on flux surface
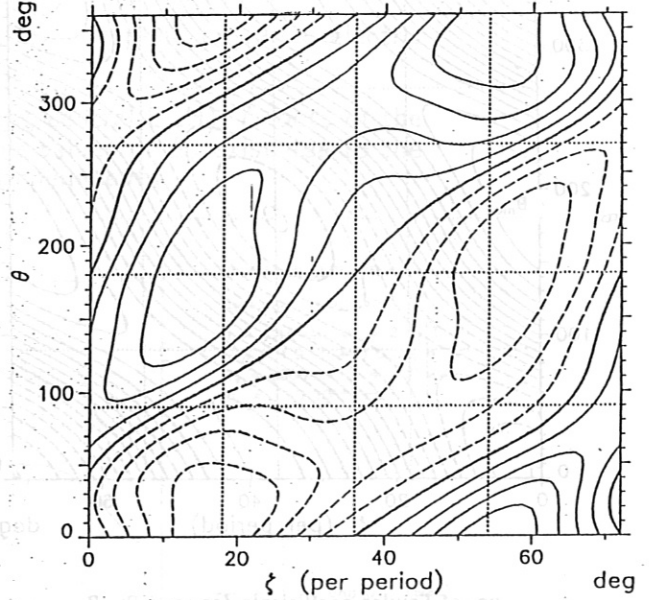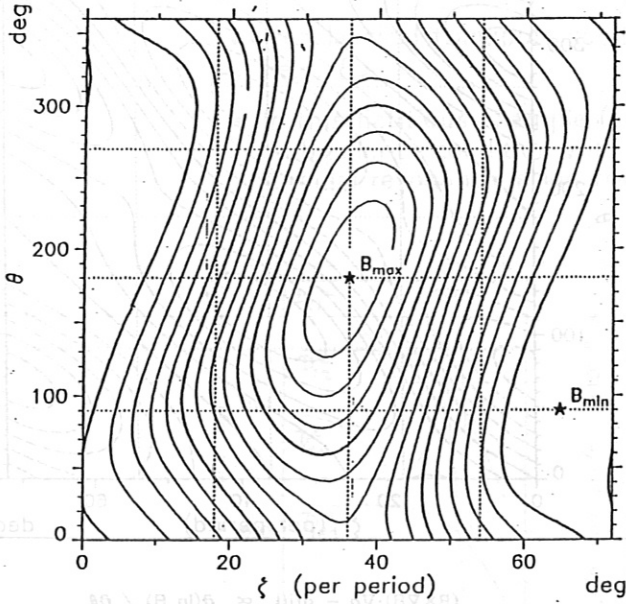
no. of Fourier coefficients for mod B: 10
Increment of mod B values: 0.02
$B_{max} / B_0 = 1.279$ $B_{min} / B_0 = 0.973$

weighted $(B \times \nabla B) \cdot \nabla \rho$ — drift

$(B \times \nabla B) \cdot \nabla \rho$ — drift $\propto \partial(\ln B) / \partial\theta$
Increment of v^D values: 0.01
$v^D_{max} = 0.049$ $v^D_{min} = -0.049$

deeply trapped particle fraction
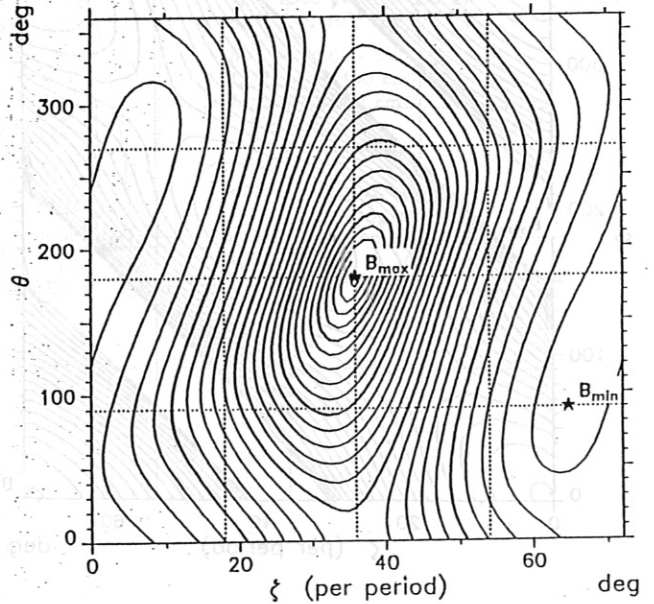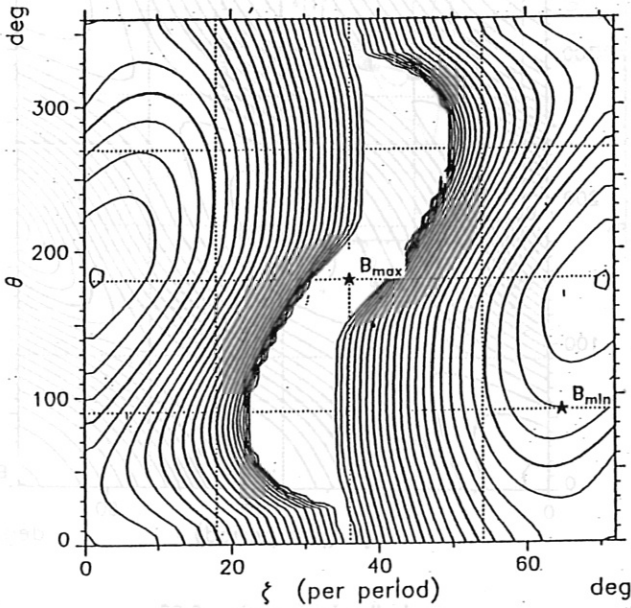
isoline increment: 0.02
26.90 % trapped particles (average)
48.09 % trapped particles (maximum)

maximum trapped particle fraction

isoline increment: 0.02
36.53 % trapped particles (average)
48.88 % trapped particles (maximum)

54

Neoclassical Transport Coefficients: D_{ij} (DKES, H–H, Kov. and S–H)
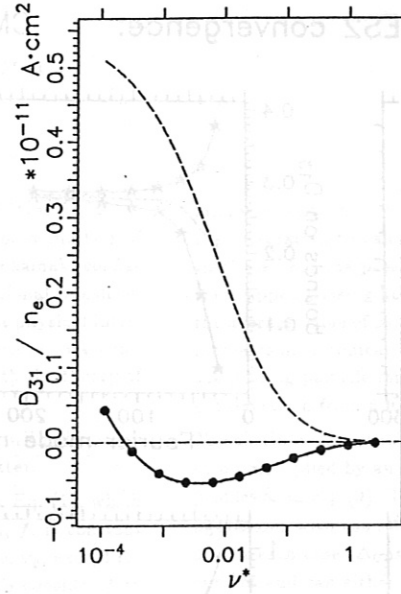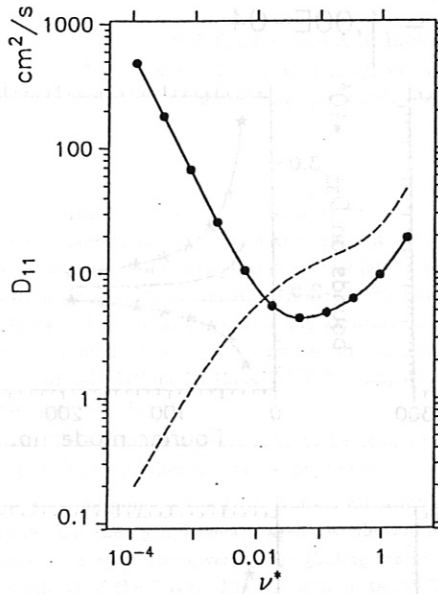
configuration: HS5081

electrons $Z_{eff} = 1.0$

minor radius: 38.55 cm
major radius: 650.0 cm
$B_0 = 3.00$ T $\leftarrow = 0.901$
$T_e = 1000$ eV (const.)
H–H: $\epsilon_t = 0.0593$
S–H: $\epsilon_h = 0.0000$

———— DKES code
– – – Hinton–Hazeltine
–·–·– Shaing–Houlberg
electric fields:
• $E_r = 0$ V/cm
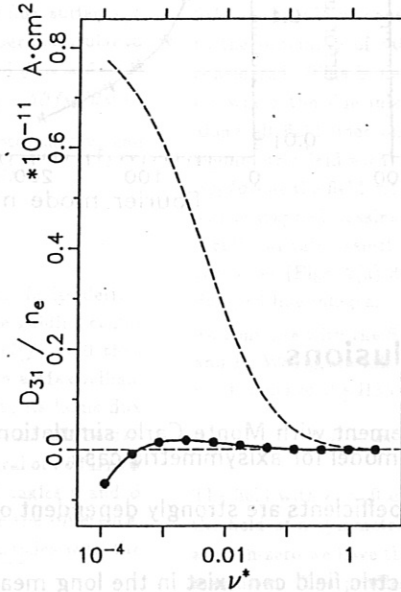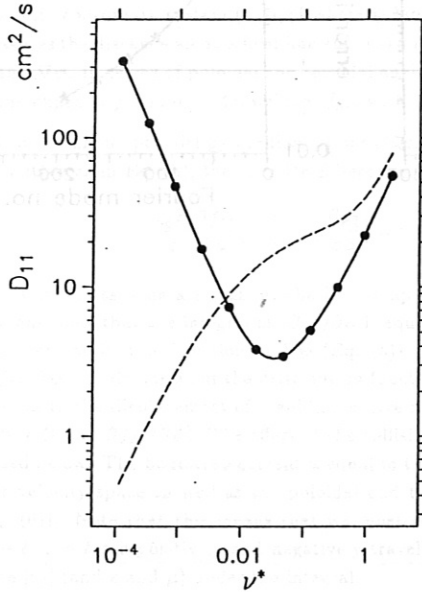
configuration: HS50B49

electrons $Z_{eff} = 1.0$

minor radius: 28.75 cm
major radius: 650.0 cm
$B_0 = 2.50$ T $\leftarrow = 0.804$
$T_e = 1000$ eV (const.)
H–H: $\epsilon_t = 0.0442$
S–H: $\epsilon_h = 0.0000$

———— DKES code
– – – Hinton–Hazeltine
–·–·– Shaing–Houlberg
electric fields:
• $E_r = 0$ V/cm

Bootstrap Current

HS5081 : $Z_{eff} = 1.5$, $B = 3$ T, $R = 6.5$ m, $\iota \approx 0.9$

r [cm]	j_b^{DKES} [A/cm²]	j_b^{HH} [A/cm²]	T_e [keV]	T_i [keV]	n_e [10¹⁴cm⁻³]	β [%]	ν^*
19.9	-14.8	30.0	4.25	3.4	0.95	4.9	0.005
38.5	-16.2	39.3	2.5	2.0	0.85	2.6	0.012
56.1	-4.22	12.3	1.25	1.0	0.5	0.75	0.026
Σ	-130	318	[kA]				

HS50B49 : $Z_{eff} = 1.5$, $B = 2.5$ T, $R = 6.5$ m, $\iota \approx 0.78$

r [cm]	j_b^{DKES} [A/cm²]	j_b^{HH} [A/cm²]	T_e [keV]	T_i [keV]	n_e [10¹⁴cm⁻³]	β [%]	ν^*
14.37	5.04	40.0	4.25	3.4	0.95	7.0	0.006
28.75	4.90	50.3	2.5	2.0	0.85	3.7	0.014
43.12	1.07	14.7	1.25	1.0	0.5	1.1	0.029
Σ	23	230	[kA]				

HS50B4-9

r= 2 9 cm

test DKES2 convergence: CMUL = 1.00E−04

Plots (top row): bounds on D_{11}, bounds on D_{13}, bounds on D_{33} *10^4 vs Fourier mode no.
Plots (bottom row): error in D_{11}, error in D_{13}, error in D_{33} vs Fourier mode no.
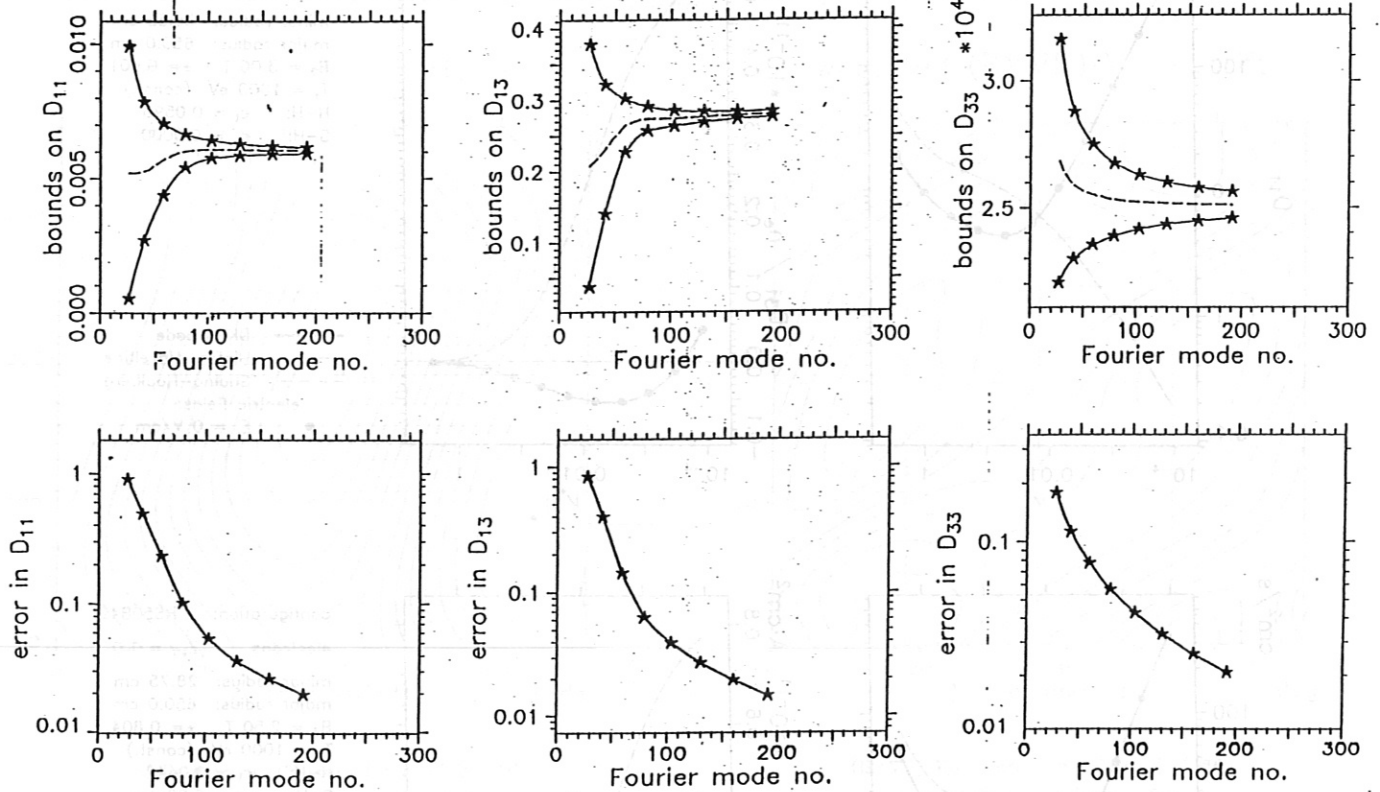
Conclusions

- DKES code results are in agreement with Monte Carlo simulations and with the Hinton-Hazeltine model for axisymmetric case.

- Particle and energy transport coefficients are strongly dependent on the radial electric field.

- Up to seven values of radial electric field can exist in the long mean free path regime (4 stable, 3 unstable roots of the ambipolarity condition).

- Also the bootstrap current coefficient depends on the radial electric field in the long mean free path regime.

- The W VII-X configurations HS5081 and HS50B49 show reduced transport coefficients with respect to the equivalent axisymmetric model (Hinton-Hazeltine) and the standard stellarator model (Shaing-Houlberg).

- In the configuration HS50B49, the bootstrap current is approximately only 10% of the equivalent axisymmetric case.

- For the most interesting W VII-X configuration, DKES runs must be done for different radii, collisionalities and radial electric fields. Based on the neoclassical transport coefficients, TEMPLE code predictions of plasma density, bootstrap current, electron and ion temperatures with the ambipolar radial electric field included can be used to estimate the maximum $< \beta >$ for given heating power in different scenarios.

Calculation of the Bootstrap Current by Direct Integration

of the Drift Kinetic Equation

H.J. Gardner and A.H. Boozer*

*Permanent address: College of William and Mary
Williamsburg, VA 23185, USA

An important critereon for distinguishing WVII-X candidates is the expected magnitude of the bootstrap current. We describe a method of calculating the bootstrap current for any (stellarator or tokamak) configuration for which the magnetic field strength and the rotational transform is known. The method is simple and accurate and gives a physical interpretation of the bootstrap current within the kinetic picture. We compare our calculations for three WVII-X configurations with the theory of Shaing and Callen [1].

Note: This summary is designed to be read conjointly with the viewgraphs. The equation and figure numbers refer to the latter.

The starting point is the Drift Kinetic Equation (DKE), Eq. (1), which states that the gyrophase-averaged distribution function, f, is constant along the trajectories given by the guiding-center velocity, $\mathbf{v}_g$, except for the effects of the Fokker-Planck collision term $C(f)$. We consider f to be a function of the three spatial coordinates, the kinetic energy, ϵ, the magnetic moment, μ, and the sign of the parallel velocity. We use a magnetic coordinate system $(\psi, \alpha, \varsigma)$ where ψ labels the flux surfaces, ς measures the distance along a field line and α is an angle perpendicular to $\mathbf{B}$ and $\nabla\psi$. In terms of poloidal and toroidal angles, θ and ϕ, $\alpha = \theta - \iota\phi$. If one expands f about a Maxwellian, f_M, with $f = f_M - \delta\partial f_M/\partial\psi$ to first order in the parallel-gyroradius, $\rho_\parallel = v_\parallel/\omega c$, and notes that $\mathbf{v}_g$ can be written as in Eq. (3), then the DKE becomes (Eq. (4))

$$\frac{v_\parallel B}{g}\frac{\partial f_M}{\partial\psi}\left[-\frac{\partial\delta}{\partial\varsigma} + g\frac{\partial\rho_\parallel}{\partial\alpha}\right] = C(f).$$

Equation (4) tells us a lot about the bootstrap current. In its derivation one finds that the integral of $g\partial\rho_\parallel/\partial\alpha$ is equal to the guiding center displacement in the direction of $\nabla\psi$ (Eq. (5)). So if $C(f) = 0$ then $\delta\partial f_M/\partial\psi$, the deviation of the distribution function from a Maxwellian, is equal to the displacement of a guiding centre normal to its home flux surface (times $\partial f_M/\partial\psi$). The effect of the collision operator will be discussed below. The bootstrap current is equal to the integral of $\delta\partial f_M/\partial\psi$ over velocity space as well as the poloidal and toroidal angles θ and ϕ (Eq. (6)). Note that this means that we must consider the difference, $\delta_+ - \delta_-$, in δ for positively and negatively travelling particles with the same $|v_\parallel|$ (and ϵ and μ) under the integral.

The rest of the calculation is done in the limit of small collision frequency, ν, and small fraction of trapped particles. With the second assumption (valid for any configuration where the variation in the field strength is a small fraction of the field itself) one can use the pitch-angle scattering operator which is of the first order in ν. Thus to zeroth order δ is simply equal to the integration of $g\partial\rho_\parallel/\partial\alpha$ along a field line (Eq. (7)). The constant of integration can be obtained by taking surface averages of the first order (in ν) equation.

Rather than considering the full calculation, we consider the example of a symmetric field where the field strength is dependent only on an angular variable $\Theta = l\theta - M\phi$. This example includes the large aspect ratio tokamak ($M = 0$) and quasi-helical stellarator limits (M = no. of periods). The zeroth order equation integrates to give a constant times $\rho_\parallel$ plus an integration constant δ_c. For trapped particles we know that δ_c at a turning point must be independent of the sign of $v_\parallel$. But, because we are

interested only in $\delta_+ - \delta_-$, and only odd functions of $\sigma = v_\parallel/|v_\parallel|$ survive the integration to calculate the bootstrap current, we can set $\delta_c = 0$ in this case. For the passing particles δ_c is determined by integrating from the trapped passing boundary in μ space. In the trapped-particle region the average value of $\rho_\parallel$, and thus the net displacement from a flux surface, increases monotonically with decreasing μ (or decreasing $\xi = \mu B_0/\epsilon$). In the passing-particle region the effect of $C(f)$ is to choose δ_c to make the net deviation from a flux surface almost independent of μ.

To calculate the actual bootstrap current the net displacement, Δ_0, has to be multiplied by an expression involving the temperature and density profiles as in Eq. (9). To compare the bootstrap currents in different configurations with the same profile dependence one only needs to calculate Δ_0 for each case. Δ_0 isolates the geometric dependence of the bootstrap current and can either be calculated directly or, for example, by using a Monte Carlo code.

When integrating the zeroth order equation, Eq. (7), for an asymmetric field one should be conscious of the danger of resonances in the result due to the proximity of rational surfaces to the particular value of ι being considered. This is because Eq. (7) is a magnetic differential equation for which the line integral of the right hand side is not equal to zero along all field lines on every rational surface [2]. In point of fact an asymmetric field with one field maximum will have a cliff in the function $\partial\rho_\parallel/\partial\alpha$ at the field maximum (Fig. 1). The resonances in the integration at the trapped passing boundary then arise because a field line close to a rational value selectively samples one side of this cliff before selecting the other (Figs. 2(a) and 2(b)). We ignore these resonances by using a damped line integral.

To compare with the Shaing Callen theory, as calculated by J. Kisslinger and H. Wobig, we take a sample field which is made up of the first three coefficients of the HS5-6 field:

$$B = B_0[1 - \epsilon_0\cos 2\pi\theta - \epsilon_1\cos 2\pi(\theta - 5\pi)].$$

The field with $\epsilon_1 = 0$ is that of a symmetric tokamak. If $\epsilon_0 = 0$ we have the field of a symmetric quasi-helical stellarator. Finally if both terms are non-zero we have the field of an asymmetric stellarator with one field maximum. The profiles of ϵ_0, ϵ_1 and ι are as shown in Fig. 3 and the results for all three cases are shown in Fig. 4. The deviation between the theories is greatest where the fraction of trapped particles becomes significant. This can been seen in Fig. 5 where $k = 1 - f_t$ is plotted for all three cases. Finally, the values of Δ_0/k, normalised to an equivalent tokamak, for the fields HS5-6, HS5-7, HS5-8 and HS50BIBO are plotted in Fig. 6.

[1] K. C. Shaing and J. D. Callen, Phys. Fluids 26, 3315 (1983).

[2] H. Grad, Phys. Fluids 10, 137 (1967).

Calculation of the Bootstrap Current by Direct Integration of the Drift Kinetic Equation

A. H. Boozer and H. J. Gardner

Drift Kinetic Equation: $\underset{\sim}{v}_g \cdot \underset{\sim}{\nabla} f = C(f)$ ①

Gyrophase-averaged distribution function:

$$f = f(\underset{\sim}{x}, \epsilon, \mu, \sigma)$$

$$\epsilon = \tfrac{1}{2} m v^2 + e\Phi \; ; \quad \mu = \tfrac{1}{2} m v_\perp^2 / B$$

$$v_{\shortparallel} = \sigma |v_{\shortparallel}| = \pm \left(\tfrac{2}{m}\right)^{1/2} \sqrt{(\epsilon - \mu B - e\Phi)}$$

Restriction: $\Phi \equiv 0$

Field-line integrations are simplified by using a magnetic coordinate system $(\psi, \alpha, \varsigma)$ where

$$\underset{\sim}{B} = \underset{\sim}{\nabla}\psi \times \underset{\sim}{\nabla}\alpha$$

$$= g(\psi)\underset{\sim}{\nabla}\varsigma + \beta_* \underset{\sim}{\nabla}\psi$$

$$g = \mu_0 (G + 2I)$$

$$G = \oint \underset{\sim}{j} \cdot d\underset{\sim}{a}_\theta$$

$$I = \oint \underset{\sim}{j} \cdot d\underset{\sim}{a}_\varphi$$

$$\psi = \oint_\theta \underset{\sim}{B} \cdot d\underset{\sim}{a}_\varphi$$
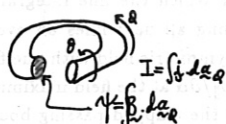
Also use poloidal, toroidal angles (θ, φ)

$$\alpha = \theta - \imath\varphi \; ; \quad \varsigma = \frac{G\varphi + I\theta}{G + \imath I}$$

Stellarators $\Rightarrow I = 0$
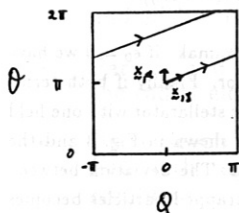
Expand f to $1°$ in parallel gyroradius $\rho_{\shortparallel} = v_{\shortparallel}/(eB/m)$

$$f \simeq f_M(\epsilon, \psi) - \delta(\underset{\sim}{x}, \epsilon, \mu, \sigma) \, \partial_\psi f_M \qquad ②$$

$$f_M = \frac{n(\psi)}{(2\pi T/m)^{3/2}} \exp\left(-\epsilon/T(\psi)\right)$$

Substitute into DKE using $\underset{\sim}{v}_g = \frac{v_{\shortparallel}}{B}\left[\underset{\sim}{B} + \underset{\sim}{\nabla}\times(\rho_{\shortparallel}\underset{\sim}{B})\right]$ ③

To $1°$ in $\rho_{\shortparallel}, \delta$

$$\boxed{\frac{v_{\shortparallel} B}{g}\frac{\partial f_M}{\partial \psi}\left[-\frac{\partial \delta}{\partial \varsigma} + g\frac{\partial \rho_{\shortparallel}}{\partial \alpha}\right] = C(f)} \qquad ④$$

δ is the "deviation from the home flux surface"

$$g\frac{\partial \rho_{\shortparallel}}{\partial \alpha} = \frac{\underset{\sim}{v}_g \cdot \underset{\sim}{\nabla}\psi}{\underset{\sim}{v}_g \cdot \underset{\sim}{\nabla}\varsigma} \qquad ⑤$$

Assume — collision frequency small
— fraction of trapped particles, f_t, is small

$$\xi = \frac{\mu B_0}{\epsilon} \; ; \; B_0 = B_{max}$$

$$0 \le \xi \le B_0/B_{min}$$
trapped: $1 \le \xi \le B_0/B_m$
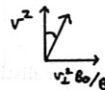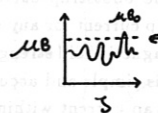
$\Rightarrow$ C is the pitch angle scattering operator

$$C(f) = \frac{\nu m}{B} v_{\shortparallel} \frac{\partial}{\partial \mu}\left[\mu\left(v_{\shortparallel}\frac{\partial f}{\partial \mu} + Wf\right)\right]$$

C "trys to make δ independent of μ"

$\Rightarrow \delta$ is the "deviation of a typical particle"

Bootstrap current: $\frac{j_{bs}}{B} = -\int \varsigma\left(\frac{v_{\shortparallel}}{B}\right)\delta \, \partial_\psi f_M \, d^3v \, d\theta \, d\varphi$ ⑥

zero deviation $\Rightarrow f = f_M$
$$j_{bs} = 0$$

Zeroth order: $\boxed{\dfrac{\partial \delta^0}{\partial \varsigma} = -g\dfrac{\partial \rho_{\shortparallel}}{\partial \alpha}}$ ⑦

first order: $\dfrac{\partial \delta^1}{\partial \varsigma} = \dfrac{-g\,C(f)}{v_{\shortparallel}B\,\partial_\psi f_M}$

$1°$ equation determines the integration constant for the $0°$ order equation.

Example: $B = B(\theta)$ $④ = \imath\theta - M\varphi$

tokamak $\Rightarrow M = 0$
quasi helical $\Rightarrow M = $ no. of periods

then $(\imath\imath - M)\partial_{④}\delta^0 = -\mu_0(\imath G + MI)\partial_{④}\rho_{\shortparallel}$

$$\delta^0 = \delta_c(\epsilon, \mu, \psi, \kappa, \sigma) - \frac{\mu_0(\imath G + MI)}{(\imath\imath - M)}\rho_{\shortparallel} \qquad ⑧$$

trapped particles: δ_c must be even in σ

[NB: Must redefine δ to subtract off the step per bounce in asymmetric fields]

But, in the expression for j_{bs} need only $\langle \delta_+ - \delta_- \rangle$ in the "net displacement":

$$\Delta_0 = \int_0^1 \frac{3 e B_0}{4 g m v}\langle \delta_+ - \delta_- \rangle \, d\xi$$

passing particles: δ_c is determined by integrating $\frac{\partial \delta}{\partial \xi}$ from the t.-p. boundary, $\xi = 1$.

In a tokamak j_{bs} flows to increase ι.

In a stellarator the sign of j_{bs} depends on $2\ell - M$.

    toroidicity $\Rightarrow$ increasing ι
    helicity $\Rightarrow$ decreasing ι

  NB: _Physical_ direction of j_{bs} (in relationship to the main field) depends on "chirality"

Form of $\langle \partial_+ - \partial_- \rangle$ as a function of $\zeta = \frac{\mu B_0}{\varepsilon}$:

  - in the trapped region get a linear variation with $0 \leq v_{\parallel} \leq v\sqrt{(1 - B_{min}/B_0)}$

  - in the passing region the effect of $C(f)$ is to keep the surfaces uniform

$\langle \partial_+ - \partial_- \rangle$ vs $\frac{\mu_0 B}{\varepsilon}$ (sketch)
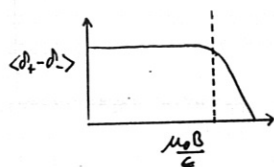
Δ_0 is a "geometric constant" (depending only on $B(\psi)$ and $\iota(\psi)$) which multiplies the profiles

eg: (Rosenbluth, Hazeltine and Hinton, Phys. Fluids $\underline{15}$, 116 (1972))

$$j_{bc} = -\Delta_0 \frac{g}{B_0}\left[1.67\,(T_e + T_i)\frac{dn}{d\psi} + 0.47\,n\frac{dT_e}{d\psi} - 0.29\,n\frac{dT_i}{d\psi}\right]$$

$$\frac{\partial \partial^0}{\partial s} = -g\frac{\partial \rho_{\parallel}}{\partial \alpha} \tag{9}$$

$\Leftrightarrow \quad \underset{\sim}{B} \cdot \underset{\sim}{\nabla} \partial = B^2 \partial_\alpha \rho_{\parallel}$ a magnetic differential equation

Obtain resonances near rational surfaces.
Ignore using damped field-line integration.

Numerical comparison with the theory of Shaing and Callen (Phys. Fluids 26, 3315 (1983))

  - higher order effects due to the fraction of trapped particles.

  - surface averages of the solutions of a pair of magnetic differential equations. Evaluated by Fourier transforming in the angles θ and ϕ.

Fig 1: Plot of one period of $\partial \rho_{\parallel}/\partial \alpha$ for an asymmetric field with one field maximum.

Fig 2a

Fig. 2b

Fig 2: Cuts through the surface formed by integrating $\partial_\alpha \rho_{\parallel}$ along lines of constant α from the field maximum, ς_m, of a model field similar to that of Fig. 1. The values of ι (in (a) $\iota = 0.4838$ and in (b) $\iota = 0.4839$) are close to $\iota_0 = 15/31 = 0.48387$. The oscillatory curves are obtained for a path length of $\Delta\varsigma = 1000$. Their peaks in (a) (troughs in (b)) lie on the surface traced out with $\Delta\varsigma = 10$.
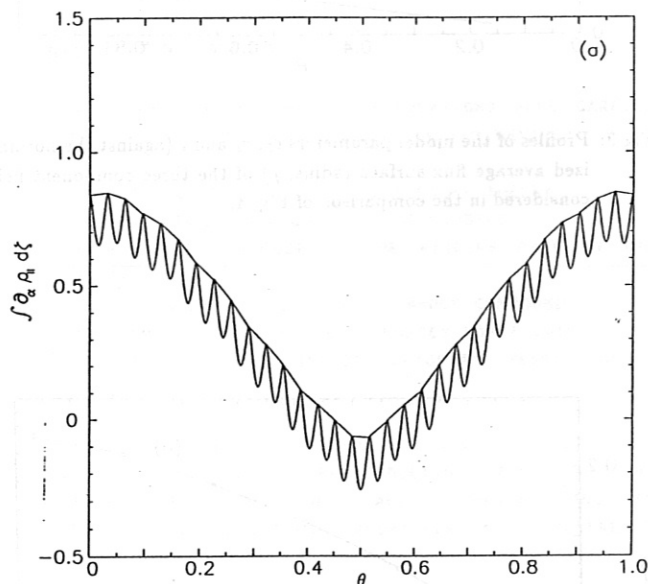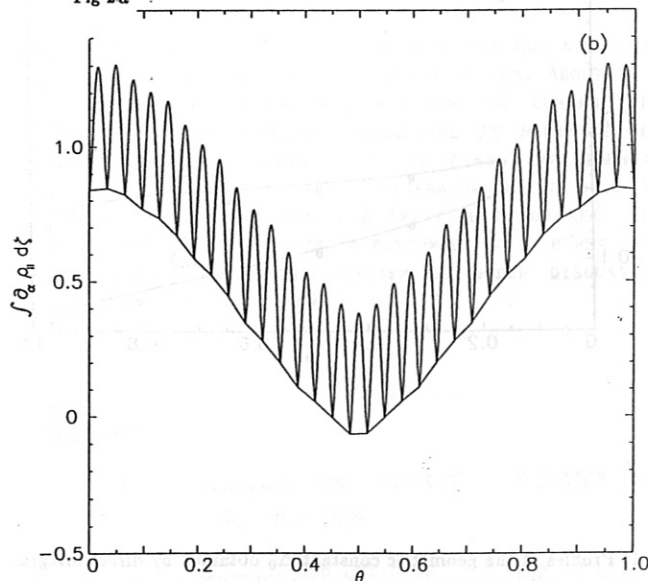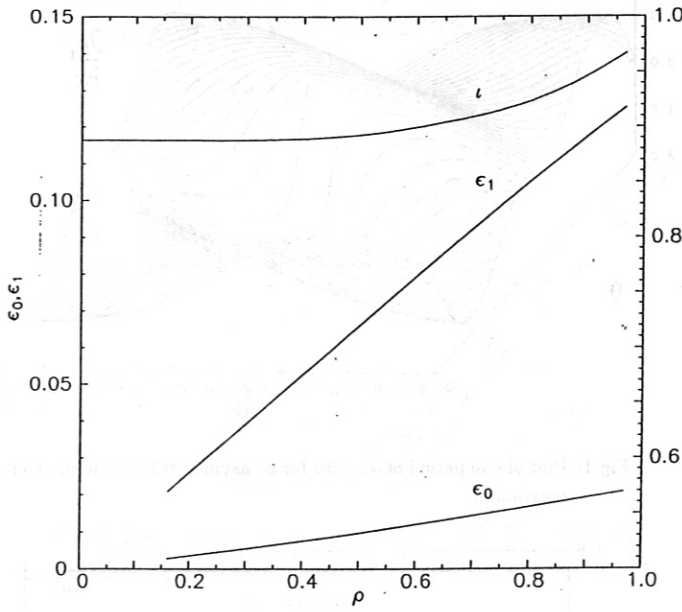
Fig 3: Profiles of the model parameters ϵ_0, ϵ_1 and ι (against the normalized average flux-surface radius, ρ) of the three component field considered in the comparison of Fig. 4.
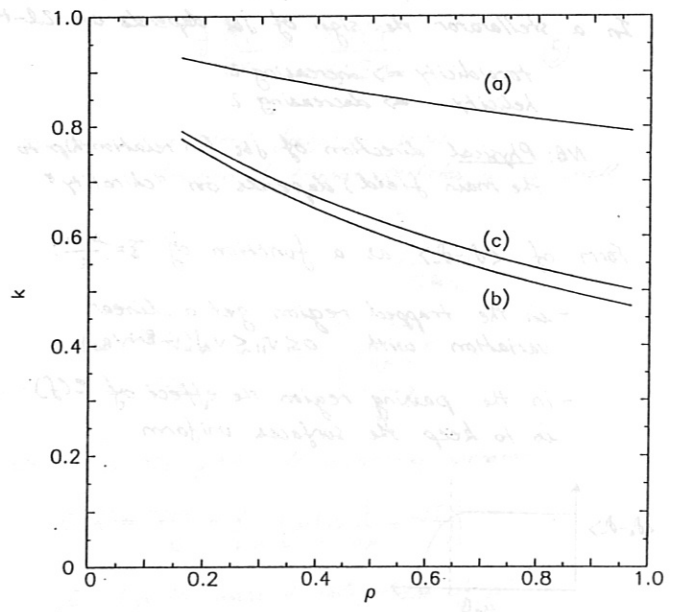
Fig. 5: Profiles of $k \approx 1 - f_t$ corresponding to the three cases in Fig. 4.
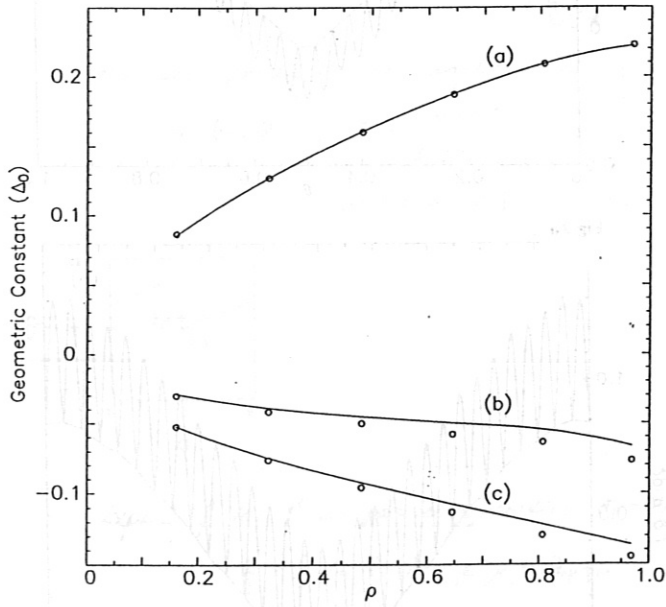
Fig 4: Profiles of the geometric constant Δ_0 obtained by direct integration of the Drift Kinetic Equation (open circles) against those due to Shaing and Callen (solid lines) for (a) the tokamak, (b) asymmetric and (c) quasi-helical test cases considered in the text.
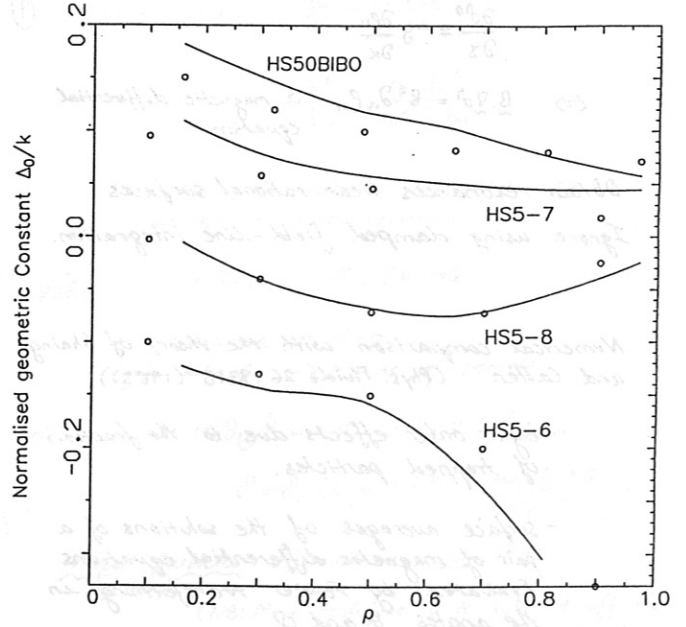
Fig. 6: Profiles of Δ_0/k obtained from direct integration (solid lines) and Shaing and Callen (open circles) for the WVII-X candidates HS5-6, HS5-7, HS5-8 and HS50BIBO.

W VII-X ENGINEERING

J. Sapper

INTRODUCTION

The size and the performance data of the planned experimental W VII-X device require investigations to determine whether the technical solution should be a machine with either a superconducting coil set or with a "classical" watercooled, pulsed copper coil magnet system. While the design and the cost of a normalconducting machine can be derived from the specific cost of W VII-AS, the design, schedule, and cost of a superconducting machine have to be investigated with the help of study contracts placed with industry because the number of existing and representative superconducting fusion devices is too small for a practical and direct calculation basis. Therefore, the IPP has placed two study contracts with industry /1/,/2/ aiming at providing realistic information about the problems of a superconducting magnet system, cryostat and refrigerator plant. In the following, first comprehensive results obtained from these studies are reported (see figs. 1 to 3).

SUPERCONDUCTING CABLE

Both companies (ABB and SIEMENS/INTERATOM) recommend a cable-in-conduit conductor. Copper strands with embedded NbTi-fibres are cabled and enclosed in a He-tight envelope. The volume between the strands serves for forced-flow He-cooling.

It is ensured that cable lengths of approx. 300 m can be manufactured, so the coils can be wound in double layer technique. The cooling medium pressure drop along one double layer is in the range of 10 bar. There is a difference in the cable envelope selected by the two companies: SIEMENS/INTERATOM prefer a stainless steel tube, while ABB works with extruded soft annealed aluminium which has to be hardened after the winding process (see figs. 4 and 5).

WINDING TECHNIQUE

The choice of two different cable envelopes with significantly differing stiffnesses consequently needs an adequate winding technique. The steel conductor has to be wound with a computer numerical controlled bending and winding machine which has to be trained with dummy conductors to evaluate the springback effects and final curvatures which have to be pre-bent. The soft aluminium conductor can be handled as the flexible conductors of the W VII-AS coils, e.g. in the simplest case wound by hand into the mould (see figs. 6 and 7). In both cases, the winding pack will be vacuum-pressure impregnated in epoxy resin in a high precision mould or in its final coil casing.

STRUCTURE AND CRYOSTAT

It is foreseen to arrange the individual coils (enclosed in their casings) in a modularly designed cold structure shell of approx. 80 mm wall thickness. The whole toroidal compound of a weight of typically 450 tons is free of externally acting magnetic forces and therefore will be hanged on tension rods in a modular outside cryostat vacuum vessel (see figs. 8 and 9).

The cryostat is completed by a second inside vacuum vessel which is also the plasma vacuum vessel. Ports for plasma observation, current and helium supplies are arranged in between (fig. 10).

FINITE ELEMENT CALCULATIONS

A series of finite element calculations were carried out for the mechanical components of the device:

(a) magnetic load on the cold structure shell;
(b) magnetic load on a coil in its housing with sliding effect of the winding pack in the housing;
(c) cool down calculation of the whole compound and combined with magnetic forces for a coil
(d) buckling of the inside cryostat vessel under vacuum load.

All results of these calculations (see fig. 11) show that the design of a superconducting magnet will be possible with sufficient safety margins and in agreement with existing experience from reference projects.

REFRIGERATOR PLANT

The refrigerator plant has to be designed for a nominal output of 3 to 6 kW at 4 K, liquid helium. About 90 % of the cold power are required for the current fed throughs. It is therefore essential to minimize the number of these elements in the final experimental design. The size of the refrigerator plant will be similar to that one for HERA (partially) or KfK. The amount and the size of additional cold power for cooling down the magnet system is under discussion (e.g. liquid helium tank).

REFERENCES

/1/ Study contract IPP 44519/SB, INTERATOM Nr. 32.07831.9, May 1989.

/2/ Study contract IPP 45118/SB, ABB, HIM 12 658, September 1989.

Input: Physicist's Design

i.e.

HS4-12	HS5-8
$R_o = 5\,m$	$R_o = 6,5\,m$
$n/n_p = 48/12$	$n/n_p = 60/12$
split coils	add. coils = 20

- { SC coil system
   Studies with industry }
- NC coil system
- SC coil system (IPP design)
- NC coil system (Harmeyer)

Interatom / Siemens
- Total magnet design
- Coils, Supply, SCC
- Structure
- Cryostat
- Schedule and Costs
- Prototyp Coil

ABB (Swiss + German)
- SCC, Supply
- Coil winding technique

KfK Consultants

FIG. 1: PROBLEM LIST

Development Strategy

Siemens / Interatom   **ABB**

1) Superconductor

Cable-in-conduit	Cable-in-conduit
Internally cooled	Internally cooled
(ICCS)	(ICCS)

2) Cable Envelope

| Stainless Steel | Aluminium, soft-annealed |

3) Cable Manufacture

| Drawing Process | Extruding Process |

4) Winding Technique

| CNC-Bending and Winding Machine (teach-in-roboter) | Semi-automatic, combined hand-winding technique (similar to WVII-AS) |

5) Coil Baking / Curing

High Precision Mould
Vacuum-Resin-Impregnation → } same treatment
Curing of Resin →
+ Hardening of Al

FIG. 2: DEVELOPMENT STRATEGY OF THE TWO STUDIES

1) Normal conducting magnets:

WVII-AS coils → ABB - Mannheim

2) Superconducting magnets:

Euratom LCT contribution	→ Siemens + KfK
NMR - magnets, 2T/4T	→ Siemens / Interatom
HERA, quadrupoles	→ Siemens
Swiss LCT contribution	→ ABB - Zürich / SIN
HERA, dipoles	→ ABB - Mannheim

3) Test Facilities
PSI / SIN
KfK

4) Refrigerators
KfK
HERA

FIG. 3: EXAMPLE LIST OF REFERENCES FOR MAGNET SYSTEMS

Abb L4: Querschliffe des Vierkant-Leiters für unterschiedl. Fertigung

8.5 : 1
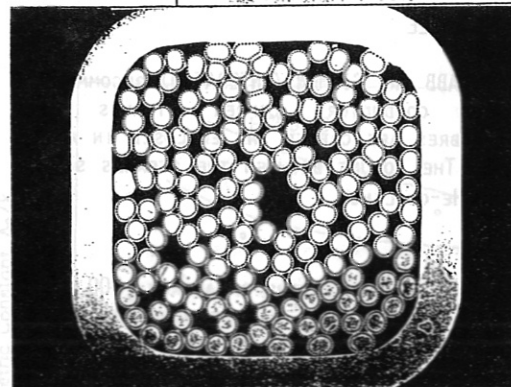
Fertigungsvariante mit Verdichtungszug (Ø 11.7 mm) auf Endabmessung 10 mm x 10 mm; Eckenradien (außen) 2.75 mm (Vormuster)

8.5 : 1
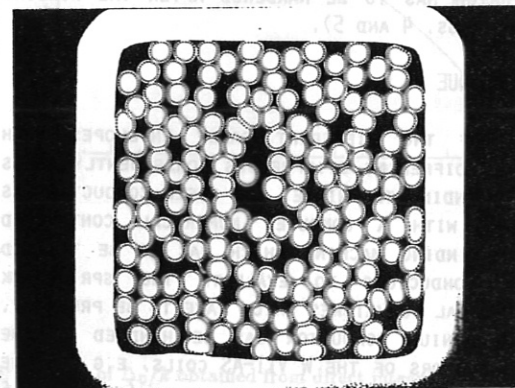
Fertigungsvariante ohne Verdichtungszug, Profilzug auf 10 mm x 10 mm ausgehend von Ø 13 mm; Eckenradien ca. 2.00 mm (Probefertigung)

FIG. 4: SUPERCONDUCTING CABLE WITH STEEL ENVELOPE

WVII-X Leiterstudie
ICCS mit Aluminiumhülle

Dimensionen:

Vereinheitlicher
Basisaufbau für
FE-Berechnungen

Die Materialdaten
dem Datenblatt
entnehmen.

Leiter isol.: 14.7 x 14.0 mm

Leiter blank: 13.2 x 12.6 mm

Kantenradius: 2.0 mm

SI-Kabel: 9.2 x 8.6 mm
Kantenradius: 2.0 mm

Glas-Epoxy

Aluminium

SI-Kabel mit
Umbändelung
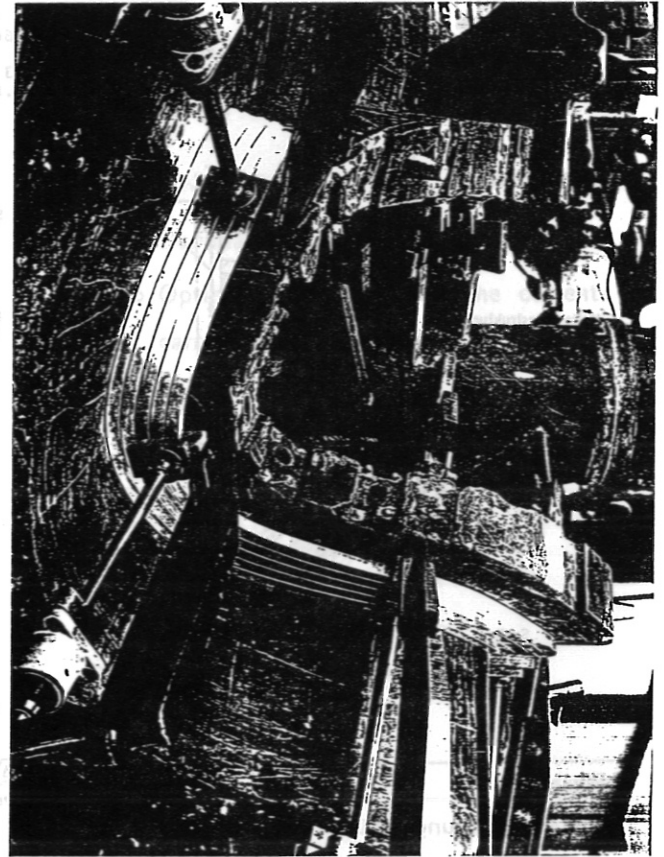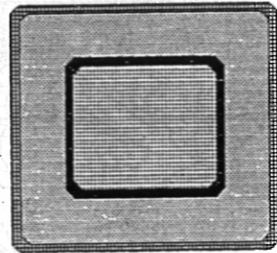
FIG. 5: SUPERCONDUCTING CABLE WITH AL-ENVELOPE

89-04-06   IMV-S/Mx

FIG. 7: WINDING TEST OF THE AL-CABLE IN A W VII-AS MOULD

Andrück- und   Biegekopf   Vorratsrolle für   Verschieblicher Portalrahmen (Träger
Meßeinrichtung   2. Hälfte Dopellage   von Biegekopf und Reinigungsstrecke)
Wickel- und   (auf der Wickel-
Tränkform   form befestigt)   Reinigungsstrecke

Coil-Station

Profilrichtanlage

Drehtisch,
(Z`-verfahrbar)

Äusserer Portal-   Innerer Portalrahmen (Z-ver-   Grundrahmen (X-verfahrbar)
rahmen (Y-ver-   fahrbar, drehbar um Y-Achse);
fahrbar)   Basis der mehrachsig verfahrbaren
                   Andrück- und Meßeinrichtung

Anordnung der Komponenten der
Wickelanlage (Prinzipskizze)

Abb. 3.3-5

FIG. 6: WINDING DEVICE FOR THE STEEL CABLE

INTERATOM
Ident-Nr./No.32.07831.9
Seite/Page : 3-45

Figure 8

Prinzipskizze für
Spulenkryostat
mit Sichtöffnung

Innerer Vakuumbehälter mit Durchführungsstutzen
und Spulen 7 bis 13 mit Versorgungsanschlüssen,
Ansicht von oben

Spulenaufhängung

Sichtöffnung

Kalte Tragstruktur

130 - 180

(1000)

Vakuumtank

80

240

Spule

80 K-Schild

90°

Spulen

13

12

11

10

9

8

7

45°

Durchführungsstutzen

äußere Begrenzung
innerer Vakuumbeh.

Versorgungsanschlüsse

Plasmaseele

FIG. 10: ARRANGEMENT OF PORTS, CURRENT AND HELIUM
SUPPLIES

Figure 9

Stutzenausführung mit Lateralkompensator

äußerer Vakuumbehälter

≈370

Ø3900

60

270

40   230   40

10

Strahl –
ungs-
schild

Stütz-
struktur

Spule

innerer Vakuumbehälter

ABAQUS STRESSES LOAD XYZ E=150GPA

SHELL SURFACE:TOP

LOADCASE:101
FRAME OF REF:GLOBAL
STRESS - VON MISES MIN: 7.76E+00 MAX: 2.34E+02

Spule

oberhalb der Spulen geschnitten
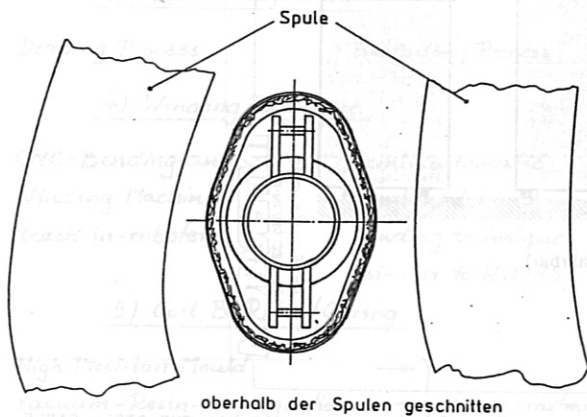
FIGS.8 AND 9: CROSS-SECTIONS OF THE CRYOSTAT
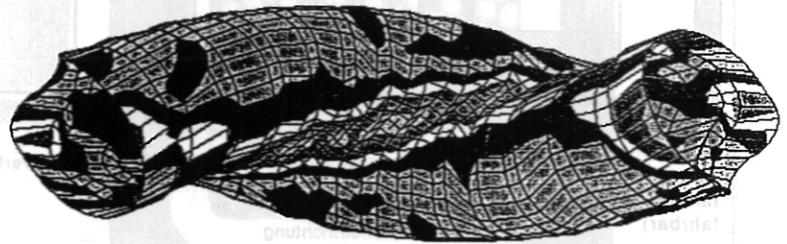
FIG. 11: FEM CALCULATION OF BENDING STRESSES IN THE
COLD STRUCTURE SHELL

Coil Studies for Helias Configurations

P. Merkel

Max-Planck-Institut für Plasmaphysik
IPP-EURATOM Association
D-8046 Garching bei München
Federal Republic of Germany

The NESCOIL code for determining coils [1, 2, 3] has been applied to the optimized Helias50B configuration [4]. A solution with excellent accuracy is obtained by solving the boundary value problem with surface currents. A set of dense flux surfaces is shown in Figs. 3, 4. The value of iota on axis is $\iota = 0.836$ and at the edge $\iota = 0.99$.

Realizations of the Helias50B vacuum field with 10 and 12 current filaments per period are presented for two slightly different coil systems (case 996 and case 98B) (Figs. 5–28). In comparison with the exact solution the iota profile was slightly changed to $0.76 < \iota < 1.0$ and two major chains of islands appeared: a chain of 5 islands at the boundary ($\iota = 1$) and one chain of 6 islands in the interior region at $\iota = 5/6$. Islands of higher order are negligibly small. The islands at the boundary can serve as a basis for a divertor concept. The islands in the interior should be eliminated.

In Figs. 9, 10 the vacuum field of a modified Helias50B configuration is shown. The iota profile is shifted to $0.6 \leq \iota \leq 0.95$, so that the position of $\iota = 5/6$ is moved into the interior of the plasma domain. The exact solution of the boundary value problem shows islands at $\iota = 5/6$, which could indicate that the occurrence of islands at $\iota = 5/6$ may be more a property of the Helias50B configuration than the result of using a finite number of filaments.

These islands were eliminated by adding small correction fields resonant with the geometry of the island chain. This method was proposed by Hanson and Cary [5]. Convincing results were obtained by adding appropriately chosen Fourier amplitudes $\Phi(m,n)$ to the surface current potential Φ which are either directly resonant to the island geometry or which act by nonlinear coupling with the Fourier harmonics of the surface current boundary representation.

Figures 27, 28 present tables with the filament properties. In Figs. 29–32 it is demonstrated that resonant correction fields can also be used to shift the poloidal position of the islands.

It may be of advantage to operate the Helias50B with a chain of 6 islands at the boundary ($\iota = 5/6$). In this case the island configuration consists of one connected "tube", while in the case of $\iota = 1$ at the boundary the islands consist of 5 "tubes" so that different types of divertor are conceivable.

References

1 P. Merkel, Nucl. Fusion **27** (1987) 867.

2 P. Merkel, In: Theory of Fusion Plasmas, Eds. A. Bondeson, E. Sindoni, and F. Troyon, Varenna, Italy, EUR1136EN, 25-46.

3 P.Merkel, In: Proc. 2nd Workshop on Wendelstein VII-X, Schloss Ringberg, Eds. F. Rau, G.G. Leotta, CEC Brussels 1988, EUR11705EN, 231-243.

4 W. Lotz, P. Merkel, J. Nührenberg, A. Schlüter, R. Zille, Seventh Int. Workshop on Stellarators, 1989, Oak Ridge/USA.

OUTLINE OF TALK

- The NESCOIL code

  o Boundary value problem

  o Optimization by varying the current-carrying surface

- Application to the HELIAS 50B configuration

  o Control of islands

    — Islands as a basis for a divertor

    — Dense flux surfaces

  o Coils for HELIAS 50B

- Summary

Fig. 1

Optimization by Varying the Current-carrying Surface

- Minimization of the error $\varepsilon = \langle \dfrac{|\vec{B} \cdot \vec{n}|}{|\vec{B}|} \rangle$

- Prescribing the number of harmonics Φ_{mn}, $m \leq 5$, $|n| \leq 5$ of the current potential

- Prescribing the minimal and maximal plasma-coil distance

- Prescribing the maximal coil curvature

- Prescribing the maximal surface current density

Fig. 2

Fig. 3
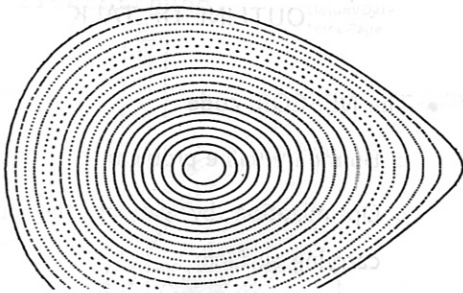
3–4 Poincaré plots of the Helias50B vacuum field generated
by surface currents on the outer boundary (see Figs. 5–
6). High accuracy of the solution for the boundary
value problem is obtained with a number of $m \leq 20$
poloidal and $|n| \leq 20$ toroidal Fourier modes $\tilde{\Phi}(m,n)$
of the surface current potential. Iota profile $0.836 \leq$
$\iota \leq 0.99$. Number of periods $N_p = 5$.

Fig. 4

HELIAS 50B, CZ(1,−1) = −CR(1,−1) =.41191

PKM549

PKM548
24.07.89
20.06.89
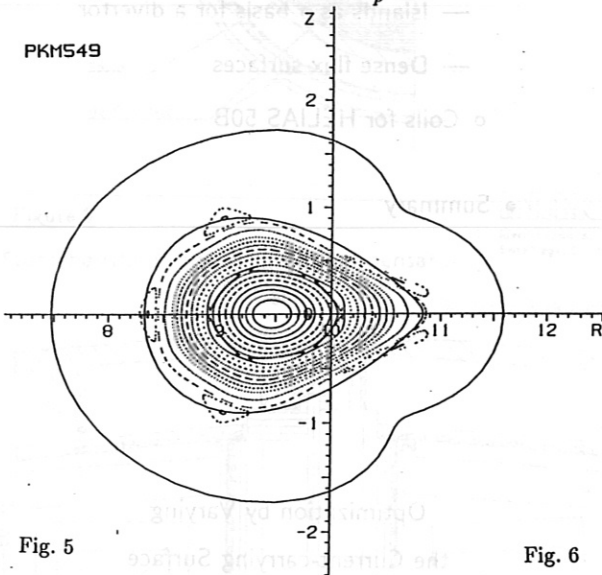
Fig. 5

Fig. 6

HELIAS 50B,12 COILS/PERIOD, NR. 996121 1

Fig. 7

Fig. 8

996121 1

HELIAS 50B,12 COILS/PERIOD, NR. 996121
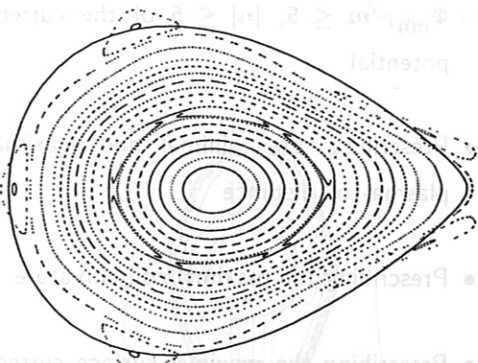
5–8 Poincaré plots of the Helias50B vacuum field generated
by 12 current filaments per period (case 996). Iota
profile $0.76 < \iota < 1$. Island chains at value of iota $\iota = 1$
and $\iota = 5/6$.
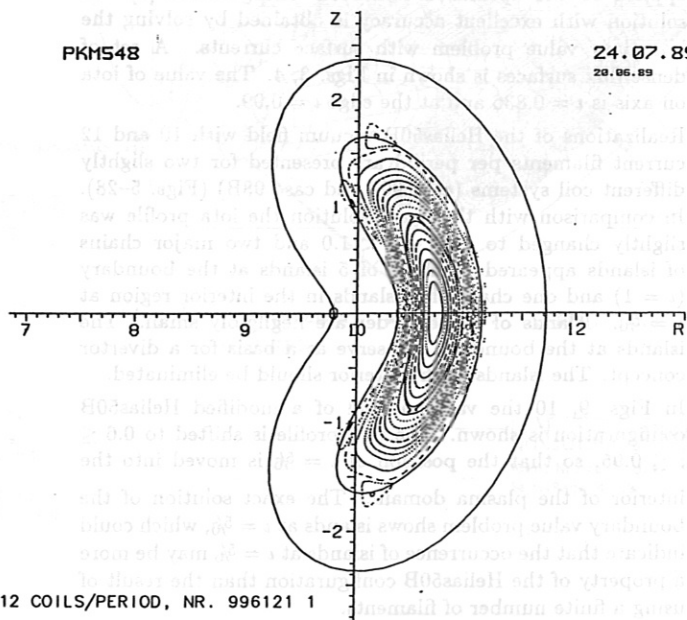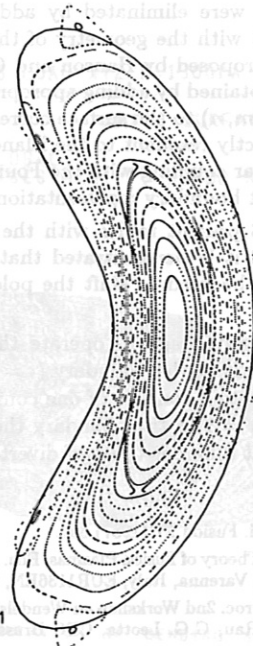
Fig. 9

PKM585

HELIAS 50B, CZ(1,-1) = -CR(1,-1) =.4
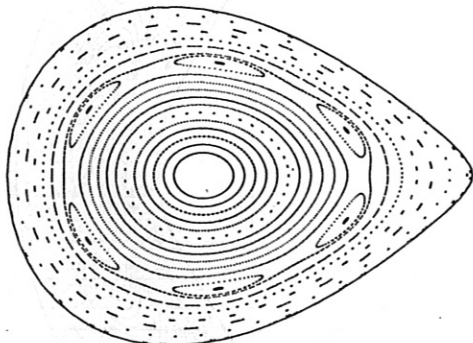
9-10 Poincaré plots of a modified Helias50B vacuum field
generated by surface currents as in the case shown
in Figs. 3-4. The iota profile is lowered to $0.8 \leq \iota \leq 0.95$ by changing the coefficient of the plasma
boundary Fourier representation: $r(m = 1, n = -1) = z(1,-1) = 0.41191$ to 0.4. The field satisfies the
boundary condition with high accuracy and shows
islands at $\iota = 5/6$.

Fig.10

PKM586   24.07.89
                                                21.06.89
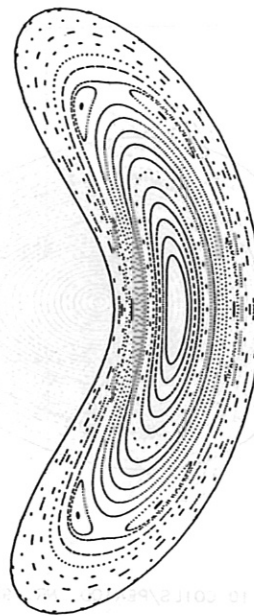
25.07.89
20.06.89

Fig.11

PKM553
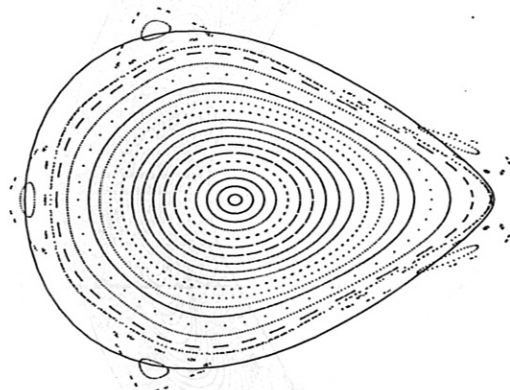
HELIAS 50B,12 COILS/PERIOD, NR. 996122 2

Fig.12

PKM554
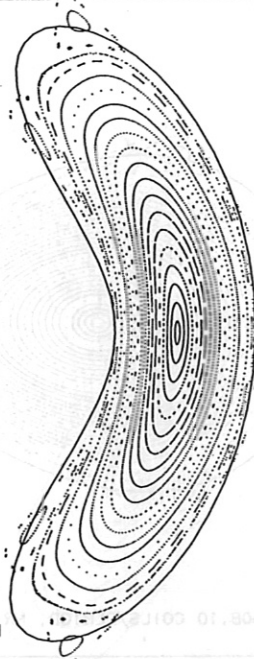
996122 1

11-12 Poincaré plots of the configuration described in Figs. 5-
8 with the islands at $\iota = 5/6$ eliminated by a resonant
field which is generated by one additional Fourier
amplitude $\Phi(6,0) = 5 \cdot 10^{-4}$ of the surface current
potential.

Fig.13

PKM559

Fig.14

PKM560

25.07.89
20.06.89
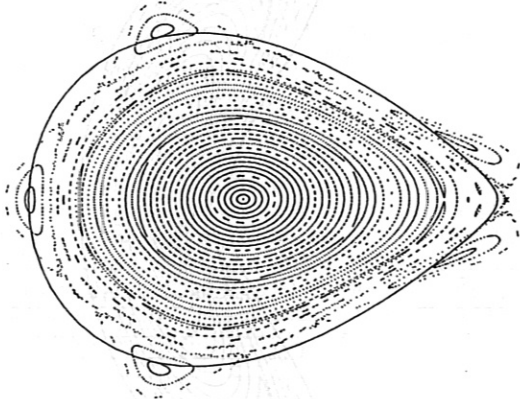
HELIAS 50B,10 COILS/PERIOD, NR. 996102 2
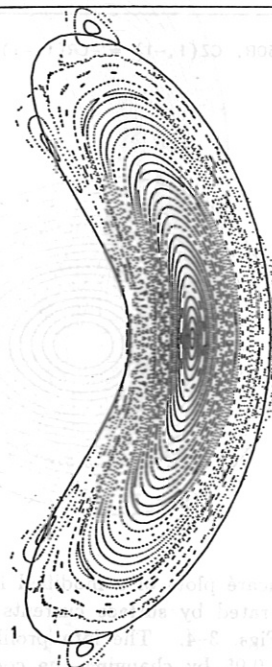
NR. 996102 1

Fig.15

PKM517

Fig.16

PKM514

25.07.89
20.06.89
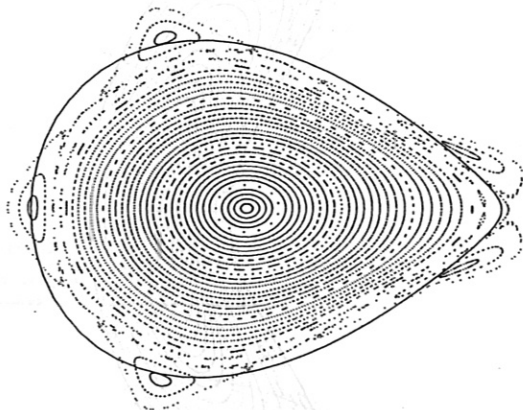
HELIAS 50B,10 COILS/PERIOD, NR. 996103 2
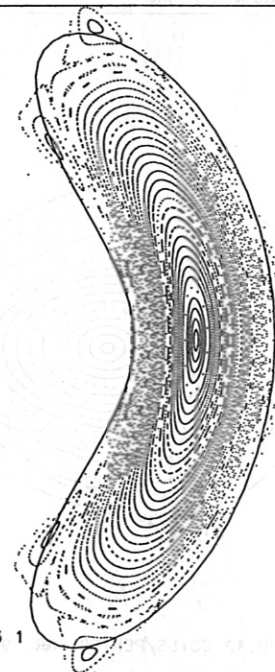
NR. 996103 1

13–16 Poincaré plots of the Helias50B vacuum field produced
by 10 filaments per period (case 996). The magnetic
surfaces in Figs. 13–14 are obtained by adding a Fourier
amplitude $\Phi(6,0) = 5 \cdot 10^{-4}$ to the surface current
potential. The remaining islands at $\iota = 5/6$ and $\iota = 10/11$
are eliminated by a second correction term
$\Phi(11,-1) = -1.6 \cdot 10^{-4}$.

Fig.17

PKM536
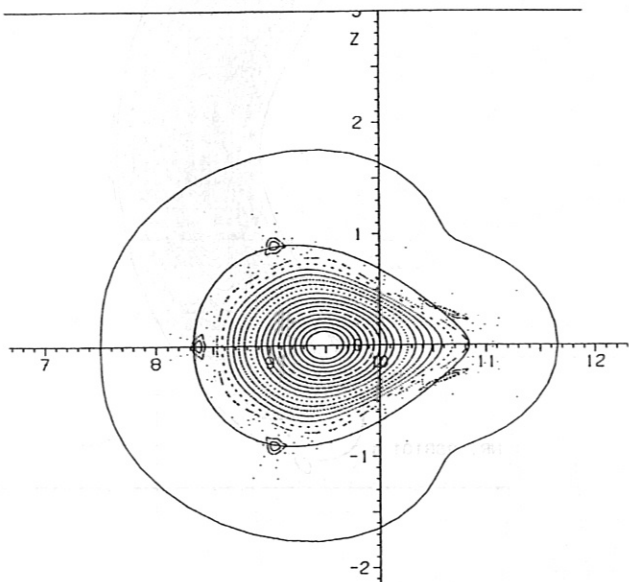
Fig.18

PKM537

25.07.89
20.06.89

HELIAS 50B.12 COILS/PERIOD, NR. 98B121 2
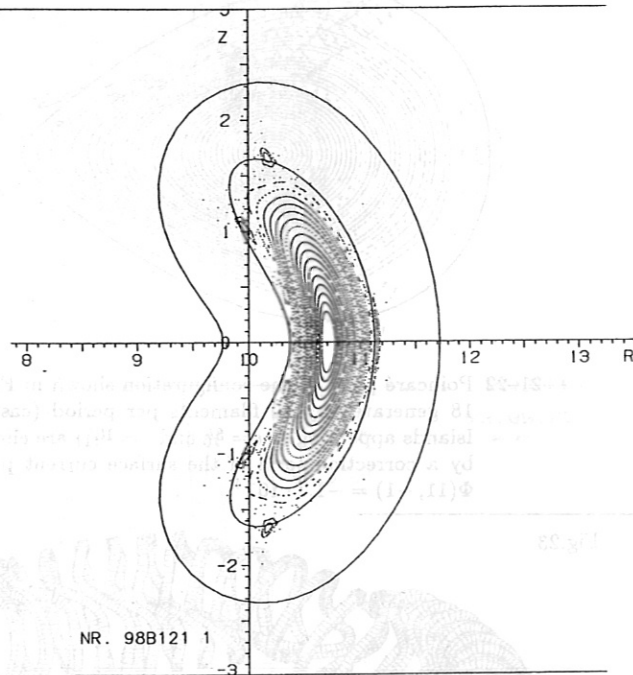
NR. 98B121 1

Fig.19

PKM545
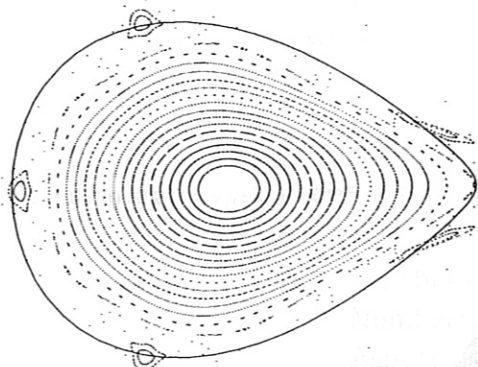
Fig.20

PKM544

25.07.89
20.06.89

HELIAS 50B.12 COILS/PERIOD, NR. 98B121 2
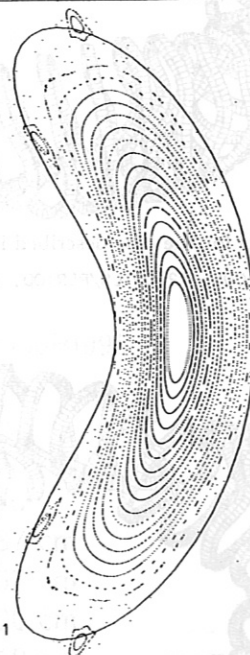
NR. 98B121 1

17–20 Poincaré plots of the Helias50B vacuum field produced
by 12 filaments per period (case 98B) on the outer
surface (shown in Figs. 17–18).

69

Fig.21 PKM520

HELIAS 50B, 10 COILS/PERIOD, NR. 98B101 2

Fig.22 | PKM523   25.07.89

NR. 98B101 1
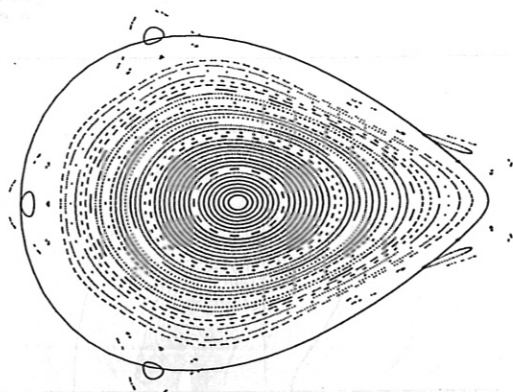
21–22 Poincaré plots of the configuration shown in Figs. 17–18 generated by 10 filaments per period (case 98B). Islands appearing at $\iota = 5/6$ and $\iota = 10/11$ are eliminated by a correction term of the surface current potential $\Phi(11, -1) = -1.7 \cdot 10^{-4}$.

Fig.23
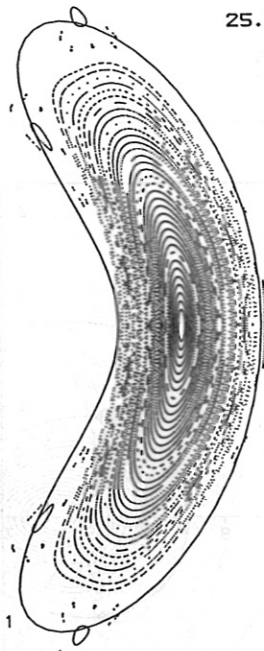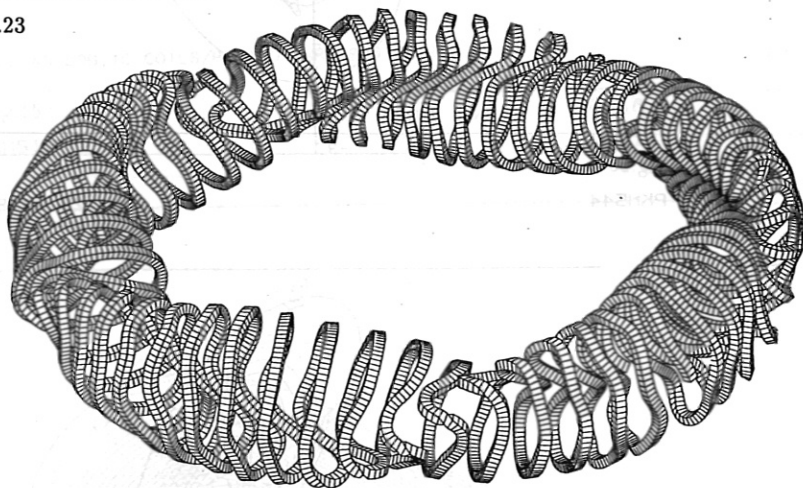
23 Modular coils for the case described in Figs. 17–20.

HELIAS 50B, 5 PERIODS, 12 COILS/PERIOD, NR. 98B121

PKM531   25.07.89
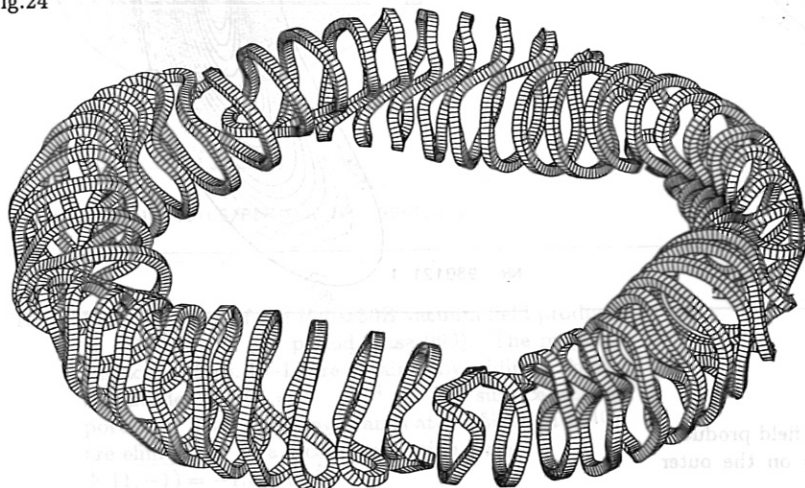
PKM519   25.07.89

Fig.24

24 Modular coils for the case described in Figs. 21–22.

HELIAS 50B, 5 PERIODS, 10 COILS/PERIOD, NR. 98B101

70

Fig.25
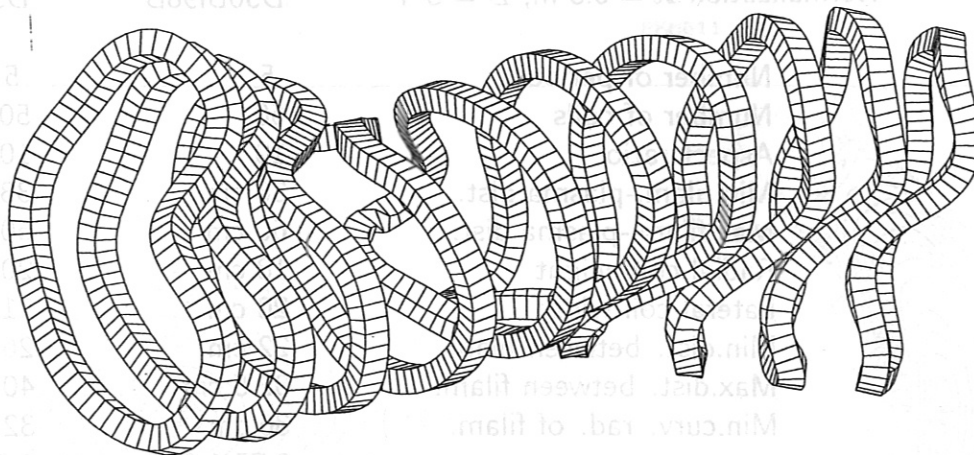
25   One period of modular coil of the configuration shown in Fig. 24.

HELIAS 50B, 5 PERIODS, 10 COILS/PERIOD, NR. 98B101

Coil Nr.1   Coil Nr.2   Coil Nr.3

32.5 cm
40.0 cm
50.0 cm

Coil Nr.4   Coil Nr.5   Coil Nr.6

32.5 cm
40.0 cm
50.0 cm

Fig.26
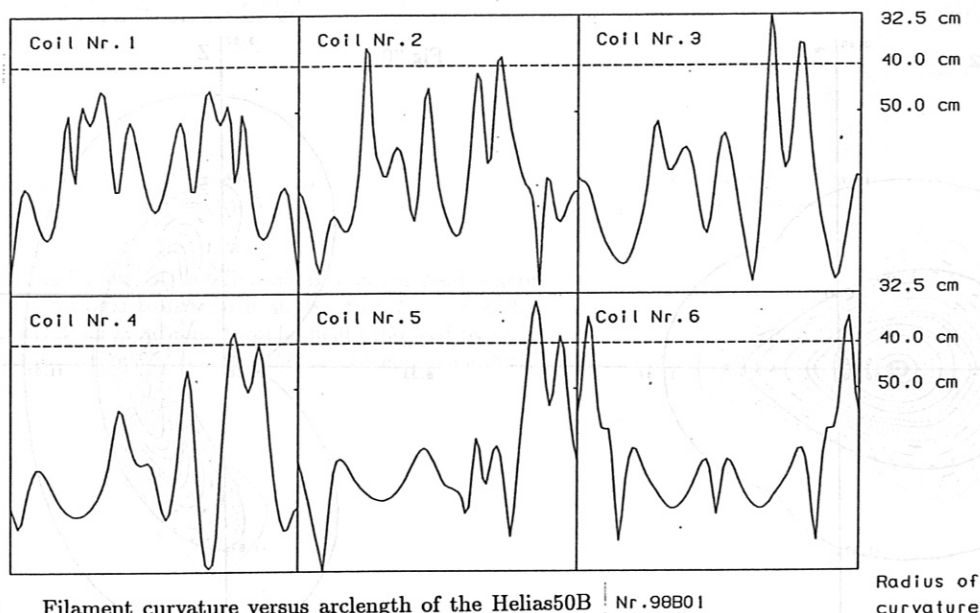
Radius of curvature

26   Filament curvature versus arclength of the Helias50B Nr.98B01
coils shown in Fig. 25.

HELIAS 50B

Normalization $R = 6.5$ m, $B = 3$ T

	D50BI996	D50BI996
Number of periods	5	5
Number of coils	60	50
Aspect ratio	10	10
Min.filam.-plasma dist.	37 cm	37 cm
Max.filam.-plasma dist.	57 cm	57 cm
Radial coil height	20 cm	20 cm
Lateral coil width	18 cm	21.5 cm
Min.dist. between filam.	19.5 cm	24 cm
Max.dist. between filam.	32.5 cm	40 cm
Min.curv. rad. of filam.	35 cm	34 cm
ι_0 ι_1	0.76-1.0	0.76-1.0
Magnetic well	1.2%	1.1%

Fig.27

Number of periods	5	5
Number of coils	60	50
Aspect ratio	10	10
Min.filam.-plasma dist.	38 cm	38 cm
Max.filam.-plasma dist.	60 cm	60 cm
Radial coil height	18 cm	20 cm
Lateral coil width	20 cm	21.5 cm
Min.dist. between filam.	22 cm	26.5 cm
Max.dist. between filam.	32.5 cm	40 cm
Min.curv. rad. of filam.	36 cm	32.5 cm
ι_0 ι_1	0.75-1.0	0.75-1.0
Magnetic well	1%	1%

Fig.28

Fig.29   PKM002
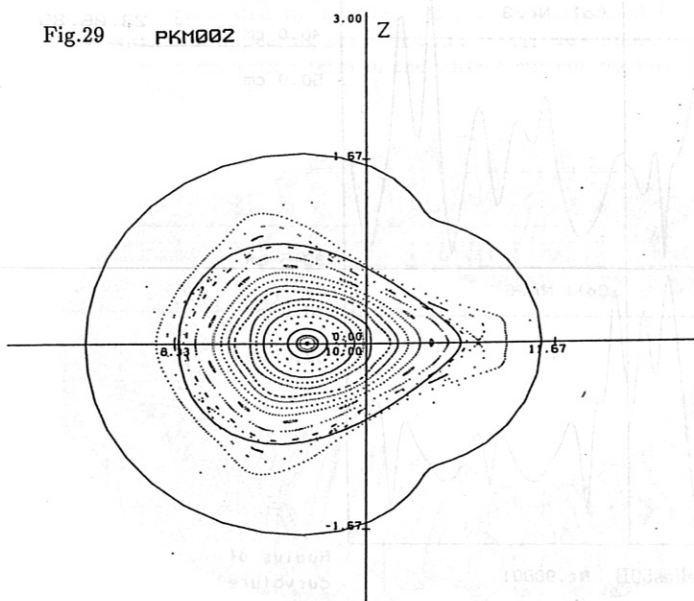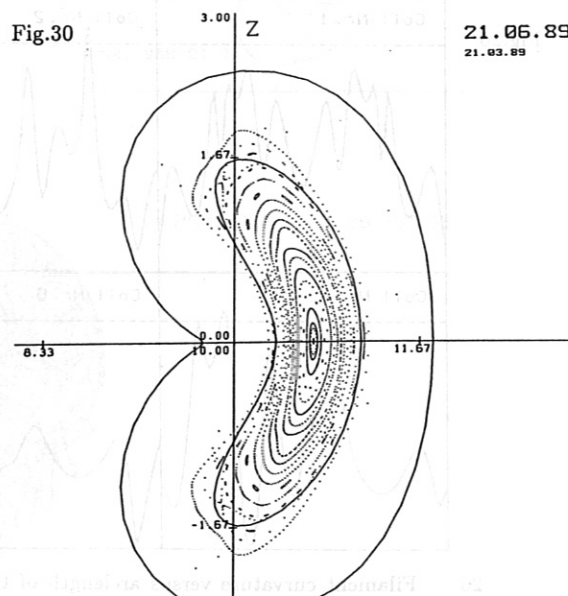
Fig.30   21.06.89
21.03.89

Fig.31   PKM794

Fig.32   18.05.89
18.05.89
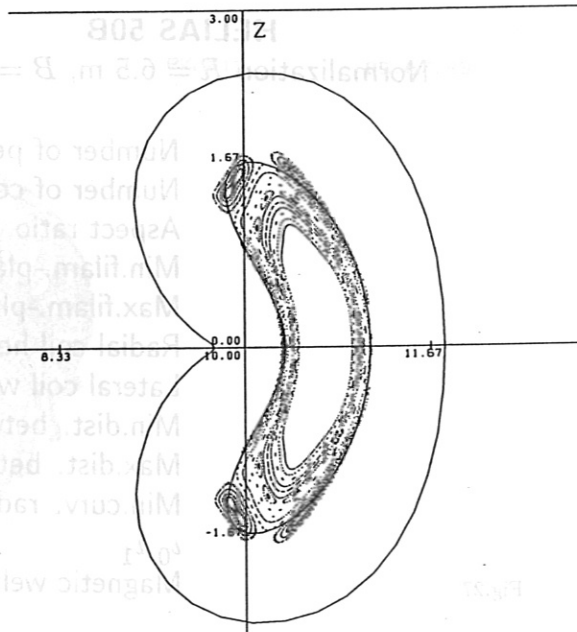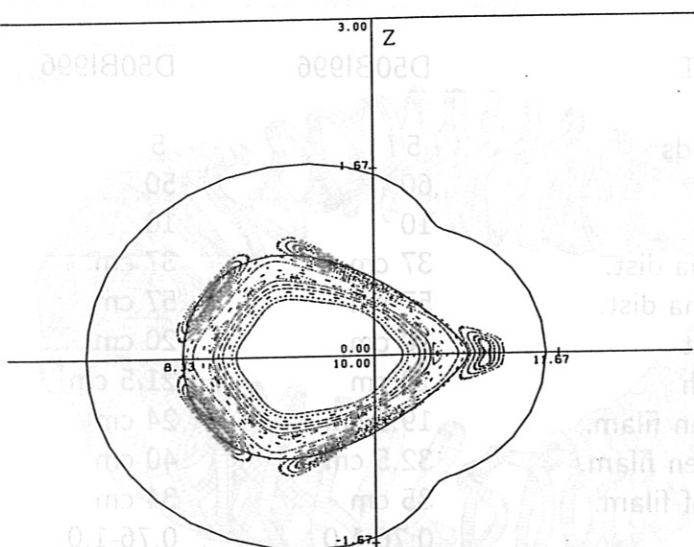
29–32 In these Poincaré plots it is demonstrated that the
poloidal position of the islands at $\iota = 1$ can be moved
by adding appropriate resonant fields. The islands in
Figs. 31–32 are obtained by adding a Fourier amplitude
$\Phi(5, -1) = 5 \cdot 10^{-4}$ to the surface current potential of
the configuration shown in Fig. 29–30.

Fig.33

PKM612

Fig.34

PKM611

22.06.89

HELIAS 50B, iota shifted: 0.7< ι < 5/6

0.7< ι < 5/6

33–34 Poincaré plots of the Helias50B vacuum field where the rotational transform is shifted to 0.7 < ι < 5/6 by applying an additional toroidal field produced by coils with a current $I_t = 0.19 I_p$ (I_p = current of modular coils).

Parameter Variations for W VII-X Vacuum Fields

J. Kißlinger

Max–Planck Institut für Plasmaphysik, D–8046 Garching, FRG,
EURATOM–Association.

For experimental flexibility, some variations of the vacuum field parameters are required, e.g. rotational transform, shear and magnetic axis position. Different possibilities are investigated and results for the configurations HS 4–12 and HS 5–8 are given.

At the 2nd W VII–X Ringberg - Workshop 1988, (page 263 of the proceedings) F. Rau presented investigations on the configurations HS 4–11 and HS 4–12, using 'double layer' coils, external TF - coils, and systems of coaxial coils generating vertical and 'quadrupole' fields. These investigations are extented by using double layer coils and varying the current center individually from coil to coil. In case A (JOK710, fig. 1), the current center moves from the middle of the outer layer of coil 1, near the beginning of a field period, to the middle of the inner layer of coil 6, near the middle of the field period. The opposite is done in case I (JOK714), where the current center changes from the inner layer of coil 1 to the outer layer of coil 6. A clear effect is seen on the shear and magnetic well when comparing to the standard case; see fig. 2. A shift of the magnetic axis also occurs; 2 cm inwards in case A, and 1.5 cm outwards in case I (fig. 3), correlated with a change of the modulation of mod B along the magnetic axis (fig. 4).

In HS 5–8 a set of 4 planar coils per period, arranged on a helical axis (see fig. 5) allows one to superimpose toroidal and vertical fields as well. A current of $\pm$ 0.5 MA in each planar coil, which alters the magnetic field of the modular coils by about $\pm$ 10%, changes the rotational transform from about -10 to +15% of its standard value (figs. 6 and 7). In the low ι -case the magnetic well is reduced to about 50% of its standard value. Opposite currents of 0.5 MA in the planar coils A and B of fig. 5 generate a net vertical field and shift the magnetic axis by about 1% of the major radius. The toroidal modulation of mod B, introduced by the currents of the planar coils, can be considerably reduced if the currents in the modular coils are also modulated (figs. 8 and 9). In the compensated case JOK794, the shift of the magnetic axis is reduced, mainly at $\varphi = 0$. Fig. 10 shows the Poincafe plots for the inward shifted case JOK796 and the outward shifted case JOK797. In the latter case the magnetic well is reduced; the shear remains nearly constant (fig. 11).

Because of the locally large coil curvature, the superconducting coils are to be constructed using small conductor dimensions and many turns. To keep the discharge voltage in the case of a quench below a level set by the admissible insulation voltage, it is necessary to split the electrical connections of the whole coil set in sections. To retain the fivefold symmetry, all coils of the same type (there are 6 types of coils in HS 5–8) should be connected in series, otherwise power supplies with rather high current accuracy and constance are necessary, on the order of 10^{-4} of the nominal current. Such a current supply system permits one to change the modular magnetic ripple by energizing each coil type with different currents. In the case of JOK663

(fig. 12) the current varies from +10% of the nominal current in coil 1 to -10% in coil 6; in the case of JOK666 (fig. 13) the opposite is done with currents from -10% in coil 1 to +10% in coil 6. The induced modulations of mod B have different phases in the two cases (figs. 14 – 16). This will change the number and location of the trapped particles, thus the neoclassical transport and the bootstrap current are influenced. The computed geometrical factor G_b, which describes the value of the bootstrap current in the lmfp regime, is shown in fig. 17. In JOK663 G_b is nearly the same as in the standard case; it is clearly larger in the case of JOK666. The ratio of $\langle |j_{\parallel}/j_{\perp}| \rangle$ increases its value from 0.54 (JOK663) to 0.74 (JOK666). Only a weak influence on the rotational transform, shear and magnetic well is seen in these cases (fig. 18).

The principle of double layer coils for field parameter variation is also investigated for the configuration HS 5–8. For this application the coil height is extented from 20 cm to 27 cm; 2 cm radially inwards and 5 cm radially outwards (fig. 19). In the case of JOK767 (fig. 20), only the outer layers of the coils are energized - in JOK784, 1/3 of the current flows in the outer layer and 2/3 in the inner layer of the coils - in JOK778, only the inner parts of the coils are used. The shift of the current center from the inner to the outer layer has the principal effect of reducing the rotational transform at the edge (shear) and the magnetic well; simultaneously a significant shift of the magnetic axis radially inward occurs, as shown in fig. 21 and fig. 22. In the case of JOK761 (fig. 23), the current center is varied from coil to coil, by energizing in coil 1 (near $\varphi = 0$) only the outer layer, and in coil 6 (near the middle of a field period) only the inner layer. This leads to a configuration with slightly higher shear, a constant increase of the magnetic well towards the edge (fig. 24) and a lower maximum value of the unfavorable curvature which should have a positive influence on the stability of the plasma.

CONCLUSIONS

- The proposed additional planar coils allow in HS 5–8 a variation of the rotational transform from -10% to +15% or a shift of the magnetic axis of 1% of the major radius. For combined ι variation and axis shift a cross-section of the planar coils of 14 cm × 14 cm and a coil current up to 1 MA are required.

- An additional possibility for field parameter variation results if one connects the coils of each coil type to a seperate group. Using different currents for different coil types the magnetic ripple, introduced by the planar coils, can be reduced or a toroidal modulation of mod B can be generated which influences the neoclassical transport and the bootstrap current.

- Using double layer coils in HS 5–8, the variation of the current center mainly changes the rotational transform at the edge and less on the magnetic axis. Simultaneously the magnetic well is varied and a shift of the magnetic axis occurs. In the case JOK761, where the current center is individually varied from coil to coil, the constant increase of the magnetic well towards the edge and a lower maximum value of the unfavorable curvature should have a positive influence on the stability of the plasma.

- In all cases a strong coupling between shear and magnetic well exists.

HS4V12   R₀ 5 m
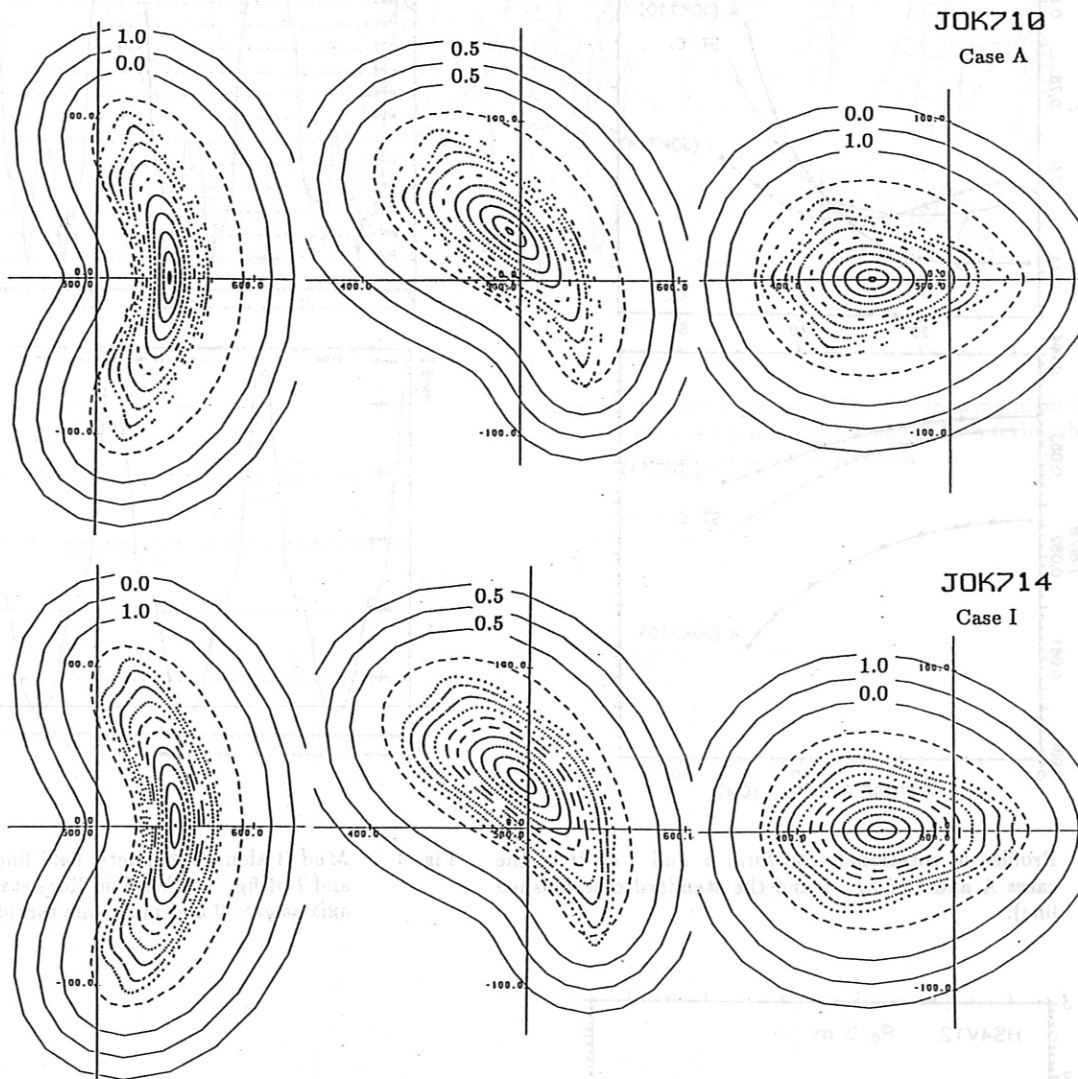
CURRENT DISTRIBUTION

Coil number	1	2	3	4	5	6	7	8	9	10	11	12
Case A (JOK710)												
Inner coil	0.0	0.25	0.5	0.5	0.75	1.0	1.0	0.75	0.5	0.5	0.25	0.0
Outer coil	1.0	0.75	0.5	0.5	0.25	0.0	0.0	0.25	0.5	0.5	0.75	1.0
Case I (JOK714)												
Inner coil	1.0	0.75	0.5	0.5	0.25	0.0	0.0	0.25	0.5	0.5	0.75	1.0
Outer coil	0.0	0.25	0.5	0.5	0.75	1.0	1.0	0.75	0.5	0.5	0.25	0.0

Fig. 1 : Poincare' plots of vacuum fields using double layer coils in HS 4–12. In case A (JOK710) the current center moves from the middle of the outer layer at the beginning of a field period, to the middle of the inner layer at the middle of a field period. The opposite is done in case I (JOK714) where the current center changes from the inner layer to the outer layer.
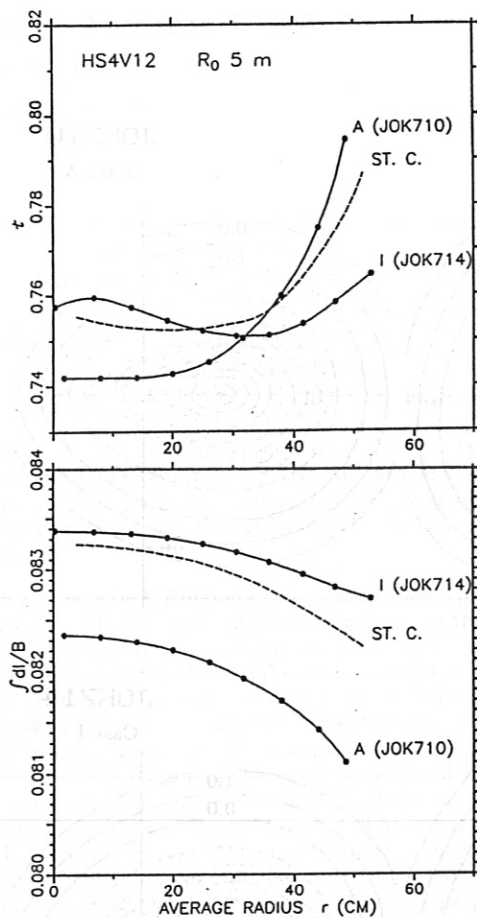
Fig. 2 : Profiles of rotational transform t and $\int dl/B$ of the cases A and I of fig. 1 and the standard case (dashed line).
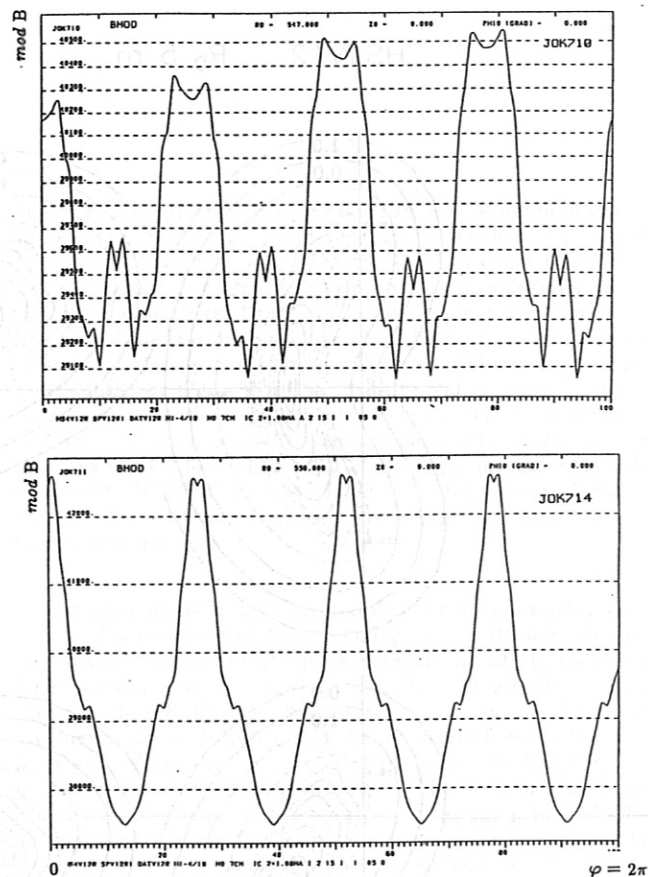
Fig. 4 : *Mod* B along a magnetic field line for the two cases A and I of fig. 1. The field lines start near the magnetic axis at $\varphi = 0$ and make one toroidal transit.
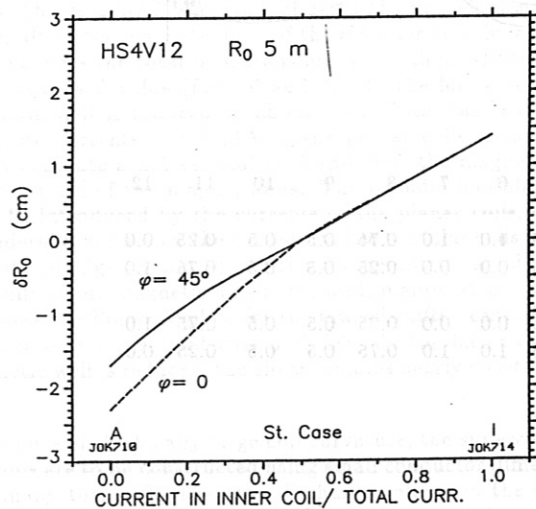
Fig. 3 : Shift of the magnetic axis vs the ratio of the currents in the inner layers of the coils to the total coil currents.

A   B   B   A
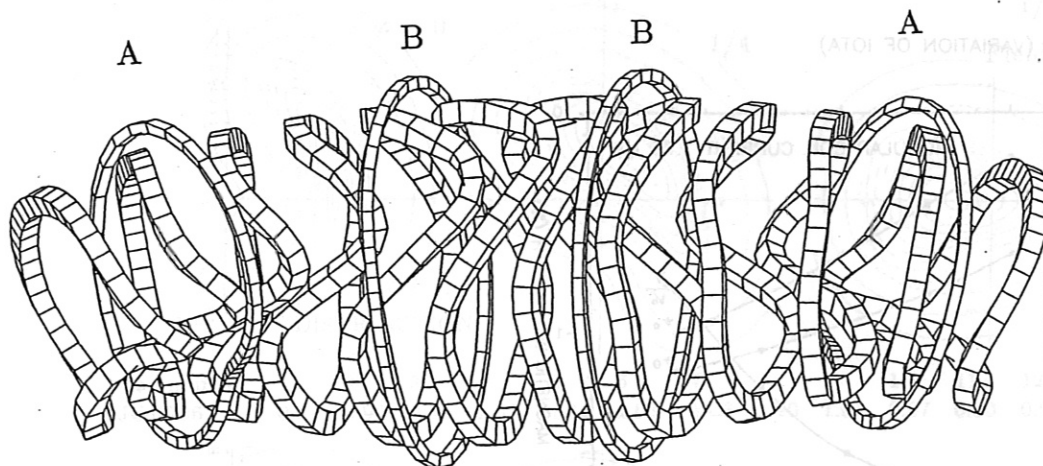
HS5V8   TORUS DAV12R8A SPULEN SP12R8A

Fig. 5 : One field period of HS 5–8 showing modular coils and external planar coils A and B for varying the rotational transform and axis position.

STANDARD CASE
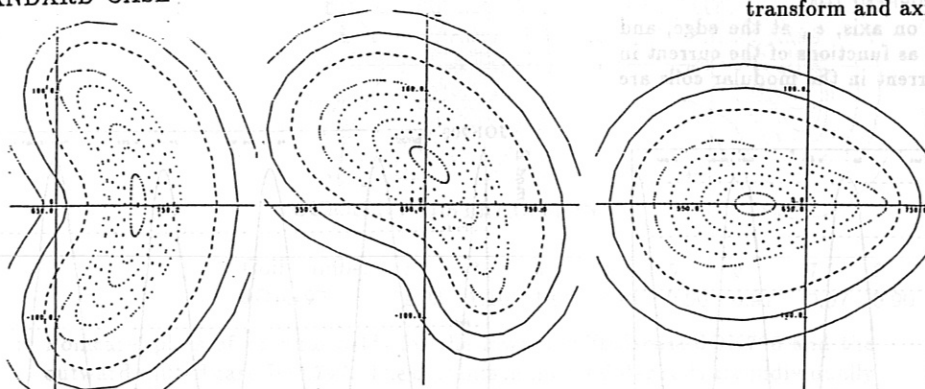
HIGH TRANSFORM
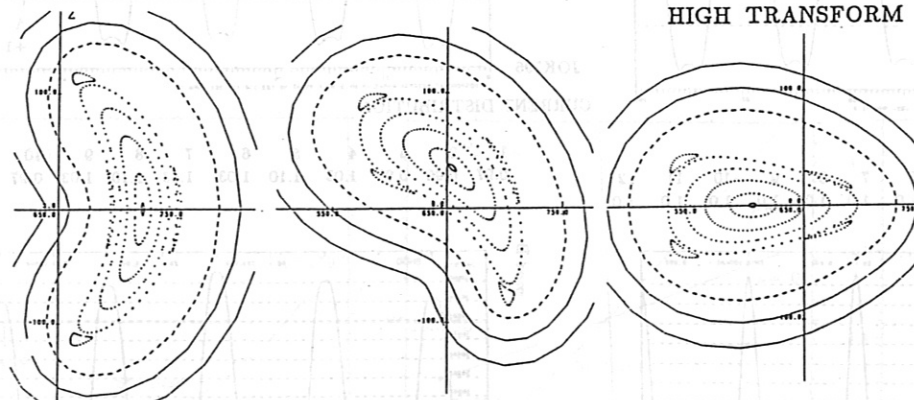
LOW TRANSFORM
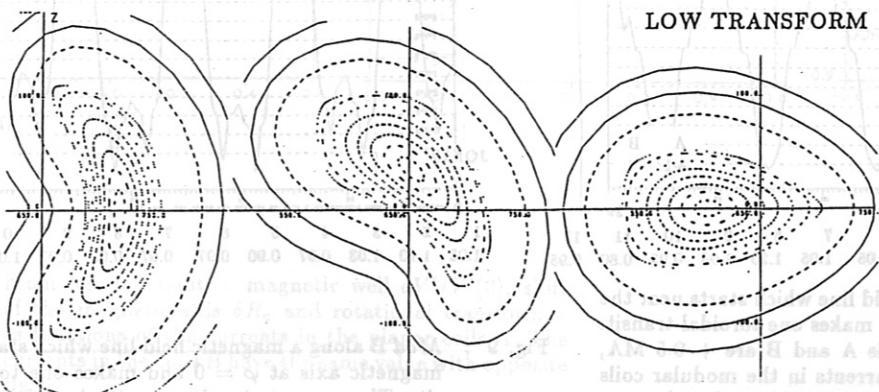
Fig. 6 : Poincare' plots of vacuum fields of HS 5–8. Top: standard case, $t = 1.02 - 1.18$, average plasma radius 70 cm. Middle: high transform, $t = 1.08 - 1.25$, 5/4 islands at the edge. Bottom: low transform, $t = 0.91 \leq 1$.

MODULAR COIL CURRENT 1.75 MA

ROTATIONAL TRANSFORM ℓ

MAGNETIC WELL DEPTH (%)

$\frac{\delta V'}{V_o}$

ℓ_a

ℓ_0

PLANAR COIL CURRENT (MA)
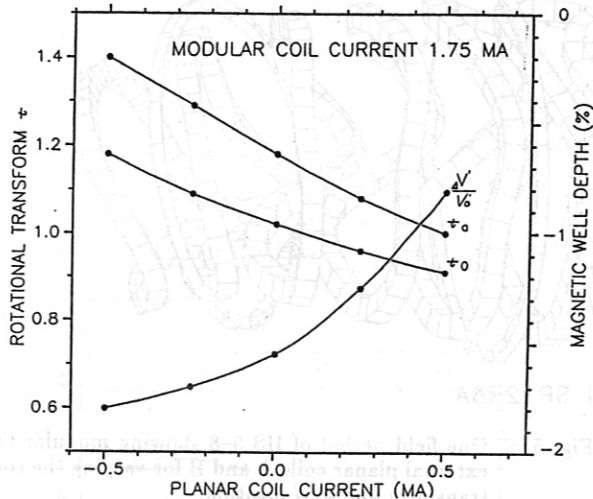
Fig. 7 : Rotational transform ℓ_o on axis, ℓ_a at the edge, and magnetic well $\delta V'/V'(0)$ as functions of the current in the planar coils. The current in the modular coils are 1.75 MA.

mod B

CURRENT DISTRIBUTION

						A	B				
						+1	−1				

Coil number	1	2	3	4	5	6	7	8	9	10	11	12
JOK790	1.0	1.0	1.0	1.0	1.0	1.0	1.0	1.0	1.0	1.0	1.0	1.0

JOK796

mod B

JOK796

CURRENT DISTRIBUTION

1	2	3	4	5	6	7	8	9	10	11	12
0.97	0.90	0.97	1.03	1.10	1.03	1.03	1.10	1.03	0.97	0.90	0.97

mod B

						A	B
						+1	−1

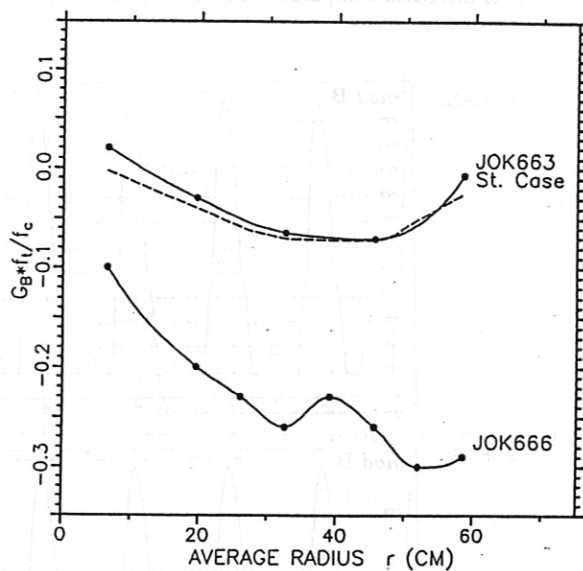| Coil number	1	2	3	4	5	6	7	8	9	10	11	12
JOK794	0.95	0.80	0.95	1.05	1.20	1.05	1.05	1.20	1.05	0.95	0.80	0.95
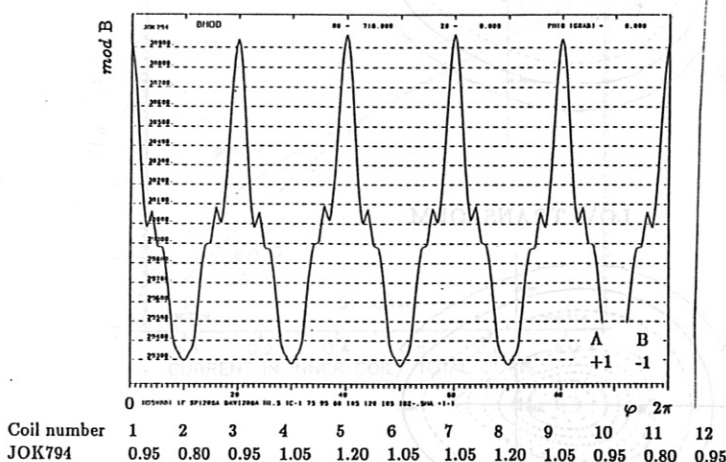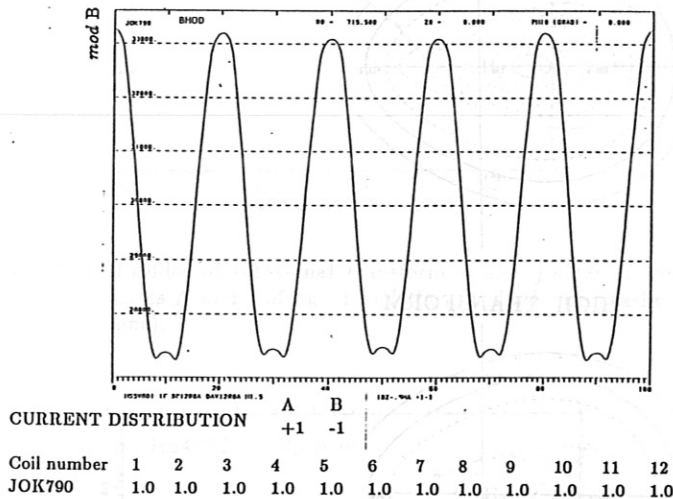
Fig. 8 : *Mod* B along a magnetic field line which starts near the magnetic axis at $\varphi = 0$ and makes one toroidal transit. The currents in planar coils A and B are +−0.5 MA, respectively. On top the currents in the modular coils have their standard value of 1.75 MA, and at bottom they are individually adjusted for reducing the magnetic ripple introduced by the currents in the planar coils. The table 'Current Distribution' shows the relative current value for each coil.

mod B

JOK797

						A	B
						−1	+1

φ 2π

1	2	3	4	5	6	7	8	9	10	11	12
1.03	1.10	1.03	0.97	0.90	0.97	0.97	0.90	0.97	1.03	1.10	1.03
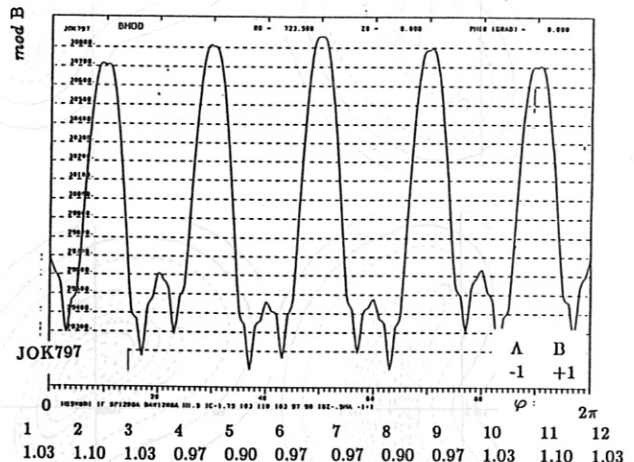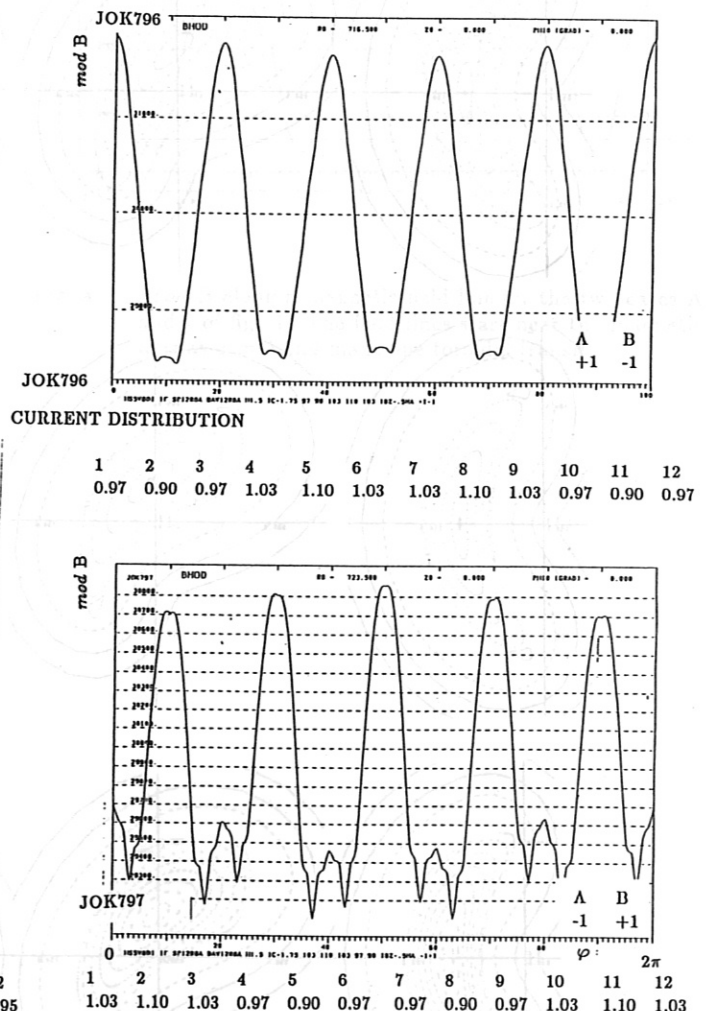
Fig. 9 : *Mod* B along a magnetic field line which starts near the magnetic axis at $\varphi = 0$ and makes one toroidal transit. The currents in planar coils A and B are on top +− 0.5 MA, and at bottom −+ 0.5 MA, respectively. The currents in the modular coils are individually adjusted for reducing the magnetic ripple to about 50%, compared with the uncompensated case.

78

JOK796

$\varphi = 0$

1/4

1/2

Field Period

CURRENT DISTRIBUTION
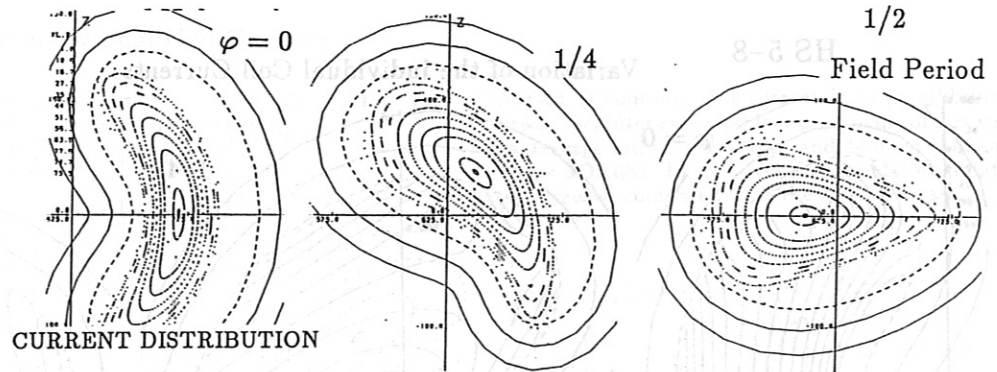
Coil number	1	2	3	4	5	6	7	8	9	10	11	12	A	B
JOK796	0.97	0.90	0.97	1.03	1.10	1.03	1.03	1.10	1.03	0.97	0.90	0.97	+1	-1

JOK797

CURRENT DISTRIBUTION
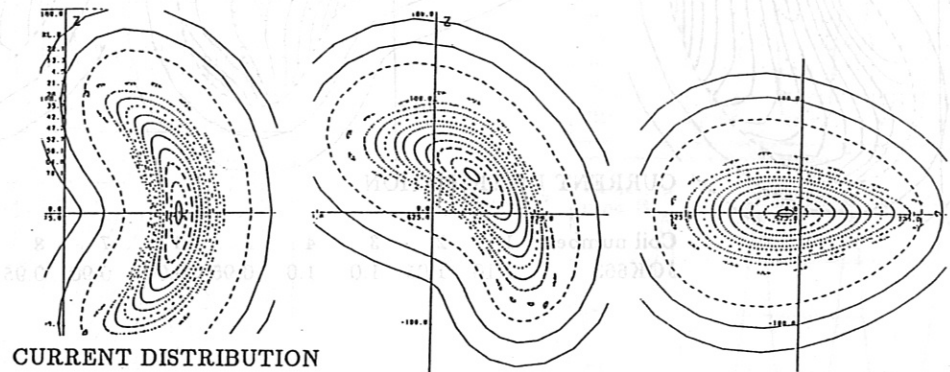
Coil number	1	2	3	4	5	6	7	8	9	10	11	12	A	B
JOK797	1.03	1.10	1.03	0.97	0.90	0.97	0.97	0.90	0.97	1.03	1.10	1.03	-1	+1

Fig. 10 : Poincare' plots of vacuum fields for the inward shifted case JOK796 and the outward shifted case JOK797. The currents in the modular coils are individually adjusted for reducing the magnetic ripple (see table 'Current Distribution').
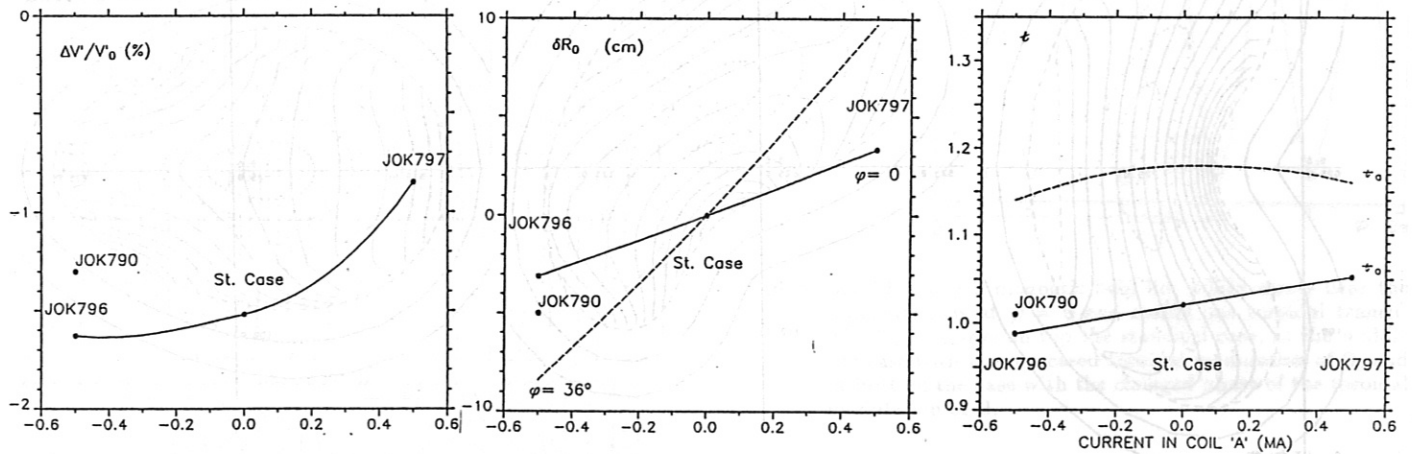
Fig. 11 : From left to right : magnetic well $\delta V'/V'(0)$, shift of the magnetic axis δR_o and rotational transform ι as functions of the currents in the planar coils A. The currents in the coils B have the same value with opposite sign.

HS 5–8   Variation of the individual Coil Currents

$\varphi = 0$ 1/4   JOK663

1/2 Field Period

CURRENT DISTRIBUTION

Coil number	1	2	3	4	5	6	7	8	9	10	11	12
JOK663	1.10	1.05	1.0	1.0	0.95	0.90	0.90	0.95	1.0	1.0	1.05	1.10
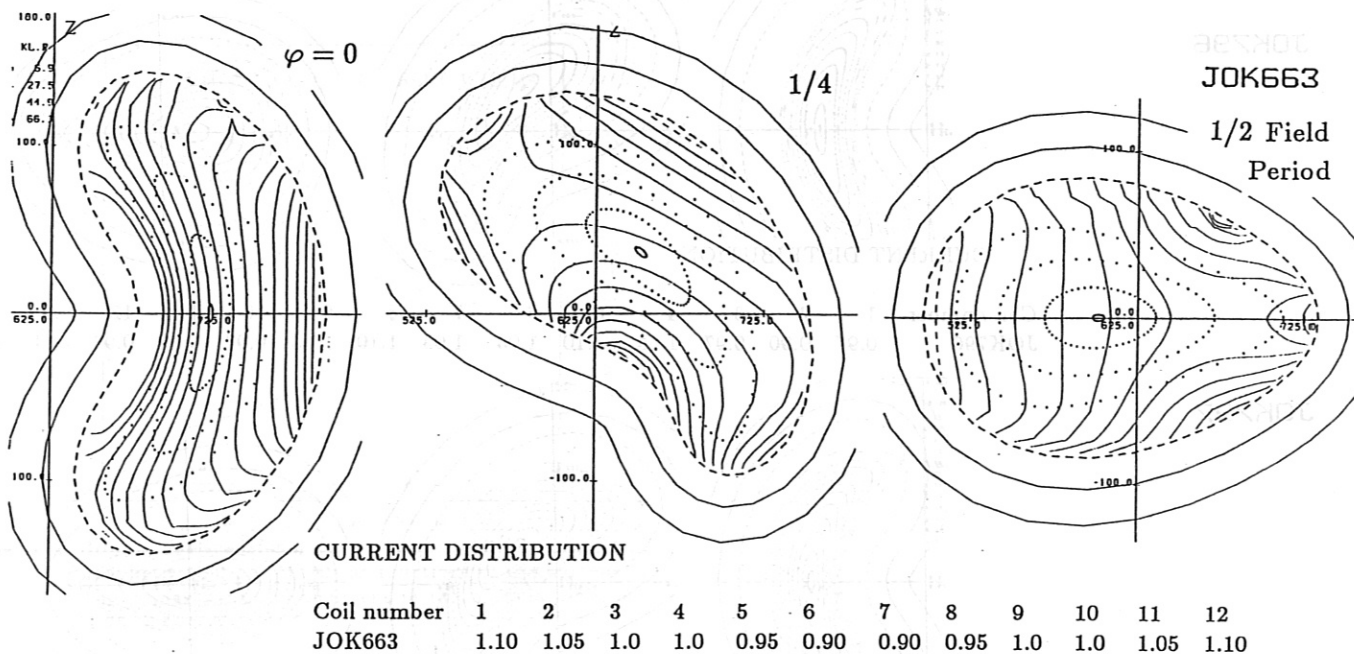
Fig. 12 :   Poincare' plots of vacuum fields and lines of *mod* B = constant
for a case of HS 5–8 with 10% modulation of the coil current,
see table 'Current Distribution'.

$\varphi = 0$ 1/4   JOK666

1/2 Field Period

CURRENT DISTRIBUTION

Coil number	1	2	3	4	5	6	7	8	9	10	11	12
JOK666	0.90	0.95	1.0	1.0	1.05	1.10	1.10	1.05	1.0	1.0	0.95	0.90
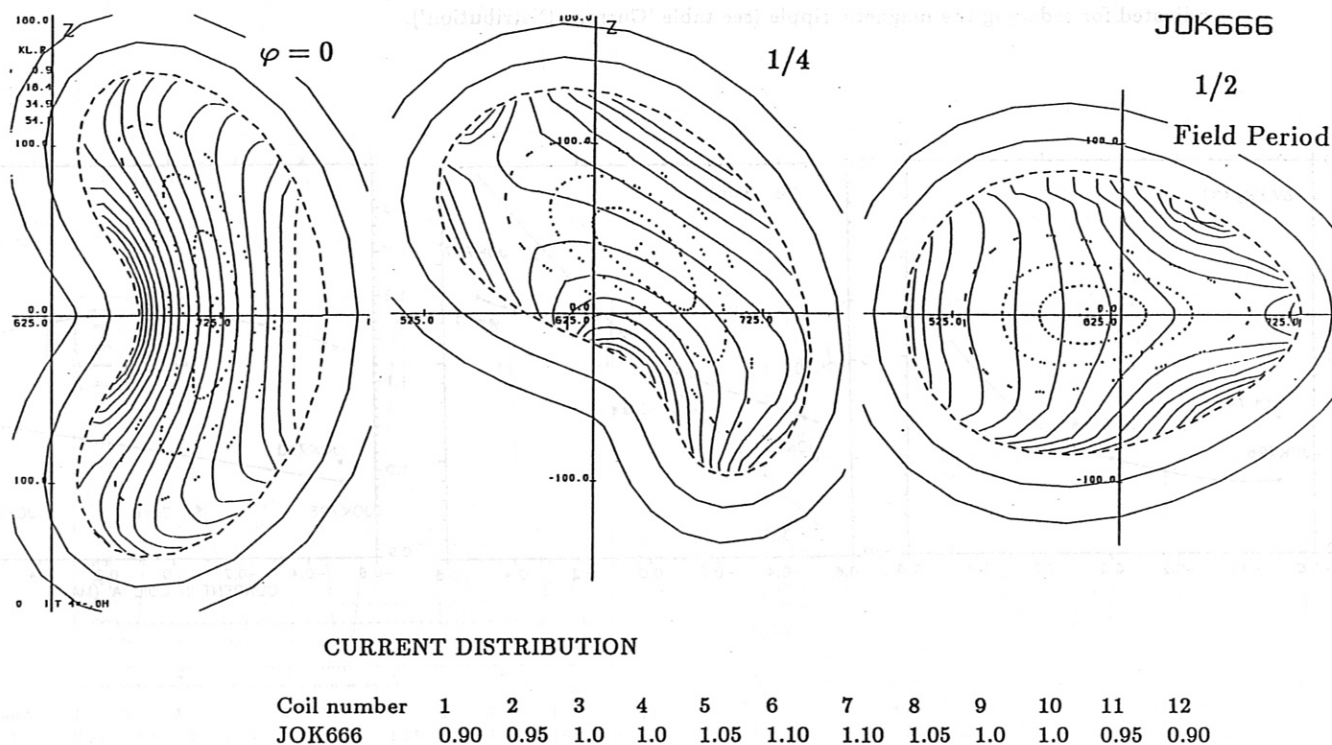
Fig. 13 :   Poincare' plots of vacuum fields and lines of *mod* B =
constant for a case of HS 5–8 with 10% modulation of the
coil current with the opposite sign compared with the case
JOK663 of fig. 12.

80

Fig. 14 :   Constant B contours and current lines (equilibrium and 'Pfirsch - Schlüter currents) in a $\varphi - \theta$ plane of flux surfaces with average radii 6.9 cm (top) and 44.9 cm (bottom) for the case JOK663. In this case the toroidal modulation of B is increased compared with the standard case.
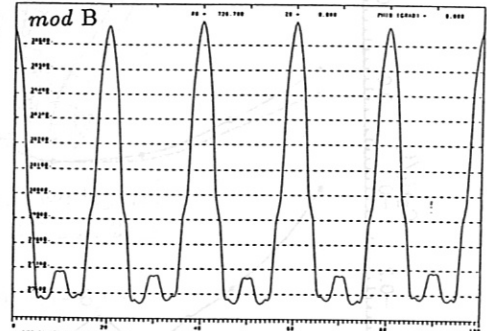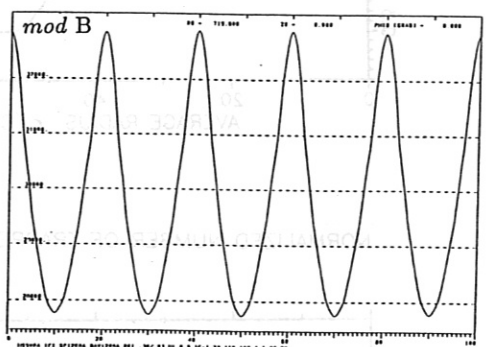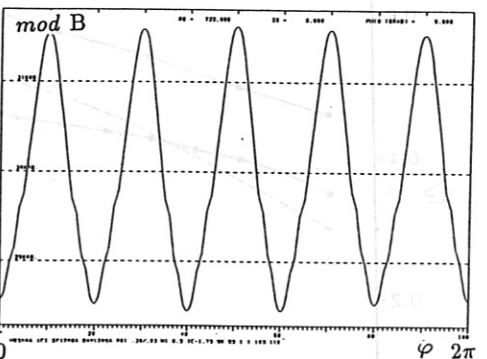
Fig. 16 :   *Mod* B along a magnetic field line which starts near the magnetic axis at $\varphi = 0$ and makes one toroidal transit. The figure shows on top the standard case, at the middle the case with the increased toroidal modulation of B, and at bottom the case with the changed phase of the toroidal modulation of B.

Fig. 15 :   Constant B contours and current lines (equilibrium and 'Pfirsch - Schlüter currents) in a $\varphi - \theta$ plane of flux surfaces with average radii 0.9 cm (top) and 34.9 cm (bottom) for the case JOK666. In this case the phase of the toroidale modulation of B is changed compared with the standard case.

81

BOOTSTRAPCURRENT COEFFICIENT G_B*F_T/F_C

NORMALIZED NUMBER OF TRAPPED PARTICLE f_t/f
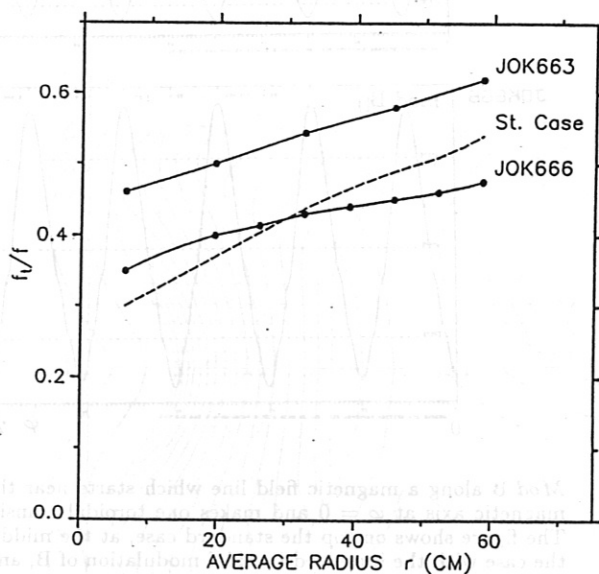
Fig. 17 : Geometrical bootstrap current coefficient $G_b f_t/f_c$ for the lmfp regime and the normalized number of trapped particles f_t/f vs the average radius of the flux surfaces. f_c is the number of circulating particles, $f = f_c + f_t$.
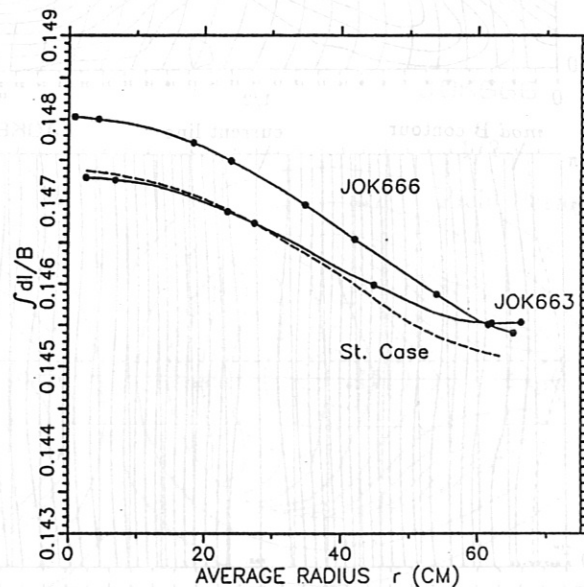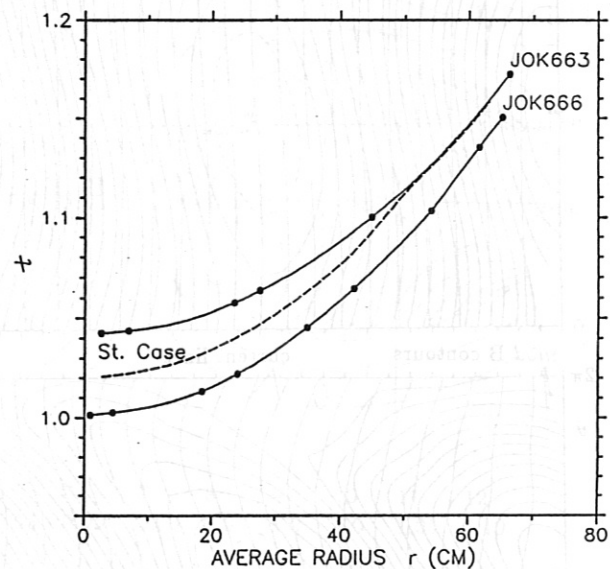
Fig. 18 : Profiles of rotational transform ι and $\int dl/B$ of the cases JOK663, JOK666 and the standard case (dashed line).
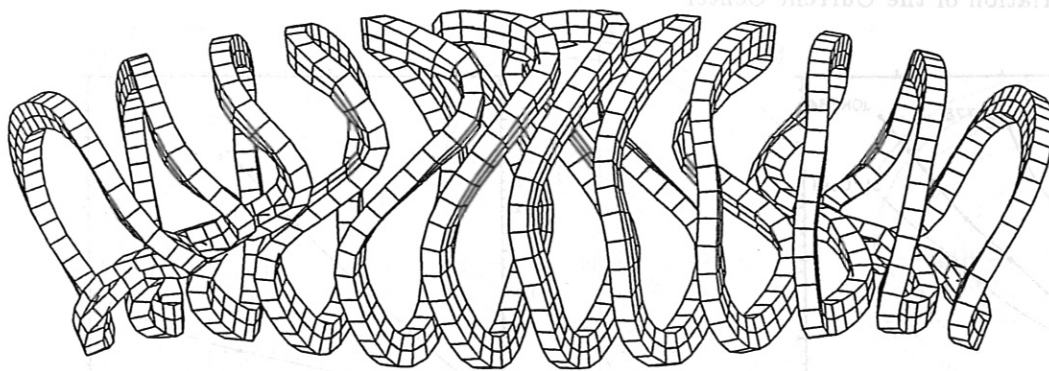
Fig. 19 : One field period of HS 5–8 showing modular coils with two layers.
In this case the coil height is extented from 20 cm to 27 cm; 2cm
radially inwards and 5 cm radially outwards.

HS5V8D   TORUS DAV12R8A SP12R8A H0 13/14 H1–6/8
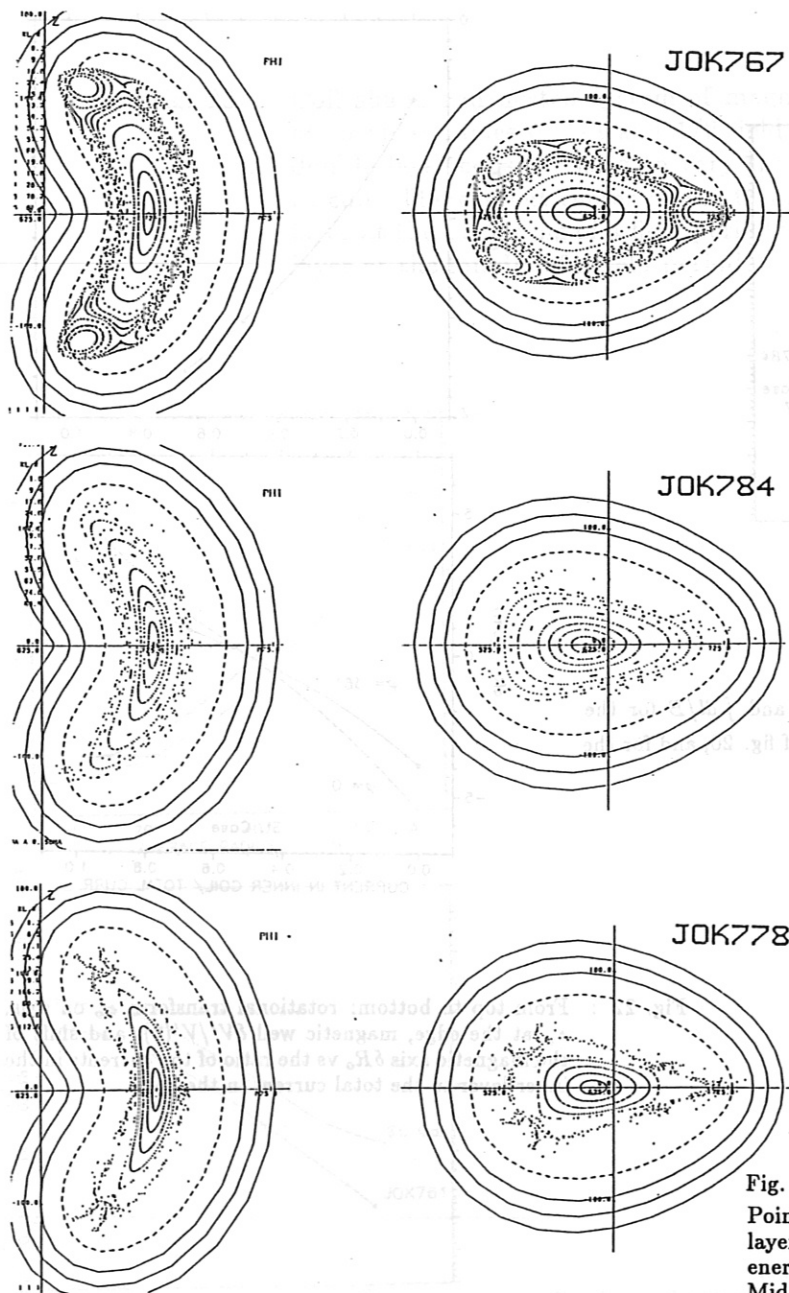
Fig. 20 :
Poincaré plots of vacuum fields of HS 5–8 using double
layer coils. Top: only the outer layers of the coils are
energized, $\iota = 0.965 - 1.01$, low shear and magnetic well.
Middle: 1/3 of the current flows in the outer layer, 2/3
in the inner layer, $\iota = 1.035 - 1.25$, 5/4 islands at the
edge. Bottom: only the inner parts of the coils are used,
$\iota = 1.08 - 1.25$, reduced minor radius.
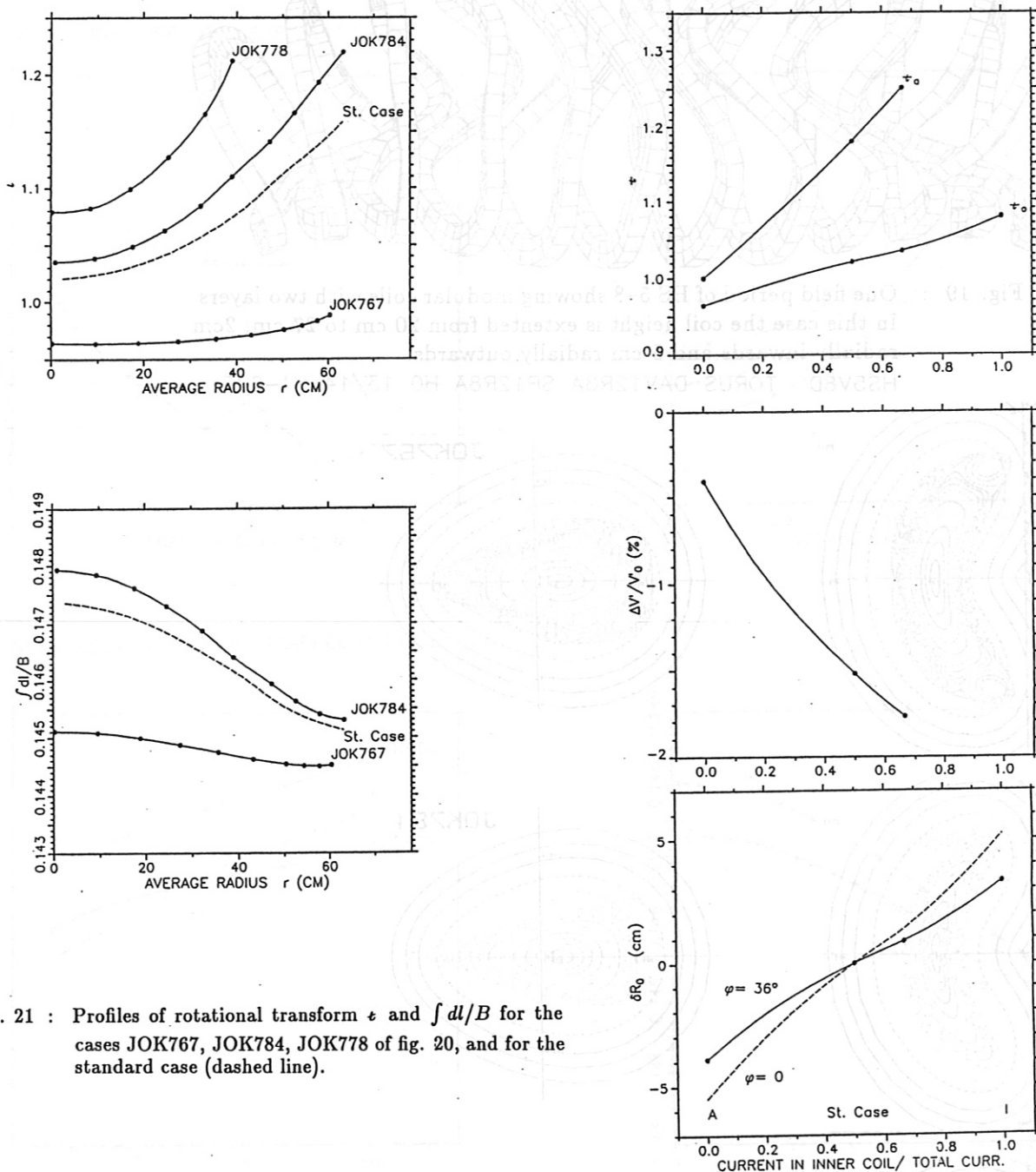
Fig. 21 : Profiles of rotational transform ι and $\int dl/B$ for the
cases JOK767, JOK784, JOK778 of fig. 20, and for the
standard case (dashed line).

Fig. 22 : From top to bottom: rotational transform ι_o on axis,
ι_a at the edge, magnetic well $\delta V'/V'(0)$, and shift of
the magnetic axis δR_o vs the ratio of the currents in the
inner layer to the total current in the coils.
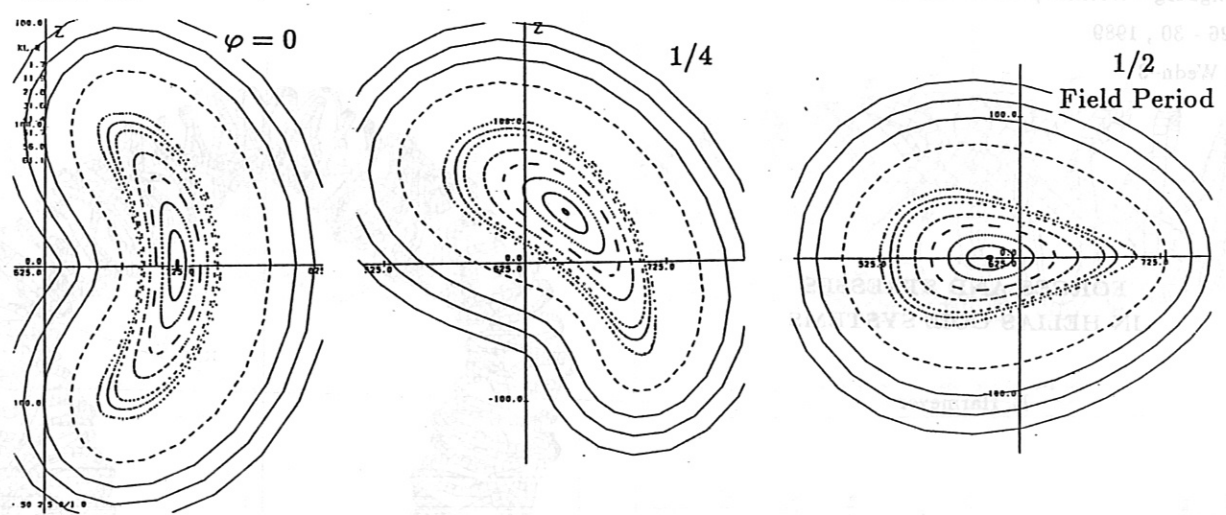
Fig. 23 : Coil shape and nested system of magnetic surfaces for HS 5-8
at toroidal angles 0, 1/4 and 1/2 field period. In this case the
double layer coils are used to vary the current center from coil
to coil. The current center moves from the middle of the outer
layer at the beginning of a field period to the middle of the inner
layer at the middle of a field period.
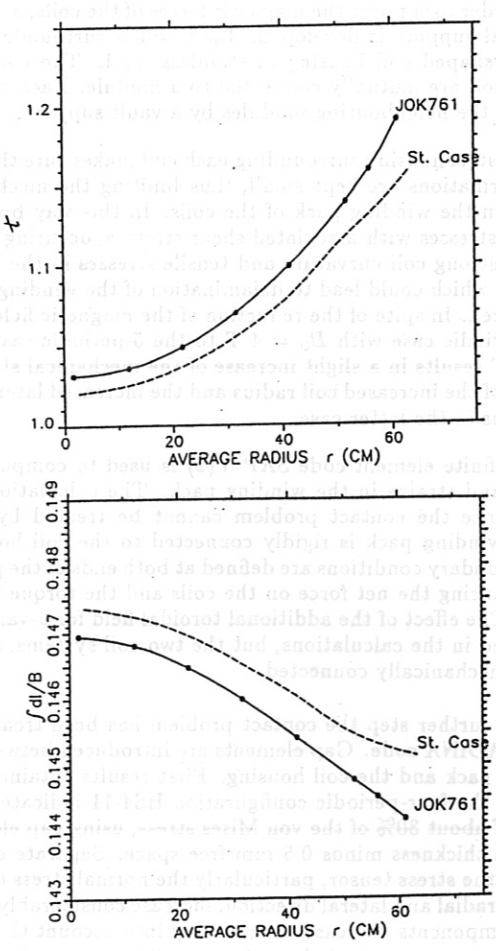
Fig. 24 : Profiles of rotational transform ι and $\int dl/B$ for the
case JOK761 of fig. 23 and for the standard case
(dashed line).

FORCES AND STRESSES
IN HELIAS COIL SYSTEMS

E. Harmeyer

- Force density distributions in the coils
- Net force of coils in a coil arrangement
- Numerical stress calculations

Coil configuration HELIAS 5-8

HS5–8.A+ZF   TOP VIEW   Z=0.0 TX=0. Y=−90. TX=−800. S=1.000 D=0.0001

$R_0 = 6.5$ m

EBH391   13.04.89
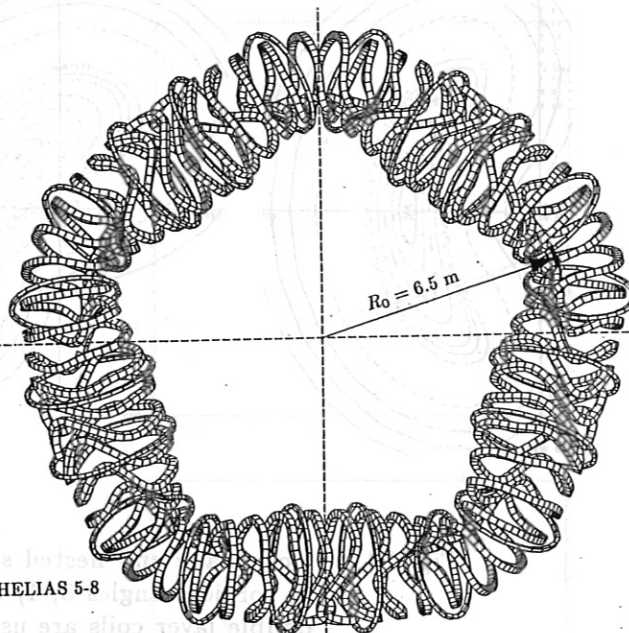
Forces and Stresses in HELIAS Coil Systems

Numerical calculations of the distribution of magnetic forces and mechanical stresses are mainly concentrated on the 5-period configuration HS5-8. The calculations of the magnetic forces are performed with the EFFI code. Mechanical stresses and strains are computed with the SAPV(2) and ADINA programme systems.

Magnetic forces:

The distribution of the magnetic forces in the coils is inhomogeneous because of the different local coil curvatures and the slightly helical arrangement of the coils. The average value of the magnetic force density over the cross-section of the non-planar coils consist of both a radial and a lateral force density component which vary along the circumference of the coils. The variation of the lateral force density component largely depends on the lateral excursion of the coil under consideration and is not very strongly influenced by the remainder of coils in the system. The coils generally exhibit overturning moments about the horizontal and the vertical axis, and a torque about the coil axis (magnetic axis), the overturning moments, by the magnitude, prevailing. The volume integral of the magnetic force densities, in general, results in a net force for each coil in the coil assembly. Because of the slight helicity of the coil arrangement the vector of the coil net forces is of helical type and varies considerably in magnitude. The net force vector for the individual coils may even be directed radially outwardly. For a whole toroidal field period the resulting net force vector is directed towards the torus centre because of the toroidal arrangement. In addition, there is a torque on the coil assembly of the field period, in the direction of this vector.

For experimental flexibility it is necessary to vary the rotational transform in the W VII-X experiment. In the five-period configurations this variation is achieved by superposed external coils which generate about 10% of the modular field, thus allowing the rotational transform to be varied by about 25%. The different currents in the external coils for ι-variation causes different force density distributions in the modular and also in the external coils. The lateral component of the resulting net force vector in some cases even changes its direction when varying the rotational transform.

Mechanical stresses:

In order to support the magnetic forces of the coils, a scheme of mutual support is developed. Each coil is surrounded by a suitably shaped coil housing of stainless steel. The coils of a field period are mutually connected to a module. Each module supports the neighbouring modules by a vault support.

The steel housing surrounding each coil makes sure that the coil deformations are kept small, thus limiting the mechanical stresses in the winding pack of the coils. In this way both the bending stresses with associated shear stresses, occuring in the areas of strong coil curvature and tensile stresses in the lateral direction which could lead to delamination of the winding pack, are reduced. In spite of the reduction of the magnetic field from the 4-periodic case with $B_0 = 4$ T to the 5-periodic case with $B_0 = 3$ T results in a slight increase of the mechanical stresses, because of the increased coil radius and the increased lateral coil excursions in the latter case.

The finite element code SAP V(2) is used to compute the stresses and strains in the winding pack. The calculations are linear, since the contact problem cannot be treated by SAP V. The winding pack is rigidly connected to the coil housing. Fixed boundary conditions are defined at both ends of the period thus balancing the net force on the coils and the torque in one period. The effect of the additional toroidal field for ι-variation is included in the calculations, but the two coil systems, so far, are not mechanically connected.

In a further step the contact problem has been treated using the ADINA code. Gap elements are introduced between the winding pack and the coil housing. First results obtained with coil 1 of the four-periodic configuration HS4-11 indicate an increase of about 30% of the von Mises stress, using gap elements of 5 mm thickness minus 0.5 mm free space. Separate components of the stress tensor, particularly the normal stress components in radial and lateral direction, increase considerably; while other components decrease when taking into account these gap elements as more realistic boundary conditions.

HS4V11.C C1-12 Z-45.TX-05. Y-90. TX--800. S-3.000 D-0.0001

HS5-8.A C1-12 Z-36.TX-06.5Y-90. TX--800. S-3.000 D-0.0001

HS4V11.C C1-12 Z-45.TX-05. Y-180.TX--800. S-3.000 D-0.0001
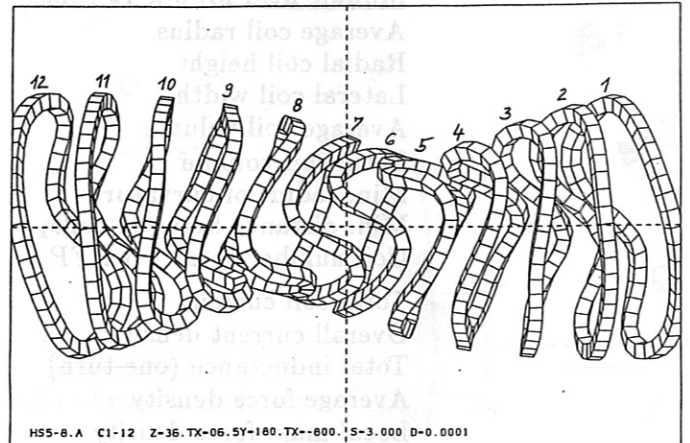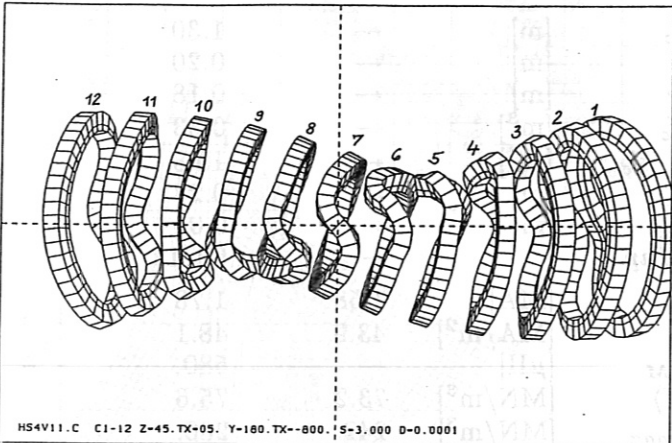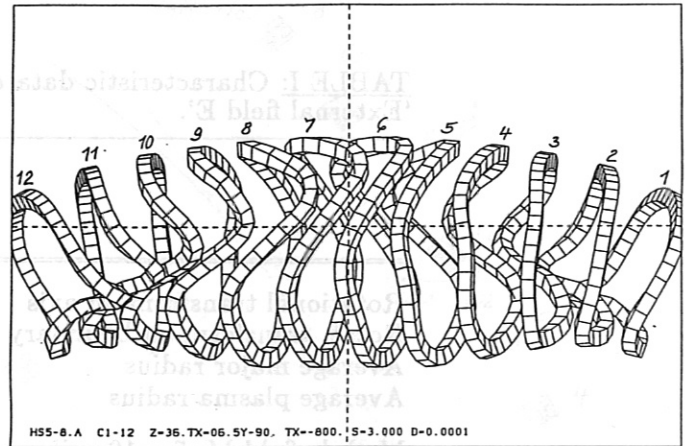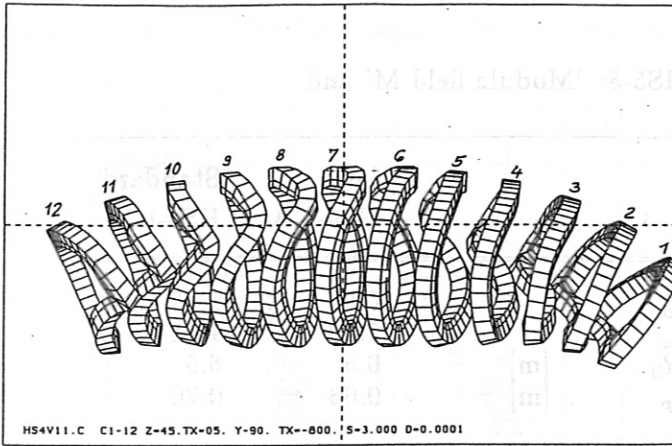
Coil configuration HS4V11: One field period

HS5-8.A C1-12 Z-36.TX-06.5Y-180.TX--800. S-3.000 D-0.0001

Coil configuration HS5-8: One field period

HS5-8A (VARIATION OF IOTA)
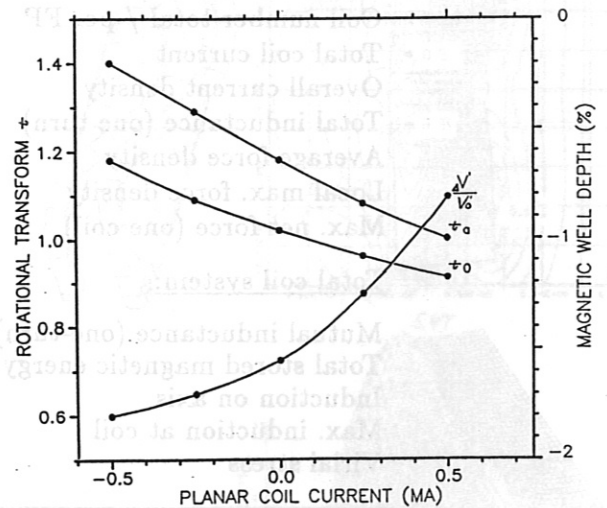
t_o on axis, t_a at the edge, and the magnetic well $\Delta V'/V_0'$ as functions of the current in the planar coils. The current in the modular coils is 1.75 MA.

87

TABLE I: Characteristic data of HS5-8: 'Module field M' and 'External field E'.

			low-τ HS5-8.A	Standard HS5-8.B
Rotational transform on axis	τ_o		0.91	1.02
Rotat. transform on boundary	τ_a		1.00	1.18
Average major radius	R_0	[m]	6.5	6.5
Average plasma radius	r_p	[m]	0.66	0.70
Module field M: 5 x 12 coils				
Average coil radius	r_c	[m]	←	1.30
Radial coil height	t	[m]	←	0.20
Lateral coil width	w	[m]	←	0.18
Average coil volume	V_c	[m^3]	←	0.33
Total coil volume	$n \cdot V_c$	[m^3]	←	19.8
Min. radius of curvature	ρ_c	[m]	←	0.28
Min. distance between coils	Δ_c	[m]	←	0.04
Coil number total / per FP	n/np		←	60/12
Total coil current	I_c	[MA]	1.58	1.73
Overall current density	j_c	[MA/m^2]	43.9	48.1
Total inductance (one-turn)	L_M	[μH]	←	580.
Average force density	$\langle f \rangle$	[MN/m^3]	73.2	75.6
Local max. force density	f_{max}	[MN/m^3]	242.	280.
Max. net force (one coil)	F_{res}	[MN]	3.8	3.9
External field E: 5 x 4 coils				
Average coil radius	r_c^E	[m]	←	1.55
Radial coil height	t^E	[m]	←	0.10
Lateral coil width	w^E	[m]	←	0.10
Average coil volume	V_c^E	[m^3]	←	0.104
Total coil volume	$n^E \cdot V_c^E$	[m^3]	←	2.08
Min. radius of curvature	ρ_c^E	[m]	←	0.52
Coil number total / per FP	n^E/np^E		←	20/4
Total coil current	I_c^E	[MA]	0.46	0.
Overall current density	j_c^E	[MA/m^2]	46.	0.
Total inductance (one-turn)	L^E	[μH]	178.	0.
Average force density	$\langle f^E \rangle$	[MN/m^3]	18.7	0.
Local max. force density	f_{max}^E	[MN/m^3]	112.	0.
Max. net force (one coil)	F_{res}^E	[MN]	0.78	0.
Total coil system:				
Mutual inductance (one-turn)	M_{ME}	[μH]	167.	0.
Total stored magnetic energy	W	[GJ]	0.86	0.87
Induction on axis	B_o	[T]	3.0	3.0
Max. induction at coil	B_{max}	[T]	5.5	5.8
Virial stress	σ_V	[MPa]	39.5	39.7(44.)

Coil configuration HS5-8: Magnetic field distribution

Coil No.

$R_0 = 6.5$ m

$\varphi = 36°$

$\varphi = 0°$

Coil configuration HELIAS 5-8

Section $z = 0.0$

Coil 6

Coil 1 and 60

Coil 1

0 T

0 T

Coil 60

5.4 T

5.4 T

5.2 T

5.4 T

89

$$\vec{f}_E = (f_R, f_S, 0)$$

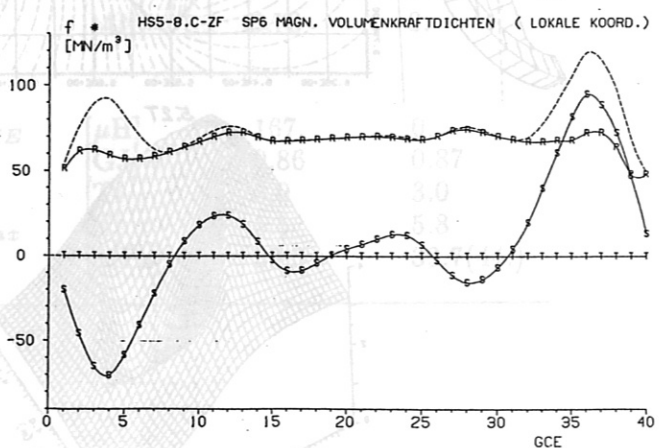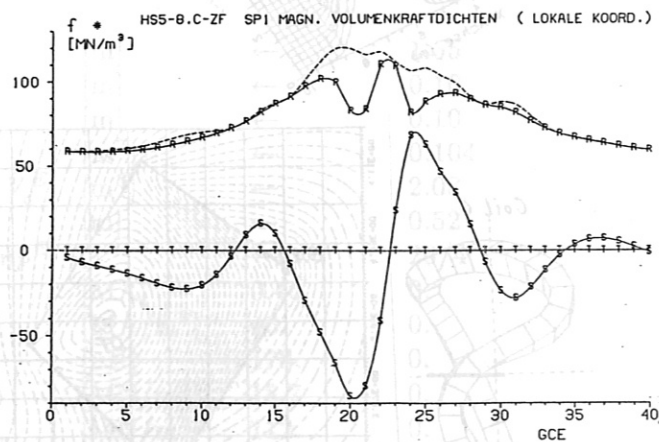$$\vec{f}_E = \frac{1}{V_E} \int_{V_E} \vec{j} \times \vec{B} \, dV$$
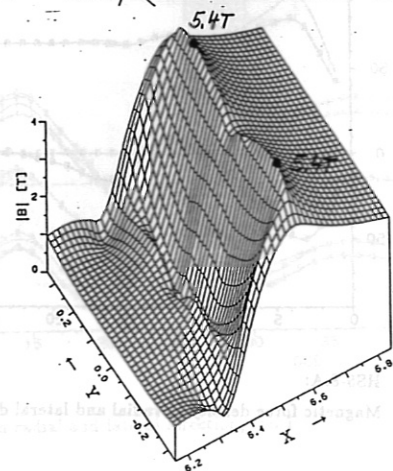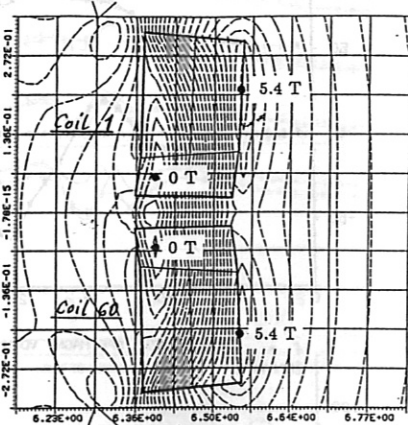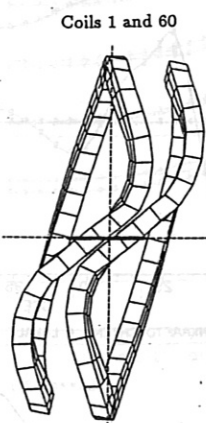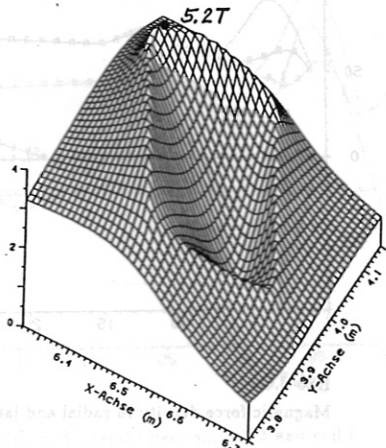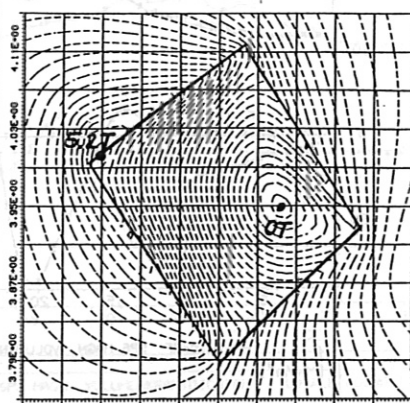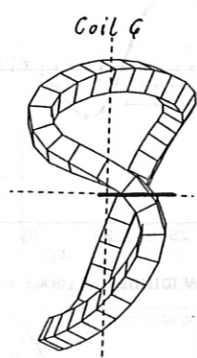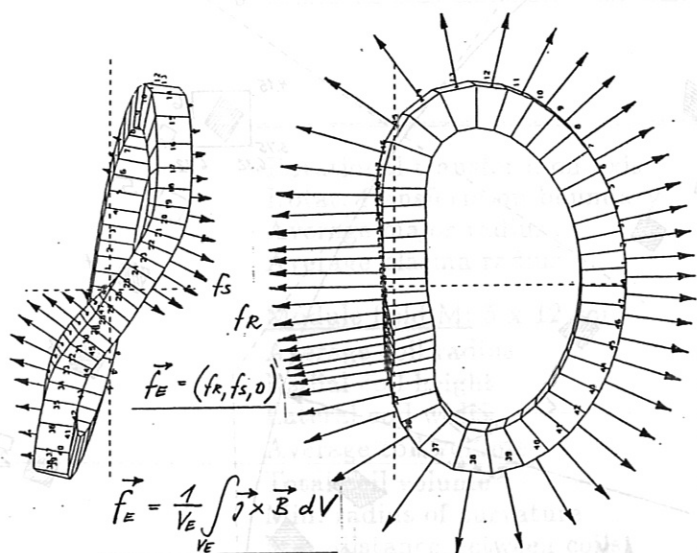
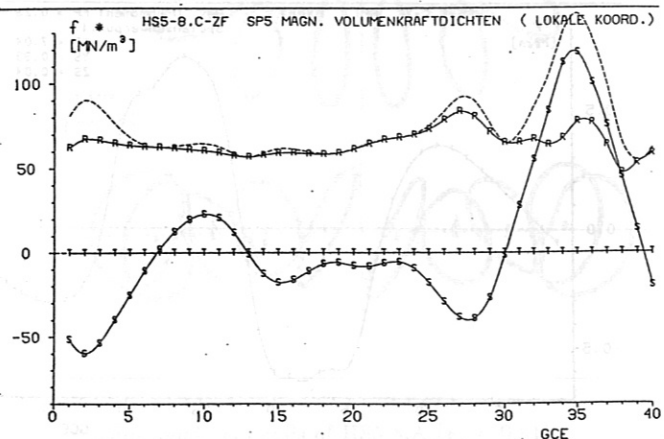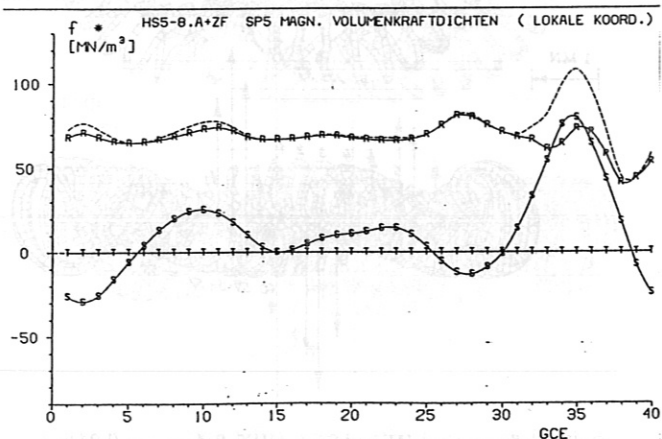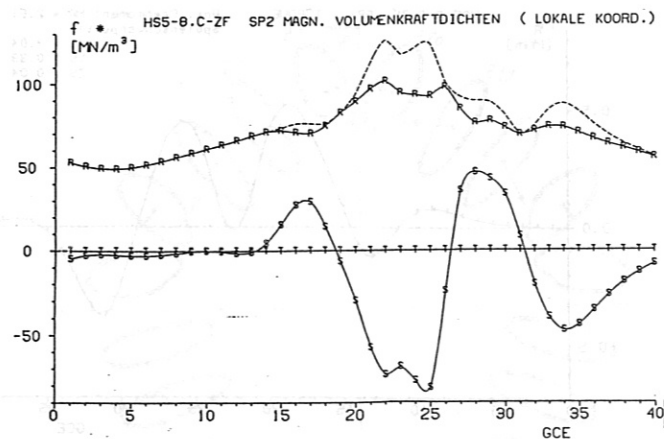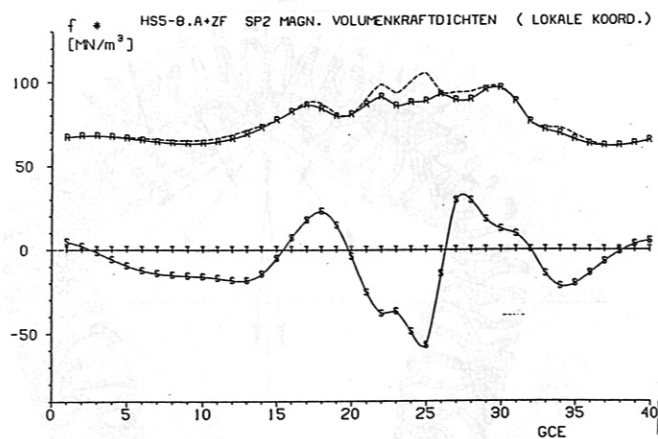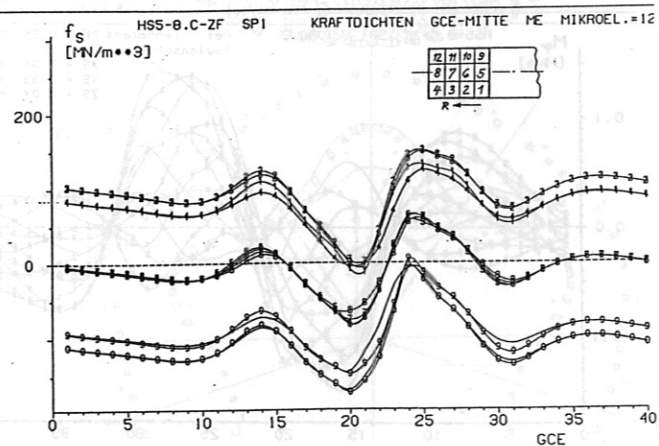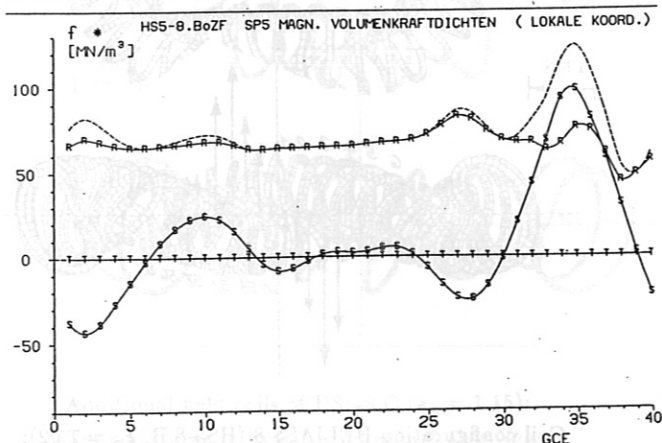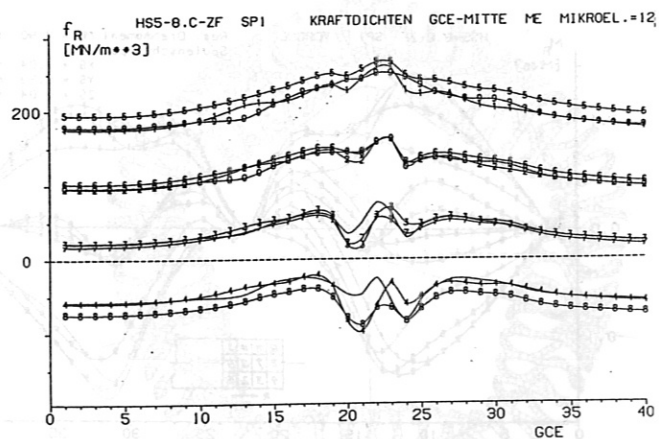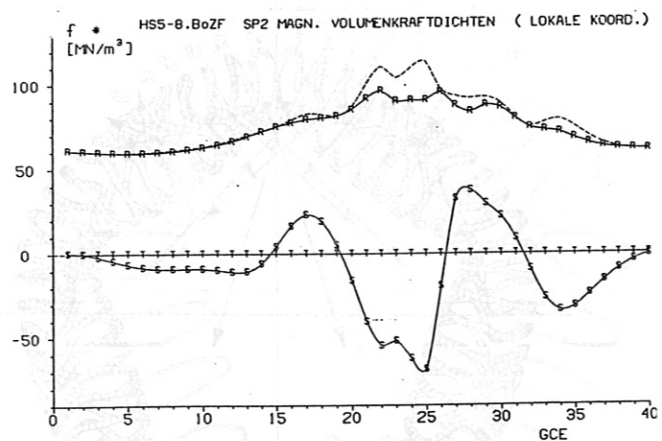HELIAS 4-5 : Magnetic force density in radial and lateral direction, Coil 1.
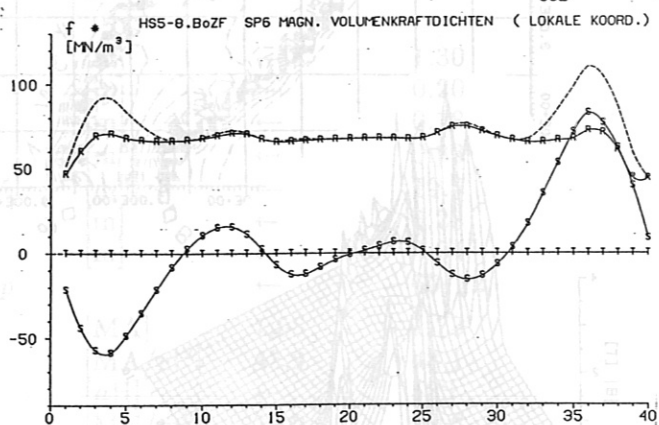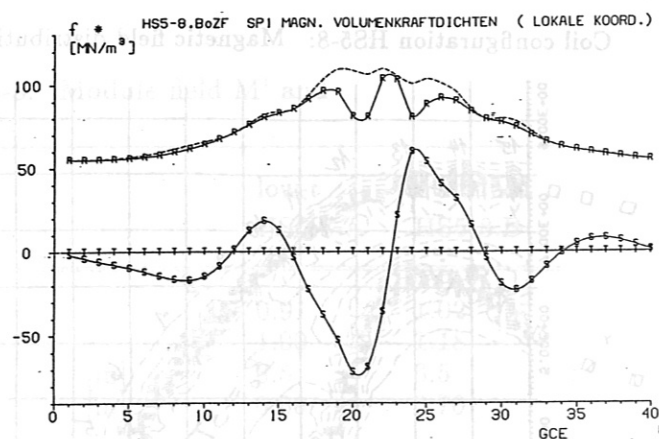
HS5-8.B:
Magnetic force density in radial and lateral direction, coil 1 and coil 6.
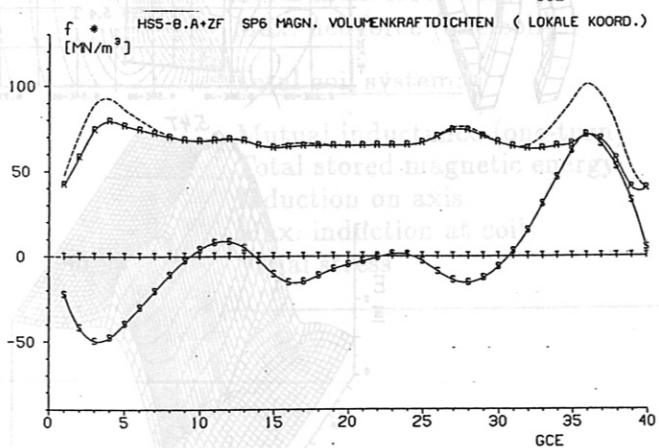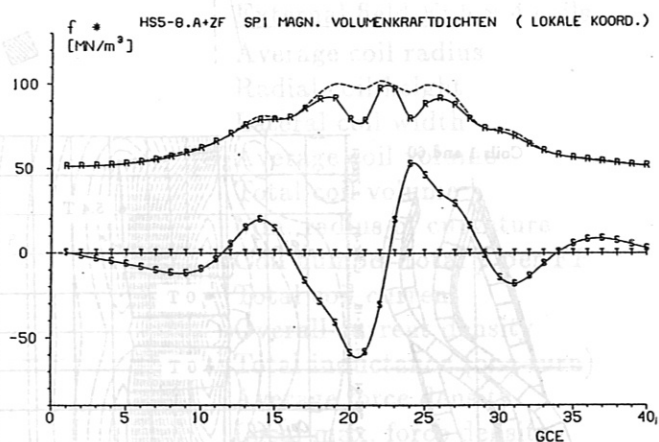
HS5-8.A:
Magnetic force density in radial and lateral direction, coil 1 and coil 6.

HS5-8.C:
Magnetic force density in radial and lateral direction, coil 1 and coil 6.

HS5-8.A:
Magnetic force density in radial and lateral direction, coil 2 and coil 5.

HS5-8.C:
Magnetic force density in radial and lateral direction, coil 2 and coil 5.

HS5-8.B:
Magnetic force density in radial and lateral direction, coil 2 and coil 5.

HS5-8.C:
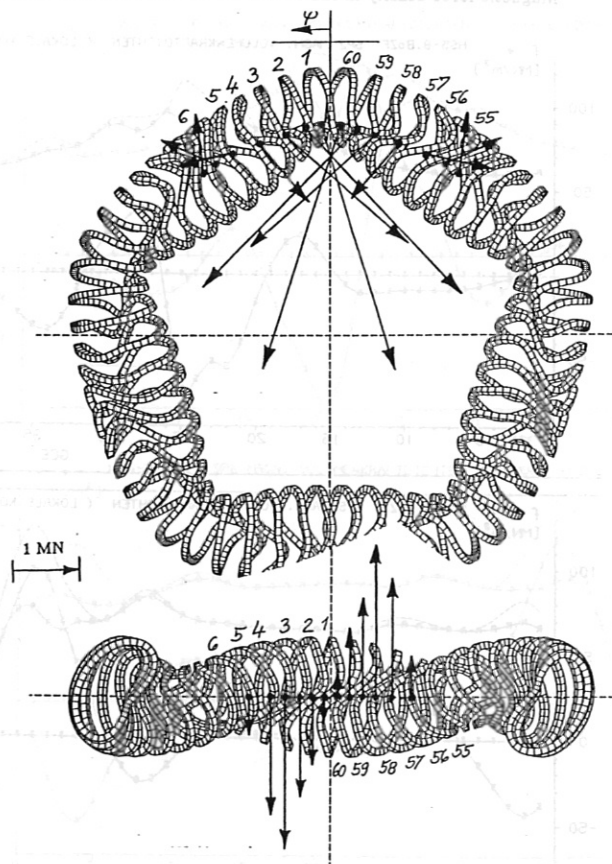Magnetic force densities in radial and lateral direction, coil 1.
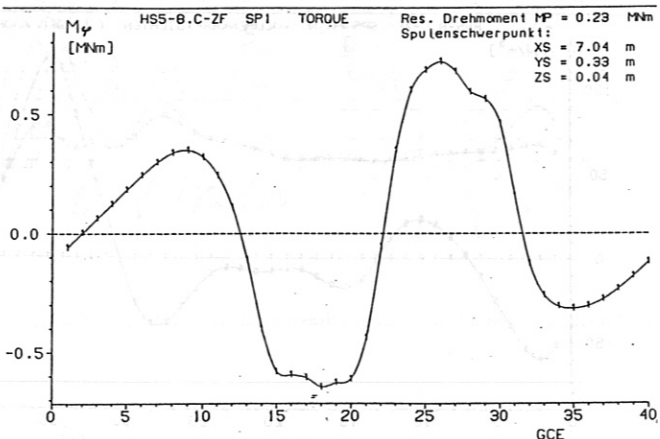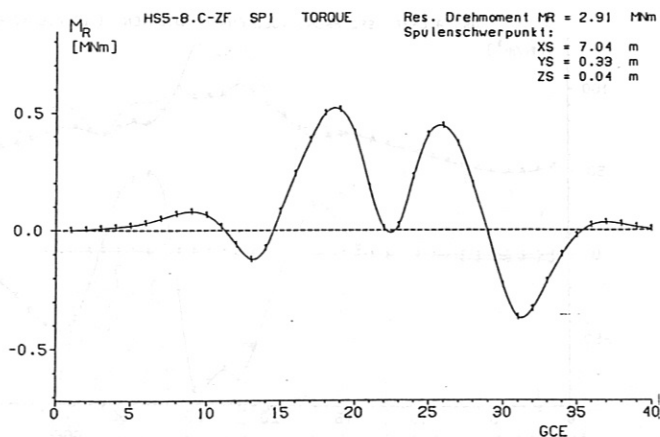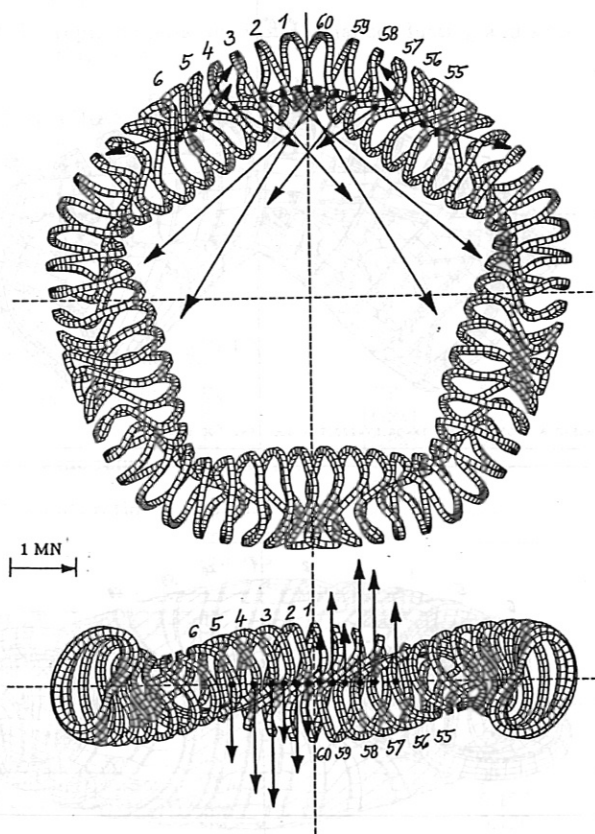
HS5-8.C: Torque on coil 1 about the R-axis and φ-axis.
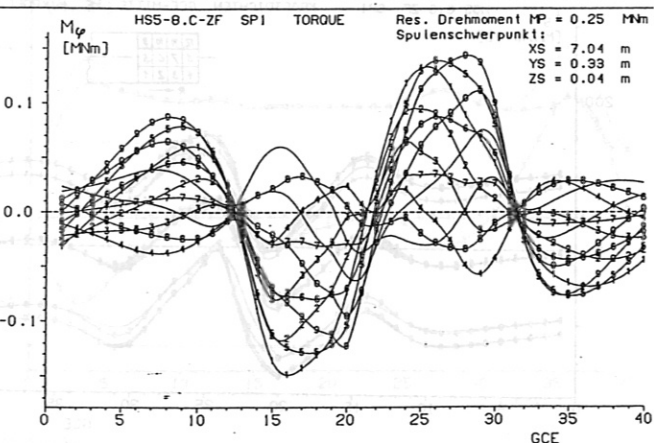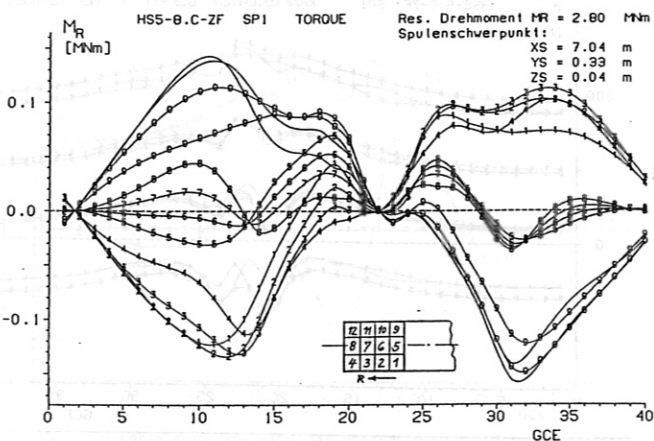
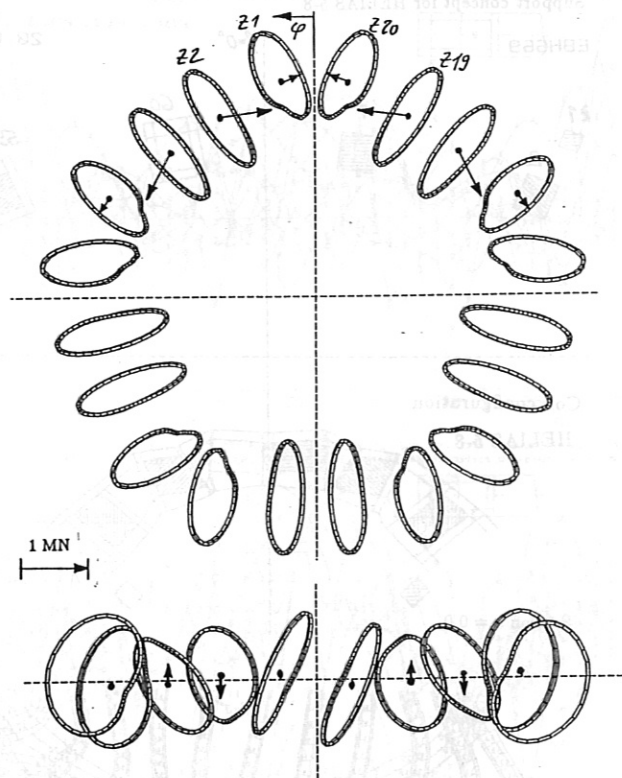HS5-8.C: Torque on coil 1 about the R-axis and φ-axis.
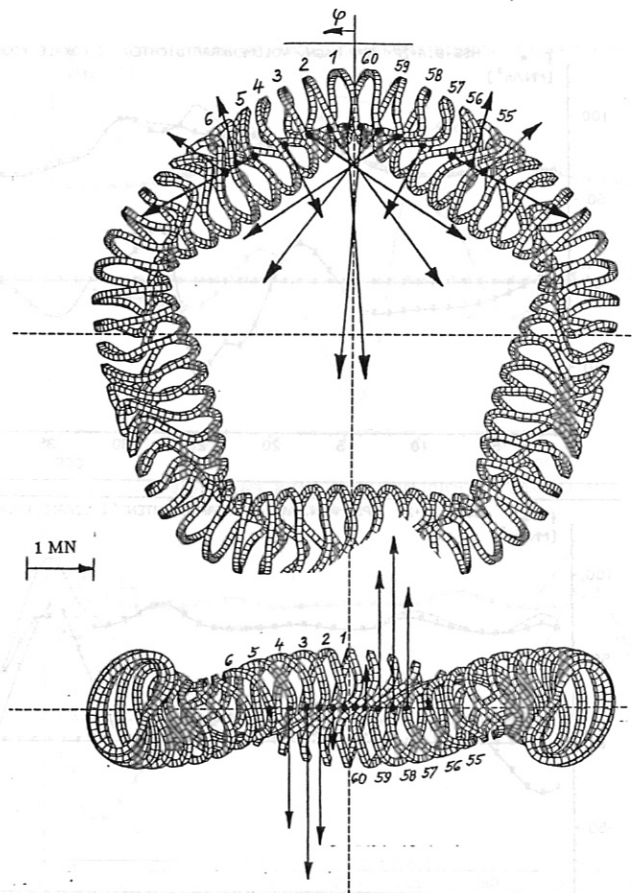
Coil configuration HELIAS5-8 (HS5-8.A, $t_o = 0.91$):
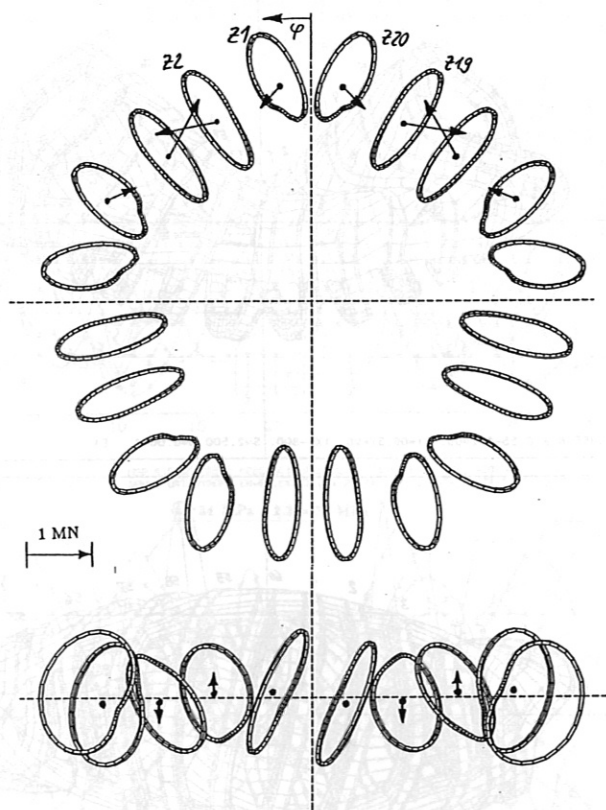Net coil forces in radial and vertical direction.

Coil configuration HELIAS5-8 (HS5-8.B, $t_o = 1.02$):
Net coil forces in radial and vertical direction.
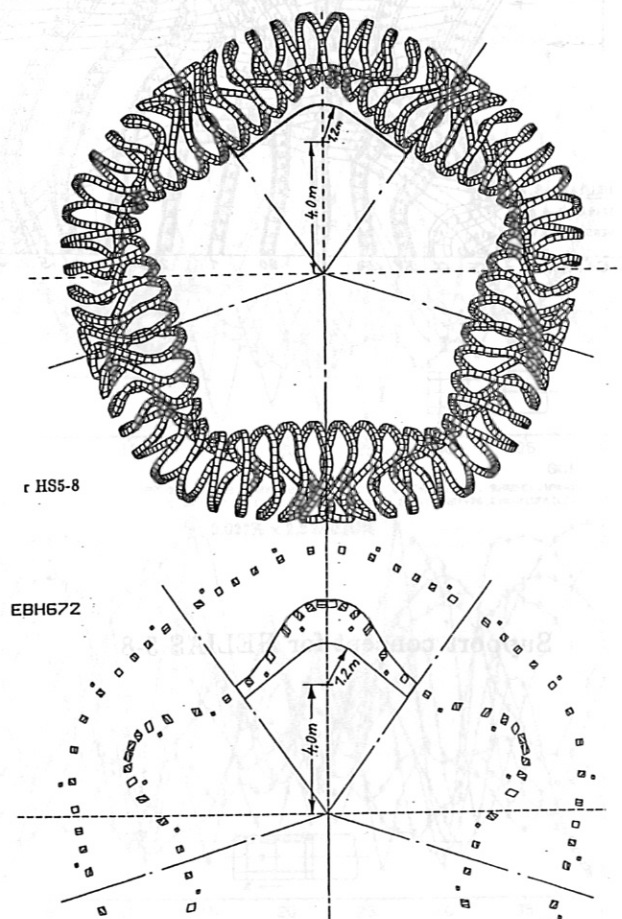
92

Coil configuration HELIAS5-8 (HS5-8.C, $t_o = 1.15$):
Net coil forces in radial and vertical direction.

Additional field coils of HS5-8.A ($t_o = 0.91$):
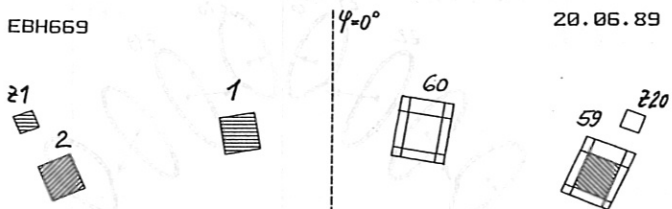Net coil forces in radial and vertical direction.

Additional field coils of HS5-8.C ($t_o = 1.15$):
Net coil forces in radial and vertical direction.
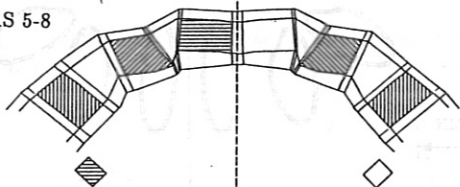

Support concept for HELIAS 5-8
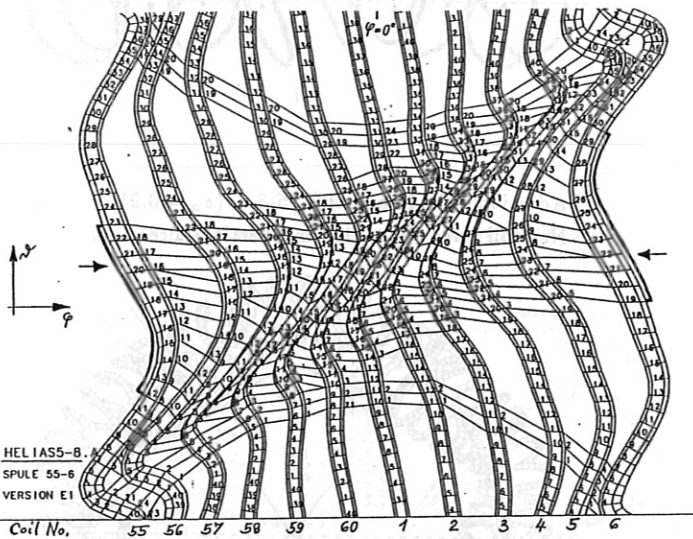
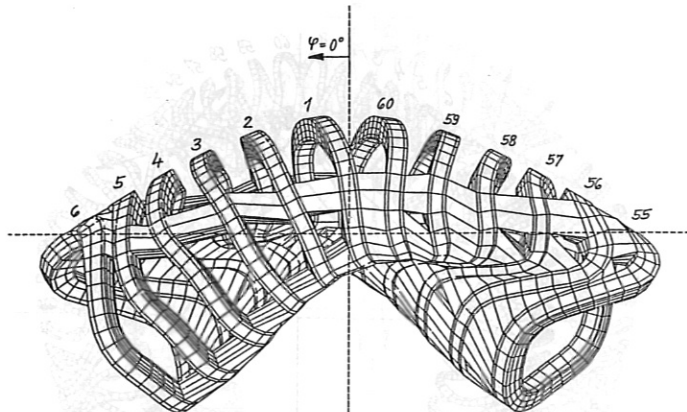Support concept for HELIAS 5-8

EBH669 $\varphi=0°$ 20.06.89

Coil configuration

HELIAS 5-8

Section $z = 0.0$
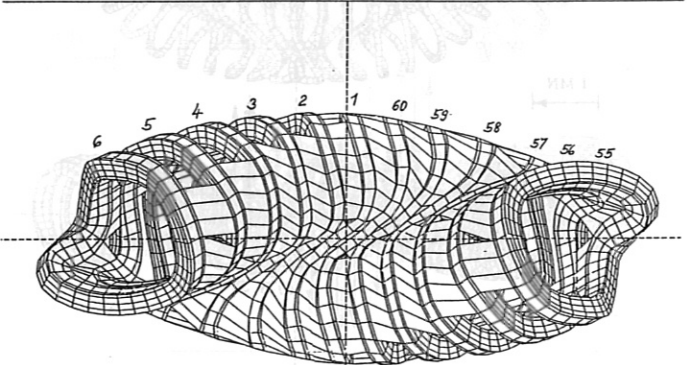
HELIAS5-8.A
SPULE 55-6
VERSION E1

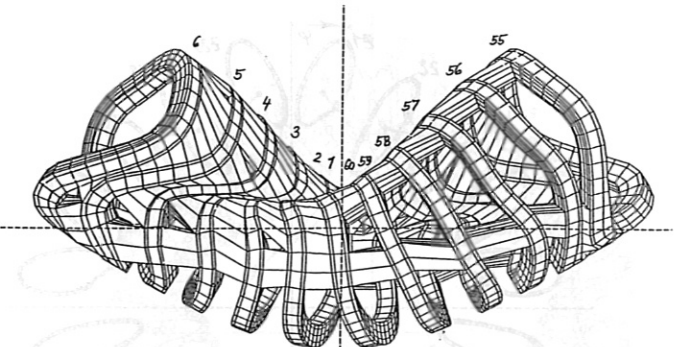Coil No.   55 56 57 58 59 60 1 2 3 4 5 6
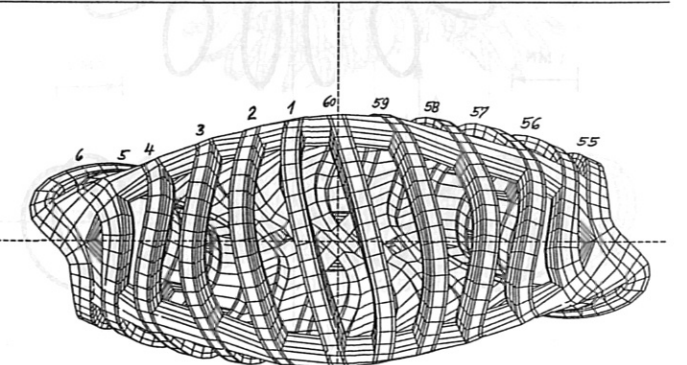
Support concept for HELIAS 5-8

HS5-8.A C.55-6 Z=00. TX=06.5Y=270.TX=-800. S=2.500 D=0.0001   E1

HS5-8.A C.55-6 Z=00. TX=06.5Y=00. TX=-800. S=2.500 D=0.0001   E1

HS5-8.A C.55-6 Z=00. TX=06.5Y=90. TX=-800. S=2.500 D=0.0001   E1

HS5-8.A C.55-6 Z=00. TX=06.5Y=180.TX=-800. S=2.500 D=0.0001   E1

94

TABLE II

Orthotropic material data of normal-conducting and super-conducting coils.

a.) W VII-AS Coils:

Young's modulus	E_R, E_S	[GPa]	25.
	E_T	[GPa]	70.
Shear modulus	G_{RS}, G_{ST}, G_{TR}	[GPa]	10.7
Poisson's ratio	ν_{RS}, ν_{SR}		0.219
	ν_{ST}, ν_{RT}		0.112
	ν_{TR}, ν_{TS}		0.302

b.) Coils of TORE SUPRA:

Young's modulus	E_R	[GPa]	52.
	E_S	[GPa]	9.7
	E_T	[GPa]	69.
Shear modulus	G_{RS}, G_{ST}	[GPa]	2.
	G_{TR}	[GPa]	8.
Poisson's ratio	ν_{RS}, ν_{SR}		
	ν_{ST}, ν_{RT}		
	ν_{TR}, ν_{TS}		

c.) Euratom-LCT-Coil:

Young's modulus	E_R	[GPa]	62.
	E_S	[GPa]	53.
	E_T	[GPa]	120.
Shear modulus	G_{RS}	[GPa]	10.
	G_{ST}	[GPa]	26.
	G_{TR}	[GPa]	21.
Poisson's ratio	ν_{RS}		0.198
	ν_{ST}		0.126
	ν_{TR}		0.298
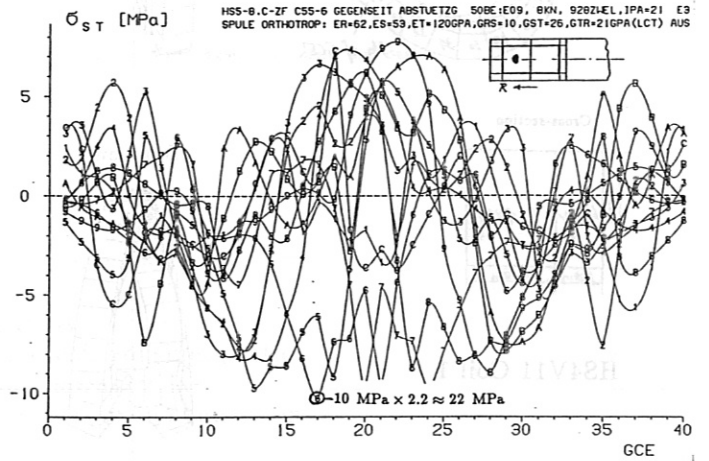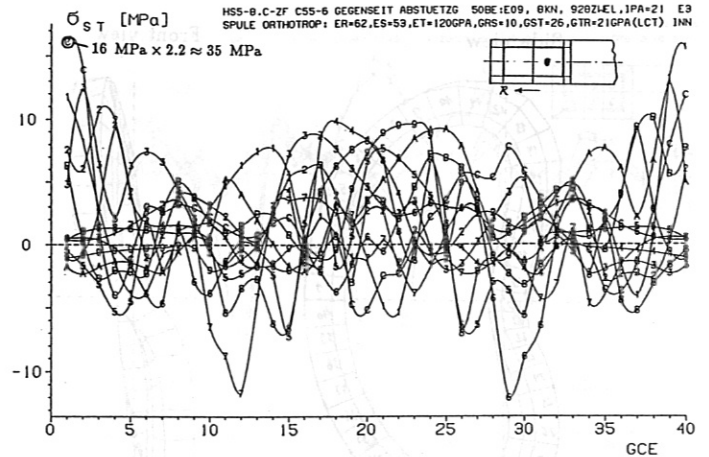
HS5-8: Shear stress σ_{ST}, orthotropic coil data.
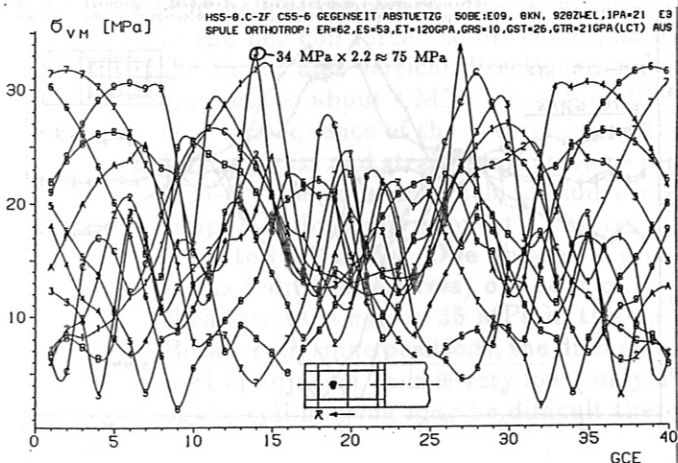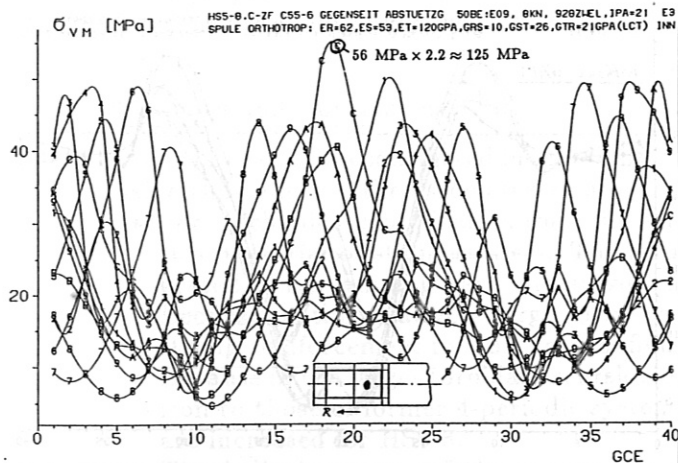
HS5-8: Equivalent stress σ_{VM}, orthotropic coil data.
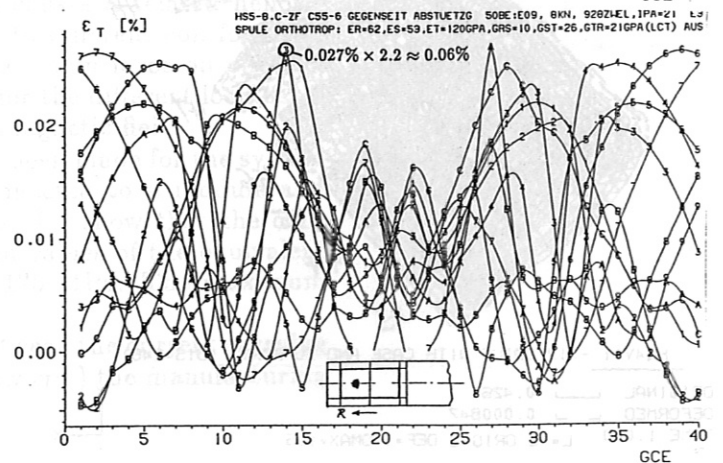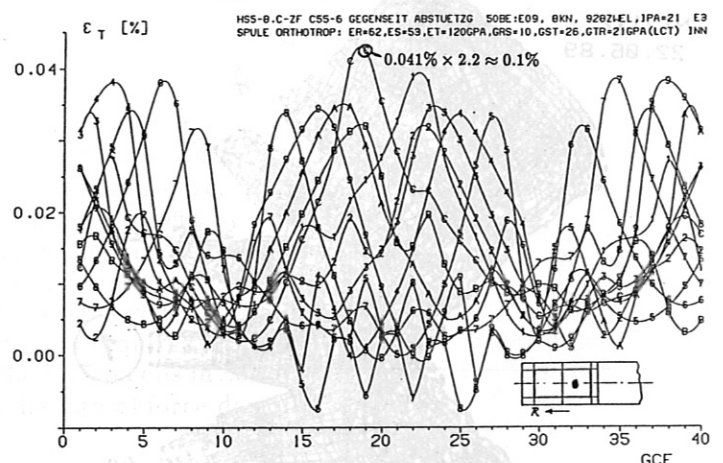
HS5-8: Tangential strain ε_T, orthotropic coil data.

Side view   Front view

No. of GCE's

Cross-section

40 $\frac{HA}{m^2}$ 32.1 $\frac{HA}{m^2}$
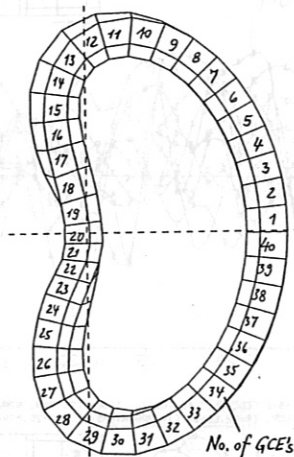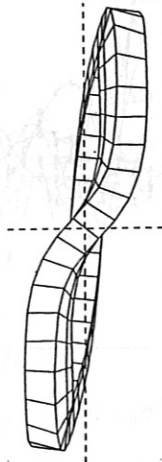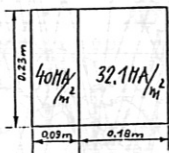
HS4V11 Coil 1.

Top view
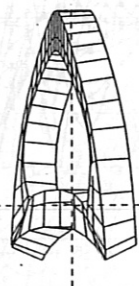
ADINA

NIJ117
22.06.89

6
5
4
3
2
(1)
48
47
46
45
44
43
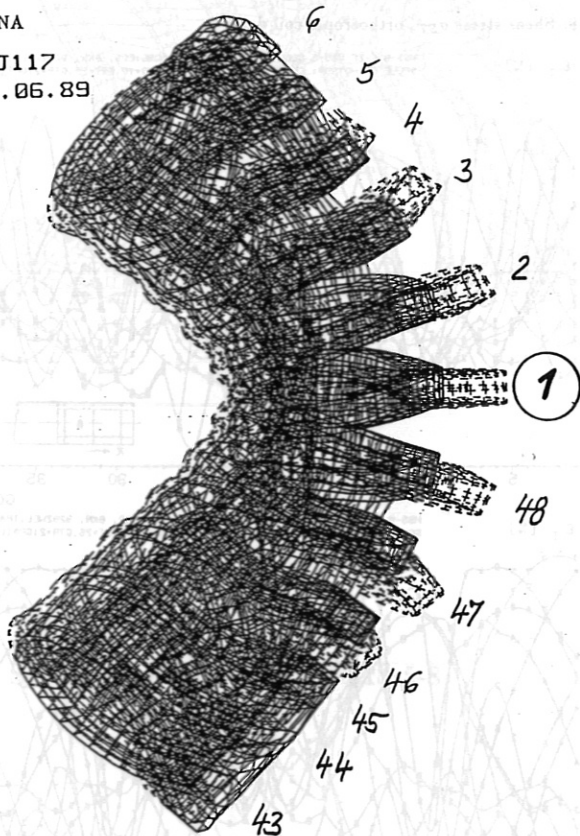
HS4V11 - 12 COILS WITH CASE AND SUPPORT (DIS=248)

ORIGINAL   0.426
DEFORMED   0.000847
TIME 1.000   L=-3 ORIG=2 DEF=1 DMAX=1.5

Coil configuration HELIAS 4-11: Displacement plot

HS4V11- SPULE 1*,6E/0, PKT=21, 12-SPULEN IN VERBAND MIT 3-D ABSTUE. EL.
SPULE-LINEAR ORTHOTROPIC-Er=62,Es=53,El=120GPa,Grs=10,Gst=26,Glr=21GPa.

σ_R [MPa]

without GAPS

HS4V11-GAPS,SPULE-1,6E/0-2X3,PKT=21 : JC=40.0/32.1 MA/(M*+2) : VER+KR
SP.-LIN. ORTHO.-Er=62,Es=53,El=120GPa,Grs=10,Gst=26,Glr=21GPa.dL=0.50mm

σ_R [MPa]

IPP--CMS NIJ

with GAPS

ADINA

GCE

HS4-11: Radial stress σ_R, orthotropic coil data.

HS4V11- SPULE 1*,6E/0, PKT=21, 12-SPULEN IN VERBAND MIT 3-D ABSTUE. EL.
SPULE-LINEAR ORTHOTROPIC-Er=62,Es=53,El=120GPa,Grs=10,Gst=26,Glr=21GPa.

σ_S [MPa]

without GAPS

HS4V11-GAPS,SPULE-1,6E/0-2X3,PKT=21 : JC=40.0/32.1 MA/(M*+2) : VER+KR
SP.-LIN. ORTHO.-Er=62,Es=53,El=120GPa,Grs=10,Gst=26,Glr=21GPa.dL=0.50mm

σ_S [MPa]

IPP--CMS NIJ

with GAPS

ADINA

GCE
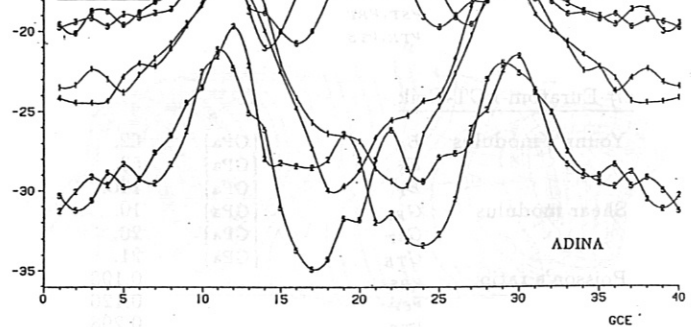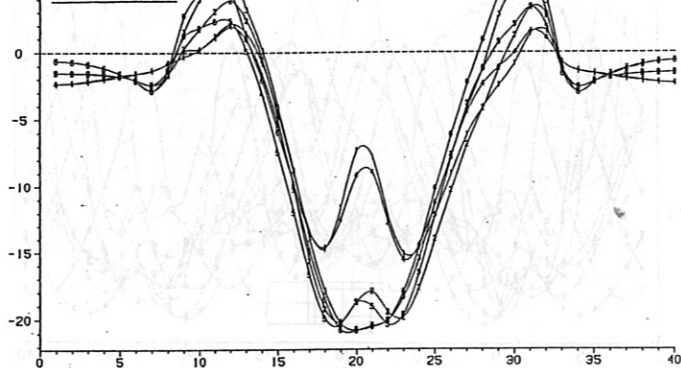
HS4-11: Lateral stress σ_S, orthotropic coil data.

96

HS4-11: Shear stress σ_{ST}, orthotropic coil data.

Critical issues

- High local current concentrations at the positions $\varphi = i\frac{2\pi}{M}, i = 1, .., M$, at the coil sides facing the torus centre.
- Low distances between the coils at these positions.
- Transfer of the forces between winding pack and coil housing, particularly in view of the gaps generated by cooling down.
- Support concept for the modular and the external coils in connection with the cryostat.
- Different load cases as a consequence of the τ-variation of the magnetic field.
- Shear stresses inside the coils.

Summary and Conclusions

From the load cases considered in view of the force and stress distribution inside the coils and the associated structure one can summarize:
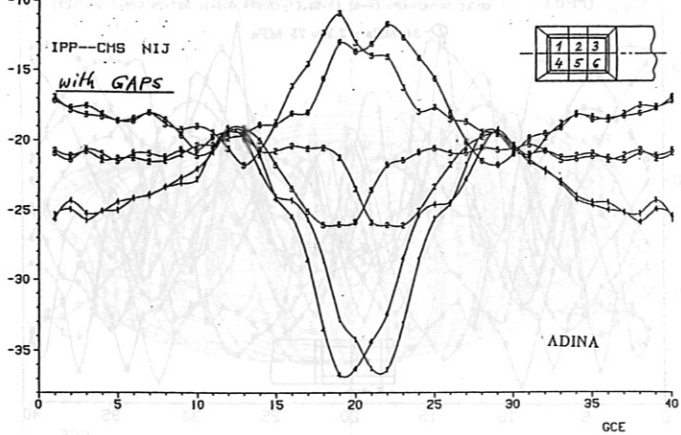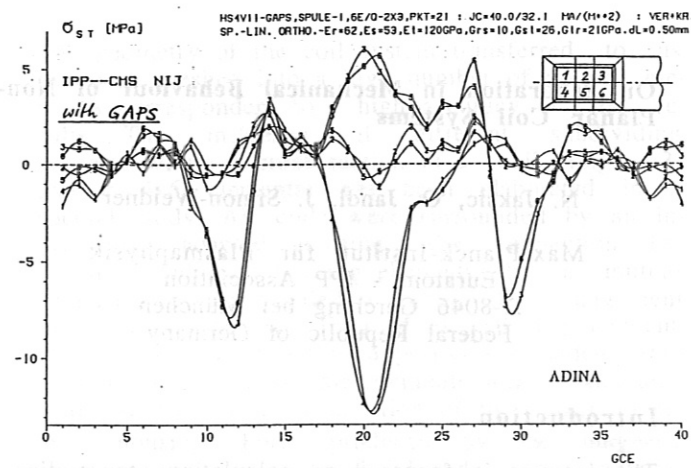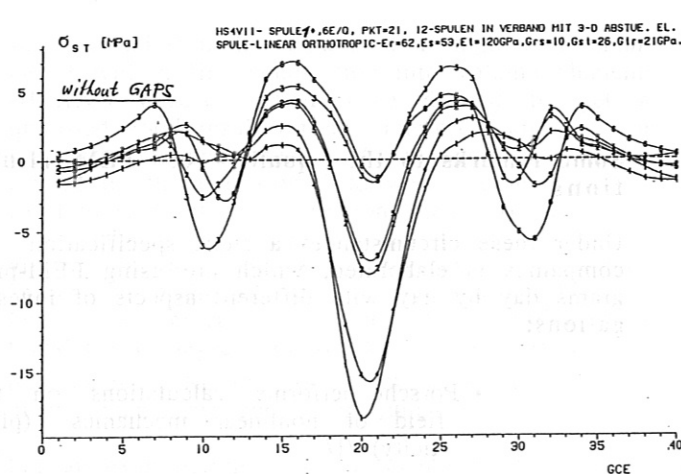
- For mechanical stabilization the coils need a reinforcement by structure material of stainless steel. The structure material can be integrated in the winding pack and surround the coils as a coil housing. Because of the relatively large virial stress of the system HS5-8 a strong reinforcement for this coil configuration is required.
- Because of the larger toroidal excursion of the HS5-8 coils in comparison to those of former 4-periodic systems, the lateral force densities are increased for HS5-8.
- The helical contour of the magnetic axis causes a related helicity in the net coil force vector, corresponding to different coil forces in the radial and vertical directions. The maximum force on one coil amounts to about 4 MN. The values differ for the different load cases as a consequence of the τ-variation of the magnetic field.
- Linear stress and strain computations have been made for the system HS5-8. The coils of a field period are connected to a module and supported by vault support. The results so far show that the coils seem to be feasible. One obtains maximum values of the equivalent stress (von Mises stress) of about $\sigma_{vM} = 125$ MPa. The maximum shear stress is $\sigma_{ST} \approx 35$ MPa in this case.
- Because, in some positions, the distance between the current carrying part of adjacent coils is very low (only a few cm) the manufacturing of the coil housing may be difficult there.

On Separation in Mechanical Behaviour of Non-Planar Coil Systems

N. Jaksic, O. Jandl, J. Simon-Weidner

Max-Planck-Institut für Plasmaphysik
Euratom - IPP Association
D-8046 Garching bei München
Federal Republic of Germany

Introduction

The interest is focussed on calculations to studies of the W VII-AS and W VII-X performed by a small team of engineers. The actual investigations are belonging to the following points:

1) Examination of calculations with regard to separation effects of coil 3 (W VII-AS)

2) Investigations of separation effects on the mechanical behaviour of non-planar coil systems to get familiar with possible candidates for W VII-X

The actual state of these calculations and some of the considerations in this context will be presented here.

Observations on the mechanical displacements of W VII-AS coils

The coil system of the experiment W VII-AS, which is under operation now, contains 5 periods, each of them is composed of 9 non-planar coils. Under these coils we distinct between 5 basic coil typs, which differ in there geometry basically. The interesting coil of the type 3 is located next to the additional TF-coil. An illustration of the coil system W VII-AS presents figure 1.

The W VII-AS coil system is assembled to achieve a magnetic field of 3 T in the case of 100% operating power. A certain milky shading of the coil 3 in the region of the pancake insolation at 50% of the operating power has got to the assumption, that the coil is exposed to some strong mechanical stresses or strains. Due to measurements we got the information of a circumferencial displacement, which is about the factor 6 higher compared to the correspondent displacement component predicted earlier.

Some remarks to the quality of FEM-calculations

Under these circumstances a short specification of companies is elaborated, which are using FEM-programs day by day with different aspects of investigations:

- Porsche performs calculations on the field of nonlinear mechanics (plasticity) /1/

- VW, Opel are using programs to predict the crash behaviour of cars /2,3/

- Daimler-Benz investigates on crash test by numarically simulations and performs e.g. research on 3-D stress analysis of gas turbine wheels /4,5/

- Ford optimizes body components /6/

- MBB optimizes the shape of the tail unit using a selfwritten code (without references)

- Fokker calculates acoustic effects on the dynamic behaviour of leightweight structures /7/

- Norwegian Contractors need automation procedures for there very large structure calculations /8/

As a consequence of these different applications based on FEM-calculations, a broad confidence exists to the quality and accuracy of numarically based results. Nevertheless it is possible to get wrong results by the usage of programs for problems, for which these programs are not written, or by application of unsatisfied boundary conditions.

Actual examination of earlier FEM-calculations

Some of the characteristics of the W VII-AS coil system calculations performed at IABG /9/ shall be descript shortly:

In a first step a global analysis of the mechanical displacements and stresses has been performed. The EFFI-code was used to evaluate the magnetic forces, the well known MSC/NASTRAN program was chosen for the stress analysis. The basic assumption at this state was the transposition of compression forces only by rigid-body elements linked between coil and support structure. In the case of tension forces the correspondent connections were disconnected. Figure 2 presents the geometry of coil 3.

In a second step the stresses of a single coil number 3 with a fine subdivision into volume elements (HEXA´s) were calculated. It was desired to get a qualified good result for an interpretation of the displacements and stresses. As before, the forces caused by the magnetic field were produced by the EFFI-code. At the cross section next to the support of the coil at the inner contour of the torus all the displacements were prescribed with values as results obtained from the first step. Frictionless coil movement was realized by coupling two translational degrees of freedom normal to the interfaces only. Results of formely calculated coil displacements are shown in <u>figure 3</u>.

For an examination of the mechanical behaviour of the coil 3 we proceeded in the following way:

The data set prepared for calculations with the FEM-Program MSC/NASTRAN has been transferred and transformed for a correspondent calculation with ANSYS which is available for the NET-team. The results produced by ANSYS show a good comparability, the displacements are about 20% to 30% higher, illustrated in <u>figure 4</u>.

A model was built up for the case of an extremly unrestricted movement of the coil without a supporting structure. To have a certain numerical stability, the coil was fixed by four smooth bars at the central point. This model was chosen to get the influence of a theoretical solution for the free movement. Results showed an increase of the circumferencial displacement component at a location, where measurements pointed to high displacements in circumferencial direction.

For a more realistic case a study was performed with different initial gap openings between coil and support structure. Initial openings of 0.0 and 0.1 mm had no effect on the coil movement, whereas the influence of 1.0 and 2.0 mm gap opening had an influence on the circumferencial displacement illustrated in <u>figure 5</u>.

Though these investigations are not currently finished, a preliminary resume might be deducted: The influence on the circumferencial displacement seems to be dependent on the initial gap width between coil and supporting structure. The initial gap width was not objective of former investigations.

Investigations on non-planar coil systems HS4V12 and HS4V11 for W VII-X

Objective of this study are considerations with respect to possible coil systems as candidates for W VII-X. Basic questions are the mechanical behaviour of the coils with fixed support within a toroidal arrangement. Further calculations should illustrate the effect of separation of a single coil on local mechanical stresses.

The geometry of the coil system transferred to us has been meshed into a high number of volume elements correspondent to a high accuracy of the results. The influence of different subdividing schemes within a cross section of a coil (e.g. 2x3, 3x4 or 4x6 elements) has been elaborated in a special study. All coils were surrounded by an individually adapted housing. The connection between the adjacent housing elements by a mutual support structure yielded a compact arrangement of the coil assembly. First of all, all displacements of the coil system within a period subdivided into a high number of volume elements were calculated restricted by a fixed connection of the coils with their housing. Forces produced by the magnetic field were defined by the EFFI code. The material of the housing and support elements is based on stainless steel (E=210 GPa), whereas the values of the material of the coils correspond the LCT coil (orthogonal material with E_{RR}=62 GPa, E_{SS}=53 GPa, E_{TT}=120 GPa, G_{RS}=10 GPa, G_{ST}=26 GPa, G_{TR}=21 GPa). Results of the v. Mises stress of the coil system are presented in <u>figure 6 and 7</u>.

The result of the displacement of the coil assembly were taken as a boundary condition to study the influence of the separation of a chosen coil 1 from their housing on the local stress behaviour: The structure of the coil subdivided into volume elements has been added by a separated housing connected by gap elements only. A certain separability combined with a free body motion could be realized by the use of different initial gap widths (coil - housing). The magnetic forces calculated by EFFI had been connected to the coil, the selected set of displacements of the global analysis has been prescribed on the outer surfaces of the housing.

The results of the candidate HS4V11 at coil 1 do not have any remarkable effect with respect to the radial and circumferencial stress components in the case of an initial gap width of 0.0 mm (the maximum radial stress values is -22 MPa, and in circumferencial direction 53 MPa). Some stress components of coil 1 can be seen in <u>figure 8 to 11</u>, <u>figure 12</u> shows the difference of the circumferencial displacements between coil and housing. Almost all stress components show increasing values with an increase of the intial gap width 0.1 and 0.2 mm (correspondent to an initial gap width of 0.2 mm the maximum stress value is radial -28 MPa, lateral -25 MPa and circumferencial 78 MPa).

99

Other techniques which are applicable for great non-linear structures

Some characteristics of further methods will be described here which might be applied for calculations of great non-linear structures. Simultaneously some remarks to programs used at IPP will be given:

- Submodeling Technique:
  Characteristic: Global model -> Submodel
  (ADINA, ANSYS, MARC)

  Some relevant displacements of a global analysis are used as prescribed values at the boundaries of a submodel with a finer mesh. The interpolation of the result is improved. A corrspondent improvement of the displacements which are results of the global analysis (these are prescribed boundaries of the submodel) can not be realized. This technique was used to calculate the separation behaviour of e.g. HS4V12 and HS4V11.

- Superelement-Technique:
  Characteristics: Superel. A <-> Superel. B
  (ADINA, ANSYS, MARC)

  Some restrictions are necessary for non-linear calculations: All non-linearities have to be handled within the superelement 0 (residual structure). A mutual influence between the superelements is realized by the definition of the boundary nodes of each superelement. Applying implicit methods (closed solution) it has to be mentioned, that neither the global stiffness matrix nor the submatrix of a superelement has to be singular.

- Multibody-Technique:
  Characteristics: Body A <-> Body B
  (MARC, ADINA)

  The contact behaviour of individual bodies can be calculated by special programs. The material of each body can be plastified. The application of mutual force vectors acting on the surface of the bodies is realized by special techniques (explicit methods).

Summary

Different programs are available for calculations of the mechanical behaviour of non-planar coil systems. Depending on the actual requirement the use of a code has to be chosen very carefully. The performance and calculated results have to be presented with a high level of accuracy. Simultaneously, we observe a high computer capacity offered on the market today. These two points - high accuracy of results and high computer capacity - lead to structural models with a high number of elements with the effect of more time needed to build up data sets and to interpret the results. Nevertheless we hope to present the results to content employers.

References

/1/ E. Schelkle
Supercomputers: A Milestone for Non-Linear Finite Element Applications
Supercomputer Applications in Automotive Research and Engineering Development, Oct. 86,
Computational Mechanics Publications, Boston

/2/ T. Scharnhorst, R.-W. Schettler-Köhler
FEM-CRASH- Experiences at Volkswagen
Supercomputer Applications in Automotive Research and Engineering Development, Oct. 86,
Computational Mechanics Publications, Boston

/3/ K. Hieronimus, E. Nalepa
Introduction and Use of a Supercomputer at OPEL E.G. for Crash Simulations
Supercomputer Applications in Automotive Research and Engineering Development, Oct. 86,
Computational Mechanics Publications, Boston

/4/ D. Radaj
History, Status and Trends of Automotive Numerical Analysis
Supercomputer Applications in Automotive Research and Engineering Development, Oct. 86,
Computational Mechanics Publications, Boston

/5/ H. Hempel
3-Dimensional Stress Analysis of Gas Turbine Wheels - Strategy for Generating the Finite Element Model and Thermal Boundary Conditions Automatically
Proceedings of the MSC/NASTRAN European Users's Conference, April 85

/6/ D. Zimmermann, E. Birkholz
Design Sensitivity Analysis for Body Components
Proceedings of the MSC/NASTRAN European Users's Conference, April 85

/7/ J.J. Wijker
Acoustic Effects on the Dynamic Behaviour of Leightweight Structures
Proceedings of the MSC/NASTRAN European Users's Conference, April 85

/8/ A.J. Abbey, C.A. Knights
Automation of Structural Analysis Using MSC/NASTRAN
Proceedings of the MSC/NASTRAN European Users's Conference, April 85

/9/ R. Mathis, J. Sapper
Application of Finite-Element Methods to the Design of a Torus-Shaped Magnetic Confinement System for Fusion Experiments
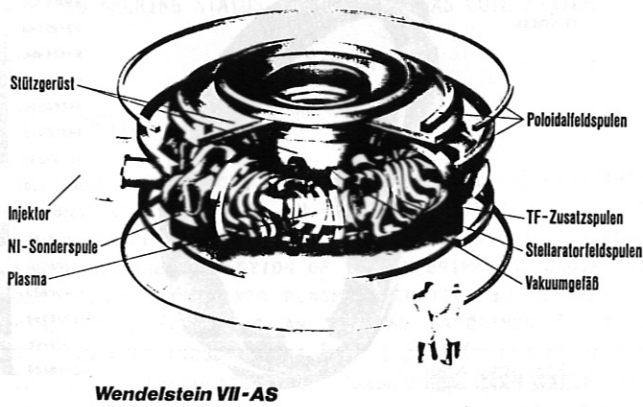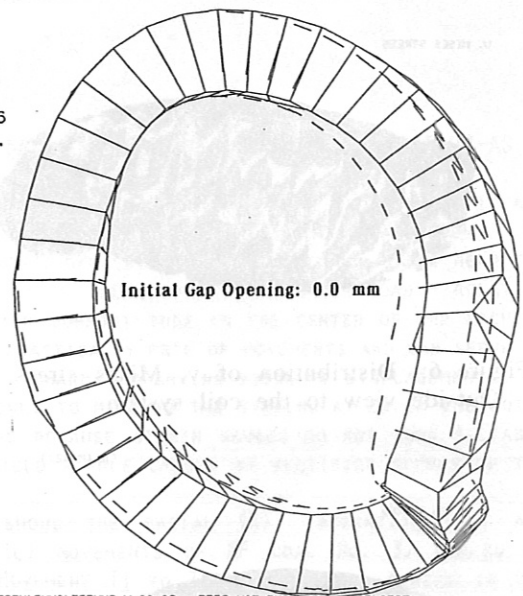Computational Techniques & Applications: CTAC-87, 1988

Figure 1: Illustration of the W VII-AS stellarator

Labels in Figure 1:
Stützgerüst
Injektor
NI-Sonderspule
Plasma
Poloidalfeldspulen
TF-Zusatzspulen
Stellaratorfeldspulen
Vakuumgefäß

Wendelstein VII-AS

2 pancakes
8 turns

R   radial coil direction
S   lateral coil direction
T   circumference coil direction

R,S,T   local Cartesian coordinates
x,y,z   global Cartesian coordinates

overall diameter 1300

glass fiber tape,
overlapping half
stranded copper wire
(flexible)
preimpregnated glass
fiber (winding insula-
tion, 3 layes)
water cooled wire
(solid, soft annea-
led copper)

Figure 2: Cross section of a coil used for W VII-AS

a)
$\Delta l_{therm} = 1,16 mm$

b)
top
$\Delta l = 2,77 mm$
outward
deformed
bottom

Figure 3: Calculated displacements of coil 3

ANSYS 4.3
MAY 22 1989
12:17:45
PLOT NO.   6
POST1 DISPL.
STEP=1
ITER=5

YV=1
DIST=.684
XF=1.92
YF=.676
ZF=-.0025
HIDDEN
DMAX=.00082
DSCA=83.4

Initial Gap Opening: 0.0 mm

MAGNETSPULENHALTERUNG W-11-AS   RBES MIT ZUGKRAEFTEN GELOEST

Figure 4:

Correspondent calculations of coil 3 with ANSYS got displacements which are 20% to 30% higher (initial gap width: 0.0 mm)
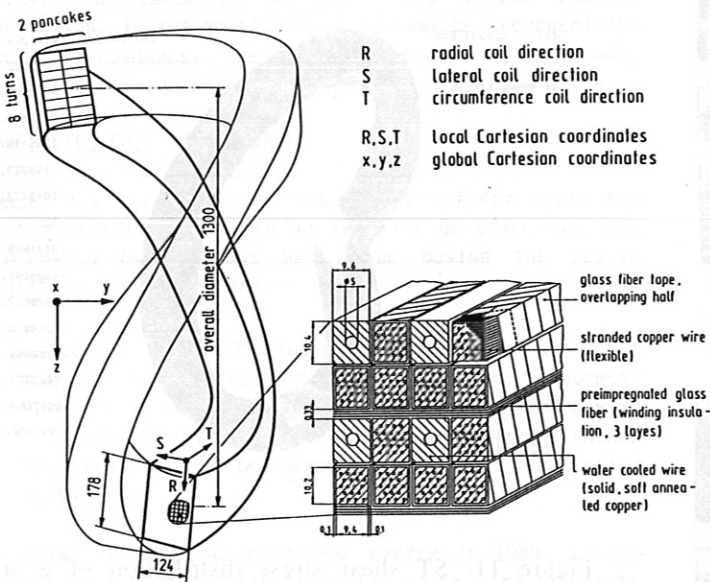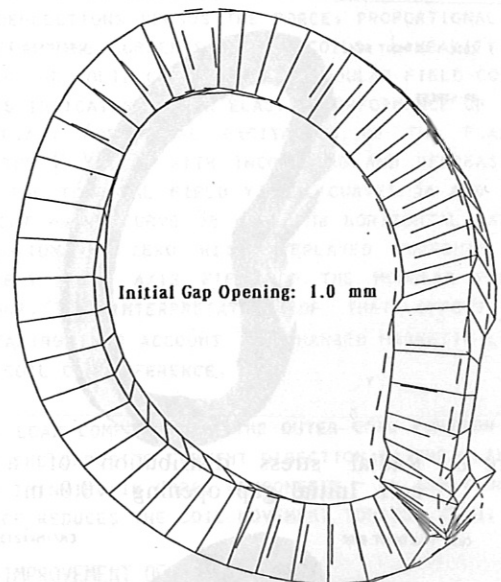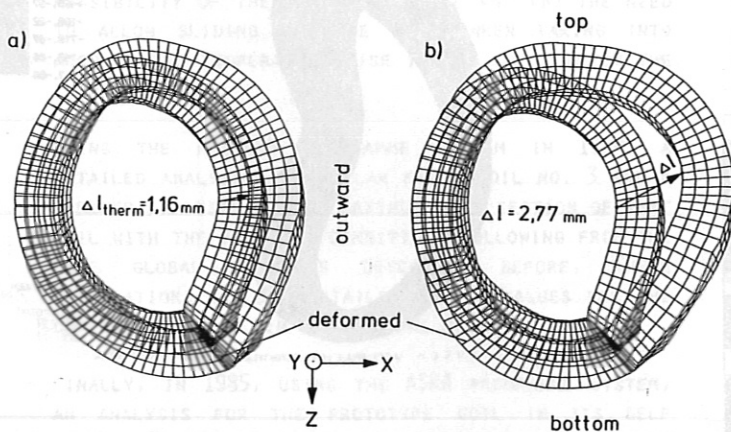

Initial Gap Opening: 1.0 mm

MAGNETSPULENHALTERUNG W-11-AS   RBES MIT ZUGKRAEFTEN GELOEST

ANSYS 4.3   YV=1
JUN 21 1989   DIST=.684
13:24:34   XF=1.92
PLOT NO.   1   YF=.676
POST1 DISPL.   ZF=-.0025
STEP=1   HIDDEN
ITER=5   DMAX=.00169
                  DSCA=40.5

Figure 5:

Increasing gap width of 1.0 mm shows an influence on the circumferencial displacement